BERGISCHE
UNIVERSITÄT
WUPPERTAL

Analysis, Extending and Embedding of Tellinen's Scalar Hysteresis Model

Dissertation

Jan Kühn

2023

Supervisor	Prof. Dr. Matthias Ehrhardt
Co-Supervisor	PD Dr. Andreas Bartel

Contents

List of Figures

List of Tables

1 | Introduction

This chapter gives an overview of the application areas in which magnetic fields occur. Based on these examples, motivational questions are raised, which this dissertation attempts to answer. The reader is presented what the expectations and objectives are. The structure and organization of this thesis will be outlined.

In order to give an idea of what the term hysteresis is based on in general, this topic is explained by means of an example. This example already exhibits some similarities with later problems.

Furthermore, this work is placed in the current state of research in order to achieve a clear distinction on what has already been researched and what part of this work represents new findings.

1.1. Application Examples and Motivation

Magnetic fields are ubiquitous. Even the very weak earth magnetic field can be used in the form of a compass and has thus significantly influenced the history of mankind. An increasing level of technology has made measuring magnet fields common. The majority of today's smartphones have a built-in magnetometer that enables a digital compass.

The current environmental policy focuses on electrically powered vehicles (e.g. cars, trucks and trains), especially in combination with battery power. This circumstance poses various challenges for the electric motors used, e.g., the space limitations, the desired high efficiency or the use at various outside temperatures. So both industry and research communities are currently very interested in efficient electric motors that are well adapted to their intended use case.

However, there is currently also a great public interest in the use of generators, especially with the background of regenerative energy generation. Wind turbines and hydroelectric power plants, for example, convert kinetic energy into electrical energy. Here, the efficiency of the conversion is a key issue. This efficiency has been increased by modern materials and optimized designs and continues to be a research goal.

From the electro-technical field, transformers can be cited as an example. There, two circuits are coupled with each other via magnetic fields in order to achieve a transformation of the voltage.

Highly technological examples include applications in magnetic resonance imaging in the medical field and particle accelerators in the field of experimental physics. There, very strong and at the same time very controlled magnetic fields are required.

Nowadays, a wide range of materials is available (for examples see [25]). This means that the best possible selection of materials can be made depending on the application.

Motivation The above examples are intended to give a small insight into the wide range of applications of magnetic fields. In addition to measurements of prototypes, theoretical modeling is of course also a core part of the development process. In many applications, efficiency plays a central role. In order to optimize this efficiency, precise knowledge of the course of the magnetic fields and their propagation in different materials is necessary. Therefore, there are different approaches for material models.

However, efficiency also depends on losses. There are various sources of losses in an electromagnetic system. These are characterized by loss models. Losses are usually accompanied by the generation of heat. Hence, not only the magnetic material properties are interesting, but also the thermal ones. In the end, the magnetic properties are again dependent on the temperature. This results in a complex integrated system. The more computing capacity is available, the more complex models can be used and more effects can be taken into account.

This dissertation focuses on the special choice of ferromagnetic materials. These materials have the special effect of magnetic hysteresis and are important, because of the particularly strong resulting magnetic fields. The following questions will be the motivation of this dissertation. A visual overview is given in Figure 1.1 and a more detailed version of the expectations and objectives can be found in the next section.

▶ What magnetic behavior do ferromagnetic materials possess?
Chapter 2 presents the basic features of magnetism including the hysteresis effect.

▶ How can magnetic hysteresis be mathematically modeled?
Chapter 3 defines a hysteresis model without thermal dependence.

▶ Are there particular losses associated with the effect of hysteresis and how can they be modeled?
Section 4.1 describes a hysteresis loss model.

▶ What effect does a temperature change have on the hysteresis model?
Section 4.2 states an extension of the hysteresis model including thermal dependence.

▶ How to combine all these aspects into a numerical simulation?
Chapter 5 develops a numerical simulation of a benchmark problem.

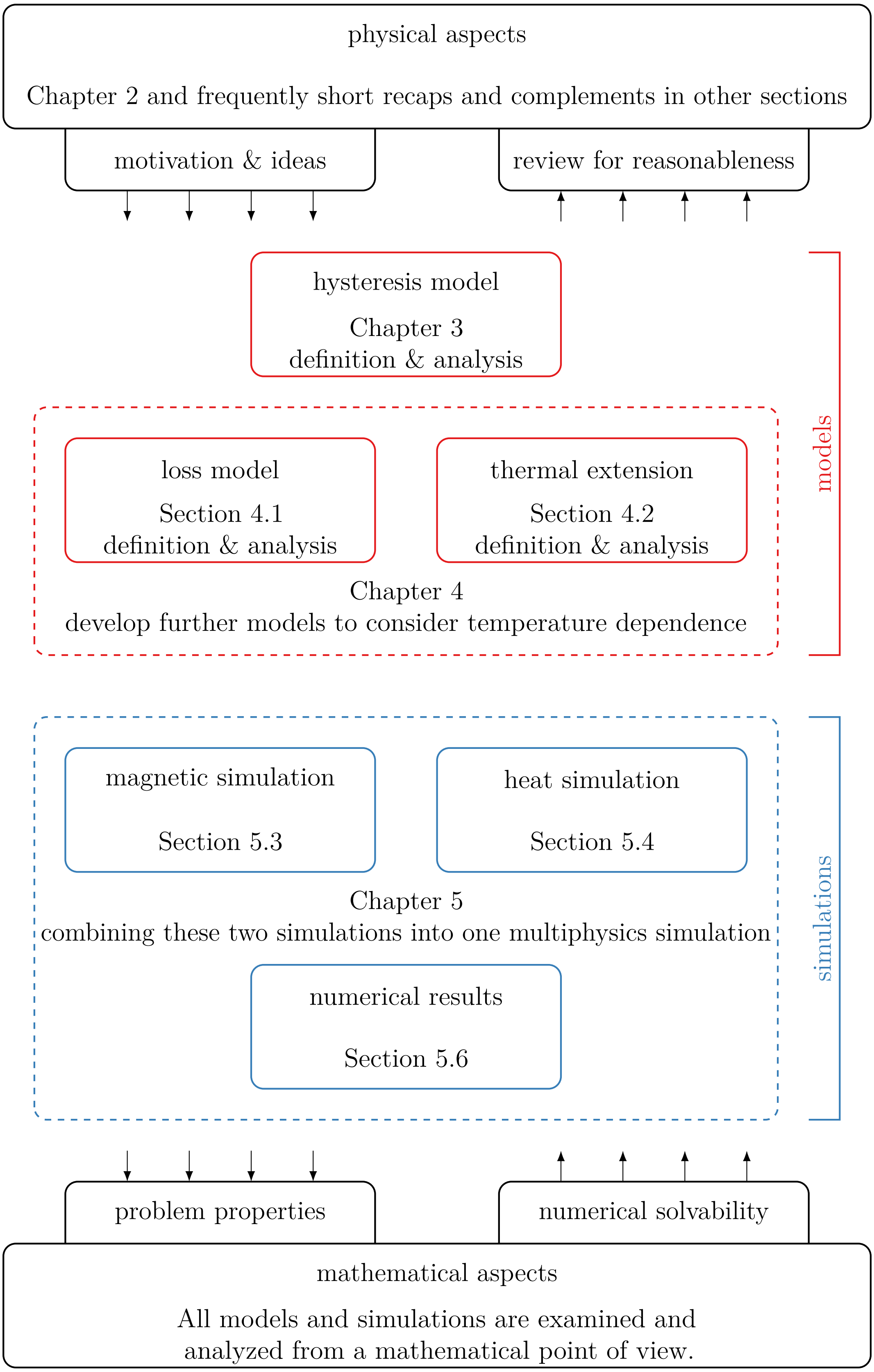

Figure 1.1.: Overview of the structure of this thesis.

1.2. Expectations and Objectives

This dissertation has several focus areas. All sections have in common that it is a dissertation with mathematical background. Nevertheless, it is tried to perform the analyses from different points of view. From the purely mathematical area, methods for proving existence and uniqueness of solutions are used. From a physical point of view it is discussed whether these solutions are reasonable for the underlying models. The existing models will be extended by further parameters, with special focus on a temperature dependence. Under the numerical aspect, the models and physical relations will be combined to a thermal magnetic simulation.

Unfortunately, what this dissertation cannot provide are real measured values on the extended models. It tries to compare the results with available literature and to check for general reasonability. Thus, in some places, examples and parameters of an academic nature will have to suffice.

Due to the wide interdisciplinary spread of the approaches, it is unfortunately not possible to discuss each approach in detail under every aspect. The achievement of this dissertation is mainly bringing together the different aspects. The final result is a numerical simulation for thermal magnetic field calculation, including magnetic hysteresis, a hysteresis loss model and temperature dependence.

The document is structured as follows.

▶ The remainder of this chapter is intended to provide a very rough overview and motivation. A concrete example is used to illustrate the concept of hysteresis. A rough positioning within the literature is given.

▶ In Chapter 2, the reader is introduced to electromagnetism. The physical quantities involved are introduced and Maxwell equations are presented. These equations are describing the interaction of electrical and magnetic fields with electric charges and currents. In addition to the fundamental Maxwell equations, one needs other models for material equations. Here the focus lies on the relationship of the two magnetic fields $\vec{H}$ and $\vec{B}$.

Simplifying assumptions are made and alternative formulations are introduced, such that the overall problem is reduced. The result is the so-called Curl-Curl Equation, which is the basis for all further considerations. From a numerical point of view, this equation is adjusted and embedded in a benchmark problem. Thereby, the relation between $\vec{H}$ and $\vec{B}$ still remains open.

To explore the physical claims and relationships of $\vec{H}$ and $\vec{B}$, an introduction and overview of magnetism is given in the second part of Chapter 2. Phenomena at the micro and macro levels are presented. This allows materials to be classified. The class of ferromagnetic materials shows effects of hysteresis. In this context, it is explained what hysteresis means in relation to magnetic fields. A motivation in which application the effect of hysteresis is explicitly desired and where it is undesired is explained by means of an example of a stepper motor.

At the end of Chapter 2, the reader should have gained a basic understanding of magnetic hysteresis and should have an idea of what is required of a mathematical hysteresis model from a physical point of view. Furthermore, it should be clear which missing part of the hysteresis model is supposed to fill in the numerical simulation of the benchmark problem.

► In Chapter 3, the focus is on the mathematical consideration of a particular magnetic hysteresis model, the Tellinen model [54]. It is first formally defined and the chosen approaches are physically motivated. Then, basic properties are presented.

For a deeper investigation, suitable mathematical approaches have to be introduced beforehand. This leads to the consideration of first order reversal curves (FORCs) and the artificial extension of their definition range. These extended FORCs allow an investigation if and under which conditions Tellinen's model fulfills the physical requirements.

The existence and uniqueness of solutions of the model are examined and whether the model shows a basically stable behavior. Approaches are developed and it is explained how the model could be incorporated into the numerical simulation of the benchmark problem.

At the end of Chapter 3, the reader should be familiar with the notation and approaches used by the interpretation of Tellinen's model. The approaches used to study the model should be comprehensible.

► Chapter 4 deals with extensions of the original Tellinen model. On the one hand, a loss model is presented that is adapted to Tellinen's model in its approaches. On the other hand, a thermal dependence is added to Tellinen's model. This allows a simulation of the approximations where heat generation occurs due to losses and how the model reacts to it. Both model extensions are examined using similar approaches as in Chapter 3. Their physical meaningfulness is discussed.

By the end of Chapter 4, the reader should be familiar with both extensions and their properties.

► Chapter 5 takes up the preparations from Chapter 2 and elaborates the benchmark in detail. The finite difference method is used with offset grids. This simulation brings together the findings of the previous chapters. The magnetic field simulation and the thermal simulation are executed one after the other. Special attention is paid to the boundary conditions and the material transition inside. The presented numerical results are analyzed and it is discussed again, if the results fit the physical requirements.

With the results of Chapter 5 the approaches are evaluated. The results show good agreement with the expected results and the models are considered as validated.

► The conclusion in Chapter 6 summarizes the insights of the dissertation. These are finally evaluated and placed in the overall context. The disadvantages and limitations of the models are also explicitly addressed. The reader should therefore be presented

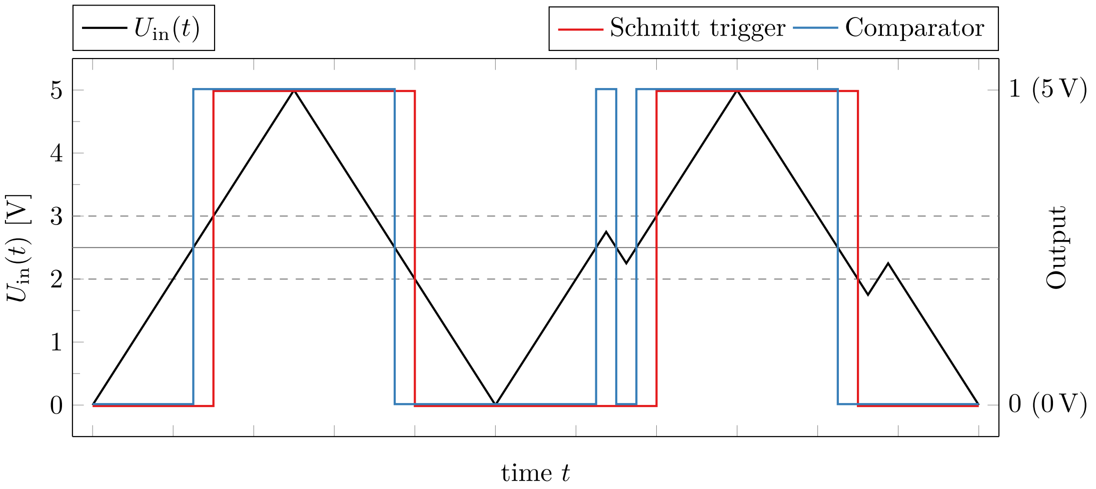

Figure 1.2.: Comparison of the output of a comparator and a Schmitt trigger.

with a most unbiased view of the research results. An outlook on possible further research is given.

1.3. Introduction to Hysteresis: an Example

Before the explicitly used magnetic hysteresis model is presented in Chapter 3, a short overview on the term hysteresis shall be given. This will be illustrated by an example from electrical engineering [136, 138–140].

The hysteresis effect can be observed in a wide variety of applications [22, 51, 56]. In general, a system with hysteresis depends not only on its independent input values. It additionally depends on the previous values of its output. To illustrate this behavior, an example is given below.

A continuous input voltage $U_{\text{in}} \in [0, 5]$ (in V) shall be discretized to the binary states 1 (5 V) and 0 (0 V). This is done once with a simple *comparator* (without hysteresis) and once with a *Schmitt trigger* (with hysteresis). Figure 1.2 shows a graphical comparison of the different behaviors for a selected excitation $U_{\text{in}} = U_{\text{in}}(t)$.

The comparator can easily be described by a function $f_{\text{comp}} : [0, 5] \to \{0, 1\}$ with

$$f_{\text{comp}}(U_{\text{in}}) = \begin{cases} 1 & \text{if } U_{\text{in}} \geq 2.5 \ , \\ 0 & \text{if } U_{\text{in}} < 2.5 \ . \end{cases} \tag{1.1}$$

It is comparable to a simple toggle switch with switching point at 2.5 V. The Schmitt trigger has two switching points $U_{\text{T}-} = 2\,\text{V}$ and $U_{\text{T}+} = 3\,\text{V}$. $U_{\text{T}+}$ is the *positive-going threshold voltage* and $U_{\text{T}-}$ the *negative-going threshold voltage*. The Schmitt trigger changes its output to 1, only if $U_{\text{in}} \geq U_{\text{T}+}$ holds and likewise to 0 only if $U_{\text{in}} \leq U_{\text{T}-}$ holds. In all other cases it does not change its output and keeps its old state.

This feature has advantages in the application for noisy inputs. The simple comparator changes its state over and over as soon as there is even a minimal noise in the

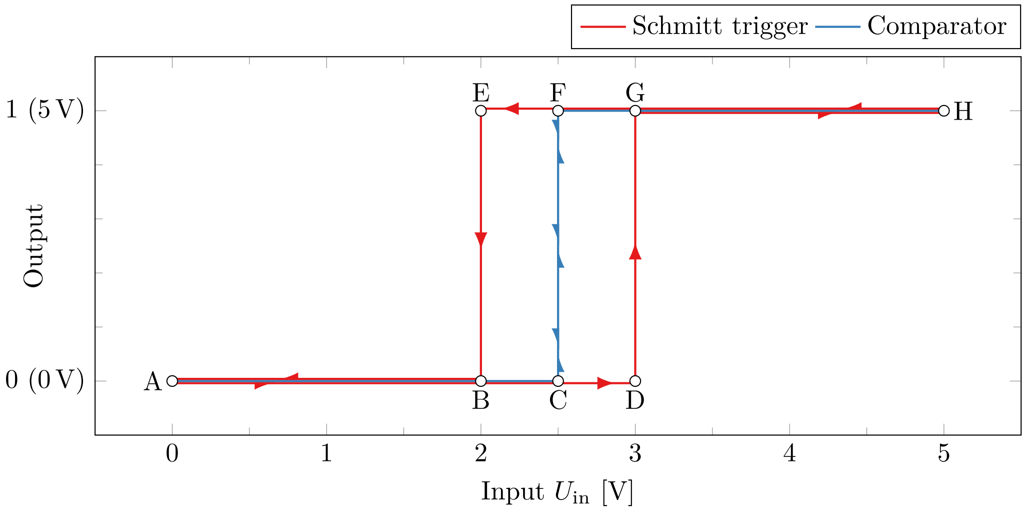

Figure 1.3.: Input vs output for a comparator and a Schmitt trigger.

range of its switching point. The Schmitt trigger on the other hand is immune to small noise. After it has changed its state, the input voltage must change its value by $U_{\text{T}^+} - U_{\text{T}^-}$ to trigger another change of state. Therefore, the value $U_{\text{T}^+} - U_{\text{T}^-}$ can be used to quantify the strength of the hysteresis effect.

As seen in Figure 1.2 the Schmitt trigger has some time delay in comparison to the simple comparator. Commonly, hysteresis effects add some sort of delay to the system. Or from another point of view hysteresis can add additional resistance, work, energy or in general some sort of obstacle to change the current state of the system.

Another visual representation of hysteresis behavior is shown in Figure 1.3. It shows the input voltage versus the output state for the comparator and the Schmitt trigger. Assuming both systems start in the state of 0 (0 V) and with $U_{\text{in}} = 0\,\text{V}$. U_{in} is increased to 5 V and decreased back to 0 V. The comparator follows in the sequence of points

$$\text{A} \rightarrow \text{B} \rightarrow \text{C} \rightarrow \text{F} \rightarrow \text{G} \rightarrow \text{H} \rightarrow \text{G} \rightarrow \text{F} \rightarrow \text{C} \rightarrow \text{B} \rightarrow \text{A}\,. \tag{1.2}$$

The forward and backward paths are the same. Thus the output can be defined as a function of the input U_{in}, as done in (1.1). The Schmitt trigger proceeds along the sequence

$$\text{A} \rightarrow \text{B} \rightarrow \text{C} \rightarrow \text{D} \rightarrow \text{G} \rightarrow \text{H} \rightarrow \text{G} \rightarrow \text{F} \rightarrow \text{E} \rightarrow \text{B} \rightarrow \text{A}\,. \tag{1.3}$$

The forward and backward paths differ and thus no function solely depending on U_{in} can model this behavior. In the above cycle, for an input of $U_{\text{in}} = 2.5\,\text{V}$ the output is once 0 (at C) and another time 1 (at F). Thus, for the same input the model outputs different values, depending on the history of the system (in this case: if it is in state 0 or 1). Such a system is denoted as a path dependent system.

This section should give a brief insight that systems with hysteresis are not necessarily easy to model and calculate. The relationship between the input variables and output variables cannot necessarily be represented by functions. In the further course of this work, hysteresis will be examined in special relation to magnetic fields and ferromagnetic materials.

1.4. State of the Art

At this point, a brief overview and positioning in the current state of research will be given.

Models for magnetic hysteresis were and still are actively researched [20]. It currently exists a broad spectrum of models with many different approaches (examples: [29, 40, 42, 43, 46, 56, 57]). A comparison of different hysteresis models can be found in [50].

These models form the basis, but it is not necessarily easy to embed them in a numerical simulation, i.e., the chosen hysteresis model should fit the chosen numerical approach. As examples [24, 55] can be mentioned.

The effect of hysteresis holds another source of electrical losses. Quantifying these is an important task for loss models. Thus, many hysteresis models have been extended by loss calculations [15, 18, 23, 26]. The difference between those approaches has been studied intensively [33, 44, 50].

The effect of magnetic hysteresis is temperature dependent. Accordingly, there are temperature-dependent extensions to various hysteresis models [16, 27, 47].

This closes the circle that a temperature change can be calculated from the hysteresis losses and this fact is taken into account by the hysteresis model. Thus, however, the numerical simulation must also include several physical aspects. For example, an excitation of the materials can be generated by external currents. The induced magnetic field generates hysteresis losses. Heat propagates within the materials and in turn influences the hysteresis behavior. When talking about a simulation in the context of this dissertation, is is a synonym for a multiphysics simulation. However, this also poses numerical challenges since effects such as electric currents, magnetic fields, and temperature can be on different time scales. Thus, in order to implement such a simulation in a meaningful way, appropriate numerical approaches have to be pursued. Worthwhile to mention are the co-simulation and multirate approach [145–149, 152, 153].

The chosen hysteresis model within this dissertation is Tellinen's model [36, 54]. It will be presented and discussed in Chapter 3. According to [50], this model is considered to be more simple. Nevertheless, it agrees relatively good with measured values. An approach to loss calculation has already been stated in the original source. In [38], the author of this dissertation and his coauthors presented an alternative approach. This approach is presented and further explored in Section 4.1. A thermal extension of Tellinen's model is presented in [37], again by the author of this dissertation and his coauthors. This is stated and analyzed in more detail in

Section 4.2. A numerical integration of the Tellinen's model and its extensions into a finite difference approach is done in Chapter 5.

Thus, this dissertation fits well into existing literature and fills a gap. The steps that have already been performed for various other hysteresis models are repeated here using Tellinen's model. This has not yet been published in this form, at least the author is not aware of anything to this end.

2 Electromagnetism – Theoretical Background Knowledge

In this chapter a rough overview of the theoretical background of electromagnetism is given. Thereby, the topic is approached from different sides.

▶ From the field of theoretical physics, the fundamental Maxwell's equations, the material equations and all required physical quantities are introduced in Section 2.1. For the general case, certain assumptions are made and thus simplify the system of consideration. This leads to the Curl-Curl Equation, a partial differential equation (PDE) of parabolic type. It serves as the basis for the numerical benchmark in Chapter 5. Also, it is presented how to reduce the consideration from multidimensional to scalar quantities for the specifically chosen benchmark problem. It remains an open question how to incorporate the effect of hysteresis into the benchmark problem.

▶ In order to explain the effect of magnetic hysteresis, the underlying physical phenomena are explained in Section 2.2. Weiß domains and Bloch walls are examined. Based on this background information, a classification of materials is established. It shows the characteristic properties of ferromagnetic materials and their difference from other materials.

▶ From these physical motivations the effect of hysteresis can be quantified in a mathematical sense in Section 2.3. The properties of the saturation curve are presented and requirements for a hysteresis model are derived from these. Different approaches for hysteresis models are discussed.

▶ In Section 2.4 the operation of a stepper motor is presented. With this concrete example, it is illustrated that applications depend on different types of materials. This example should also motivate why the combination of magnetic field calculation including the effect of hysteresis and temperature is of particular interest.

The objective of this chapter is to lay the foundations for the hysteresis model in Chapter 3. From a mathematical point of view, the task of such a model and its objective shall be motivated. From the physical point of view, the relationships are to be presented, so that the hysteresis model can be checked for physical meaningfulness.

2.1. Maxwell's Equations

The fundamentals of electromagnetism are described by Maxwell's equations (2.1) [134, 135, 21, 78]. The quantities involved are listed in Table 2.1.

Table 2.1.: Overview of the symbols, units and descriptions of the used quantities.

Symbol	Unit	Description
ρ	$\mathrm{C/m^3}$	electric charge density
$\vec{J}$	$\mathrm{A/m^2}$	electric current density
$\vec{E}$	$\mathrm{V/m}$	electric field
$\vec{D}$	$\mathrm{C/m^2}$	electric displacement field, electric induction
$\vec{H}$	$\mathrm{A/m}$	magnetic field strength
$\vec{B}$	T	magnetic flux density
μ	$\mathrm{H/m}$	magnetic permeability
ϵ	$\mathrm{C/(V\,m)}$	permittivity
σ	$\mathrm{S/m}$	electric conductivity

$$\vec{\nabla} \cdot \vec{D} = \rho \tag{2.1a}$$

$$\vec{\nabla} \cdot \vec{B} = 0 \tag{2.1b}$$

$$\vec{\nabla} \times \vec{E} = -\frac{\partial \vec{B}}{\partial t} \tag{2.1c}$$

$$\vec{\nabla} \times \vec{H} = \vec{J} + \frac{\partial \vec{D}}{\partial t} \tag{2.1d}$$

In the selected representation (2.1), all fields are assumed to have three spatial dimensions. The Maxwell equations contain both of Gauss's laws, i.e., eqs. (2.1a) and (2.1b), Faraday's law (2.1c) and Ampère's law with added displacement current (2.1d). With this basic theory, the interaction between the fields and globally the phenomena of electromagnetism are described. For example, magnetic monopoles cannot be realized. However, since the full set of equations is quite difficult to solve numerically, there are approximations for certain assumptions. This will be discussed in Section 2.1.2. The focus will be on fields $\vec{H}$ and $\vec{B}$, but these quantities must be embedded in the overall system. An isolated calculation is not possible.

Remark 2.1. Maxwell's equations (2.1) form an underdetermined system of equations. These equations still have to be supplemented by material equations such that a uniquely solvable system results. Each of these material equations describes the relation between two fields. While Maxwell's equations are fundamental equations, the user has the choice of the material model. Material equations are the focus of the next section.

2.1.1. Material Equations

To extend Maxwell's equations (2.1) to a fully determined system, three additionally relations are added. They are a mathematical description of the materials behavior and relate two of the fields in the combination

$$\vec{J} \leftrightarrow \vec{E}\,, \qquad \vec{D} \leftrightarrow \vec{E}\,, \qquad \vec{B} \leftrightarrow \vec{H}\,. \tag{2.2}$$

Depending on how these relations are defined, different material properties may or may not be reflected. First, one of the simplest choices of material models is introduced. After that, approaches for more complex models will be presented. In particular, the focus will be on the relation between $\vec{B}$ and $\vec{H}$.

The quantity σ in the SI unit S/m is the electrical conductivity (cf. Table 2.1). It describes the ability of a material to conduct electric fields and is closely related to the electrical resistance and Ohm's law. If σ is assumed to be a constant, it yields

$$\vec{J} = \sigma\vec{E}\,. \tag{2.3a}$$

The quantity ϵ in the unit of C/(V m) describes the permittivity of the material and is a measure of the electric polarizability (cf. Table 2.1). Assuming it is a constant, it yields the relation

$$\vec{D} = \epsilon\vec{E}\,. \tag{2.3b}$$

The focus will lie on the quantity μ. It is the magnetic permeability in the SI unit H/m and it is a measure on how a material amplifies or dampens magnetic fields. Similarly, the constant approach is given by

$$\vec{B} = \mu\vec{H}\,. \tag{2.3c}$$

One possible choice for the material equations is given by the set of equations (2.3). This choice uses a constant, multiplicative and scalar approach for each of the equations. This represents the most rudimentary material model.

In order to show how (2.3) can be extended to cover further material properties, μ is considered exemplary. The same approach can be applied to the quantities σ and ϵ.

Instead of using $\mu \in \mathbb{R}$, a function $\mu : \mathbb{R}^3 \to \mathbb{R}$ with $\mu = \mu(\vec{x})$ and $\vec{x}$ being the spatial coordinate can be used. This would allow different spatial domains to be assigned to various values for μ. Thus, one can perform a simulation with several materials. If the simulation is not stationary in time, μ should be extended to include a time dependency. Likewise, a temperature dependency can be useful, if the temperature changes significantly. This is useful when losses are considered within the simulation. Thus, if a constant μ is replaced by a function $\mu = \mu(\vec{x}, t, T, \ldots)$, some dependencies – e.g., spatial coordinate $\vec{x}$, time t, temperature T – can be taken into account.

However, the approaches from (2.3) also have very clear limitations as to which effects cannot be modeled. From the basic mathematical structure, one field ($\vec{H}$) is multiplied by a scalar (μ) and yields the other field ($\vec{B}$). This means that the field $\vec{B}$ and $\vec{H}$ are parallel at any time and μ is considered to be independent of direction. Materials for which this approach is suitable are called isotropic. But not every material falls in this category. Anisotropic materials can not be modeled by this scalar approach.

Remark 2.2. The anistropy can also be used to motivate the complexity and interdisciplinarity of magnetic hysteresis [19, 30, 32, 35, 49, 53]. Magnetic properties of materials depend on their production and processing process. Metal sheets, for example, can be manufactured by rolling them out in a cold state. The magnetic properties along and perpendicular to the rolling direction differ (often referred to with hard and easy axis). Subsequent mechanical processing and internal stresses in the material also have an influence on the magnetic properties. By means of temperature and annealing, the magnetic properties can be changed.

Another important aspect with respect to the mathematical approach by multiplying one field by a scalar quantity is that no magnetic hysteresis can be modeled in this way. In Section 1.3 it has already been motivated that the hysteresis effect is caused by the fact that different output quantities can result from the same input data. This cannot be modeled by (2.3). To give another short illustrative example, it should be mentioned that there cannot be permanent magnets in the formulation (2.3c). A permanent magnet is characterized by the fact that a magnetic field $\vec{B} \neq \vec{0}$ is formed without any excitation $\vec{H} = \vec{0}$. This constitutes an impossible condition, if $\vec{B} = \mu \cdot \vec{H}$ holds.

Remark 2.3. In the further course of this dissertation, equations (2.3a) and (2.3b) will remain the proper choice for these material parameters. But (2.3c) will be replaced later by a hysteresis model. For the current consideration, (2.3c) is assumed to be in effect.

Remark 2.4. Given the above observations, it is the task of a hysteresis model to link the two fields $\vec{H}$ and $\vec{B}$ with each other. Hysteresis models can be roughly classified into scalar [31, 45, 48, 54] and vector [16, 26, 27, 46] models. Scalar models are solely suited for isotropic materials and vectorial may be suited for anisotropic materials. A scalar model will be introduced later in this dissertation. For this reason, μ is still considered to be a scalar and not a tensor. Historically, some scalar models were extended to vector models and isotropic to anisotropic ones. Within this section, $\vec{H}$ and $\vec{B}$ will be considered as three dimensional fields. But in Section 2.1.5, a benchmark problem will be introduced such that they can be reduced to scalar values h, b. The hysteresis model presented in Chapter 3 will be based solely on scalar quantities. However, the upcoming sections should be as general as possible. Thus, fields $\vec{H}$ and $\vec{B}$ are used.

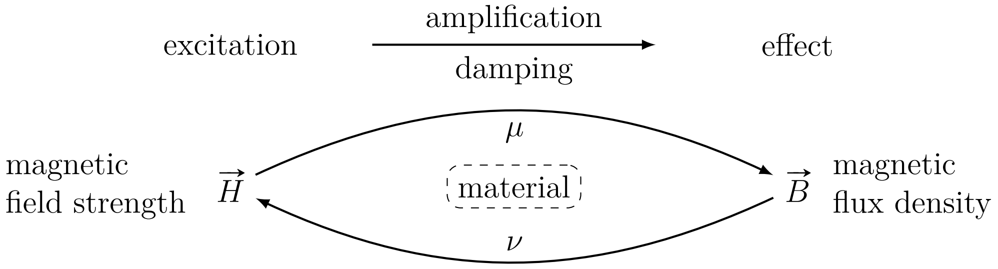

Figure 2.1.: The task of a magnetic hysteresis model is a definition of the relationship of the excitation $\vec{H}$ and the resulting effect $\vec{B}$. Depending on the direction of calculation this is either denoted with μ or ν.

Table 2.2.: Naming conventions for the approximations of Maxwell's equations.

name	effects		
	electr. energy	magn. energy	losses
electrostatic	✓		
magnetostatic		✓	
stationary field			✓
electroquasistatic (EQS)	✓		✓
magnetoquasistatic (MQS)		✓	✓
wave equation	✓	✓	
full set	✓	✓	✓

Remark 2.5. Within theoretical considerations $\vec{H}$ is often used as the independent variable. It is considered as the excitation, μ the amplification and $\vec{B}$ as the resulting field. In some computations the inverted direction is needed. This is denoted with ν. An overview is given in Figure 2.1.

2.1.2. Approximation of Maxwell's Equations in the Magnetoquasistatic Case

The full set of Maxwell's equations (2.1) is not easy to solve. Different approximations depending on the application exist. In the context of this dissertation, the so-called magnetoquasistatic approximation – abbreviated as MQS in the following – is used.

The effects – integrated into the full Maxwell equations – can be roughly divided into three categories. They are either based on the electric energy, the magnetic energy or losses. Each possible combination of effects is denoted differently as shown in Table 2.2. These approximations have already been well studied in the literature [80, 82–85].

This dissertation focuses on magnetic fields and losses and neglects the electrical energy. It is a good approximation for fields that change only slowly.

Under the assumptions of the MQS approximation, the displace current density vanishes, i.e.,

$$\frac{\partial \vec{D}}{\partial t} \approx 0\,. \tag{2.4}$$

Thus, one term from the complete Maxwell equations (2.1) is omitted while the rest remains valid. The system simplifies in a mathematically sense.

These reduced Maxwell equations are introduced in the following Section 2.1.3. In the follow-up Section 2.1.4, they are used to reduce the system into s single PDE.

2.1.3. Reformulation via Potentials

A common reformulation of the combination of the Maxwell equations (2.1) and the material equations (2.3) is based on the introduction of the magnetic vector potential $\vec{A}$ and the electric scalar potential φ [77–79, 81]. This formulation defines

$$\vec{B} = \nabla \times \vec{A}\,, \qquad\qquad \vec{E} = -\nabla\varphi - \frac{\partial \vec{A}}{\partial t}\,. \tag{2.5}$$

Remark 2.6. $\vec{A}$ and φ are not unique. If $\vec{A}$ and φ are solutions to the Maxwell equations (2.1), so are $\vec{A}^{\dagger} = \vec{A} + \nabla\xi$ and $\varphi^{\dagger} = \varphi - \frac{\partial\xi}{\partial t}$ for any scalar field ξ. The resulting values of $\vec{B}$ and $\vec{E}$ are invariant w.r.t. this transformation. Common approaches called gauges make further demands on $\vec{A}$ and φ, such that only one unique solution results. Two well known versions are the Lorenz and Coulomb gauge. The MQS approximation from Section 2.1.2 will be used and combined with the potential formulation (2.5) from this section and then a very compact representation results in the following Section 2.1.4. Using this compact version a benchmark problem will then be defined in Section 2.1.5. This benchmark problem uses rotational symmetry and other assumptions to reduce the dimension of the involved fields to scalar quantities. By a suitable choice of the boundary conditions, the solution becomes unique even without explicitly gauging of the potentials. Therefore, it is not needed to pursue the problem of gauging any further at this point.

2.1.4. Curl-Curl Equation

Within this section the Curl-Curl Equation will be derived. In a somewhat modified form, this equation can be found in literature[1]. This section will now combine the preparations from Sections 2.1.1 to 2.1.3.

---

[1] [78, equation 3.97], [84, equation 2.20], [150, equation 2.28], [151, equation 2.27]

Starting with (2.1d), the displacement current is omitted by the MQS approximation. Using the material equations (2.3a) and (2.3c) to replace the quantities $\vec{H}$ and $\vec{J}$ yields

$$\vec{\nabla} \times \underbrace{\vec{H}}_{=\nu\vec{B}} = \underbrace{\vec{J}}_{=\sigma\vec{E}} + \underbrace{\frac{\partial\vec{D}}{\partial t}}_{\approx 0} . \tag{2.6}$$

Now the quantities $\vec{B}$ and $\vec{E}$ can be expressed using the potentials (2.5). This results in

$$\vec{\nabla} \times \left(\nu \underbrace{\vec{B}}_{=\vec{\nabla}\times\vec{A}}\right) = \sigma \underbrace{\vec{E}}_{=-\vec{\nabla}\varphi-\frac{\partial\vec{A}}{\partial t}} . \tag{2.7}$$

Introducing $\vec{J}_{\mathrm{src}} = -\sigma\nabla\varphi$ as the source current density, i.e., the current that is applied externally, and rearranging the equation gives

$$\sigma\frac{\partial\vec{A}}{\partial t} + \vec{\nabla} \times \underbrace{\left(\nu\overbrace{\left(\vec{\nabla}\times\vec{A}\right)}^{=\vec{B}}\right)}_{=\vec{H}} = \vec{J}_{\mathrm{src}} . \tag{2.8}$$

At this point it is very important to pay attention to the exact definition of ν. In this derivation ν was considered a constant scalar with $\vec{H} = \nu \cdot \vec{B}$. In this case ν can be factored out from the outer curl. If the term $\sigma\frac{\partial\vec{A}}{\partial t}$ is ignored, the expression

$$\vec{\nabla} \times \left(\vec{\nabla} \times \vec{A}\right) = \frac{1}{\nu}\vec{J}_{\mathrm{src}} = \mu\vec{J}_{\mathrm{src}} \tag{2.9}$$

is obtained. This version can be found more frequently in the literature[1]. But it was consciously refrained on this simplification.

If ν is instead a function that somehow converts from $\vec{B}$ to $\vec{H}$, i.e., $\vec{H} = \nu\left(\vec{B}\right)$, the representation (2.8) is still valid. Or in general, as soon as ν is not constant, the simplification (2.9) is not necessarily easily possible.

Remark 2.7. ν in (2.8) is still up to closer inspection and is currently a placeholder function for the hysteresis model presented in Chapter 3. It is supposed to be representative for a conversion from $\vec{B}$ to $\vec{H}$. For the problem to be well posed, the function ν must be determined. Further investigations are carried out for a general ν at first.

Remark 2.8. The equation (2.8) represents a PDE. A viable numerical method for solving such a PDE is the finite difference method [94, 96].

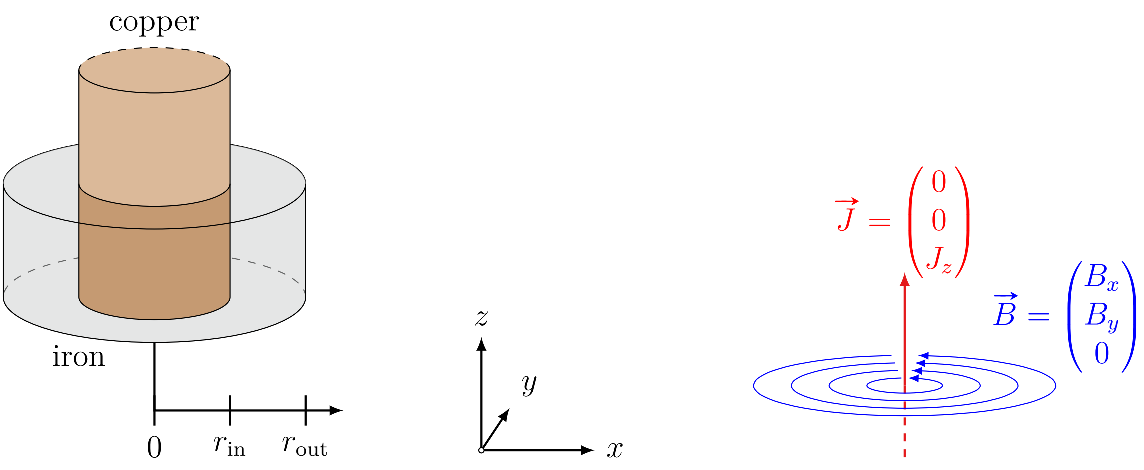

(a) Overview of material distribution.
(b) Coordinate system.
(c) Field orientation.

Figure 2.2.: Visualization of the coordinate systems of the benchmark problem.

The Curl-Curl Equation presented in (2.8) serves as a starting point and is valid for general multidimensional problems with advanced ν. Equation (2.8) is used in the following Section 2.1.5 and applied to a special benchmark problem. There, the fields $\vec{H}$ and $\vec{B}$ are reduced to scalar quantities. This results in the actual differential equation, which will be solved numerically in Chapter 5 later on.

The reader is given a rough overview of the physical background in Section 2.2 before the hysteresis model is presented in Chapter 3. In Section 3.3, the problem – how to define ν – is resumed and different approaches for ν in combination with the specific hysteresis model are investigated.

2.1.5. Application of the Curl-Curl Equation in a Rotationalsymmetric Benchmark Problem

In this section, preparations for the benchmark problem in Chapter 5 are made. The key insight will be that, with a suitable construction of the benchmark problem, the vector field quantities $\vec{H}$, $\vec{B}$ can be reduced to scalar quantities h, b. This is not generally possible, rather it is a constraint on the used approaches. Unfortunately, this is necessary because the hysteresis model in the form presented in Chapter 3 can only be applied to scalar fields.

This reduction of dimensions is achieved by having the benchmark problem to specify the orientation of the fields $\vec{H}$ and $\vec{B}$. For each point in space a reference vector $\vec{V}_{\text{ref}}$ is given by the benchmark problem such that the relation $\vec{H} = h \cdot \vec{V}_{\text{ref}}$ and $\vec{B} = b \cdot \vec{V}_{\text{ref}}$ result. Using rotational symmetry and constraining the orientation of certain vector quantities, a scalar equivalent to (2.8) is derived.

A standard example of magnetic field calculation is an infinitely long conductor. This example is modified and a sheath around the conductor is added. The setup is shown in Figure 2.2(a). Three different materials are used.

The conductor is assumed to be copper-like. It is conductive with electric conductivity $\sigma_{\mathrm{Co}} \in \mathbb{R}$, but has no magnetic hysteresis. Thus, the relations $b = \mu_{\mathrm{Co}} \cdot h$ and $h = \nu_{\mathrm{Co}} \cdot b$ with $\mu_{\mathrm{Co}} = \frac{1}{\nu_{\mathrm{Co}}} \in \mathbb{R}$ can be applied.

The environment is assumed to be in vacuum. A vacuum has no electrical conductivity and the known relation $b = \mu_0 \cdot h$ prevails. If possible, the vacuum is integrated via suitable boundary conditions instead of simulating it explicitly.

The main focus is on the sheathing. The sheath is modeled as iron-like and features both a constant electrical conductivity and magnetic hysteresis. The hysteresis is modeled by the hysteresis model of Chapter 3. At this point, ν is used as a placeholder to convert the fields with $h = \nu(h) = \nu(b, h_0, b_0)$ for the current state (h_0, b_0).

The conductor is straight and aligned along the z–axis, which also serves as the axis of rotation. The benchmark problem is assumed to be constant along the z–axis and such that all derivatives $\frac{\partial}{\partial z}$ are assumed to be zero.

(2.8) is converted from cartesian coordinates $(\hat{\boldsymbol{x}}, \hat{\boldsymbol{y}}, \hat{\boldsymbol{z}})$ to cylindrical coordinates $(\hat{\boldsymbol{r}}, \hat{\boldsymbol{\varphi}}, \hat{\boldsymbol{z}})$. Further details on this procedure can be found, for example, in [78]. In doing so, some quantities are restricted to certain dimensions. With the following representations of the curl operator in the different coordinate systems,

$$\vec{\nabla}_{\mathrm{car}} \times \begin{pmatrix} A_x \\ A_y \\ A_z \end{pmatrix} = \begin{pmatrix} \frac{\partial A_z}{\partial y} - \frac{\partial A_y}{\partial z} \\ \frac{\partial A_x}{\partial z} - \frac{\partial A_z}{\partial x} \\ \frac{\partial A_y}{\partial x} - \frac{\partial A_x}{\partial y} \end{pmatrix}, \qquad \vec{\nabla}_{\mathrm{cil}} \times \begin{pmatrix} A_r \\ A_\varphi \\ A_z \end{pmatrix} = \begin{pmatrix} \frac{1}{r}\frac{\partial A_z}{\partial \varphi} - \frac{\partial A_\varphi}{\partial z} \\ \frac{\partial A_r}{\partial z} - \frac{\partial A_z}{\partial r} \\ \frac{1}{r}\left(\frac{\partial (r A_\varphi)}{\partial r} - \frac{\partial A_r}{\partial \varphi}\right) \end{pmatrix} \tag{2.10}$$

a suitable system can be created. The current density $\vec{J}$ and the vector potential $\vec{A}$ are restricted to the z component, i.e.,

$$\vec{J} = \begin{pmatrix} 0 \\ 0 \\ J_z \end{pmatrix} = j\hat{\boldsymbol{z}}\,, \qquad \vec{A} = \begin{pmatrix} 0 \\ 0 \\ A_z \end{pmatrix} = A\hat{\boldsymbol{z}}\,. \tag{2.11}$$

With this setup the field $\vec{B}$ is restricted to the xy–plane, or respectively the φ–plane, i.e.,

$$\vec{B}_{\mathrm{cart}} = \vec{\nabla}_{\mathrm{cart}} \times \vec{A}_{\mathrm{cart}} = \begin{pmatrix} \frac{\partial A_z}{\partial y} \\ -\frac{\partial A_z}{\partial x} \\ 0 \end{pmatrix}, \qquad \vec{B}_{\mathrm{cil}} = \vec{\nabla}_{\mathrm{cil}} \times \vec{A}_{\mathrm{cil}} = \begin{pmatrix} 0 \\ -\frac{\partial A_z}{\partial r} \\ 0 \end{pmatrix} = b\hat{\boldsymbol{\varphi}}\,. \tag{2.12}$$

The field $\vec{B}$ has only a tangential and no radial part, as seen in Figure 2.2(c). The same is true for the $\vec{H}$ field. Thus, the fields $\vec{H}$ and $\vec{B}$ are parallel for each spatial coordinate, respectively. All in all, this results in a system that couples the quantities

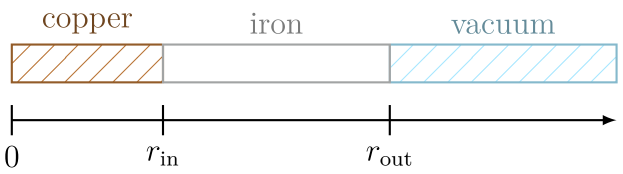

Figure 2.3.: Material distribution of the benchmark problem along the radius r.

to fixed directions. With this information and using scalar values A, h, b, j an equivalent representation of (2.8) in cylindrical coordinates is given by

$$\sigma\frac{\partial A}{\partial t} + \frac{1}{r}\left(\frac{\partial}{\partial r} r \underbrace{\nu\Big(\overbrace{-\frac{\partial}{\partial r}A}^{=b}\Big)}_{=h}\right) = j\,. \tag{2.13}$$

The different materials are aligned along the radius r as shown in Figure 2.3. Thus, the objective for the further thesis is the numerical solution of (2.13) under consideration of the different materials from Figure 2.3. For this purpose, the physical basics for ferromagnetism and magnetic hysteresis are presented in the further course of this chapter. To concretize the current placeholder μ and ν, a hysteresis model is defined in Chapter 3 and its properties are studied. Due to the coordinate transformation, a singularity results at $r = 0$. Also the material transitions at r_{in} and r_{out} have to be investigated separately. Solutions to these problems are presented in Chapter 5. For the directly following sections and chapters, this short discourse and foreshadowing of Chapter 5 serves to clarify that some multidimensional problems can be reduced to scalar quantities.

2.2. A Brief Introduction to Ferromagnetism

As motivated in Remarks 2.4 and 2.7, the hysteresis model in Chapter 3 is intended to link the magnetic field strength $\vec{H}$ and the magnetic flux density $\vec{B}$. Ferromagnetic materials generate particularly strong magnetic fields, have a hysteresis effect and are therefore of particular interest.

This section is intended to introduce the reader to the basics of ferromagnetism such that the mathematical approaches of the hysteresis model in Chapter 3 can be physically motivated. To this end, the physics of magnetism is presented in a minimalistic manner from the molecular to the macroscopic level. For more profound insights, it is referred to the specialized literature [14, 21, 24, 52].

First, the formation of Weiß domains and Bloch walls is motivated. Based on the response of the material to an excitation, a classification can be made. This allows us to differentiate ferromagnetic materials from others and to show the distinctive properties.

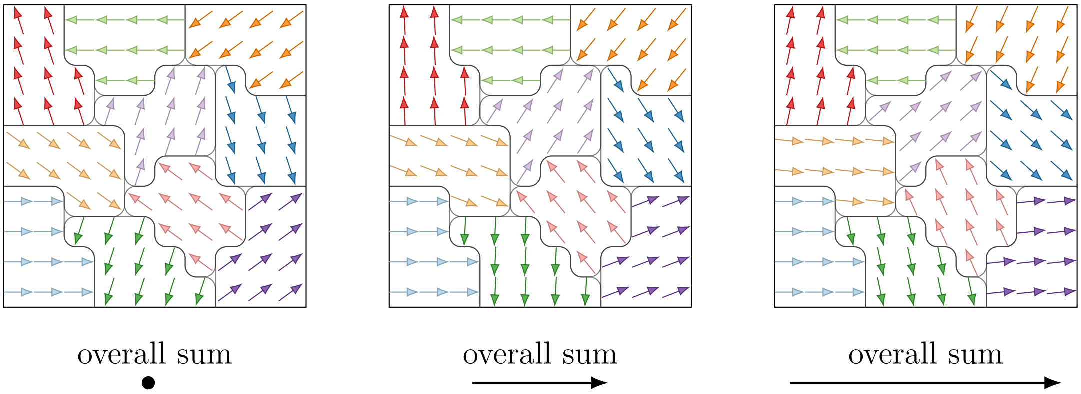

(a) no resulting field (b) weak resulting field (c) strong resulting field

Figure 2.4.: Sketch of magnetic domains. The domain of the material is subdivided into small parts that share a magnetic orientation. The resulting field depends on the sum of all subdomains.

The reader is presented with a superficial physical motivation as to why the effect of hysteresis occurs in ferromagnetic materials. Furthermore, characterizing key figures are introduced.

Remark 2.9. Equation $\vec{B} = \mu_0 \vec{H}$ with $\mu_0 \approx 4\pi \cdot 10^{-7}\text{H/m}$ describes the relationship between $\vec{H}$ and $\vec{B}$ without a material, i.e., in vacuum. It serves as a reference whether a material amplifies ($\mu > \mu_0$) or dampens ($\mu < \mu_0$) a magnetic field.

Remark 2.10. The SI unit system revised μ_0 on 20th of May 2019 [2]. Before, it was considered a constant with exact value of $4\pi \cdot 10^{-7}\text{H/m}$. But currently it is considered a quantity that has to be specified experimentally. The numerical value differs only slightly. In the context of this dissertation, $\mu_0 = 4\pi \cdot 10^{-7}\text{H/m}$ is used for calculations.

2.2.1. Weiß Domains and Bloch Walls

The following section justifies the behavior of ferromagnetic materials with physical processes. This cannot necessarily be generalized to other classes of materials. A rough classification and delimitation of the material types is then given in Section 2.2.2.

Molecules of a material with a dipole moment can be vividly viewed as small magnets. These molecules are not randomly aligned but follow the physical principle of energy minimization, i.e., they always try to achieve the most favorable state in terms of energy. Since each molecule generates a magnetic field, they interact with each other based on their magnetic fields.

Now the question arises, what is the most favorable state in terms of energy? This depends on the scale. Simplified, there are two dominant effects. At the microscopic level, molecules that are very close to each other try to align themselves constructively,

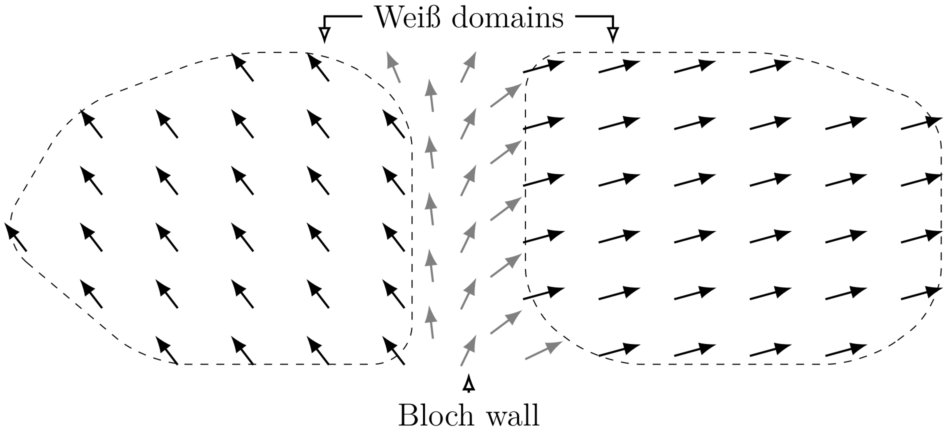

Figure 2.5.: The basic schematic principle of Weiß domains and Bloch walls is shown. Between the areas with very similar orientation (Weiß domains), there are narrow areas that act as a transition between them (Bloch walls).

i.e., as parallel as possible with the same orientation of the magnetic poles. However, if all molecules were to align themselves in the same way, a very strong magnetic field would form at the macroscopic level. This is, however, unfavorable in terms of energy. On this macroscopic level, it is most favorable from an energy point of view, if the individual molecules align themselves as destructively as possible, resulting in a magnetic field that is as weak as possible in total. These two opposing effects cause local clusters to form in which the molecules constructively overlap. However, the clusters each have different orientations, so that the magnetic fields of the clusters destructively cancel each other out.

An actual visual measurement of these clusters is given in [5] and an abstracted sketch in Figure 2.4. These clusters are called magnetic domains or Weiß domains. The Weiß domains are separated by thin areas where the molecules are changing their orientation from one domain to the adjacent one. The typical transition is called Bloch wall, but there are also special variants like the Néel wall. See [34] for a comparison of the wall types. For a rough overview, the scope of this thesis will be limited to Bloch walls. If the magnetization is considered in a plane, the transition is found also within this plane and is continuous, as shown in Figure 2.5.

The superposition of all magnetic fields results in a complex system. Assuming that the material is not externally excited in any way, it takes the most favorable attainable state w.r.t. energy. For example, let x be the position of one random Bloch wall. As shown in Figure 2.6(a), the current position must be at a local minimum in terms of energy.

Now the material is excited a little by applying a magnetic field, for example. Then the Bloch wall continues to try to stay in the local energy minum, but experiences a small force due to the interaction with the external magnetic field. For simplicity, it is assumed that all other Bloch walls do not change and the single Bloch wall has no significant effect on the energy levels shown in Figure 2.6. The now increased energy level is not sufficient to overcome the adjacent local maximum. If the external

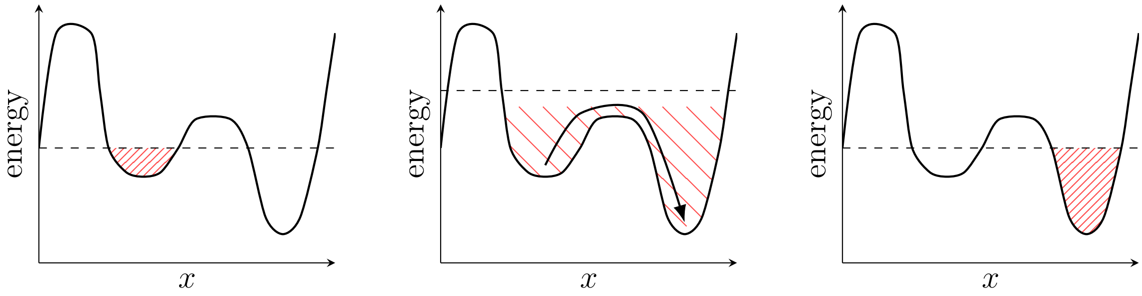

(a) Starting position.

(b) Increasing the available energy allows the jump.

(c) Final position.

Figure 2.6.: Shown is a schematic view of potential energy w.r.t. to the Bloch wall position x. The shaded area represents the achievable states and the dashed line represents the maximum energy. Compare to [62, Fig. 4] and [75, Fig. 1].

excitation vanishes, the Bloch wall falls back to its starting point. It is concluded that if the external excitation is small, the process is reversible and x is confined around the local minimum, as marked in Figure 2.6(a).

But what happens if the external excitation is not small? As shown in Figure 2.6(b), a higher energy level than the adjacent local maximum allows the Bloch wall to "jump" over the local maximum into the next more preferred local minimum. Again let the external excitation now be off again, the Bloch wall remains in the new lower local minimum. The material has permanently changed its configuration and this process is irreversible. This specific Bloch wall is now restricted to another domain as shown in Figure 2.6(c).

The above assumptions were highly simplistic, but are sufficient for basic motivation. Of course, all Bloch walls must be considered at the same time and any change in the position of these will affect all the others. Often, if one Bloch wall is changing its position, it triggers further ones to change their position as well. So there is some kind of avalanche effect [70]. However, one can still roughly categorize the resulting effects into reversible and irreversible ones. This distinction will be relevant several times in this thesis.

The phenomenon of jumping over a local energy maximum is called the Barkhausen effect, jumps or noise. This is a well-known and widespread effect in the application [58, 62, 63, 69–71, 73, 75]. These jumps happen nearly spontaneously and induce an electric current. They were first noticed when amplified with a loudspeaker and perceived as auditory noise. Because this effect is based upon electric current, losses occur and are part of recent research [68, 72]. Since losses cause a temperature change, the temperature dependence must be investigated [60, 74].

The irreversibility of the Barkhausen effect is directly linked with the hysteretic properties and affect the magnetic properties of the material [67]. Especially material defects or the deliberate introduction of other chemical substances in the form of

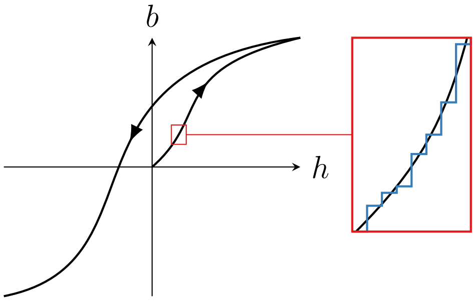

Figure 2.7.: Shown is the relation between a scalar applied magnetic field h and the resulting magnetic flux density b. The actual relation is based upon many very small discrete events: the Barkhausen noise (blue). A continuous approximation (black) is used. Figure based on [61, Fig. 1].

alloys influence the magnetic hysteresis. The Bloch walls get pinned to them and can thus significantly increase the irreversible aspect. In applications, the Barkhausen effect is used for example in non-invasive material testing [59, 61, 64–66, 76]. The strength with which a Bloch wall is held in position also depends on mechanical properties.

Remark 2.11. According to the above motivation, the magnetization process of a material is not a continuous phenomenon. It is caused by many very small discrete changes in the position of Bloch walls, as shown in Figure 2.7. The exact representation and calculation of each Bloch wall is not necessary if the consideration is on a coarser scale. The sizes of the Weiß domains are depending on several factors. As measured in [5], the scale of a Weiß domain is in the order of µm. The intention is the simulation of magnetic materials in the order of mm, cm or above. Due to the sheer number of Bloch walls in a material of this scale, the discrete situation is approximated by a continuous approach, as shown in Figure 2.7.

Remark 2.12. The magnetic behavior of a material depends on how it responds to excitation by an external magnetic field. The above motivation is strongly focused on ferromagnetic materials. For others, different physical backgrounds apply. Since this work deals exclusively with ferromagnetic materials, other materials will not be considered in detail. Nevertheless, the distinctive properties in comparison to other material classes are shown. Therefore, a rough classification of materials is introduced in the following section.

2.2.2. Classification of Materials

For a rough classification diamagnetic, paramagnetic and ferromagnetic materials are introduced with respect to the reference in vacuum as mentioned in Remark 2.9. Scalar fields h and b are assumed.

To quantify the difference w.r.t. to vacuum, the dimensionless scalar quantity of relative permeability defined by $\mu_r = \frac{\mu}{\mu_0}$ is introduced. Additionally the dimensionless magnetic susceptibility is defined by $\chi_m = \mu_r - 1$. Information on the numerical values of these quantities are taken from [1, 6, 8, 9, 13] and differ a little bit depending on the source. These numbers are only for an overview on the order of magnitude.

A diamagnetic material reacts with an external magnetic field in a destructive way, i.e., it hinders the field. The field inside a diamagnetic material is weaker than in vacuum, i.e., $\mu_r^{\text{dia}} < 1$ and $\chi_m^{\text{dia}} < 0$. Examples are gold with $\chi_m = -3.4 \cdot 10^{-5}$, silver with $\chi_m = -2.4 \cdot 10^{-5}$, copper with $\chi_m = -9.4 \cdot 10^{-6}$ and zinc with $\chi_m = -1.6 \cdot 10^{-5}$.

A paramagnetic material slightly amplifies the magnetic field, i.e., $\mu_r^{\text{par}} > 1$ and $\chi_m^{\text{par}} > 0$. Here examples are aluminum with $\chi_m = 2.2 \cdot 10^{-5}$, lithium with $\chi_m = 1.4 \cdot 10^{-5}$ and tungsten with $\chi_m = 6.8 \cdot 10^{-5}$.

Both, diamagnetic and paramagnetic materials, exhibit only reversible magnetic properties and therefore return to the original state without external excitation. There is no hysteresis effect. If the external magnetic field is not unusually strong, μ_r or χ is assumed to be independent of the external magnetic field [7]. These materials can be modeled with $b = \mu \cdot h$. Note that μ can be temperature dependent.

Ferromagnetic materials are characterized by the properties presented in Section 2.2.1, which includes the non-linear properties and irreversible, i.e., hysteresis, behavior. A direct comparison of the μ values between diamagnetic, paramagnetic and ferromagnetic materials is not meaningful because the linear approach $b = \mu \cdot h$ cannot be used for ferromagnetic materials. Because of this fact, there are other different approaches to defining μ. In the remainder of this paper, a differential definition is used, i.e.,

$$\mu_{\text{diff}} = \frac{\mathrm{d}B}{\mathrm{d}H}, \qquad \mu_{\text{r,diff}} = \frac{\mu_{\text{diff}}}{\mu_0}. \tag{2.14}$$

For the linear approach $b = \mu \cdot h$ it yields $\mu = \mu_{\text{diff}}$ and a comparison of the relative values μ_r and $\mu_{\text{r,diff}}$ is possible. A not fully saturated ferromagnetic material can exhibit values of $\mu_{\text{r,diff}}$ up to 10^6 [133, 137]. Because of this difference over several orders of magnitude, diamagnetic and paramagnetic materials are considered nonmagnetic in common language, and by magnetic materials one typically means ferromagnetic materials.

Remark 2.13. Summarizing the above statements, ferromagnetic materials have a several order of magnitudes stronger magnetic effect in comparison to other material classes. The magnetic field is highly amplified by ferromagnetic materials. Such materials exhibit non-linear and irreversible, i.e., hysteresis, behaviour. These properties characterize ferromagnetic materials [137] and make them interesting for application.

The strength of the hysteresis effect and whether or not this effect is desired in the application plays an elementary role in the material selection. Therefore, within the ferromagnetic category there is a distinction between irreversible effects that are not so pronounced and a strong manifestation of these effects. Such materials are called

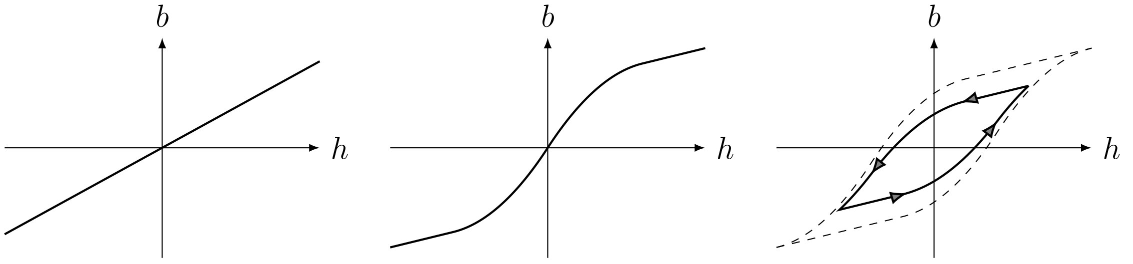

(a) linear, $b = \mu \cdot h$ (b) non-linear, $b = \mu(h) \cdot h$ (c) non-linear with hysteresis

Figure 2.8.: Various possible relationships between b and h are shown.

soft or hard ferromagnetic materials. An application example of how to combine soft and hard materials for an electric motor is given in Section 2.4.

The division into dia-, para- and ferromagnetic materials is only a rough classification. In the corresponding literature (e.g., [7, 10]) there are even finer breakdowns based on the physical properties, which are predominating the magnetic interaction. At this point it is sufficient to work out which properties distinguish ferromagnetic materials from other materials.

2.3. Hysteresis & Ferromagnetic Materials

Having shown the physical background of ferromagnetism in Section 2.2.1 and worked out the main distinguishing features from other classes of materials in Section 2.2.2, the effect of hysteresis are now looked at from a mathematical point of view. The statements are limited to scalar quantities. It have already been shown in Section 2.1.5 that the benchmark problem can be reduced to scalar problems.

In the following sections, the foundations for the special hysteresis model in Chapter 3 is laid. For this purpose, the following substantive points are worked through.

▶ First, in Section 2.3.1, the problem of hysteresis is examined in the mathematical sense. It is worked out what exactly a hysteresis model should calculate.

▶ In Section 2.3.2 saturation curves are introduced. On the one hand these are used to explain further notation and the characteristic numbers of a ferromagnetic material. In particular, different equivalent coordinate systems are defined. On the other hand, these curves limit the definition range of a hysteresis model.

▶ From the context already presented, in Section 2.3.3 requirements and conditions for hysteresis models will be formulated. This information allows to derive approaches for hysteresis models.

2.3.1. Mathematical Problem Definition

Within Section 2.2.2 different material classes were introduced. The simplest ones are based on a linear model for the relationship between h and b. If μ is allowed to be a function instead of a constant, non-linear materials without hysteresis effects are also feasible. These cases are shown in Figures 2.8(a) and 2.8(b). However, a process with hysteresis as shown in Figure 2.8(c) is not possible with an approach of calculating b via some function μ, i.e., $b = \mu(h)$.

Since $b = \mu(h)$ does not work globally, the requirement are weakened a bit for the hysteresis model. It should describe the course of b in dependence of h for the current state (h_0, b_0), i.e.,

$$b = b(h) = \mu(h, h_0, b_0)\,. \tag{2.15}$$

This approach corresponds to an expansion or approximation with reference to point (h_0, b_0). The validity of states (h_0, b_0) is investigated next in Section 2.3.2.

This approach restricts the applicability or rather sets new conditions. It is assumed that the current behavior is uniquely defined by the current state. It is irrelevant how the current state has been reached. This is a weakening of a general path dependence as noted in the previous sections.

However, it must also be discussed that this approach must be coordinated with the global approach. In this case, the Curl-Curl Equation (2.8) or (5.9a) is to be solved numerically. To do this, the finite difference method is used in Chapter 5. With this in mind, discrete steps are assumed in time and this allows to update the current state (h_0, b_0) at each time step.

But in Equations (2.8) and (5.9a) it is not asked for μ, but for the inversion ν, i.e.,

$$h = h(b) = \nu(b, h_0, b_0)\,. \tag{2.16}$$

Since not every hysteresis model is easy to invert, the chosen model must fit the global context. To forestall Chapter 5, both versions – (2.15) and (2.16) – are needed in the benchmark problem. The chosen hysteresis model in Chapter 3 allows this inversion.

Remark 2.14. To summarize, in the context of this thesis, a hysteresis model starting from current state (h_0, b_0) defines the progression of fields via functions μ and/or ν w.r.t. Equations (2.15) and (2.16). An example is given in Figure 2.9.

2.3.2. Characteristics of Saturation Curves

As already seen in Figure 2.9, the range of reachable states (h, b) is constrained. These boundaries will be physically motivated and their importance for a hysteresis model is stated. In the process, new notations and coordinate systems will be

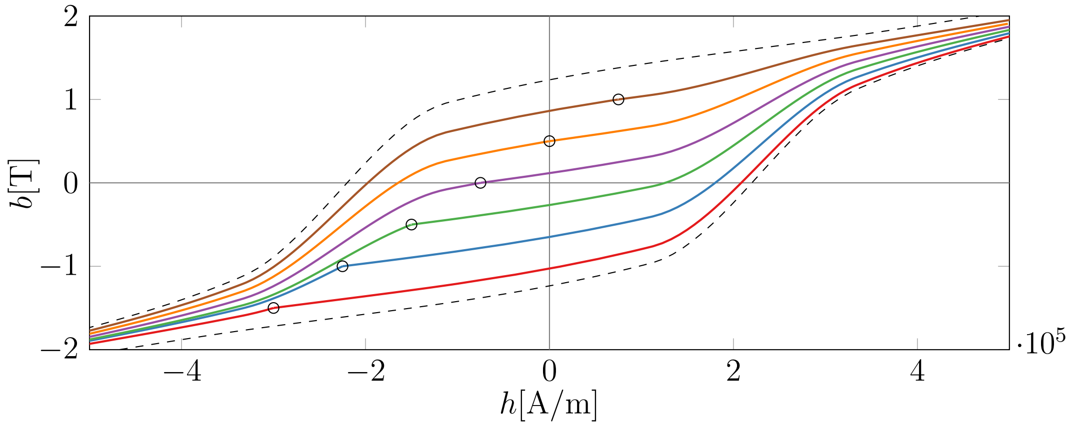

Figure 2.9.: Relation between h and b for different initial states (black circles). Saturation curves are shown with dashed lines.

introduced. In this section, the approach that h is the independent variable is chosen and $b = b(h)$ is to be calculated depending on it.

As already explained in Section 2.2.1, the strong amplification of the magnetic field in ferromagnetic materials is caused by the alignment of the Weiß domains. Assuming the material is fully saturated, i.e., the Weiß domain and Bloch walls are orientated and positioned optimally to amplify the magnetic field. This state is reached at $h \ll 0$. Now, using a smooth and monotonous transition, h is increased until a full saturation in the opposite direction occurred, i.e., $0 \ll h$. This transition is material specific and will be denoted with $B^+_{\text{sat}}(h)$. Since physics has no preferred direction, the transition from $0 \ll h$ to $h \ll 0$ is symmetric to B^+_{sat}. This will be denoted with B^-_{sat} and defined by

$$B^-_{\text{sat}}(h) = -B^+_{\text{sat}}(-h)\,. \tag{2.17}$$

The saturation curves $B^{\pm}_{\text{sat}}$ can be measured experimentally and allow a quick rough overview of the magnetic behavior of a ferromagnetic material. Therefore, some key characteristics will be introduced on the basis of this curve.

But $B^{\pm}_{\text{sat}}$ are also of interest in a mathematical sense. The curves represent a natural boundary. There can be no physically meaningful state (h, b) outside these curves. From the context follows

$$B^+_{\text{sat}}(h) \leq B^-_{\text{sat}}(h) \text{ for all } h \in \mathbb{R}\,. \tag{2.18}$$

Thus, the further considerations can be restricted to the set I with

$$I = \left\{ (h, b) \in \mathbb{R}^2 \,\middle|\, B^+_{\text{sat}}(h) \leq b \leq B^-_{\text{sat}}(h) \right\}\,. \tag{2.19}$$

I is the definition domain of the hysteresis models.

In the previous sections, it have already been explained that without material the relation $b = \mu_0 \cdot h$ exists. Thus, the relationship between h and b can be divided into components with and without material influence. This can be achieved in two ways, depending on whether one wants to make this distinction with respect to h or b. If the intrinsic induction b_{i} and the magnetization M are introduced, it results in

$$b(h) = \mu_0 \cdot h + b_{\mathrm{i}}(h) = \mu_0 \cdot \Big(h + M(h)\Big)\,. \tag{2.20}$$

Because b_{i} and M differ only in scaling by μ_0, the investigations are restricted to the study of b_{i} for the purposes of this thesis. This results in two different coordinate systems, (h, b) and (h, b_{i}). Mathematically, these are connected by the simple relationship

$$b(h) = \mu_0 \cdot h + b_{\mathrm{i}}(h)\,, \qquad\qquad b_{\mathrm{i}}(h) = b(h) - \mu_0 \cdot h\,. \tag{2.21}$$

Analogously, a corresponding $B^{\pm}_{\mathrm{i,sat}}$ from the saturation curves $B^{\pm}_{\mathrm{sat}}$ can be defined.

Remark 2.15. An analysis of the magnetic field can be done in different ways. If one considers h as the independent variable, then considerations in the (h, M), (h, b_{i}) and in the (h, b) planes are possible. These possibilities have also caused confusion in the literature. A study on this issue can be found in [52]. In the context of this thesis, the analysis and definition will occur either in the (h, b) or (h, b_{i}) plane. A distinction within the quantities is done by a sub-script of “i”. Since both versions are simply connected by (2.21), both formulations are equivalent. The most suitable version is selected in the respective context and where possible it is tried to present both in parallel.

From the physical backgrounds properties for $B^{\pm}_{\mathrm{sat}}$ and $B^{\pm}_{\mathrm{i,sat}}$ can be derived. The material can only achieve a limited amplification of the magnetic field. This is reached, if all Weiß domains and Bloch walls are optimally oriented for amplification. And results in the first key parameter $B^{\infty}_{\mathrm{i,sat}}$, the contribution of the material in saturation. It is defined by

$$\lim_{h\to-\infty} B^{\pm}_{\mathrm{i,sat}}(h) = -B^{\infty}_{\mathrm{i,sat}}\,, \qquad\qquad \lim_{h\to+\infty} B^{\pm}_{\mathrm{i,sat}}(h) = B^{\infty}_{\mathrm{i,sat}}\,. \tag{2.22}$$

$B^{\infty}_{\mathrm{i,sat}}$ is a measure of the maximum achievable gain of the material’s magnetic field.

Remark 2.16. Complete magnetization is one of the few ways to create a defined state in the material. A state in the non-saturation state is dependent on all previous states of the material. This is of course a challenge from a numerical point of view. The acquisition and integration of many previous states is memory and computation intensive. A possible approach of hysteresis models is to use only the current state for calculations. But also in practical applications this plays an important role. To produce a material with a fixed magnetization or demagnetize it, profound knowledge and approaches are necessary. Some application examples can be found in [113–116].

Through (2.22), the asymptotic behavior of $B^{\pm}_{\mathrm{sat}}$ is also declared and it yields

$$\lim_{h\to-\infty} \left(B^{\pm}_{\mathrm{sat}}(h) - \left(\mu_0 \cdot h - B^{\infty}_{\mathrm{i,sat}}\right)\right) = 0\,, \tag{2.23a}$$

$$\lim_{h\to+\infty} \left(B^{\pm}_{\mathrm{sat}}(h) - \left(\mu_0 \cdot h + B^{\infty}_{\mathrm{i,sat}}\right)\right) = 0\,. \tag{2.23b}$$

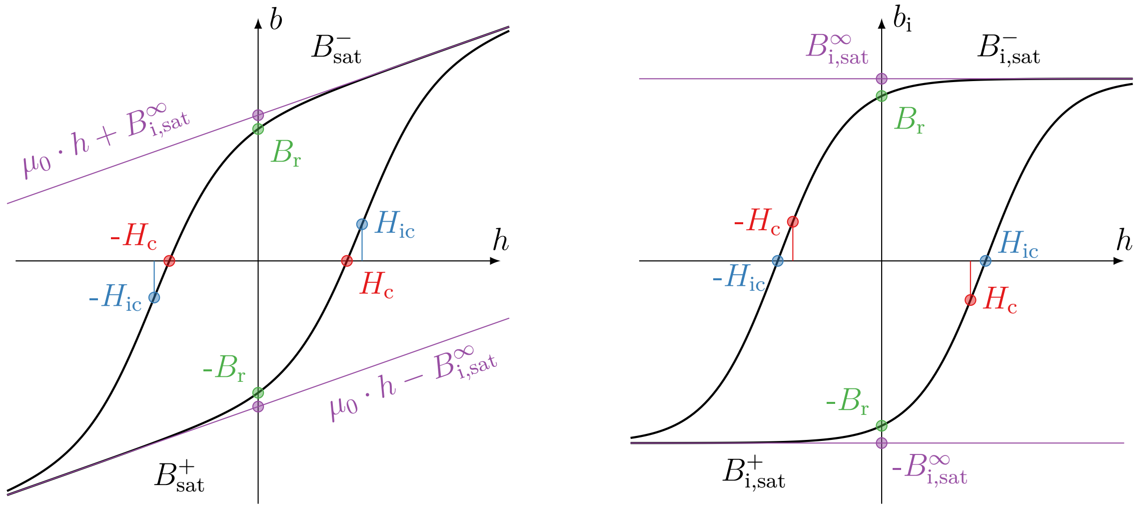

(a) (h, b)–plane

(b) (h, b_{i})–plane

Figure 2.10.: Illustration of the main characteristics of saturation curves $B_{\mathrm{sat}}^{\pm}$. Comparable figures can be found with modified notation in various literature [14, 25, 28, 36, 52].

From this, a rough shape of the saturation curves $B_{\mathrm{sat}}^{\pm}$ can already be derived, as can be seen in Figure 2.10. Now, a few characteristic quantities of such saturation curves are introduced. These quantities allow a first rough estimation of a material [112].

Due to the general shape of $B_{\mathrm{sat}}^{\pm}$ intersections with the coordinate axis exist. These represent the other key characteristics. The remanence B_{r} is the intersection with the b or b_{i} axis, i.e.

$$B_{\mathrm{r}} = B_{\mathrm{sat}}^{-}(0) = B_{\mathrm{i,sat}}^{-}(0)\,, \qquad\qquad -B_{\mathrm{r}} = B_{\mathrm{sat}}^{+}(0) = B_{\mathrm{i,sat}}^{+}(0)\,. \tag{2.24}$$

After a material is excited to positive saturation and then this excitation is monotonically attenuated until there is none, the material retains the remanence flux density B_{r}. The remanence is therefore the maximum achievable flux density without excitation. Only with remanence a material can be a permanent magnet.

The intersection with the h–axis is denoted as magnetic coercivity H_{c}, i.e.,

$$B_{\mathrm{sat}}^{+}(H_{\mathrm{c}}) = 0\,, \qquad\qquad B_{\mathrm{sat}}^{-}(-H_{\mathrm{c}}) = 0\,. \tag{2.25}$$

If a material is negatively saturated and the excitation is monotonously increased, the coercivity field strength is the needed excitation to compensate the magnetization so that there is no flux density. Note that $H_{\mathrm{c}} \neq H_{\mathrm{ic}}$ holds. H_{c} is therefore a measure of how easy or difficult it is to repolarize or demagnetize a material. As mentioned in Section 2.2.2, ferromagnetic materials can be divided into hard and soft materials. Soft ferromagnetic materials have a small H_{c}, while hard ferromagnetic materials have a large H_{c}. Application examples for both types are presented in Section 2.4 in form of a stepper motor.

The typical profile of the saturation curves $B_{\mathrm{sat}}^{\pm}$ are "S" or sigmoidal shaped, as shown in Figure 2.10. Such curves can be approximated with logistic approaches (e.g., [36]).

Remark 2.17. In this thesis, it is assumed that the saturation curve B^{+}_{sat} exists as a continuously differentiable real function, i.e., $B^{+}_{\mathrm{sat}} \in C^1$. Later in Section 4.2 the condition are tightened to $B^{+}_{\mathrm{sat}} \in C^2$. It is not of importance, how B^{+}_{sat} was constructed.

In order to be able to evaluate this assumption a little bit, a few approaches are presented briefly. Starting from experimentally measured values, these can be interpolated and approximated in a suitable way [88, 90, 91]. However, suitable approach functions can also be adapted to the measured values by means of curve fitting [36].

2.3.3. Demands on and Approaches for Hysteresis Models

The previous sections are now summarized and the expectations for the hysteresis model in Chapter 3 are presented. For an overview, however, other approaches are also briefly motivated. In doing so, the requirements and assumptions are explicitly adapted to the approaches of this dissertation. That is, differences may well arise in a different context.

The simulation in Chapter 5 aims at solving the analytical Equations (2.8) and (5.9b) numerically. For this purpose, starting from the current state (h_0, b_0), the relationship between h and b is required (see Remark 2.14). This is represented by μ and ν respectively and shall be the output of the hysteresis model. An analytical solution is not expected, an embedding in the numerical methods is sufficient. Neither is an exact description of the physical states expected, a simplified statistical or smoothed view is sufficient as mentioned in Remark 2.11.

The allowed values for the states $(h_0, b_0) \in I$ have already been worked out in (2.19) and I should be the definition domain of the hysteresis model. In addition, the saturation curves $B^{\pm}_{\mathrm{sat}}$ represent a restriction and the hysteresis model should respect these in the form, such that no solution can leave the domain I. This automatically determines the limit behavior for $h \to \pm\infty$ according to (2.23). The hysteresis model must have basic symmetrical properties, since from a physical point of view there is no preferred direction.

The hysteresis model must fit the current technical possibilities. On the one hand, this concerns the numerical aspects such as computational costs and memory requirements. This is particularly important because it must be embedded in partially already complex numerical approaches. On the other hand, it must be possible to adapt the model to materials that are actually produced. A purely mathematical modeling is not the goal of this dissertation. This is mainly intended to determine which measurement data of the material must be available. In this case, the saturation curves $B^{\pm}_{\mathrm{sat}}$ and the characteristic quantities H_{c}, B_{r} and $B^{\infty}_{\mathrm{i,sat}}$– as possible experimental measurements – have already been presented.

Now, approaches for hysteresis models based on the presented correlations are outlined. The first approach is based on a large number of hysterons arranged in parallel. This approach is usually called the *discrete Preisach model* and based on this model, there are many variations and extensions [19, 23, 26, 33, 42, 43, 45].

A hysteron has a similar behavior as the Schmitt trigger already discussed in Section 1.3. The characteristics of a hysteron are the activation levels and the amplitude. If the excitation is above the activation level, the hysteron contributes a specific amount to the magnetization. If the excitation is below the deactivation level, the hysteron does not contribute to the magnetization. In case that the excitation is between these two levels, it holds its previous state. Using an appropriate number of hysterons, fitting their characteristics to the measured data and sum over all hysterons, yields a valid hysteresis model.

Also the phenomenon that hysteresis is vividly associated with lagging behind or overcoming friction or resistance allows approaches to hysteresis [17, 41, 48].

The hysteresis model presented in Chapter 3 is based on differential equations. Based on the current state $(h_0, b_0) \in I$ an associated value $\mu_{\text{diff}}(h, b) = \frac{\mathrm{d}b}{\mathrm{d}h}$ as in (2.14) is defined.

Remark 2.18. With this overview, it is justified that approaches for hysteresis models can be derived from the phenomenological observations. These approaches are also used for the self-derived loss model in Section 4.1.

Historically, many different hysteresis models have been formed, each with their own advantages and disadvantages. A comparison of the models is therefore of interest and has been carried out in various literature [40, 42, 50].

2.4. Application Example – Stepper Motor

Before a hysteresis model is presented in Chapter 3, a short side note with an application example will be presented in this section. It is motivated that only a suitable choice of different materials can make an effective motor. Also, a certain pattern of excitation emerges from this example, which will be picked up again later.

Stepper motors are a specific design of electric motors with selected areas of application. First, the general structure and function of such a motor shall be described. Second, the requirements and properties of the materials used shall be considered. This provides a clear motivation why researchers are dealing with the aspects of hysteresis, temperature and losses.

2.4.1. Basic Design and Functionality

In the context of this thesis, only a rough and simplified review of the functional principle is carried out. For more detailed explanations it is referred to specialized literature such as [122–131].

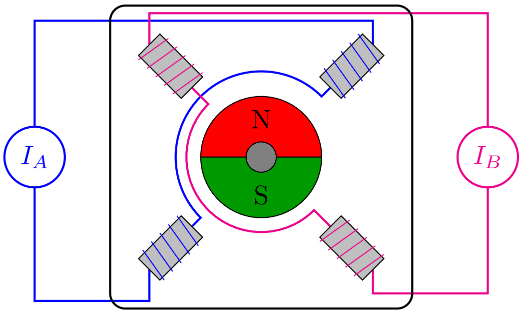

Figure 2.11.: A simplified illustration of a stepper motor.

Table 2.3.: Discrete states of operation of a stepper motor in Full-Step-Mode. (cw = clockwise, ccw = counterclockwise)

states		I	II	III	IV
coil currents	I_A	+1	−1	−1	+1
in unit of $I_{\max}$	I_B	+1	+1	−1	−1
rotation	cw	⟵			
	ccw	⟶			

The main application area of stepper motors is the relatively exact positioning even without complicated control or sensor processing. It is controlled via a list of discrete input states, as shown in Table 2.3. If the motor is operated within its specifications, it follows the control input and moves to discrete angles. If you run through the list of excitations, you get a rotation of the motor. At any time the position of the motor is known from the excitation state.

In the example motor a circular motor is considered consisting of two parts: rotor (rotating) and stator (non-rotating). A permanent magnet is mounted on the motor shaft and represents the rotor. The stator consists of several coils which can be excited via 2 phases. The coils are usually current controlled. This results in $I_A(t)$ and $I_B(t)$ as control signals at time t. One of the key characteristic of such a motor is the maximum allowed current $I_{\max}$. In the example are two pairs of opposing coils, arranged as shown in Figure 2.11.

In the example only the simplest and most basic mode of operation is considered. It is called Full-Step-Mode. In this mode the coil currents $I_A(t)$ and $I_B(t)$ are always either $I_{\max}$ or $-I_{\max}$. So there exist only four discrete input states, as listed in Table 2.3. To change the state, exactly one coil current is inverted. Running through this sequence of states in the correct order, the motor's direction of rotation can be determined. For each change of state the motor rotates by a specific angle. A typical value is 1.8°, which correspond to 200 steps per revolution. The example motor has a step angle of 90°.

The stator and the rotor are only coupled by the magnetic field. By changing the currents in the coils the magnetic field is shifted and by the physical principle of

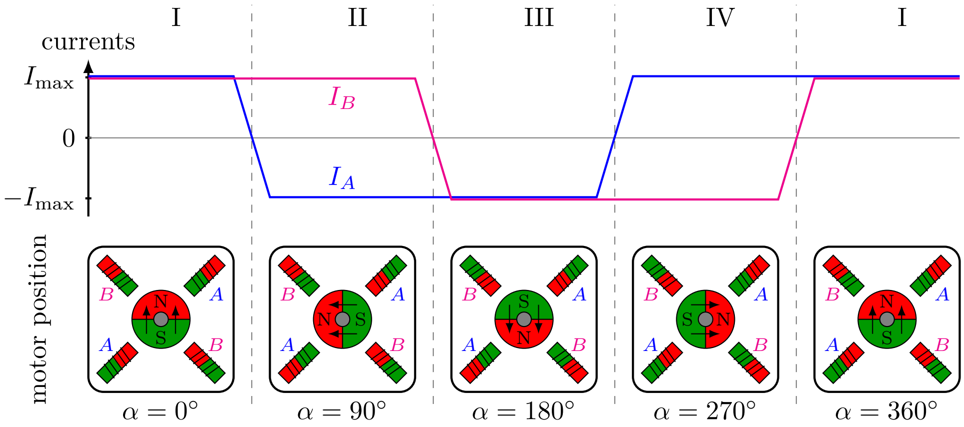

Figure 2.12.: An illustration of the excitation of a stepper motor.

energy minimization, the rotor is not anymore in optimal position. The resulting force turns the rotor, so that it tries to get back in optimal position. If this magnetic force of the motor is greater than the force required to turn the rotor, the motor will rotate. And according to the conception of the motor and the known excitation state, one can conclude the (approximate) angular position of the motor. A simplified illustration can be found in Figure 2.12.

2.4.2. Important Aspects in the Context of this Thesis

Based on the previous example, approaches – that are taken up in the further course of this thesis – are motivated.

In general, electric motors are based on the interaction of magnetic fields. The strength and course of the fields can be heavily influenced by the use of certain materials and geometric arrangements. From a mathematical point of view, approaches are needed to model such a motor and then optimize it according to certain criteria, e.g., efficiency, torque or thermal rating. See [117–121] for a few selected examples from literature.

The focus will lie in modeling the hysteresis effect for ferromagnetic materials. In particular, Tellinen's scalar hysteresis model (see [54] and Chapter 3) will be examined and extended.

The above example clearly shows that an efficient and durable motor requires different materials. The permanent magnets should provide a strong magnetic field even after a long time of usage. This means that neither the constant remagnetization of the coils nor the resulting heat should significantly weaken the magnetization of the magnets. Therefore, a particularly strong manifestation of the hysteresis effect is desired. The materials used for permanent magnets therefore fall more into the category of hard ferromagnetic materials.

The coils contain cores for generating particularly strong and shaped magnetic fields. These cores must be easily remagnetizable and best with the lowest possible losses.

Therefore, materials from the field of soft ferromagnetic materials are more likely to be used here. Since in many applications the maximum possible current is limited by I_{max}, the application case is that the excitation always changes between $+I_{\text{max}}$ and $-I_{\text{max}}$. One focus of this thesis will be to investigate the behavior of Tellinen's hysteresis model for exactly this type of excitation (see Section 3.2).

The compactness of a motor plays a noteworthy role in the application. This makes heat management a topic of interest. In addition to ohmic losses, hysteresis losses are added due to the constant remagnetization of the coils. On the one hand Tellinen's model shall be supplemented by a loss model for hysteresis losses (see Section 4.1). On the other hand it shall be extended to include temperature changes (see Section 4.2). In the case of stepper motors this is of special importance. For a full revolution of the motor, typically the coils need to be remagnetized hundreds of times. Even if the motor is standing still, a step loss can only be avoided if a current flows continuously and thus a non-rotating stepper motor continuously has ohmic losses and heats up.

3 | Tellinen's Scalar Hysteresis Model

The objective of this chapter is to present a scalar hysteresis model based on [54]. This model defines a coupling between the magnetic flux density b and the magnetic field strength h.

Chapter 2 already explained that the proposed benchmark problem is constructed in such a way that the multidimensional fields $\overrightarrow{H}$, $\overrightarrow{B}$ can be reduced to scalar quantities h,b. μ is also assumed to be scalar.

Some knowledge already presented in the previous chapters is repeated and complemented to a complete presentation of the model. Within the consideration it is often switched between the already introduced coordinate systems (h, b) and (h, b_i). In many places both representations are presented side by side.

In this chapter, the temperature dependence is not yet considered. The temperature T is assumed to be constant. In the later Section 4.2 a temperature dependence extension will be presented.

This chapter is structured as follows.

► First, Section 3.1 defines the hysteresis model mathematically. Required equations and definition domains are specified. The basic thoughts and ideas of the model are illustrated to the reader. Afterwards, the presented definitions are physically motivated. The assumptions made and the approaches used are compared with the physical background from Chapter 2 and checked for reasonableness.

► In Section 3.2 Tellinen's model is examined and properties are shown. Thereby, properties available in the original source [54] are presented. Also further investigations already published by the author of this dissertation [36–38] but also new more detailed ones are presented. The investigations start with basic properties like symmetry and monotonicity. Based on the first order reversal curves a consideration over specially defined paths is introduced. This methodology is taken up again in the following chapters. Thus, the behavior of Tellinen's model with respect to certain excitations can be mathematically proven.

► A purely isolated consideration of the Tellinen model does not answer the question of how it can be integrated into a numerical magnetic field simulation. Therefore, in Section 3.3 initial approaches are presented, how this could be done. Thereby, different application possibilities are derived from Tellinen's model. The concrete implementation will be examined later in Section 5.3.

3.1. The Original Tellinen Model

This specific hysteresis model was introduced 1998 by Tellinen [54]. A comparison of different hysteresis models [50] describes this model as a fast and simple one. Nevertheless, in most studies it exhibits a very good agreement with the measurements. Tellinen himself already emphasized that it should be a quick and simple model. The model should also require a material analysis that is as easy as possible to measure. It is natural that in the past 20 years the measurement possibilities have developed further. A few thoughts on how this development might influence the Tellinen model are presented in Section 3.2.2.

Tellinen's model is a scalar one, i.e., the magnetic fields are regarded as scalars $h, b \in \mathbb{R}$. This means in particular that this model cannot be integrated into the general Curl-Curl Equation (2.8). But for certain problems, this equation can be reduced to scalar quantities, such as (2.13).

In this section, the model is first defined mathematically. Then, the model is physically motivated. Further properties of the model are examined afterwards in Section 3.2.

3.1.1. Mathematical Definition

As mentioned in Remark 2.15, the analysis and definition can either happen in (h, b) or (h, b_i) coordinates. At this point both versions are introduced side by side.

As input, the model only requires one measurement of the material: the limiting saturation curve B^+_{sat}. Given is either $B^+_{\text{sat}} \in C^1(\mathbb{R})$ or $B^+_{\text{i,sat}} \in C^1(\mathbb{R})$ with the following properties. Both functions are linked with (2.21) by

$$B^+_{\text{sat}}(h) = B^+_{\text{i,sat}}(h) + \mu_0 h\,, \qquad B^+_{\text{i,sat}}(h) = B^+_{\text{sat}}(h) - \mu_0 h\,. \tag{3.1}$$

Using symmetry arguments, B^-_{sat} and $B^-_{\text{i,sat}}$ are defined by

$$B^-_{\text{sat}}(h) := -B^+_{\text{sat}}(-h)\,, \qquad B^-_{\text{i,sat}}(h) := -B^+_{\text{i,sat}}(-h)\,. \tag{3.2}$$

B^+_{sat}, B^-_{sat} and analogously $B^+_{\text{i,sat}}$, $B^-_{\text{i,sat}}$ must form a closed curve without overlap. This is given by

$$\begin{aligned} &B^+_{\text{sat}}(h) < B^-_{\text{sat}}(h)\,, && B^+_{\text{i,sat}}(h) < B^-_{\text{i,sat}}(h)\,, \\ &\lim_{|h|\to\infty} \left(B^-_{\text{sat}}(h) - B^+_{\text{sat}}(h)\right) = 0\,, && \lim_{|h|\to\infty} \left(B^-_{\text{i,sat}}(h) - B^+_{\text{i,sat}}(h)\right) = 0\,. \end{aligned} \tag{3.3}$$

The derivatives of B^+_{sat} and $B^+_{\text{i,sat}}$ must be bounded from below by

$$\begin{aligned} &\frac{\mathrm{d}}{\mathrm{d}h} B^+_{\text{sat}}(h) > \mu_0 > 0\,, && \frac{\mathrm{d}}{\mathrm{d}h} B^+_{\text{i,sat}}(h) > 0\,, \\ &\lim_{|h|\to\infty} \tfrac{\mathrm{d}}{\mathrm{d}h} B^+_{\text{sat}}(h) = \mu_0\,, && \lim_{|h|\to\infty} \tfrac{\mathrm{d}}{\mathrm{d}h} B^+_{\text{i,sat}}(h) = 0\,. \end{aligned} \tag{3.4}$$

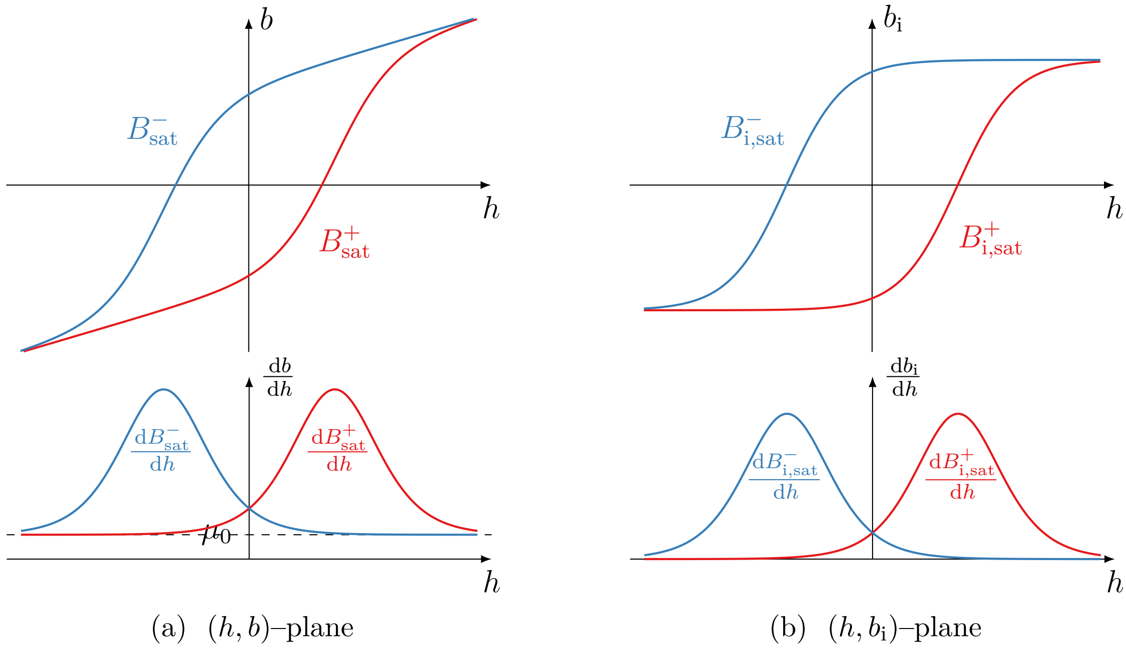

(a) (h, b)–plane (b) (h, b_{i})–plane

Figure 3.1.: Overview of $B^\pm_{\mathrm{sat}}$ and $B^\pm_{\mathrm{i,sat}}$ and their derivatives.

Typical for ferromagnetic materials are “S”-shaped or sigmoidal curves for $B^\pm_{\mathrm{sat}}$. A visual overview of $B^\pm_{\mathrm{sat}}$ and $B^\pm_{\mathrm{i,sat}}$ is given in Figure 3.1.

Remark 3.1. A simple interpolation of the measured data for B^+_{sat} or $B^+_{\mathrm{i,sat}}$ may not be valid for Tellinen's model. Some interpolation methods may overshoot and violate the condition (3.4). Specialized monotonocity preserving methods, e.g. [86, 87, 89], are necessary. Even further data processing steps like approximation and consideration of noisy measurement data [88, 90, 91] are an important factor in the creation of the material curve B^+_{sat} or $B^+_{\mathrm{i,sat}}$. In the context of this dissertation, this aspect will not be considered further. The material curve B^+_{sat} or $B^+_{\mathrm{i,sat}}$ was somehow created and is available as a $C^1(\mathbb{R})$ function with the above conditions.

Tellinen's model operates on and inside the saturation loop. The set of all valid states (h, b) is given by

$$I = \left\{ (h, b) \in \mathbb{R}^2 \,\middle|\, B^+_{\mathrm{sat}}(h) \le b \le B^-_{\mathrm{sat}}(h) \right\} . \tag{3.5}$$

A more detailed analysis of I is found in Section 3.2.3. A corresponding definition of I_i for the (h, b_i) coordinates is made via

$$I_{\mathrm{i}} = \left\{ (h, b_i) \in \mathbb{R}^2 \,\middle|\, (h, b_i + h\mu_0) \in I \right\} . \tag{3.6}$$

For any $(h, b) \in I$, Tellinen's model links h and b by the ordinary differential equation (ODE)

$$\frac{\mathrm{d}b}{\mathrm{d}h} = \mu_{\mathrm{diff}} = \begin{cases} \mu^+_{\mathrm{diff}} = \lambda \frac{\mathrm{d}B^+_{\mathrm{sat}}(h)}{\mathrm{d}h} + (1-\lambda)\mu_0 & \text{, if } h \text{ is increasing,} \\ \mu^-_{\mathrm{diff}} = (1-\lambda)\frac{\mathrm{d}B^-_{\mathrm{sat}}(h)}{\mathrm{d}h} + \lambda\mu_0 & \text{, if } h \text{ is decreasing,} \end{cases} \tag{3.7}$$

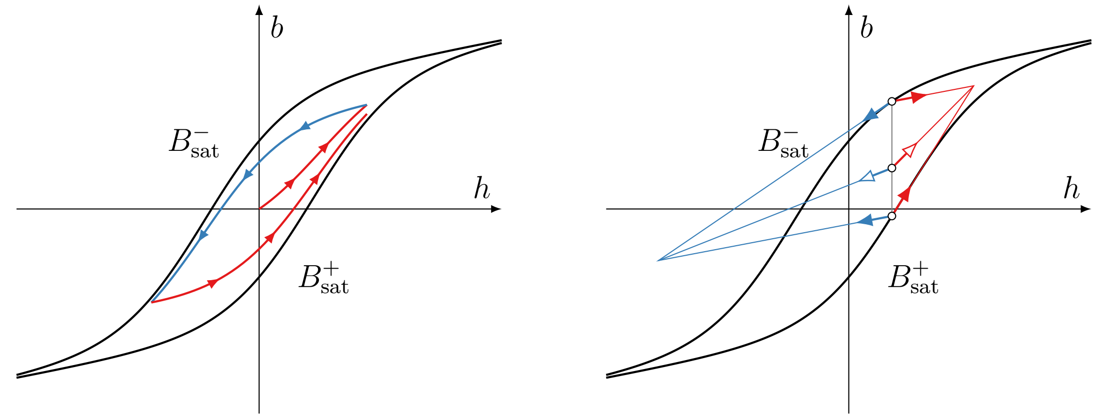

(a) Example path starting from the demagnetized state.

(b) Schematic of Tellinen's model. With predefined values on the boundaries, inner values are calculated via interpolation.

Figure 3.2.: Basic ideas and examples of Tellinen's model. $\mathrm{d}h > 0$ in red and $\mathrm{d}h < 0$ in blue. Comparable figures can be found in [37–39].

with λ being the relative vertical position inside I, respectively I_i, defined by

$$\lambda = \frac{B^-_{\mathrm{sat}}(h) - b}{B^-_{\mathrm{sat}}(h) - B^+_{\mathrm{sat}}(h)} = \frac{B^-_{\mathrm{i,sat}}(h) - b_i}{B^-_{\mathrm{i,sat}}(h) - B^+_{\mathrm{i,sat}}(h)} \in [0,1]\,. \tag{3.8}$$

Remark 3.2. For a simpler notation the abbreviation $\mu^+_{\mathrm{diff}} = \mu^+_{\mathrm{diff}}(h,b)$ and $\mu^-_{\mathrm{diff}} = \mu^-_{\mathrm{diff}}(h,b)$ are introduced. In general, it is tried to express – by a suitable notation – if quantities are directional or not. This is indicated by a superscript of + or -. If both directions are meant simultaneously, ± is used.

Equation (3.7) can be formulated equivalently in (h, b_i) as

$$\frac{\mathrm{d}b_i}{\mathrm{d}h} = \begin{cases} \lambda \frac{\mathrm{d}B^+_{\mathrm{i,sat}}(h)}{\mathrm{d}h} & \text{, if } h \text{ is increasing,} \\ (1-\lambda)\frac{\mathrm{d}B^-_{\mathrm{i,sat}}(h)}{\mathrm{d}h} & \text{, if } h \text{ is decreasing}\,. \end{cases} \tag{3.9}$$

Tellinen's model combines several approaches and ideas.

▶ First, it determines the relative vertical position of $(h,b) \in I$ inside the loop via λ. A value of $\lambda = 0$ represents $(h,b) = (h, B^-_{\mathrm{sat}}(h))$, i.e., the current working point is on the upper boundary. In a similar way $\lambda = 1$ represents $(h,b) = (h, B^+_{\mathrm{sat}}(h))$, i.e., the lower boundary.

▶ Second, it splits up the right hand side of the ODE (3.7) depending whether h is increasing or decreasing. For both cases, it assigns certain values of $\frac{\mathrm{d}b}{\mathrm{d}h}$ on the boundaries.

▶ Third, it performs a linear interpolation based on the boundary values and the relative position λ.

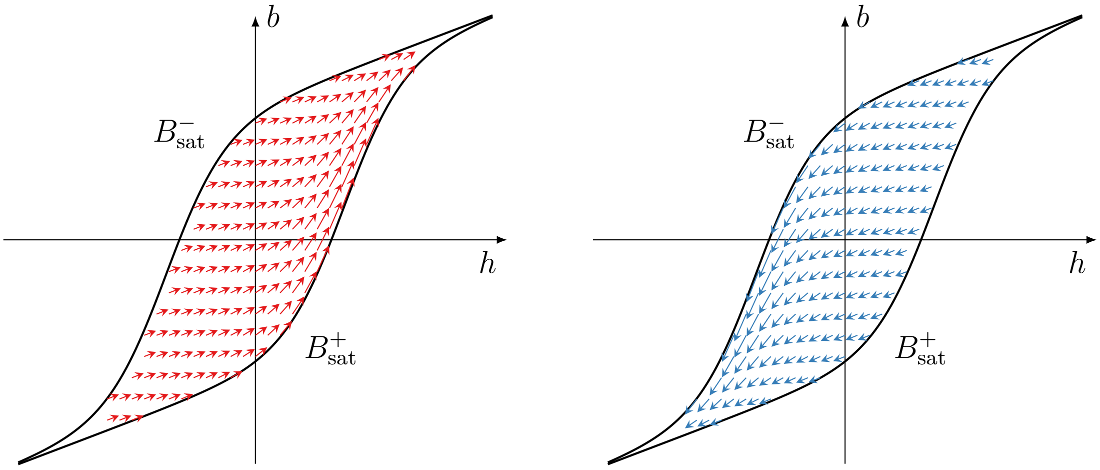

(a) $\mathrm{d}h > 0,\ \mu^+_{\mathrm{diff}}(h, b) = \frac{\mathrm{d}b}{\mathrm{d}h}$ (b) $\mathrm{d}h < 0,\ \mu^-_{\mathrm{diff}}(h, b) = \frac{\mathrm{d}b}{\mathrm{d}h}$

Figure 3.3.: Resulting vector field from Tellinen's model.

Remark 3.3. Although it might be possible to solve the ODE (3.7) analytically for certain $B^\pm_{\mathrm{sat}}$ curves, it is assumed in this thesis that this is generally not possible.

Remark 3.4. A numerical solution is nevertheless possible, see Figure 3.2(a) for an example. Since the fundamental basis of Tellinen's model is an ODE, a whole range of basic literature w.r.t. analytical and numerical properties, e.g. [92, 93, 95, 97], can be referred to for later analyses and approaches.

Unfortunately the model does not provide a direct link between the quantities h and b. Instead it connects these quantities by the ODE (3.7). Thus, the model creates a vector field as shown in Figure 3.3. A definition of the function ν, motivated in Remark 5.3, is therefore not available at this time. In the following Sections 3.2 and 3.3 this issue will be discussed again.

3.1.2. Physical Motivation

Tellinen's model [54] directly addresses the physical motivation of the saturation curves $B^\pm_{\mathrm{sat}}$ and $B^\infty_{\mathrm{i,sat}}$ as in Section 2.3.2. A small mathematical subtlety is the difference between (2.17) and (3.4), namely that $B^+_{\mathrm{sat}} \neq B^-_{\mathrm{sat}}$ holds. Saturation curves $B^\pm_{\mathrm{sat}}$ are referred to and used as the defining property of a ferromagnetic material. Especially the view that these curves are a natural limit of the possible reachable states will be mentioned in the argumentation in a moment. That the limit is respected – in a mathematically sense – by the model will be investigated in the next Section 3.2.

Tellinen's model separates between the contribution of the material and a vacuum. The two coordinate systems (h, b) and (h, b_{i}) have already been introduced in Section 2.3.2. The meaning of the maximum amplification of a magnetic field by a ferromagnetic material $B^\infty_{\mathrm{i,sat}}$ has also already been presented. Furthermore, as already argued in Remark 2.11, the model assumes such a high number of discrete

Barkhausen jumps and Bloch wall motions, that this can be approximated by a continuous stochastic process.

If the derivatives $\frac{\mathrm{d}B^{\pm}_{\mathrm{i,sat}}}{\mathrm{d}h}$ is considered as shown in Figure 3.1(b) and scale them by a factor of $\frac{1}{2B^{\infty}_{\mathrm{i,sat}}}$, in each case a valid stochastic density function is obtained. According to the reasoning of the authors in [54], this density function can be used to describe Bloch Wall motions. Depending on the direction ($\mathrm{d}h \gtrless 0$), the material behaves differently. This is achieved and represented in the model by a direction-dependent definition.

Now, three steps to explain and motivate the model are following. First, a motivation is given on the saturation curves $B^{\pm}_{\mathrm{i,sat}}$ with the proper direction. Second, a motivation is given on the saturation curves $B^{\pm}_{\mathrm{i,sat}}$ but on the opposing direction. Third, states (h, b_i) inside the saturation curves are defined via interpolation. An overview in (h, b)–coordinates can be found in Figure 3.2(b).

Assuming the current state lies on the lower saturation curve, i.e., $(h_0, b_{\mathrm{i},0}) = \Big(h_0, B^{+}_{\mathrm{i,sat}}(h_0)\Big)$. If $\mathrm{d}h > 0$ holds, the proper direction is used and the saturation curve is exactly the process described. So starting in some $(h_0, b_{\mathrm{i},0}) = \Big(h_0, B^{+}_{\mathrm{i,sat}}(h_0)\Big)$ and increasing h results in the path $\Big(h, B^{+}_{\mathrm{i,sat}}(h)\Big)$ for all $h \geq h_0$.

Instead on the lower boundary $B^{+}_{\mathrm{i,sat}}$, $(h_0, b_{\mathrm{i},0}) = (h_0, B^{-}_{\mathrm{i,sat}}(h_0))$ with increasing h is now assumed. For a fixed h_0 and increasing h, the state $(h_0, B^{-}_{\mathrm{i,sat}}(h_0))$ is the most oppositional – in the sense of being the maximal state for decreasing direction – one possible. In this state the Bloch walls and Weiß domains are maximally counter-aligned, i.e., the most favorable state, if h would be decreasing. But if an increasing h is considered, the material is in a state with maximum resistance for a change in this direction. This resistance must first be broken down to cause a change in the magnetic field. For this concrete condition, therefore, it is assumed that although h becomes larger, b_i does not change.

Now, two states results, in which once the resulting path follows the saturation curve $B^{+}_{\mathrm{i,sat}}$ and once where b_i should not change. To model this situation, the differential permeability μ_{diff} – as already introduced in (2.14) – is used and an equivalent $\mu_{\mathrm{i},\mathsf{diff}} = \mu_{\mathsf{diff}} - \mu_0$ in the (h, b_i)–coordinate system is defined. To clearly represent the directionality, superscripts are used as shown in (3.7) to indicate whether h is increasing or decreasing. If the two cases are combined, for an increasing h equation

$$\mu^{+}_{\mathrm{i},\mathsf{diff}}\Big(h, B^{+}_{\mathrm{i,sat}}(h)\Big) = \frac{\mathrm{d}B^{+}_{\mathrm{i,sat}}}{\mathrm{d}h}\,, \qquad \mu^{+}_{\mathrm{i},\mathsf{diff}}\Big(h, B^{-}_{\mathrm{i,sat}}(h)\Big) = 0 \tag{3.10a}$$

is obtained. Using symmetry arguments, if h is decreasing an analogously argumentation is used. The roles of the boundary curves are reversed and results in

$$\mu^{-}_{\mathrm{i},\mathsf{diff}}\Big(h, B^{+}_{\mathrm{i,sat}}(h)\Big) = 0\,, \qquad \mu^{-}_{\mathrm{i},\mathsf{diff}}\Big(h, B^{-}_{\mathrm{i,sat}}(h)\Big) = \frac{\mathrm{d}B^{-}_{\mathrm{i,sat}}}{\mathrm{d}h}\,. \tag{3.10b}$$

So for a fixed h, it is motivated how to do the modeling on the saturation curves. Thus, the next logical step is to extend this consideration to the intermediate space.

Now, the special case $(h, b_\mathrm{i}) = (0, 0)$ is briefly considered and the case of increasing h is chosen for purposes of motivation. For $h = 0$, equations (3.10) supply the two extreme cases, if b_i would be maximal and minimal. Or differently formulated, the maximal possible constructive and the maximal destructive alignment of the Bloch walls and Weiß domains for this specific value of h. $b_\mathrm{i} = 0$ is considered, which is right in the middle of $B^+_{\mathrm{i,sat}}(0)$ and $B^-_{\mathrm{i,sat}}(0)$. The state $(h, b_\mathrm{i}) = (0, 0)$ is characterized by the fact that there is no external excitation ($h = 0$) and the individual magnetic domains exactly balance each other out ($b_\mathrm{i} = 0$). In other words, the exact centered positioning between the extremes results in a balance because one half of the Weiß domains are maximally constructively aligned and the other half maximally destructively aligned.

In [54] this concept is generalized. The relative position λ of the current state $(h_0, b_{\mathrm{i},0})$ between the extremes $\big(h_0, B^+_{\mathrm{i,sat}}(h_0)\big)$ and $\big(h_0, B^-_{\mathrm{i,sat}}(h_0)\big)$ determines their influence on μ_diff. Mathematically, this is a simple linear interpolation. In Figure 3.2(a) it can be seen, that the path clearly adapts more to the respective saturation curve the closer it gets to it.

From this motivation the illustrative nature of Tellinen's model is explained in the following and is shown in Figure 3.2(b). In a scalar environment only two directions are possible, denoted by $+$ and $-$. A ferromagnetic material behaves differently to these excitation directions and the mathematical definitions are therefore directional. The definition domain of the model is given by I/I_i from (3.5) and (3.6). On the boundary certain values are set based on the above physical background. Points inside are calculated by vertical interpolation based on the relative position λ from (3.8). Putting all this together, equation (3.7) is obtained in (h, b) coordinates and equation (3.9) in (h, b_i). This results in a compact model that couples the two quantities h, b via a directional ordinary differential equation.

Demands on a hysteresis model have been stated in Section 2.3.3, and now it is to discussed which ones are satisfied by Tellinen's model.

The model couples the fields h and b via the differential equation (3.7). In general, it does not provide a direct relation $b = \mu(h)$ or $h = \nu(b)$. So, how this model is integrated into the benchmark problem (2.13) remains to be seen and is open for discussion in Section 3.3.

Even though it is not possible to verify Tellinen's model in the scope of this dissertation due to a lack of suitable measured values, other literature sources like [50, 54] attribute good experimental agreement to the model. This agreement includes, among other things, that the boundary curves $B^\pm_\mathrm{sat}$ are not violated. This can already be roughly seen in the definition of the model. However, a thorough mathematical proof follows in Section 3.2.

Due to its directional definition, Tellinen's model is path dependent. More precisely, the model defines the behavior of the fields for a current operating point $(h_0, b_0) \in I$.

Since in general the calculated values of μ^{+}_{diff} and μ^{-}_{diff} differ, the model is not reversible without further ado.

No contradiction in the model w.r.t. the physical motivation of ferromagnetic materials is found. On the contrary, the approaches of the model can be motivated physically and phenomenologically.

However, it should be explicitly mentioned again that such a hysteresis model is nevertheless only an approximation. Certain physical phenomena are modeled differently by different hysteresis models. The goal of Tellinen's model was not to develop a model that is as accurate as possible. The focus was on a simple and fast model. Based on the above observations, Tellinen's model is considered to be a physically reasonable model which is sufficient for the demands on the accuracy of the hysteresis effect.

Next, a mathematical analysis of the model follows and it is checked whether there are any pitfalls from a mathematical point of view that have not yet become obvious.

3.2. Properties of Tellinen's Scalar Hysteresis Model

Now the properties of Tellinen's model shall be considered in more detail. On the one hand these are basic properties like monotonicity and symmetry. On the other hand, it shall be examined, if the model actually yields physically meaningful results. For this purpose, first order reversal curves (FORCs) are introduced in Section 3.2.2 as a basis for a mathematical investigation. The definition domain I is further partitioned in Section 3.2.3. So statements can be made more differentiated depending on the current working point $(h_0, b_0) \in I$. In the course of this section, the model is investigated, how it behaves under a certain type of excitation. It will be checked, if generally only physically reasonable solutions can be found. Conditions are derived to prevent an undesired behavior.

Individual parts of this investigation have already been examined by the creator of the model in [54]. Other aspects have been published by the author of this dissertation and colleagues [36–38]. However, the holistic and profound investigation of Tellinen's model remains one of the main focuses of this thesis.

3.2.1. Basic Properties

First of all, a few fundamental properties of Tellinen's model are shown.

Computational effort and memory requirements

Evaluation of μ_{diff} at a working point $(h, b) \in I$ requires only one evaluation of each of the functions $B_{\text{sat}}^{\pm}$ and either an evaluation of $\frac{\mathrm{d}B_{\text{sat}}^{+}}{\mathrm{d}h}$ or $\frac{\mathrm{d}B_{\text{sat}}^{-}}{\mathrm{d}h}$. So it has a very small number of calls to these functions. If a path shall be determined with the model, the whole arsenal of numerical methods for solving ODEs are available. This allows the user to decide about accuracy and computational effort. This statements refers to the isolated application of the model, i.e., not integrated into an all-in-one simulation.

Remark 3.5. Tellinen's model does not need to store the chronological sequence of the previous states. Only the current state $(h_0, b_0) \in I$ is needed. Furthermore, only the two functions B_{sat}^{+} and $\frac{\mathrm{d}B_{\text{sat}}^{+}}{\mathrm{d}h}$ are needed, i.e., the memory requirements are low.

Monotonicity

Monotonicity should be considered under two different aspects. First, the internal functions are to be investigated. Afterwards, the solutions are examined.

Lemma 3.6: For any fixed h, $\mu_{\text{diff}}^{+}(h, b)$ is strictly monotone decreasing in b and likewise $\mu_{\text{diff}}^{-}(h, b)$ is strictly monotone increasing. $\lambda(h, b)$ is strictly monotone decreasing in b.

Proof. If h is fixed, so are $B^+_{\mathrm{sat}}(h)$ and $B^-_{\mathrm{sat}}(h)$. λ as defined in (3.8) is strictly monotonously decreasing in the variable b. Another valid formulation of $\mu^\pm_{\mathrm{diff}}$ in (3.7) reads

$$\mu^+_{\mathrm{diff}}(h,b) = \mu_0 + \underbrace{\lambda(h,b)}_{\in[0,1]} \underbrace{\left(\frac{\mathrm{d}B^+_{\mathrm{sat}}(h)}{\mathrm{d}h} - \mu_0\right)}_{>0}, \tag{3.11a}$$

$$\mu^-_{\mathrm{diff}}(h,b) = \frac{\mathrm{d}B^-_{\mathrm{sat}}(h)}{\mathrm{d}h} + \underbrace{\lambda(h,b)}_{\in[0,1]} \underbrace{\left(\mu_0 - \frac{\mathrm{d}B^-_{\mathrm{sat}}(h)}{\mathrm{d}h}\right)}_{<0}. \tag{3.11b}$$

Using the monotonicity of λ and the signs of the factors, the monotonicity of $\mu^\pm_{\mathrm{diff}}$ is obvious. ☐

Lemma 3.7: Let p^+ denote a solution of the ODE (3.7) with initial value $(h_0, b_0) \in I$ and increasing h. p^+ is strictly monotone increasing.

Proof. As shown in (3.11), $\mu^+_{\mathrm{diff}} \geq \mu_0 > 0$ holds. Hence the solution p^+ of the ODE (3.7), fullfils $\frac{\mathrm{d}p^+}{\mathrm{d}h} = \mu^+_{\mathrm{diff}}(h,b) \geq \mu_0 > 0$ and is strictly monotone. ☐

Remark 3.8. A direct consequence of Lemma 3.7 is, that it does not matter if it is checked whether h or b is increasing or decreasing. Further it ensures that any solution $b = p^+(h)$ is invertible and $h = (p^+)^{-1}(b)$ exists. This will be used for defining a suitable ν.

Remark 3.9. In the physical sense this means that an increase of the excitation h always leads to an increase of the resulting field b as well. The Weiß domains and Bloch walls are therefore only realigned to match the excitation and do not counteract it. This is the expected behavior for ferromagnetic materials.

Alternative formulation w.r.t. ν

Remark 3.10. In the default definition of the model, h is seen as the independent variable and b as a dependent one. But it is also possible to switch this setting, as stated in [54].

The fundamental basis is the ODE (3.7). With the above mentioned properties an equivalent formulation is given by

$$\frac{\mathrm{d}h}{\mathrm{d}b} = \nu_{\mathrm{diff}}(h,b) = \begin{cases} \nu^+_{\mathrm{diff}}(h,b) = \frac{1}{\mu^+_{\mathrm{diff}}(h,b)} & \text{,if } b \text{ is increasing,} \\ \nu^-_{\mathrm{diff}}(h,b) = \frac{1}{\mu^-_{\mathrm{diff}}(h,b)} & \text{,if } b \text{ is decreasing}. \end{cases} \tag{3.12}$$

Thus, it is possible to use either h or b as the independent variable. In both cases the right side of the ODEs (3.7) and (3.12) are based on the evaluation of the functions $\mu^\pm_{\mathrm{diff}}$.

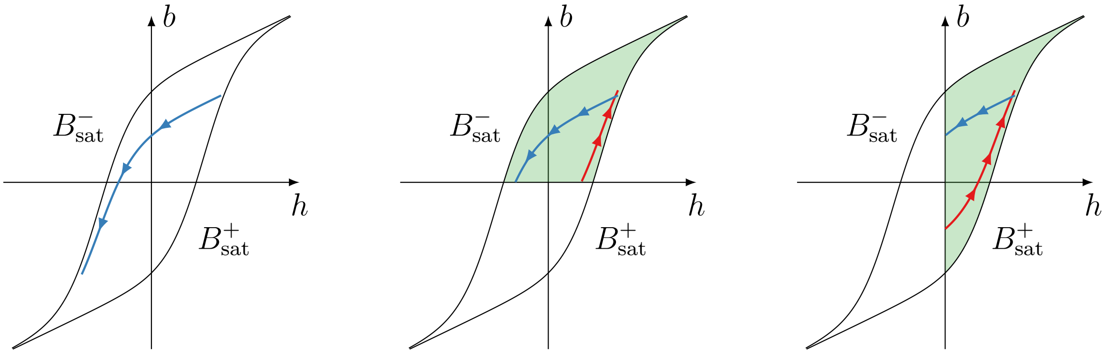

(a) without symmetry (b) using upper half (c) using right half

Figure 3.4.: Possible use of symmetry within Tellinen's model. All three plots show an equivalent path. The blue parts are based upon μ_{diff}^{-} and red ones on μ_{diff}^{+}. If the domain is restricted by symmetry, the active area is marked green.

In the following considerations and analysis it will be assumed that h is the independent variable. This assumption corresponds to the usual approach from the literature. But it has already been motivated in Chapter 2, that for the chosen simulation approach a calculation in the form $h = \nu(b)$ is necessary. As just shown, the Tellinen's model can be used equivalently well in both variants. Therefore this does not create a problem. For the case of actual solving (2.13), approaches for ν are presented in Section 3.3.

Symmetry

The model exhibits symmetry in many regards. Starting with the definition of B_{sat}^{-} in (3.2), followed by $\frac{\mathrm{d}}{\mathrm{d}h} B_{\mathrm{sat}}^{+}(h) = \frac{\mathrm{d}}{\mathrm{d}h} B_{\mathrm{sat}}^{-}(-h)$,

$$\mu_{\mathrm{diff}}^{+}(h, b) = \mu_{\mathrm{diff}}^{-}(-h, -b) \tag{3.13}$$

can be concluded. As shown in Figure 3.4, the curves behave symmetrically. This also fits to the physical background. No preferred direction can be observed.

Unfortunately, the symmetry cannot be exploited for simplification. It is possible to restrict the domain to a halfplane instead of the whole hb-plane. Two possible choices are shown in Figures 3.4(b) and 3.4(c). However it is not possible to restrict the domain to only one quadrant. Furthermore, it have to be considered that the direction changes at the skip when using symmetry.

But since there are no obvious savings in terms of memory or computing time, symmetry is not used to reduce the domain. However, symmetry is extensively used in the further studies. Usually only the case for increasing h is examined. Equivalent statements for decreasing h then follow by symmetry arguments.

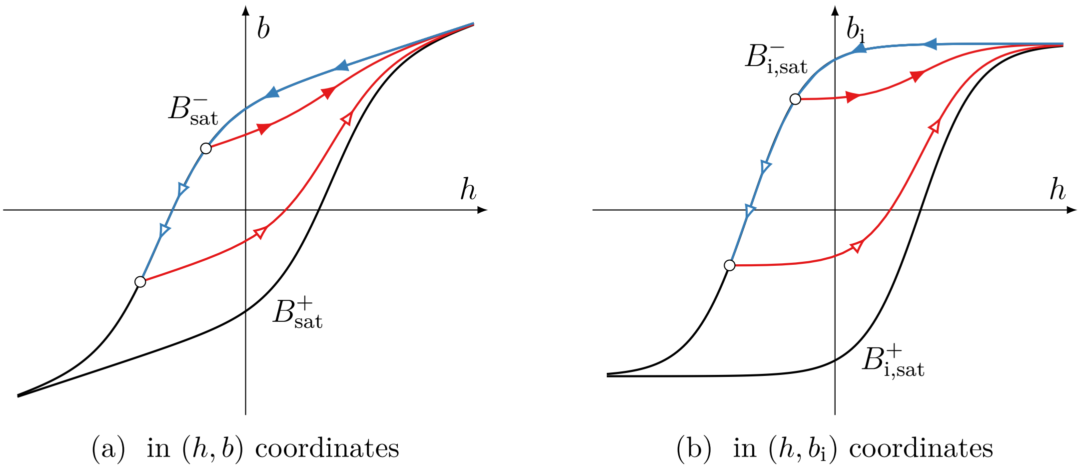

(a) in (h, b) coordinates (b) in (h, b_i) coordinates

Figure 3.5.: Idea of first order reversal curves (FORCs) and two examples.

3.2.2. First Order Reversal Curves and their Extension

First order reversal curves (FORCs) are created by magnetizing a material to full saturation, demagnetize it a specified amount and magnetize it again to full saturation. The part of this cycle inside the saturation curve is called a FORC. An overview is given in Figure 3.5. FORCs are curves that start on the boundary at some $(h_0, B^-_{\text{sat}}(h_0)) \in I$ and are defined for all $h \geq h_0$. Typically such a measurement is performed for different degrees of demagnetization. While until now only the actual saturation curves $B^\pm_{\text{sat}}$ have been considered, FORCs contain information within I.

FORCs [110] and FORC diagrams [108, 109, 112] derived from FORCs, are a valuable first-pass characterization tool [107] and basis for material analyses [106, 111].

FORCs can be approached under two different aspects. On the one hand, FORCs can provide information about the behavior of the material inside of I. Considering the time of origin of Tellinen's model and the technological progress since then, more advanced and fast measuring methods are possible today [110]. One could use the FORCS for interpolation not only based on data on the boundary curves $B^\pm_{\text{sat}}$, but also to insert further intermediate stages within I.

On the other hand, FORCs are used as a mathematical construct in the upcoming analysis. They can be computed by Tellinen's model. If designed this way, they are solutions to the ODE (3.7).

Hence the two approaches differ in the source of information. The first approach gets FORCs from measurements. The second approach generates FORCs from within Tellinen's model. If for a material only measurements of the saturation curves $B^\pm_{\text{sat}}$ are available, Tellinen's model can calculate FORCS and thus an examination of the material using FORC diagrams is possible. In the framework of this thesis, FORCs diagrams shall not be discussed further.

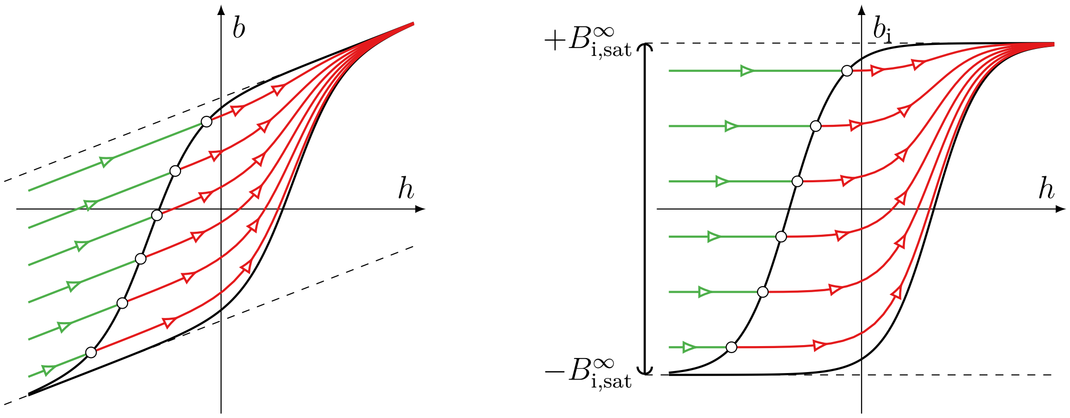

(a) in (h, b) coordinates (b) in (h, b_{i}) coordinates

Figure 3.6.: First order reversal curves (red) and the extension outside of I, I_{i} (green).

Definition and properties of extended FORC's

The paths p^+ and p_{i}^+ are defined in the following as an extension of FORCs. While the motivation will be in (h, b_i) coordinates, the definition easily carries over to (h, b) coordinates.

Remark 3.11. The extension to the area outside of I serves only mathematical purpose. In the application, only I is relevant.

Construction of p^+

Definition 3.12: The path p_{i}^+ denotes the solution of the initial value problem (IVP) with $p_{\mathrm{i}}^+(h_0) = b_{i,0}$ for given $(h, b_{i,0}) \in I_{\mathrm{i}}$ and

$$\frac{\mathrm{d}p_{\mathrm{i}}^+(h)}{\mathrm{d}h} = \begin{cases} \mu^+_{\mathrm{i,diff}}\big(h, p_{\mathrm{i}}^+(h)\big) & \text{if } \big(h, p_{\mathrm{i}}^+(h)\big) \in I_{\mathrm{i}} \\ 0 & \text{else} \end{cases} . \tag{3.14}$$

With $p^+(h) = p_{\mathrm{i}}^+(h) + h\mu_0$, an equivalent definition of p^+ is possible by the IVP $p^+(h_0) = b_0 = b_{i,0} + h_0\mu_0$ ($(h_0, b_0) \in I$) and

$$\frac{\mathrm{d}p^+(h)}{\mathrm{d}h} = \begin{cases} \mu^+_{\mathrm{diff}}\big(h, p^+(h)\big) & \text{if } \big(h, p^+(h)\big) \in I \\ \mu_0 & \text{else} \end{cases} . \tag{3.15}$$

An example is presented in Figure 3.6.

The existence, uniqueness and domain of p^+ will now be investigated.

The extension outside of I, respectively I_{i}, is done in such a way, that the right hand side of the IVP's are continuous and differentiable. Using the theory of ODEs and especially the Theorem of Picard–Lindelöf, the following properties can be proven.

Lemma 3.13: For any point $(h_0, b_0) \in I$ exists an unique path p^+, such that $p^+(h_0) = b_0$ and (3.15) holds. p^+ is defined over the whole domain of $\mathbb{R}$.

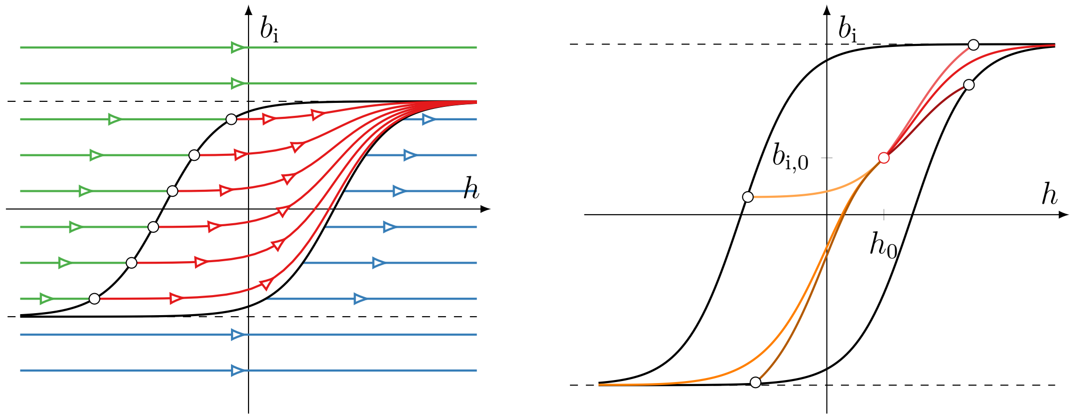

(a) Solutions of (3.14). Parts within I_i are shown in red, above in green and below in blue.

(b) The possibilities of a path p_i^+ starting in $(h_0, b_\mathrm{i,0}) \in \mathrm{int}(I_\mathrm{i})$. It could intersect the boundaries $B_\mathrm{i,sat}^\pm$ or stay between them.

Figure 3.7.: Sketch of the proof of Lemma 3.13 in (h, b_i) coordinates.

Proof. The right hand side of (3.15) is defined conditionally, whether $\big(h, p^+(h)\big) \in I$ or $\big(h, p^+(h)\big) \notin I$ holds. These transitions happen either at B_sat^+ or B_sat^-.

First, solutions that are completely in I are considered. Second, it will be proven that a solution of (3.15) does not leave the domain I along B_sat^+. Third, the transition at B_sat^- is analyzed.

Initially, the consideration is limited to the interior of the domain I, i.e., $\mathrm{int}(I)$. There the ODE $\frac{\mathrm{d}p^+(h)}{\mathrm{d}h} = \mu_\mathrm{diff}^+(h, p^+(h))$ with the initial value $(h_0, b_0) \in \mathrm{int}(I)$ holds. Another formulation of μ_diff^+ (compared to (3.7) and (3.8)) is given by

$$\mu_\mathrm{diff}^+(h, b) = \frac{B_\mathrm{sat}^-(h) - b}{B_\mathrm{sat}^-(h) - B_\mathrm{sat}^+(h)} \frac{\mathrm{d}B_\mathrm{sat}^+(h)}{\mathrm{d}h} + \frac{b - B_\mathrm{sat}^-(h)}{B_\mathrm{sat}^-(h) - B_\mathrm{sat}^+(h)} \mu_0 \,. \tag{3.16}$$

μ_diff^+ is continuous in both variables and differentiable in the second variable:

$$\frac{\partial}{\partial b} \mu_\mathrm{diff}^+(h, b) = \frac{\mu_0 - \frac{\mathrm{d}B_\mathrm{sat}^+(h)}{\mathrm{d}h}}{B_\mathrm{sat}^-(h) - B_\mathrm{sat}^+(h)} \,. \tag{3.17}$$

$\mu_\mathrm{diff}^+(h, b)$ is linear in b and with the restriction to $b \in [B_\mathrm{sat}^-(h), B_\mathrm{sat}^+(h)]$ globally limited. Therefore, μ_diff^+ is Lipschitz continuous in the second variable. The Picard-Lindelöf Theorem guarantees existence and uniqueness of a solution of the IVP as long as $\big(h, p^+(h)\big) \in \mathrm{int}(I)$ holds.

Next the definition domain of p^+ must be examined. There are three possibilities. The path p^+ can either stay between B_sat^+ and B_sat^-. In this case p^+ is defined on the complete $\mathbb{R}$. Or p^+ tends towards the boundaries $B_\mathrm{sat}^\pm$. Then p^+ can be continued up to the boundary and there exist intersections with B_sat^+ or B_sat^-. An overview is given in Figure 3.7, separately for $h > h_0$ and $h < h_0$. These two cases will be considered individually.

1) $h_0 < h$:
At the boundary B_{sat}^{-} it holds

$$\mu_{\mathrm{diff}}^{+}\Big(h, B_{\mathrm{sat}}^{-}(h)\Big) = \mu_0 < \frac{\mathrm{d}B_{\mathrm{sat}}^{-}(h)}{\mathrm{d}h} \quad \text{for all } h \in \mathbb{R}\,. \tag{3.18}$$

This means that the path p^+ cannot cross the boundary curve B_{sat}^{-} from the bottom. With $p^+(h_0) = b_0 < B_{\mathrm{sat}}^{-}(h_0)$ this results in $p^+(h) < B_{\mathrm{sat}}^{-}(h)$ for all $h > h_0$.

At the boundary B_{sat}^{+} it holds

$$\mu_{\mathrm{diff}}^{+}\Big(h, B_{\mathrm{sat}}^{+}(h)\Big) = \frac{\mathrm{d}B_{\mathrm{sat}}^{+}(h)}{\mathrm{d}h} \quad \text{for all } h \in \mathbb{R}\,. \tag{3.19}$$

Thus, also here a intersection is not possible, i.e., there remains only the possibility that p^+ can be continued for all $h > h_0$ and

$$B_{\mathrm{sat}}^{+}(h) < p^+(h) < B_{\mathrm{sat}}^{-}(h) \quad \text{for all } h \geq h_0 \tag{3.20}$$

applies.

2) $h < h_0$:
Equation (3.19) also holds in this case. Hence B_{sat}^{+} is globally a lower bound for all solutions with initial value $(h_0, b_0) \in \mathrm{int}(I)$. B_{sat}^{+} is itself a solution of (3.15). This ensures that a solution of (3.15) can never leave the feasible area I over the boundary B_{sat}^{+}.

At this point it will not be examined in detail which of the two remaining cases occurs. This is done separately in Lemma 3.16. Here it is proved that both cases yields the desired properties.

Assuming that there exists no intersection of p^+ and B_{sat}^{-}. Then (3.20) holds for all $h \in \mathbb{R}$ and p^+ is defined on complete $\mathbb{R}$.

Assuming the existence of an intersection of p^+ and B_{sat}^{-} at (h^*, b^*), path p^+ can be extended from h_0 to h^*, inclusive. At the intersection (h^*, b^*), (3.18) holds. This means that p^+ can pass the boundary B_{sat}^{-} only from one side. Equation (3.19) is valid for $h^* < h$ and $p^+(h^*) = B_{\mathrm{sat}}^{-}(h^*)$ holds. This leads in a definition domain of p^+ of at least $[h^*, \infty)$.

Consider the case distinction in (3.15), this can be extended p^+ for all $h < h^*$. The solution outside of I is given by

$$p^+(h) = b^* + \mu_0(h - h^*) \quad \text{for all } h < h^*\,. \tag{3.21}$$

Furthermore the transition of p^+ at position h^* is continuously and differentiable.

This approach works as well if the starting point (h_0, b_0) satisfies $b_0 = B_{\mathrm{sat}}^{-}(h_0)$. So for all possible initial values $(h_0, b_0) \in I$ it was shown, that solutions p^+ of the ODE (3.15) can always be extended to the whole $\mathbb{R}$.

The resulting path p^+ is continuously, differentiable and unique by construction as solution of the ODE (3.15). □

Remark 3.14. In the sequel any path denoted by p^+ is defined as a solution of (3.15) w.r.t. some initial value $(h_0, b_0) \in I$. Existence and uniqueness of such path is ensured by Lemma 3.13.

Properties of p^+

Remark 3.15. Any two paths p_0^+, p_1^+ are either identical for all $h \in \mathbb{R}$ or distinct and without intersections. The paths are ordered, such that if $p_0^+(h_0) = b_0 < b_1 = p_1^+(h_0)$ holds for any $h_0 \in \mathbb{R}$, this also applies directly to all $h \in \mathbb{R}$. This is a direct consequence of Lemma 3.13. In particular, this also applies when $p_0^+ = B_{\text{sat}}^+$ holds.

Lemma 3.16: Given p^+ w.r.t. $(h_0, b_0) \in \operatorname{int}(I)$. The following statements are true.

i) Path p^+ has exactly one intersection with B_{sat}^-, i.e., $!\exists h^* \in \mathbb{R} : p^+(h^*) = B_{\text{sat}}^-(h^*)$.

ii) Left of this intersection p^+ is outside of I, i.e., $\forall h \in (-\infty, h^*) : \big(h, p^+(h)\big) \notin I$.

iii) Right of this intersection p^+ is inside of I, i.e., $\forall h \in (h^*, \infty) : \big(h, p^+(h)\big) \in \operatorname{int}(I)$.

Proof. First, the existence of h^* is proven by contradiction. It is assumed that such h^* does not exist.

The path p^+ is defined w.r.t. $(h_0, b_0) \in \operatorname{int}(I)$, such that

$$B_{\text{sat}}^-(h_0) > b_0 > B_{\text{sat}}^+(h_0) \tag{3.22}$$

holds. As stated in Remark 3.15, this results directly in $p^+(h) > B_{\text{sat}}^+(h)$ for all $h \in \mathbb{R}$. p^+ and B_{sat}^- are both continuous functions. By assumption they have no intersection. Hence p^+ must be inside of I for all h, i.e.,

$$B_{\text{sat}}^+(h) < p^+(h) < B_{\text{sat}}^-(h) \quad \text{for all } h \in \mathbb{R}\,. \tag{3.23}$$

By construction of p^+, it follows

$$\mu_0 < \frac{\mathrm{d}p^+(h)}{\mathrm{d}h} = \mu_{\text{diff}}^+\big(h, p^+(h)\big) < \frac{\mathrm{d}B_{\text{sat}}^+(h)}{\mathrm{d}h} \quad \text{for all } h \in \mathbb{R}\,. \tag{3.24}$$

p^+ and B_{sat}^+ are both differentiable functions. Thus, the following integral representation holds:

$$\underbrace{p^+(h) - B_{\text{sat}}^+(h)}_{>0} = \underbrace{b_0 - B_{\text{sat}}^+(h_0)}_{>0,\text{constant}} + \int_{h_0}^{h} \underbrace{\mu_{\text{diff}}^+\big(t, p^+(s)\big) - \frac{\mathrm{d}B_{\text{sat}}^+(s)}{\mathrm{d}s}}_{<0} \,\mathrm{d}s > 0\,. \tag{3.25}$$

Using (3.22), (3.23) and (3.24) to determine the signs, it can be concluded that

$$p^+(h) - B_{\text{sat}}^+(h) > \underbrace{b_0 - B_{\text{sat}}^+(h_0)}_{\text{constant}} > 0 \quad \text{for all } h < h_0 \tag{3.26}$$

holds. This means in particular that

$$\lim_{h \to -\infty} \big(p^+(h) - B_{\text{sat}}^+(h)\big) > 0 \tag{3.27}$$

is true. However, by (3.3) it must hold

$$\lim_{h\to-\infty}\Big(B^{-}_{\mathrm{sat}}(h)-B^{+}_{\mathrm{sat}}(h)\Big)=0 \tag{3.28}$$

and with (3.23) it follows

$$\lim_{h\to-\infty}\Big(p^{+}(h)-B^{+}_{\mathrm{sat}}(h)\Big)=0\,. \tag{3.29}$$

The eqs. (3.27) and (3.29) form a contradiction and the existence of h^* is proven.

Second, the uniqueness is proven. By construction it holds

$$\frac{\mathrm{d}p^{+}(h^*)}{\mathrm{d}h}=\mu^{+}_{\mathrm{diff}}\Big(h^*,p^{+}(h^*)\Big)=\mu^{+}_{\mathrm{diff}}\Big(h^*,B^{-}_{\mathrm{sat}}(h^*)\Big)=\mu_0<\frac{\mathrm{d}B^{-}_{\mathrm{sat}}(h^*)}{\mathrm{d}h}\,. \tag{3.30}$$

This relation combined with the continuity of p^+ and B^{-}_{sat} excludes multiple intersections h^*. In summary, using $p^{+}(h)>B^{+}_{\mathrm{sat}}(h)$ for all $h\in\mathbb{R}$ results in:

$$p^{+}(h)\begin{cases}>B^{-}_{\mathrm{sat}}(h) & \text{if } h<h^*\\ =B^{-}_{\mathrm{sat}}(h) & \text{if } h=h^*\\ <B^{-}_{\mathrm{sat}}(h) & \text{if } h>h^*\end{cases}\Rightarrow\Big(h,p^{+}(h)\Big)\begin{cases}\notin I & \text{if } h<h^*\\ \in\partial(I) & \text{if } h=h^*\,.\\ \in\mathrm{int}(I) & \text{if } h>h^*\end{cases} \tag{3.31}$$

□

Lemma 3.17: Given paths p^{+}_{1} and p^{+}_{2} with $p^{+}_{1}<p^{+}_{2}$. Let h^*_1, h^*_2 denote the corresponding intersection with B^{-}_{sat}, see Lemma 3.16. It holds $h^*_1<h^*_2$.

Proof. B^{-}_{sat} is strictly monotonously increasing. If $p^{+}_{1}<p^{+}_{2}$ holds, their respective intersections at $\Big(h^*_1,B^{-}_{\mathrm{sat}}(h^*_1)\Big)$ and $\Big(h^*_2,B^{-}_{\mathrm{sat}}(h^*_2)\Big)$ must fulfill $B^{-}_{\mathrm{sat}}(h^*_1)<B^{-}_{\mathrm{sat}}(h^*_2)$ and $h^*_1<h^*_2$. □

Now that the existence and uniqueness of p^+ has been shown, the course of the path p^+ shall be investigated. For this purpose, the limit values of p^+ are first examined. Afterwards the behavior inside of I is further examined.

Lemma 3.18: The following statements are true.

i) For each path p^+ exists a unique equivalent p^{+}_{i} and vice versa.

ii) Any path p^{+}_{i} can be identified by its limit $\lim\limits_{h\to-\infty}p^{+}_{\mathrm{i}}(h)=b^{-\infty}_{\mathrm{i}}\in[-B^{\infty}_{\mathrm{i,sat}},B^{\infty}_{\mathrm{i,sat}})$.

iii) It holds $\lim\limits_{h\to\infty}p^{+}_{\mathrm{i}}(h)=B^{\infty}_{\mathrm{i,sat}}$ for any path p^{+}_{i}.

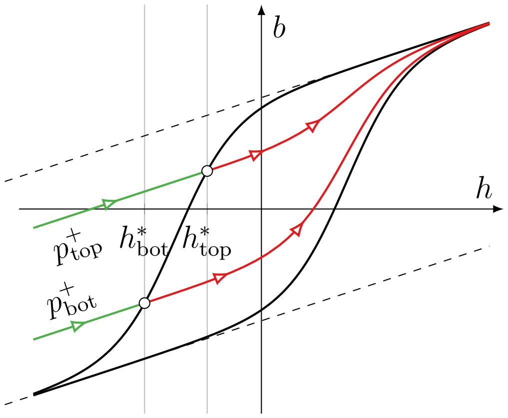

Figure 3.8.: Overview of the proof of Lemma 3.20. It can be observed that outside of I (green) the distance between the two paths p^+_{top}, p^+_{bot} does not change. As soon as at least one of the paths is inside I (red), the distance decreases.

Proof. The first statement follows directly from Definition 3.12. It can be easily switched between (h, b) and (h, b_{i}) coordinate systems.

First, assume $p^+ = B^+_{\text{sat}}$, i.e., p^+ is defined w.r.t. $(h_0, b_0) = \big(h_0, B^+_{\text{sat}}(h_0)\big)$. Equivalently, it holds $p^+_{\text{i}} = B^+_{\text{i,sat}}$. In this case, the second and third statement are true by definition of $B^\infty_{\text{i,sat}}$ in (2.22).

Second, assume p^+ is defined w.r.t. (h_0, b_0) with $b_0 \neq B^+_{\text{sat}}(h_0)$. As proven in Lemma 3.16 each p^+ has exactly one intersection with B^-_{sat} at (h^*, b^*). Equivalently, p^+_{i} has exactly one intersection with $B^-_{\text{i,sat}}$ at (h^*, b^*_i). And since p^+_{i} is constant outside of I_i, it holds $\lim_{h\to-\infty} p^+_{\text{i}}(h) = b^*_i \in (-B^\infty_{\text{i,sat}}, B^\infty_{\text{i,sat}})$.

Furthermore, Lemma 3.16 states that p^+ is inside of I for $h > h^*$. Equivalently, p^+_{i} stays inside of I_i. This property in particular means that $B^+_{\text{i,sat}}(h) < p^+_{\text{i}}(h) < B^-_{\text{i,sat}}(h)$ for all $h \in (h^*, \infty)$ holds. With $\lim_{h\to\infty} B^+_{\text{i,sat}}(h) = \lim_{h\to\infty} B^-_{\text{i,sat}}(h) = B^\infty_{\text{i,sat}}$, the third statement holds true. ☐

Remark 3.19. At this point, paths p^+ has been examined so far that it is ensured they are mathematically well defined and correspond to the physical motivation. The fact that these paths are also partly outside or more precisely above I does not bother. On the contrary, the following investigations make use of this fact.

Lemma 3.20: Given paths p^+_{top}, p^+_{bot} defined w.r.t. $(h_0, b_{\text{top}}) \in I$ and $(h_0, b_{\text{bot}}) \in I$ with $b_{\text{top}} > b_{\text{bot}}$. Then for any $h_1, h_2 \in \mathbb{R}$ with $h_1 < h_2$ it holds

$$p^+_{\text{top}}(h_1) - p^+_{\text{bot}}(h_1) \geq p^+_{\text{top}}(h_2) - p^+_{\text{bot}}(h_2) > 0\,. \tag{3.32}$$

If $\big(h_1, p^+_{\text{bot}}(h_1)\big) \in I$ is fulfilled, the statement can even be formulated stricter to

$$p^+_{\text{top}}(h_1) - p^+_{\text{bot}}(h_1) > p^+_{\text{top}}(h_2) - p^+_{\text{bot}}(h_2) > 0\,. \tag{3.33}$$

Proof. A visual overview is given in Figure 3.8. By Remark 3.15 $p^+_{\text{top}}(h) > p^+_{\text{bot}}(h)$ for all $h \in \mathbb{R}$ holds. By Lemma 3.16 exist $h^*_{\text{top}}, h^*_{\text{bot}}$ with $p^+_{\text{top}}(h^*_{\text{top}}) = B^-_{\text{sat}}(h^*_{\text{top}})$, $p^+_{\text{bot}}(h^*_{\text{bot}}) = B^-_{\text{sat}}(h^*_{\text{bot}})$ with $h^*_{\text{bot}} < h^*_{\text{top}}$. Define

$$\operatorname{dist}(h) = p^+_{\text{top}}(h) - p^+_{\text{bot}}(h) > 0 \tag{3.34}$$

as the distance (difference) between the paths. According to the section-wise definition of $p^+_{\text{top/bot}}$ the following derivative results:

$$\frac{\mathrm{d}}{\mathrm{d}h}\operatorname{dist}(h) = \begin{cases} \mu_0 - \mu_0 = 0 & \text{if } h \le h^*_{\text{bot}}\,, \\ \mu_0 - \mu^+_{\text{diff}}\Big(h, p^+_{\text{bot}}(h)\Big) < 0 & \text{if } h \in (h^*_{\text{bot}}, h^*_{\text{top}})\,, \\ \mu^+_{\text{diff}}\Big(h, p^+_{\text{top}}(h)\Big) - \mu^+_{\text{diff}}\Big(h, p^+_{\text{bot}}(h)\Big) < 0 & \text{if } h^*_{\text{top}} \le h\,. \end{cases} \tag{3.35}$$

It holds $\mu^+_{\text{diff}}\Big(h, p^+_{\text{bot}}(h)\Big) > \mu_0$ by construction and $\mu^+_{\text{diff}}\Big(h, p^+_{\text{top}}(h)\Big) < \mu^+_{\text{diff}}\Big(h, p^+_{\text{bot}}(h)\Big)$ by monotonicity (Lemma 3.6). Therefore dist is monotonously decreasing on $\mathbb{R}$, strictly monotonously decreasing over $[h^*_{\text{bot}}, \infty)$ and bounded from below by 0. ☐

Remark 3.21. A direct conclusion of Lemma 3.20 is given by

$$|p_1(h_0) - p_2(h_0)| > |p_1(h_1) - p_2(h_1)| \tag{3.36}$$

for any $p_1 \neq p_2$ and $h_0 < h_1$ with $\Big(h_0, p_1(h_0)\Big) \in I$ or $\Big(h_0, p_2(h_0)\Big) \in I$.

Lemma 3.22: Given a path p^+ w.r.t. $(h_0, b_0) \in I$. It holds

$$\lim_{h\to\infty} \Big(p^+(h) - B^+_{\text{sat}}(h)\Big) = 0\,. \tag{3.37}$$

Furthermore, $\lambda\Big(h, p^+(h)\Big)$ is monotone increasing and convergent for $h \to \infty$.

Proof. Assume $(h_0, b_0) = \Big(h_0, B^+_{\text{sat}}(h_0)\Big)$ holds. Then $p^+(h) = B^+_{\text{sat}}(h)$ and $\lambda\Big(h, p^+(h)\Big) = 1$ for all $h \in \mathbb{R}$ are true. This meets the desired conditions.

Now, assume $(h_0, b_0) \neq \Big(h_0, B^+_{\text{sat}}(h_0)\Big)$. By Lemma 3.16, h^* with $\Big(h^*, p^+(h^*)\Big) = \Big(h^*, B^-_{\text{sat}}(h^*)\Big) \in I$ exists, such that for all $h > h^*$ yields $B^+_{\text{sat}}(h) < p^+ < B^-_{\text{sat}}(h)$. With $\lim_{h\to\infty}\Big(B^-_{\text{sat}}(h) - B^+_{\text{sat}}(h)\Big) = 0$ as in (3.3), the first statement is proven.

Let $(h, b) = \Big(h, p^+(h)\Big) \in \operatorname{int}(I)$. For any (h, b) a $\lambda = \lambda(h, b)$ can be calculated by (3.8). Define

$$b^\lambda(h) = \lambda B^+_{\text{sat}}(h) + (1-\lambda)B^-_{\text{sat}}(h) \tag{3.38}$$

as the path having a constant λ, i.e., $\lambda\Big(h, b^\lambda(h)\Big) = \text{const}$. It can be observed that

$$\begin{aligned} \frac{\mathrm{d}}{\mathrm{d}h}b^\lambda(h) &= \lambda\frac{\mathrm{d}}{\mathrm{d}h}B^+_{\text{sat}}(h) + (1-\lambda)\frac{\mathrm{d}}{\mathrm{d}h}B^-_{\text{sat}}(h) \\ &> \lambda\frac{\mathrm{d}}{\mathrm{d}h}B^+_{\text{sat}}(h) + (1-\lambda)\frac{\mathrm{d}}{\mathrm{d}h}\mu_0 \qquad = \frac{\mathrm{d}}{\mathrm{d}h}p^+(h) \end{aligned} \tag{3.39}$$

holds. Therefore, $\lambda\Big(h, p^+(h)\Big)$ is monotone increasing by Lemma 3.6. Overall, λ is limited to $[0, 1]$ and in combination with the monotonicity convergent. ☐

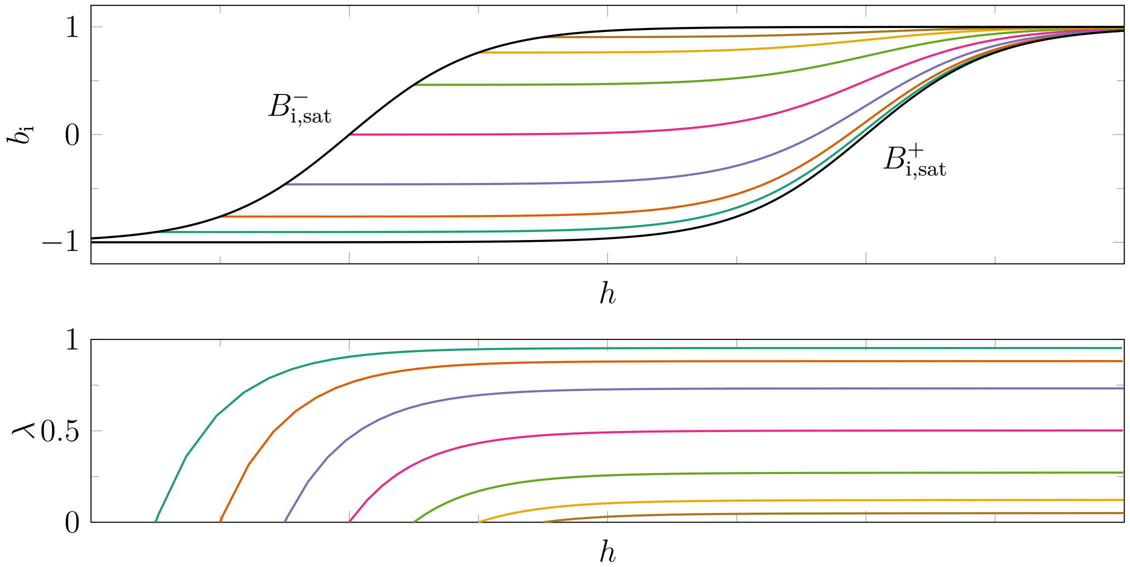

Figure 3.9.: $\lambda = \lambda\big(h, p(h)\big)$ for different paths $p(h)$. Monotonicity and convergence of λ are clearly seen.

Remark 3.23. Lemma 3.22 describes that visually the paths p^+ do converge to the lower boundary B^+_sat and also the relative position between the limiting curves is oriented downwards and convergent. But $\lim_{h\to\infty} \lambda\big(h, p^+(h)\big) = 1$ is not generally valid as shown in Figure 3.9.

Construction of p^-

So far only the case was considered that μ^+_diff is used. By symmetry the observation can be interpreted analogously to the case μ^-_diff.

Definition 3.24: Using symmetry arguments, the path p^- can be defined for any $(h, b) \in I$ by

$$p^-(h) = -p^+(-h) \tag{3.40}$$

with p^+ being defined with respect to $(-h, -b) \in I$.

Conclusions

Lemma 3.25: Any point $(h, b) \in I$ is hit exactly by a path p^+ and a p^-, i.e., $p^+(h) = b = p^-(h)$. p^+ fulfills (3.15) and p^- an analogous version of (3.15) based on μ^-_diff.

Proof. This statement follows directly by the definition of p^- and the symmetrical properties of Tellinen's model. □

An example and visualization is given in Figure 3.10. Further analysis of the paths $p^\pm$ follows in Sections 3.2.5 and 3.2.6.

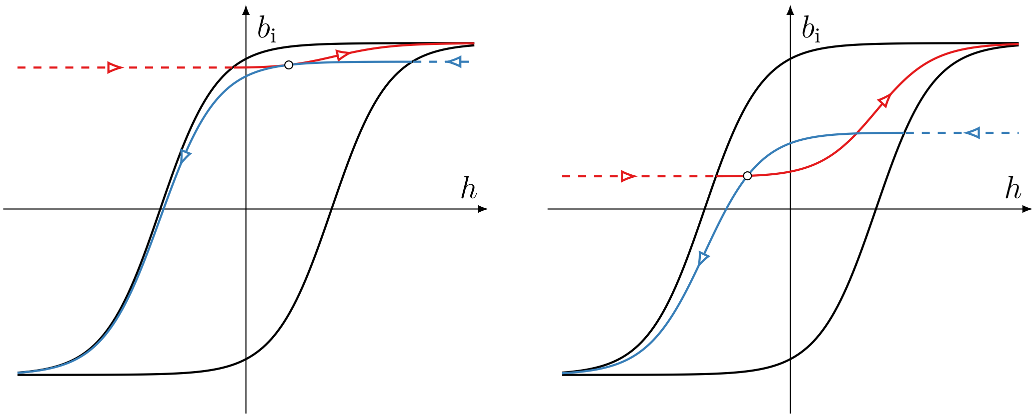

(a) only one common point

(b) two common points

Figure 3.10.: Idea of Helper Paths. Path p^+ (red) and p^- (blue) are defined w.r.t. $(h_0, b_{i,0}) \in I_i$ (marked with circle). Sections in I_i are shown with solids lines and outside segments dashed.

(a) Both path can be defined w.r.t. turning point (h_0, b_0). This allows the right turning point (h_1, b_1) of a stable curve to be calculated.

(b) Path p^+ is defined w.r.t. the left turning point (h_0, b_0) and p^- w.r.t. the right turning point (h_1, b_1). This describes the actual progression of an excitation cycle.

Figure 3.11.: Presentation of possible applications of paths p^+ and p^-.

Remark 3.26. Lemma 3.16 proves that in positive direction ($\Delta h > 0$) the path p^+ will stay inside of I. Using symmetry arguments, the same is true for any path p^- in negative direction ($\Delta h < 0$). So any path that starts in I and consists of a series of paths p_k^+ and p_k^- will stay inside of I, as long as the paths are always used according to their associated direction. Remark 3.11 is regarded as confirmed because it can be assumed that an application has a valid start value ($(h_0, b_0) \in I$). The extension of the paths p to the area outside of I is therefore not relevant for the application and does not cause any problems.

Remark 3.27. As shown in Figure 3.11, there are several applications for path p^+ and p^-. In the framework of this thesis two main approaches are used. On the one hand, the second turning point of a closed cycle can be calculated (see Figure 3.11(a)). For this purpose, both paths start from a common point (h_0, b_0) and a further intersection point (h_1, b_1) is searched for. Then (h_0, b_0) and (h_1, b_1) represent the turning points of a closed cycle. On the other hand, the actual return path can be examined, if the

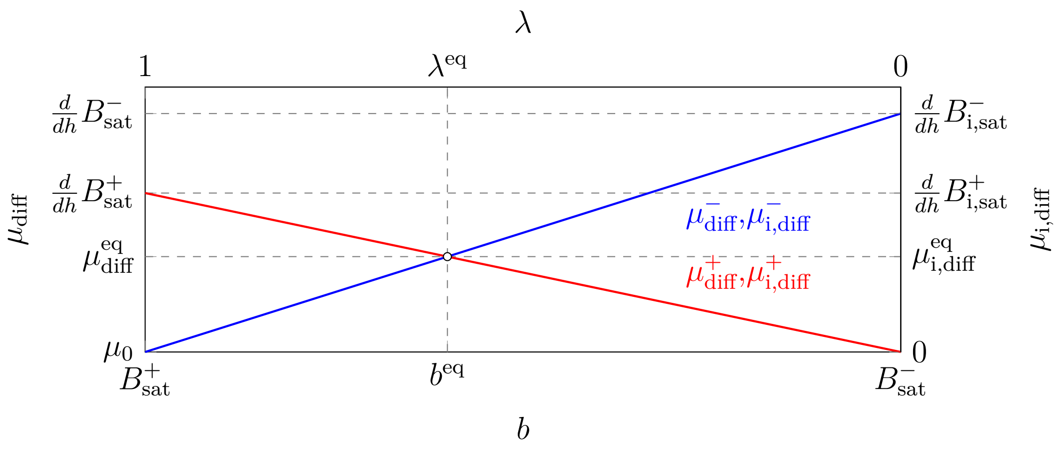

Figure 3.12.: Motivation for b^{eq} and λ^{eq}.

second turning point is selected by $(h_1, b_1) = \big(h_1, p^+(h_1)\big)$ (see Figure 3.11(b)). The path p^- is defined w.r.t. $\big(h_1, p^+(h_1)\big)$ and evaluated at (h_0). In general the point (h_0, b_0) is not hit by p^-.

After the basic definition of the paths p^+ and p^- and the motivation to use them in Remark 3.27, it is now examined in more detail under which conditions two paths $p^\pm$ have intersections.

3.2.3. Partition of I

At this point I from (3.5) is examined more closely. Therefore a partition of I is created. The goal is to be able to quickly and easily make statements at a given point $(h_0, b_0) \in I$, whether and where the corresponding paths p^+ and p^- have another intersection.

Lemma 3.28: For all $h \in \mathbb{R}$ exists an unique $b^{\mathrm{eq}} \in \big(B_{\mathrm{sat}}^{+}(h), B_{\mathrm{sat}}^{-}(h)\big)$ such that $\mu_{\mathrm{diff}}^{+}(h, b^{\mathrm{eq}}) = \mu_{\mathrm{diff}}^{-}(h, b^{\mathrm{eq}})$ holds. $b^{\mathrm{eq}} = b^{\mathrm{eq}}(h)$ is a continuous function.

Proof. A visual overview is given in Figure 3.12. Starting with $\mu_{\mathrm{diff}}^{\pm} = \mu_{\mathrm{diff}}^{\pm}(h, b)$ and $\lambda = \lambda(h, b)$ the condition

$$\mu_{\mathrm{diff}}^{+} = \lambda \frac{\mathrm{d}B_{\mathrm{sat}}^{+}(h)}{\mathrm{d}h} + (1-\lambda)\mu_0 \overset{!}{=} \lambda\mu_0 + (1-\lambda)\frac{\mathrm{d}B_{\mathrm{sat}}^{-}(h)}{\mathrm{d}h} = \mu_{\mathrm{diff}}^{-} \tag{3.41}$$

can be solved for λ^{eq} and yields

$$\lambda^{\mathrm{eq}}(h) = \lambda(h, b^{\mathrm{eq}}) = \frac{\frac{\mathrm{d}B_{\mathrm{sat}}^{-}(h)}{\mathrm{d}h} - \mu_0}{\frac{\mathrm{d}B_{\mathrm{sat}}^{+}(h)}{\mathrm{d}h} + \frac{\mathrm{d}B_{\mathrm{sat}}^{-}(h)}{\mathrm{d}h} - 2\mu_0} = \frac{\frac{\mathrm{d}B_{\mathrm{i,sat}}^{-}(h)}{\mathrm{d}h}}{\frac{\mathrm{d}B_{\mathrm{i,sat}}^{+}(h)}{\mathrm{d}h} + \frac{\mathrm{d}B_{\mathrm{i,sat}}^{-}(h)}{\mathrm{d}h}} \in (0,1)\,. \tag{3.42}$$

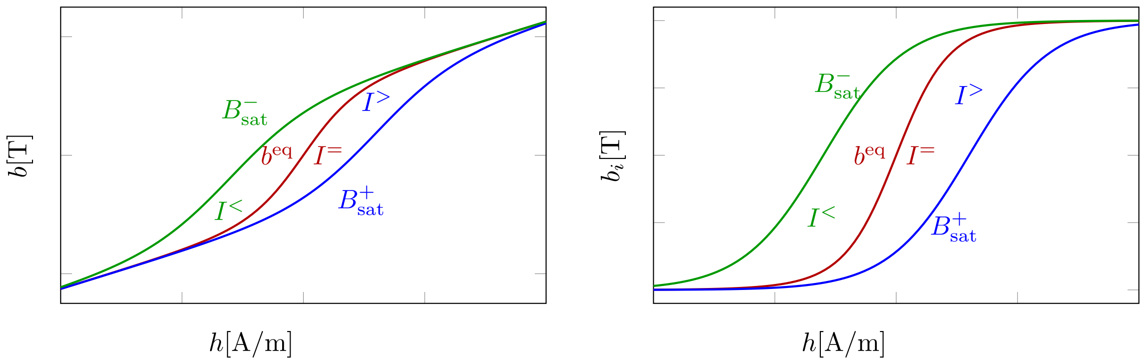

(a) in bh-space

(b) in $b_{\mathrm{i}}h$-space

Figure 3.13.: Example of the partition of I into $I^<, I^=$ and $I^>$.

Inserting in (3.8) and solving for b yields

$$b^{\mathrm{eq}}(h) = \overbrace{B^-_{\mathrm{sat}}(h) - \underbrace{\frac{\frac{\mathrm{d}}{\mathrm{d}h}B^-_{\mathrm{i,sat}}(h)}{\frac{\mathrm{d}}{\mathrm{d}h}B^-_{\mathrm{i,sat}}(h) + \frac{\mathrm{d}}{\mathrm{d}h}B^+_{\mathrm{i,sat}}(h)}}_{\in(0,1)} \underbrace{\left(B^-_{\mathrm{sat}}(h) - B^+_{\mathrm{sat}}(h)\right)}_{>0}}^{\in\left(B^+_{\mathrm{sat}}(h), B^-_{\mathrm{sat}}(h)\right)} . \tag{3.43}$$

Existence, uniqueness and continuity result directly from the definition in (3.43). ☐

Remark 3.29. An example is given in Figure 3.13. Note, that b^{eq} is not always as smooth and monotone as shown in Figure 3.13, see Figure 3.15. Further analysis of desirable and needed attributes of b^{eq} is discussed in the next section.

The whole domain I can now be partitioned into three parts: above, below and exactly on b^{eq}. This results in the following definition:

$$\begin{aligned} I^\Box &= \left\{(h,b) \in I \;\middle|\; \mu^+_{\mathrm{diff}}(h,b) \,\Box\, \mu^-_{\mathrm{diff}}(h,b)\right\} \\ &= \left\{(h,b) \in I \;\middle|\; \lambda \,\Box\, \lambda^{\mathrm{eq}}\right\} \\ &= \left\{(h,b) \in I \;\middle|\; b^{\mathrm{eq}}(h) \,\Box\, b\right\} \qquad \text{for all } \Box \in \{=, <, >\}. \end{aligned} \tag{3.44}$$

Remark 3.30. The sets $I^<, I^>$ and $I^=$ are a partition of I, i.e., they are non-empty, pairwise disjoint and their union span completely I. Each point $(h,b) \in I$ can therefore be uniquely assigned to $I^>, I^=$ or $I^<$.

Lemma 3.31: The sets $I^<, I^>, I^=$ are symmetrical, s.t.

$$(h,b) \in I^> \Leftrightarrow (-h,-b) \in I^< , \qquad (h,b) \in I^= \Leftrightarrow (-h,-b) \in I^= \tag{3.45}$$

holds.

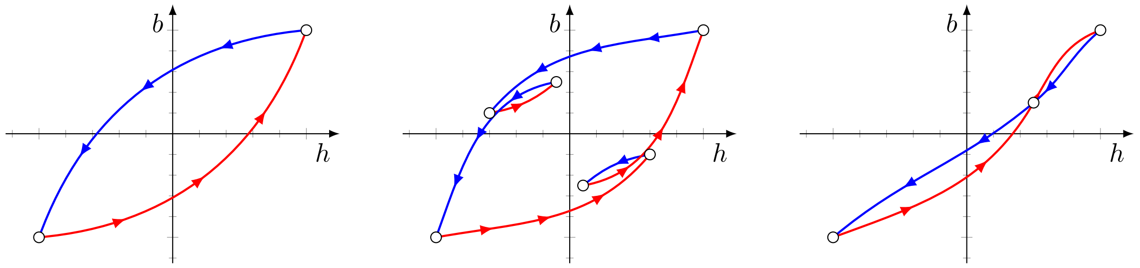

(a) A simple closed hysteresis loop.

(b) A non-simple closed hysteresis loop because it has minor hysteresis loops.

(c) A non-simple closed hysteresis loop because it hast intermediate intersections.

Figure 3.14.: Examples of simple and non-simple closed hysteresis loops. Sections based on μ^{+}_{diff} are shown in red and μ^{-}_{diff} in blue. Comparable figures can be found in [38, 39].

Proof. Utilizing $\mu^{+}_{\text{diff}}(h, b,) = \mu^{-}_{\text{diff}}(-h, -b)$ from (3.13) yields

$$\begin{aligned} (h,b) \in I^{>} \quad &\Leftrightarrow \quad \mu^{+}_{\text{diff}}(h,b) > \mu^{-}_{\text{diff}}(h,b) \\ &\Leftrightarrow \quad \mu^{-}_{\text{diff}}(-h,-b) > \mu^{+}_{\text{diff}}(-h,-b) \quad \Leftrightarrow \quad (-h,-b) \in I^{<} \end{aligned} \tag{3.46}$$

and

$$\begin{aligned} (h,b) \in I^{=} \quad &\Leftrightarrow \quad \mu^{+}_{\text{diff}}(h,b) = \mu^{-}_{\text{diff}}(h,b) \\ &\Leftrightarrow \quad \mu^{-}_{\text{diff}}(-h,-b) = \mu^{+}_{\text{diff}}(-h,-b) \quad \Leftrightarrow \quad (-h,-b) \in I^{=} \, . \end{aligned} \tag{3.47}$$

□

3.2.4. Simple closed hysteresis loops

Even though Tellinen's model can correctly reproduce more complex curve shapes [50], the focus here lies on simple closed loops. This is mainly due to the loss model in Section 4.1. This model will be only defined for simple curves.

Here, at this point it is defined what is exactly a simple loop and under which conditions it is formed. A main focus will be the stability of Tellinen's model for simple loops.

In the previous Figures 2.8(c), 3.2(a) and 3.14(a) the paths are shown in such way, that a counterclockwise flow occurs. For closed curves and the motivation in Section 2.3, that magnetic hysteresis can be viewed as a resistance to change of state, this order is considered to be physically reasonable. An arrangement that the return path p^{-} runs below the forward path p^{+}, i.e., the loop is traversed clockwise, is not motivatable from the physical background. Thus, a focus of the analysis of Tellinen's model will be the geometric arrangement of paths $p^{\pm}$ for closed curves.

First, in this context, a simple closed curve is defined and it is stated which situations are to exclude explicitly. For this, the already defined paths $p^{\pm}$ are used and argued about the geometric arrangement and intersections. It will be proven that Tellinen's model does indeed allow for undesirable situations in the context of this thesis. Therefore, the second step is the derivation of suitable conditions, such that in the further course of this dissertation a simple closed curve – which is traversed counterclockwise – can be assumed.

Remark 3.32. Any curve $\gamma : [t_0, t_1] \to \mathbb{R}^2$ that is based on Tellinen's model can be disassembled into parts that are either based on μ^+_{diff} or μ^-_{diff}. Therefore, γ can be seen and considered as a series of segments of paths p^+_k and p^-_k. See Figure 3.14(b) for an example.

Definition 3.33 (simple closed hysteresis loop)**:** A simple closed hysteresis loop consists of a closed path $\gamma : [t_0, t_1] \to \mathbb{R}^2$ which can be exactly separated up into γ^+ and γ^-. γ^+ and γ^- are segments of paths p^+ and p^-, respectively. The turning points (h_0, b_0) and (h_1, b_1) (w.l.o.g. $h_0 < h_1$) are the only common points of the paths $p^{\pm}$ on the interval $[h_0, h_1]$. See Figure 3.14(a) for an example.

As visualized in Figures 3.14(b) and 3.14(c), there are two undesirable situations, the existence of minor hysteresis loops and the existence of further intersections. Conditions are now examined so that these unwanted properties do not occur.

Simple Excitation

The existence of minor hysteresis loops can be prevented, if a suitable excitation is used. The excitation must be periodic. Furthermore, the excitation must be monotonically increasing from its minimum to its maximum and monotonically decreasing the other way round. For example a single frequency sine wave or a triangle wave are fulfilling these conditions. In this thesis only use sinusoidal wave forms will be used.

Remark 3.34. Even with simple excitation, intermediate intersections of the paths p^+ and p^- are possible. Examples are given in Figures 3.14(c) and 3.15.

Intermediate intersections

To be able to classify common points of p^+ and p^-, first a distinction between intersection and contact points is introduced.

Definition 3.35 (Intersection, Contact point)**:** Given paths p^+, p^- with a common point $p^+(h_0) = b_0 = p^-(h_0)$ for a $(h_0, b_0) \in I$. (h_0, b_0) is called an *intersection* of p^+ and p^- if $\epsilon_0 \in \mathbb{R}^{>0}$ exist, such that for all ϵ with $0 < \epsilon < \epsilon_0$

$$\Big(p^+(h_0 - \epsilon) - p^-(h_0 - \epsilon)\Big)\Big(p^+(h_0 + \epsilon) - p^-(h_0 + \epsilon)\Big) < 0 \tag{3.48}$$

holds. (h_0, b_0) is called a *contact point* of p^+ and p^- if $\epsilon_0 \in \mathbb{R}^{>0}$ exist, such that for all ϵ with $0 < \epsilon < \epsilon_0$

$$\Big(p^+(h_0-\epsilon) - p^-(h_0-\epsilon)\Big)\Big(p^+(h_0+\epsilon) - p^-(h_0+\epsilon)\Big) > 0 \tag{3.49}$$

holds.

With this definition it can be now distinguish whether the geometrical vertical order of the paths $p^\pm$ at the common point (h_0, b_0) changes (intersection) or not (contact point).

Now, criteria are set up to determine, when a common point is an intersection.

Lemma 3.36: Given paths p^+, p^-. Any common point, i.e., $p^+(h_0) = b_0 = p^-(h_0)$ with $(h_0, b_0) \in I^> \cup I^<$ is an intersection.

If $(h_0, b_0) \in I^>$ is an intersection, then

$$\Big(p^+(h_0-\epsilon) - p^-(h_0-\epsilon)\Big) < 0 < \Big(p^+(h_0+\epsilon) - p^-(h_0+\epsilon)\Big) \tag{3.50}$$

holds for $0 < \epsilon \ll 1$. If $(h_0, b_0) \in I^<$ is an intersection, then

$$\Big(p^+(h_0-\epsilon) - p^-(h_0-\epsilon)\Big) > 0 > \Big(p^+(h_0+\epsilon) - p^-(h_0+\epsilon)\Big) \tag{3.51}$$

holds for $0 < \epsilon \ll 1$.

Proof. W.l.o.g. only the case $(h_0, b_0) \in I^>$ is considered. The case $(h_0, b_0) \in I^>$ follows from symmetry arguments.

With $(h_0, b_0) \in I^>$ it holds

$$\frac{\mathrm{d}p^+(h_0)}{\mathrm{d}h} = \mu^+_{\mathrm{diff}}\Big(h_0, p^+(h_0)\Big) > \mu^-_{\mathrm{diff}}\Big(h_0, p^-(h_0)\Big) = \frac{\mathrm{d}p^-(h_0)}{\mathrm{d}h}\,. \tag{3.52}$$

This relation then applies in an open domain $d = (h_0 - \epsilon, h_0 + \epsilon)$ for ϵ small enough. For $(h_0, b_0) \in \mathrm{int}(I^>)$ this is true. For the case $(h_0, b_0) = \Big(h_0, B^+_{\mathrm{sat}}(h_0)\Big)$, the paths $p^\pm$ are continued outside of I by their construction. This covers all possible cases.

Define the function $\mathrm{dist} : d \to \mathbb{R}$ with

$$\mathrm{dist}(h) = p^+(h) - p^-(h)\,, \qquad \frac{\mathrm{d}}{\mathrm{d}h}\,\mathrm{dist}(h) = \frac{\mathrm{d}p^+(h)}{\mathrm{d}h} - \frac{\mathrm{d}p^-(h)}{\mathrm{d}h} \overset{(3.52)}{>} 0\,. \tag{3.53}$$

It holds $\mathrm{dist}(h_0) = 0$ by assumption. The function dist is strictly monotonically increasing on the domain d. Equation (3.50) is proven by the fact that

$$\mathrm{dist}(h_0 - \epsilon) < \mathrm{dist}(h_0) = 0 < \mathrm{dist}(h_0 + \epsilon) \tag{3.54}$$

holds.

The procedure for the second case is similar. Then dist would be monotonically decreasing. ☐

Remark 3.37. Lemma 3.36 describes how the paths are arranged geometrically. At an intersection $(h_0, b_0) \in I^>$, path p^+ must cross path p^- from below. If $(h_0, b_0) \in I^<$ holds, it must pierce from top.

Now it shall be examined whether the existence of further intersections is guaranteed.

Lemma 3.38: The following statements are true.

I) Given $(h_0, b_0) \in \operatorname{int}(I^<)$ and the paths p^+, p^- w.r.t. (h_0, b_0). It exists $(h_1, b_1) \in I^>$ with $h_0 < h_1$ and $p^+(h_1) = b_1 = p^-(h_1)$.

II) Given $(h_1, b_1) \in \operatorname{int}(I^>)$ and the paths p^+, p^- w.r.t. (h_1, b_1). It exists $(h_0, b_0) \in I^<$ with $h_0 < h_1$ and $p^+(h_0) = b_0 = p^-(h_0)$.

III) Given paths p^+, p^- with a finite number of intersections and contact points at $(h_0, b_0), (h_1, b_1), \ldots, (h_n, b_n) \in I$ with $h_0 < \ldots < h_n$ and $n \geq 1$. Then $(h_0, b_0) \notin I^>$ and $(h_n, b_n) \notin I^<$ holds.

Proof. Given $(h_0, b_0) \in \operatorname{int}(I^<)$ and the paths p^+, p^- w.r.t. (h_0, b_0). For the paths $p^\pm$, associated paths $p_\mathrm{i}^\pm$ exists and the following examination is done in (h, b_i) coordinates.

First the limits of the paths $p_\mathrm{i}^\pm$ are considered. By Lemma 3.18 it holds

$$\lim_{h\to\infty} p_\mathrm{i}^+(h) = B_{\mathrm{i,sat}}^\infty\,, \qquad \lim_{h\to\infty} p_\mathrm{i}^-(h) = b^{+\infty} < B_{\mathrm{i,sat}}^\infty\,. \tag{3.55}$$

The case $\lim_{h\to\infty} p_\mathrm{i}^-(h) = B_{\mathrm{i,sat}}^\infty$ only applies, if p_i^- is defined w.r.t. $(h_0, b_{\mathrm{i},0}) = \big(h_0, B_{\mathrm{i,sat}}^-(h_0)\big)$. This is excluded per prerequisite $(h_0, b_0) \in \operatorname{int}(I^<)$.

According to (3.51) it exists a $\epsilon > 0$ such that

$$p_\mathrm{i}^+(h_0 + \epsilon) < p_\mathrm{i}^-(h_0 + \epsilon) \tag{3.56}$$

holds. The paths $p_\mathrm{i}^\pm$ are continuous.

Using the vertical order at $h = h_0 + \epsilon$ in (3.56) – comparing this to the limit case (3.55) – it is concluded that there must exists at least another intersection $(h_1, b_{\mathrm{i},1})$ with $h_0 < h_1$. Since $\big(h, p_\mathrm{i}^+(h)\big) \in I_\mathrm{i}$ for all $h > h_0$ holds by Lemma 3.16, $(h_1, b_{\mathrm{i},1}) \in I_\mathrm{i}$ is true. At $(h_1, b_{\mathrm{i},1})$, p_i^+ must strike through p_i^- from below, so it yields $\frac{\mathrm{d}p_\mathrm{i}^+(h_1)}{\mathrm{d}h} > \frac{\mathrm{d}p_\mathrm{i}^-(h_1)}{\mathrm{d}h}$. Switching back to (h, b) coordinates, $(h_1, b_1) \in I^>$ holds.

Analogously one proceeds for the statement II).

To prove statement III), it will be first proven that the common points of $p^\pm$ are within I. Then it is a direct consequence of statements II) and III). Assuming paths $p^\pm$ have a common point on the boundary of I, i.e., they are defined w.r.t. $(h^*, b^*) = (h^*, B_\mathrm{sat}^\pm(h^*))$. Then either $p^+ = B_\mathrm{sat}^+$ or $p^- = B_\mathrm{sat}^-$ holds, but not both. Each path that is not the boundary has exactly one intersection with the boundary as proven in Lemma 3.16. But since the condition is that there are at least two common points, this case cannot occur. Hence the considered common points are inside of I and statements I) and II) are applicable. □

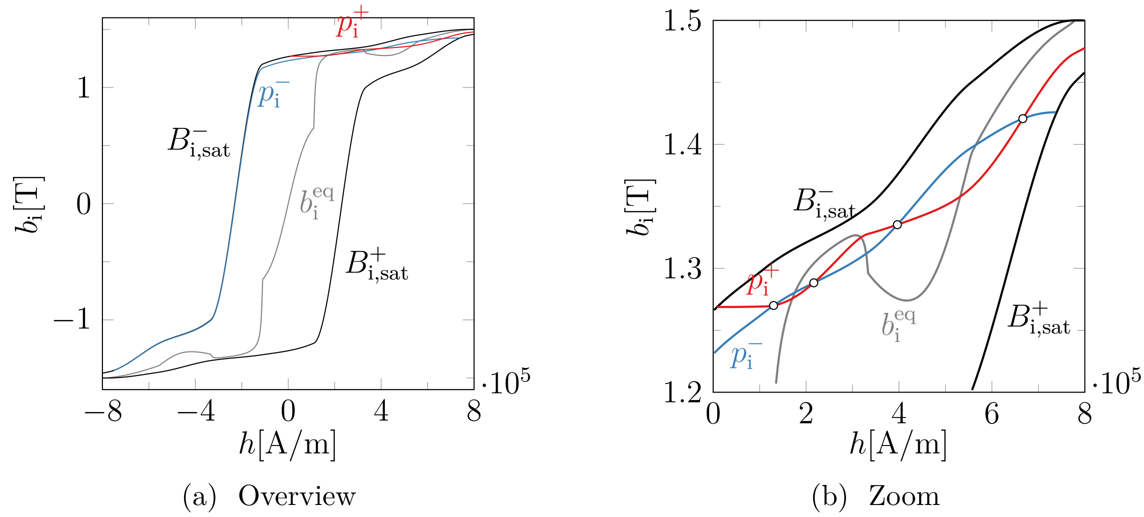

(a) Overview (b) Zoom

Figure 3.15.: Example of a non-monotone b_i^{eq}. Similar figures can also be found in [38, 39].

Lemma 3.39: Given paths p^+, p^- with a finite number of intersections and contact points at $(h_0, b_0), (h_1, b_1), \ldots, (h_n, b_n)$ with $h_0 < \ldots < h_n$ and $n \geq 1$. For any $1 \leq k \leq n$ holds that (h_{k-1}, b_{k-1}) and (h_k, b_k) are not both simultaneously element of $I^>$ or $I^<$.

Proof. This will be proven by contradiction. Assuming that two successive common points (h_{k-1}, b_{k-1}) and (h_k, b_k) are both element of $I^>$. The case of $I^<$ follows analogously. As proven in Lemma 3.36, there exists $\epsilon_1, \epsilon_2 \in \mathbb{R}^{>0}$, such that

$$p^+(h_{k-1} + \epsilon_1) > p^-(h_{k-1} + \epsilon_1), \qquad p^+(h_k - \epsilon_2) < p^-(h_k - \epsilon_2) \tag{3.57}$$

holds. ϵ_1 and ϵ_2 can be chosen small enough, such that $h_{k-1} < h_{k-1} + \epsilon_1 < h_k - \epsilon_2 < h_k$ holds. The paths $p^\pm$ are continuous and therefore at least one other common point between h_{k-1} and h_k must exist. This contradicts the assumption, that the above list of all intersections and contact points is complete. □

Remark 3.40. Motivated by Figure 3.15 and lemmas 3.38 and 3.39 it is concluded that the information whether a common point (h_0, b_0) of two paths $p^\pm$ lies in $I^>$ or $I^<$ yields important information about the existence of another common point.

Lemma 3.41: Given paths p^+ and p^-, which are respectively defined w.r.t. (h^+, b^+), $(h^-, b^-) \in \text{int}(I)$. If the number of intersections of paths $p^\pm$ is finite, this number is even.

Proof. Instead of p^+ and p^- the corresponding paths p_i^+ and p_i^- are considered. These paths are defined w.r.t. $(h^+, b_i^+), (h^-, b_i^-) \in \text{int}(I_i)$. By Lemma 3.18 the

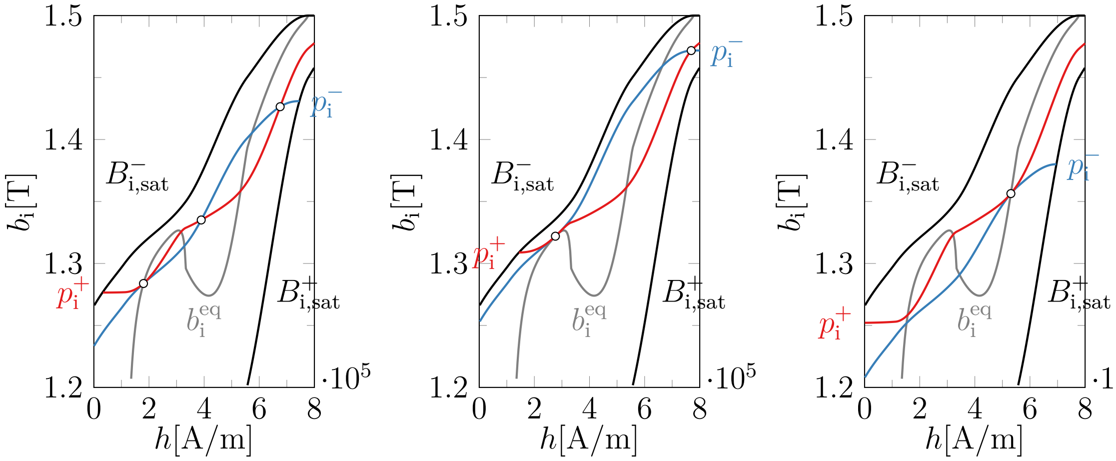

(a) 3 common points (b) 2 common points (c) 1 common point

Figure 3.16.: Additional examples for paths $p^\pm_{\mathrm{i}}$ based for the same $B^\pm_{\mathrm{i,sat}}$ as in Figure 3.15. Common points are marked. Similar figures can also be found in [38, 39].

following limits exists:

$$\begin{aligned} \lim_{h\to-\infty} p^+_{\mathrm{i}}(h) &= b^{+,-\infty}_{\mathrm{i}} > -B^\infty_{\mathrm{i,sat}}\,, & \lim_{h\to\infty} p^+_{\mathrm{i}}(h) &= B^\infty_{\mathrm{i,sat}}\,, \\ \lim_{h\to-\infty} p^-_{\mathrm{i}}(h) &= -B^\infty_{\mathrm{i,sat}}\,, & \lim_{h\to\infty} p^-_{\mathrm{i}}(h) &= b^{-,+\infty}_{\mathrm{i}} < B^\infty_{\mathrm{i,sat}}\,. \end{aligned} \tag{3.58}$$

Thus in both limits the path p^+ is above p^-. Because paths p^+ and p^- are continuous an odd number of intersection (change of vertical order) is in contradiction to this. $\square$

Remark 3.42. In the consideration, a finite number of common points between two paths p^+ and p^- is assumed. An infinite number could arise, for example, from the fact that the paths $p^\pm$ move on an interval along b^{eq} and do not just cross it. For other reasons, a condition is imposed below which restricts the number of common points in the finite case. This prevents at the same time the case of infinitely many common points. Therefore, this case will not be further investigated here.

Intersectionfree *bh*-loop

As motivated in Section 2.3 and at the beginning of this section, Tellinen's hysteresis model should enable an analysis of simple hysteresis loops. As already stated in Remark 3.34, simple excitations are not sufficient to guarantee simple hysteresis loops. Now criteria, such that this is guaranteed, are developed.

Remark 3.43. Of course it can be checked a posteriori if a simple hysteresis loop was generated. The domain of h can be restricted to suitable ranges, such that a proper hysteresis loops with the right vertical order (p^- above p^+), as seen in Figure 3.15(b), is obtained. But a globally valid criteria is desired, such that any resulting hysteresis loop is simple.

Remark 3.44. Figure 3.16 gives additional examples of common points for given paths $p^{\pm}$. Note that common points on b^{eq} can be contact points (Figures 3.16(a) and 3.16(c)) or intersections (Figure 3.16(b)). It is possible to determine from the geometric arrangement of p^{+}, p^{-} and b^{eq} which type of common point on b^{eq} is. Outgoing from this property, a condition to $B^{\pm}_{\mathrm{sat}}$ is derived, so that only simple hysteresis loops are created.

Remark 3.45. By definition (3.43) and assumption $B^{\pm}_{\mathrm{sat}} \in C^1(\mathbb{R})$, it can be concluded that b^{eq} is continuous, but in general not differentiable. For the following consideration, the requirements of $B^{\pm}_{\mathrm{sat}}$ are tightened and $B^{\pm}_{\mathrm{sat}} \in C^2(\mathbb{R})$ is presumed. With this also $b^{\mathrm{eq}} \in C^1(\mathbb{R})$ applies. This is obviously a disadvantage and must be taken into account when creating the saturation curves $B^{\pm}_{\mathrm{sat}}$. For example, the curves shown in Figures 3.15 and 3.16 have been generated using a shape-preserving piecewise cubic interpolation method (PCHIP [87]). However, at the data points this method is not twice continuously differentiable, which is reflected in the bends in b^{eq} and $b^{\mathrm{eq}}_{\mathrm{i}}$.

Remark 3.46. Conditions are now derived, such that there is a maximum of two intersections for any paths p^{+} and p^{-}. To do this, the behavior at the next higher number of four intersections, as proven by Lemma 3.41, is investigated. As proven in Lemma 3.38, two consecutive intersections cannot be both in $I^{>}$ or $I^{<}$. Thus, between two intersections the paths $p^{\pm}$ must have a common point with b^{eq}. This can be seen for example in Figures 3.15(b) and 3.16(b), i.e., if the possibilities of common points between paths $p^{\pm}$ and b^{eq} are limited, this also limits the number of intersections of p^{+} and p^{-}. Now, the paths $p^{\pm}$ shall be prevented from piercing b^{eq} from below. This is the case, for example, in Figure 3.15(b) between the second and third intersection point.

Lemma 3.47: Given any valid $B^{\pm}_{\mathrm{sat}}$ and any paths $p^{\pm}$ and p^{-}. If

$$\frac{\mathrm{d}b^{\mathrm{eq}}(h)}{\mathrm{d}h} > \mu^{\mathrm{eq}}_{\mathrm{diff}}(h) = \mu^{\pm}_{\mathrm{diff}}\Big(h, b^{\mathrm{eq}}(h)\Big) \quad \text{for all } h \in \mathbb{R} \tag{3.59}$$

holds, the following statements are true.

I) Each intersection of p^{+} and p^{-} is either in $I^{<}$ or $I^{>}$, but not in $I^{=}$.

II) Any paths p^{+} and p^{-} can have at most two intersections.

Proof. I): This is proven by contradiction. It is assumed there exists a $\Big(h^*, b^{\mathrm{eq}}(h^*)\Big) \in I^{=}$ that is a intersection of paths p^{+} and p^{-}. Let define $\mathrm{dist} : \mathbb{R} \to \mathbb{R}$ with $\mathrm{dist}(h) = p^{+}(h) - p^{-}(h)$ and $\frac{\mathrm{d}\,\mathrm{dist}(h)}{\mathrm{d}h} = \frac{\mathrm{d}p^{+}(h)}{\mathrm{d}h} - \frac{\mathrm{d}p^{-}(h)}{\mathrm{d}h} = \mu^{+}_{\mathrm{diff}}\Big(h, p^{+}(h)\Big) - \mu^{-}_{\mathrm{diff}}\Big(h, p^{-}(h)\Big)$. Since $\Big(h^*, b^{\mathrm{eq}}(h^*)\Big)$ is assumed as an intersection, it must hold $\mathrm{dist}(h^*) = 0$ and dist must change its sign at h^*.

Since (3.59) holds, there exists $\epsilon > 0$, such that

$$\begin{aligned} \Big(h, p^{+}(h)\Big), \Big(h, p^{-}(h)\Big) &\in I^{>} \quad \text{for all } h \in (h^*, h^* + \epsilon)\,, \\ \Big(h, p^{+}(h)\Big), \Big(h, p^{-}(h)\Big) &\in I^{<} \quad \text{for all } h \in (h^* - \epsilon, h^*) \end{aligned} \tag{3.60}$$

holds. Directly from (3.60) also follows

$$\frac{\mathrm{d}\,\mathrm{dist}(h)}{\mathrm{d}h} = \mu^{+}_{\mathrm{diff}}\Big(h, p^{+}(h)\Big) - \mu^{-}_{\mathrm{diff}}\Big(h, p^{-}(h)\Big) \begin{cases} < 0 & \text{for } h \in (h^{*} - \epsilon, h^{*})\,, \\ = 0 & \text{for } h = h^{*}\,, \\ > 0 & \text{for } h \in (h^{*}, h^{*} + \epsilon)\,. \end{cases} \tag{3.61}$$

So dist has a local minima at h^{*} and therefore no sign change at h^{*}. This contradicts the conditions above. Thus an intersection of paths p^{+} and p^{-} is never on b^{eq} and must be therefore either in $I^{>}$ or $I^{<}$.

II): First, assume both paths are equal to their corresponding boundary, i.e., $p^{+} = B^{+}_{\mathrm{sat}}$ and $p^{-} = B^{-}_{\mathrm{sat}}$. By condition (3.3) these paths have no intersection. Second, assume that exactly one of the paths $p^{\pm}$ is equal to its corresponding boundary $B^{\pm}_{\mathrm{sat}}$. In this case there is exactly one intersection, proven by Lemma 3.16. Hence only the case remains, that both paths $p^{\pm}$ are defined w.r.t. $(h^{+}, b^{+}), (h^{-}, b^{-}) \in \mathrm{int}(I)$, respectively.

Assuming that the paths $p^{\pm}$ have 4 or move intersections. Let them be denoted by $(h_1, b_1), \ldots, (h_n, b_n)$ and ordered, i.e., $h_1 < \ldots < h_n$. There is an even number of intersections, proven by Lemma 3.41, so n yields $n = 2k$ for $k \in \mathbb{N}^{\geq 2}$. Combining the statements I) and Lemma 3.38 the intersections lie alternately in $I^{>}$ and $I^{<}$. And it can be deduced that $(h_1, b_1) \in I^{<}$ must hold.

So $(h_2, b_2) \in I^{>}$ and $(h_3, b_3) \in I^{<}$ is true. This means that $b_2 < b^{\mathrm{eq}}(h_2)$ and $b_3 > b^{\mathrm{eq}}(h_3)$ applies. So b^{eq} must cross the paths $p^{\pm}$ from above on the interval (h_2, h_3). This contradicts (3.59). Thus only two or less intersections are possible. ☐

Remark 3.48. An alternative formulation of (3.59) is given by

$$\frac{\frac{\mathrm{d}B^{-}_{\mathrm{i,sat}}(h)}{\mathrm{d}h}}{\frac{\mathrm{d}B^{+}_{\mathrm{i,sat}}(h)}{\mathrm{d}h}} \left(\frac{\mathrm{d}B^{+}_{\mathrm{sat}}(h)}{\mathrm{d}h} + \frac{\mathrm{d}B^{-}_{\mathrm{sat}}(h)}{\mathrm{d}h} \right) > \Big(B^{-}_{\mathrm{sat}}(h) - B^{+}_{\mathrm{sat}}(h)\Big) \frac{\mathrm{d}}{\mathrm{d}h} \left(\frac{\frac{\mathrm{d}B^{+}_{\mathrm{i,sat}}(h)}{\mathrm{d}h}}{\frac{\mathrm{d}B^{-}_{\mathrm{i,sat}}(h)}{\mathrm{d}h}} \right)\,. \tag{3.62}$$

Remark 3.49. Equation (3.59) does not only limit the number of common points for any paths p^{+}, p^{-} to a maximum of two, if there are only a finite number of these points. It additionally ensures, that there can not be an interval (h_0, h_1) such that $b^{\mathrm{eq}}(h) = p^{+}(h) = p^{-}(h)$ for all $h \in (h_0, h_1)$ holds.

Remark 3.50. Unfortunately, condition (3.59) is not a sharp distinction. It also prevents situations that would actually be valid. Figure 3.16(b) shows such valid but excluded situation.

Remark 3.51. In the further course of the thesis it is assumed that any two paths $p^{\pm}$ can have a maximum of two common points. This is ensured either by a retrospective check (see Remark 3.43) or by the global condition (3.59).

Conclusion

At this point a good overview – how the paths p^+ and p^- behave – is achieved. The paths are mathematically well defined and reflect the physically motivated properties.

The definition domain of Tellinen's model I could be subdivided more finely (see (3.44)). Many properties can be examined by a simple check, whether the considered point is in $I^<$,$I^>$ or $I^=$ (see Lemmas 3.36, 3.38 and 3.47).

Conditions to conclude the existence of a second intersection (see Lemma 3.38) are derived. The limit values of the paths $p_\mathrm{i}^\pm$ and the asymptotic behavior of $p^\pm$ are clearly defined (see Lemma 3.18). And by examining the vertical arrangement at intersections (see Definition 3.35 and lemma 3.36), the global arrangement of the paths can easily be analyzed.

This specially chosen construction of the paths $p^\pm$ (see Definition 3.12) is a powerful tool for analyzing Tellinen's model.

Condition (3.59) may restrict the applicability of the model. Whether this is relevant in the application or not, cannot be answered globally. This limitation is mainly due to the fact that a loss model based on the enclosed area is defined in Section 4.1 of this thesis. There, the orientation of the enclosed area plays an important role. It is up to the user to decide whether a closed curve, where p^- is below p^+, is a problem. It has been shown that it is possible to create such loops with Tellinen's model and derive an a priori condition for B_sat^+, to prevent these kind of loops.

3.2.5. Existence and Uniqueness of Stable Loops

Parts of the following studies have already been published in [38].

In the previous chapter the mathematical basis was created. Now, the behavior of Tellinen's model is investigated with respect to a given excitation. As already mentioned in Remark 3.10, h or b can be considered as independent variables. In this section h is specified, as before, and describe the change of b using Tellinen's model.

Definition 3.52 (sweeping)**:** Given $h_0, h_1 \in \mathbb{R}$ with $h_0 < h_1$. An excitation of h is denoted as *sweeping*, if h can be described by a continuous, periodic function $f : \mathbb{R} \to [h_0, h_1]$ by $h = f(t)$. In each period f increases monotonously from h_0 to h_1 and then decreases monotonously back to h_0.

Remark 3.53. An example for Definition 3.52 is given by $f(t) = h_0 + (h_1 - h_0)\frac{1-\cos(t)}{2}$.

Remark 3.54. Sweeping is by definition a simple excitation.

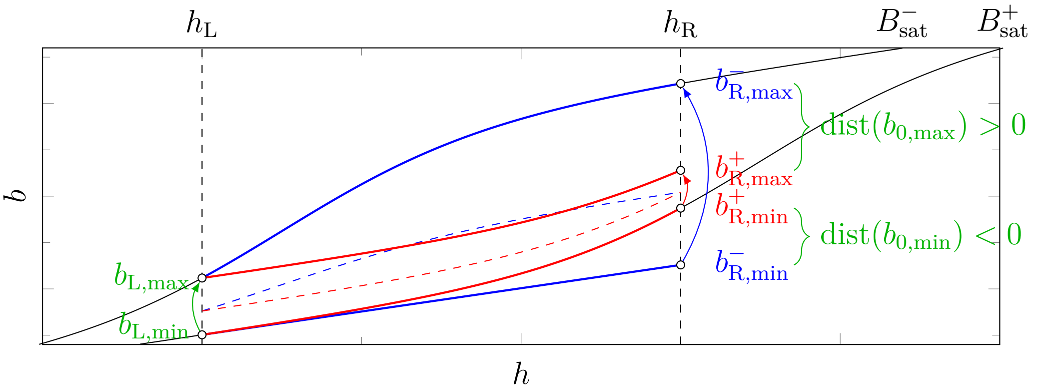

Figure 3.17.: Idea of the proof of Lemma 3.57. Paths based on μ^+_diff are shown in red and μ^-_diff in blue.

As already motivated in Remark 3.27, the examination via the paths $p^\pm$ allows to take different approaches. Up to now, the focus lied on the initial situation that an intersection is on hand and define both paths $p^\pm$ to this point. Now a different approach is taken. It is started with an arbitrary point $(h_0, b_0) \in I$ and its corresponding path p^+. A h_1 with $h_1 > h_0$ is chosen and define p^- w.r.t. $\big(h_1, p^+(h_1)\big) \in I$. Of interest is the evaluation of p^- at h_0 compared to b_0.

Definition 3.55 (stable loop, turning points)**:** Given $(h_0, b_0) \in I$ and $h_1 \in \mathbb{R}$ with $h_1 > h_0$. Let p^+ defined w.r.t. (h_0, b_0) and p^- w.r.t. $\big(h_1, p^+(h_1)\big) \in I$. If $b_0 = p^-(h_0)$ holds, the loop consisting of $p^+(h)\big|_{h\in[h_0,h_1]}$ and $p^-(h)\big|_{h\in[h_0,h_1]}$ is denoted as *stable*. Otherwise, it is *unstable*. Let denote $\big(h_1, p^+(h_1)\big)$ as a turning point. For a stable loop (h_0, b_0) is also a turning point.

Remark 3.56*.* A stable loop by Definition 3.55 correspond to a simple closed hysteresis loop. By condition (3.59) all required properties are ensured. The procedure in Definition 3.55 corresponds to the execution of one cycle of a sweeping excitation.

It will be proven, that there is exactly one $b_\mathrm{L} \in \big(B^+_\mathrm{sat}(h_\mathrm{L}), B^-_\mathrm{sat}(h_\mathrm{L})\big)$ for any $h_\mathrm{L}, h_\mathrm{R} \in \mathbb{R}$ with $h_\mathrm{L} < h_\mathrm{R}$, so that a stable curve results. Then it is shown that sweeping on $[h_\mathrm{L}, h_\mathrm{R}]$ for any $b_\mathrm{L} \in \big(B^+_\mathrm{sat}(h_\mathrm{L}), B^-_\mathrm{sat}(h_\mathrm{L})\big)$ converges to this stable curve.

Lemma 3.57: Given valid $B^\pm_\mathrm{sat}$, which fulfills (3.62). For any h_L and h_R with $h_\mathrm{L} < h_\mathrm{R}$ exists b_L and b_R, such that $(h_\mathrm{L}, b_\mathrm{L}) \in \mathrm{int}(I)$ and $(h_\mathrm{R}, b_\mathrm{R}) \in \mathrm{int}(I)$ are the only turning points of a stable curve.

Proof. Assume h_L, h_R as given and constant. Define the function

$$\begin{aligned}
\mathrm{dist} : \Big[B^+_\mathrm{sat}(h_\mathrm{L}), B^-_\mathrm{sat}(h_\mathrm{L})\Big] &= [b_\mathrm{L,min}, b_\mathrm{L,max}] \to \mathbb{R}\,, \\
\mathrm{dist}(b) &= \left(b + \int_{h_\mathrm{L}}^{h_\mathrm{R}} \frac{\mathrm{d}p^-(h)}{\mathrm{d}h}\,\mathrm{d}h\right) - \left(b + \int_{h_\mathrm{L}}^{h_\mathrm{R}} \frac{\mathrm{d}p^+(h)}{\mathrm{d}h}\,\mathrm{d}h\right) \\
&= \int_{h_\mathrm{L}}^{h_\mathrm{R}} \frac{\mathrm{d}p^-(h)}{\mathrm{d}h} - \frac{\mathrm{d}p^+(h)}{\mathrm{d}h}\,\mathrm{d}h\,. \qquad (3.63)
\end{aligned}$$

The paths $p^{\pm}$ are defined with reference to (h_{L}, b), such that (3.63) is indeed a function of the variable b. Visually dist describes the difference of the paths $p^{\pm}$ with a common starting point (h_{L}, b) at h_{R}, as shown in Figure 3.17. A value of $\operatorname{dist}(b) = 0$ represent a closed loop. It will be shown that

$$\operatorname{dist}\left(B^{-}_{\mathrm{sat}}(h_{\mathrm{L}})\right) = \operatorname{dist}\left(b_{\mathrm{L,max}}\right) > 0 \quad \text{and} \quad \operatorname{dist}\left(B^{+}_{\mathrm{sat}}(h_{\mathrm{L}})\right) = \operatorname{dist}(b_{\mathrm{L,min}}) < 0 \tag{3.64}$$

holds. With dist being continuous and having a change of sign, a zero crossing and therefore a stable curve must exists.

As an interim result it is shown, that

$$b^{-}_{\mathrm{R,min}} < b^{+}_{\mathrm{R,min}} < b^{+}_{\mathrm{R,max}} < b^{-}_{\mathrm{R,max}} \tag{3.65}$$

holds, with $b^{\pm}_{R,\mathrm{min/max}}$ being the evaluations of the paths $p^{\pm}_{\mathrm{min/max}}$ w.r.t. to $(h_{\mathrm{L}}, b_{\mathrm{L,min/max}})$ at $h = h_{\mathrm{R}}$.

The path p^{-}_{min} lies on B^{+}_{sat} for $h = h_{\mathrm{L}}$ and outside of I for all $h > h_{\mathrm{L}}$. So by definition

$$b^{-}_{\mathrm{R,min}} = B^{+}_{\mathrm{sat}}(h_{\mathrm{L}}) + \int_{h_{\mathrm{L}}}^{h_{\mathrm{R}}} \frac{\mathrm{d}p^{-}_{\mathrm{min}}(h)}{\mathrm{d}h}\,\mathrm{d}h = B^{+}_{\mathrm{sat}}(h_{\mathrm{L}}) + \int_{h_{\mathrm{L}}}^{h_{\mathrm{R}}} \mu_0\,\mathrm{d}h \tag{3.66}$$

holds. The path p^{+}_{min} lies on B^{+}_{sat} for $h = h_{\mathrm{L}}$ and is therefore, by definition, identical to B^{+}_{sat} for all h.

$$\begin{aligned} b^{+}_{\mathrm{R,min}} &= B^{+}_{\mathrm{sat}}(h_{\mathrm{L}}) + \int_{h_{\mathrm{L}}}^{h_{\mathrm{R}}} \frac{\mathrm{d}p^{+}_{\mathrm{min}}(h)}{\mathrm{d}h}\,\mathrm{d}h \\ &= B^{+}_{\mathrm{sat}}(h_{\mathrm{L}}) + \int_{h_{\mathrm{R}}}^{h_{\mathrm{L}}} \underbrace{\frac{\mathrm{d}B^{+}_{\mathrm{sat}}(h)}{\mathrm{d}h}}_{>\mu_0}\,\mathrm{d}h > b^{-}_{\mathrm{R,min}} \end{aligned} \tag{3.67}$$

From Remark 3.15 and $p^{+}_{\mathrm{min}}(h_{\mathrm{L}}) = b^{+}_{\mathrm{L,min}} < b^{+}_{\mathrm{L,max}} = p^{+}_{\mathrm{max}}(h_{\mathrm{L}})$, follows

$$p^{+}_{\mathrm{min}}(h_{\mathrm{R}}) = b^{+}_{\mathrm{R,min}} < b^{+}_{\mathrm{R,max}} = p^{+}_{\mathrm{max}}(h_{\mathrm{R}})\,. \tag{3.68}$$

From Lemma 3.16 follows that $p^{+}_{\mathrm{max}}(h) < p^{-}_{\mathrm{max}}(h)$ holds for any $h > h_{\mathrm{L}}$ and thus in particular at h_{R} with

$$b^{+}_{\mathrm{R,max}} = p^{+}_{\mathrm{max}}(h) < p^{-}_{\mathrm{max}}(h) = b^{-}_{\mathrm{R,max}}\,. \tag{3.69}$$

Evaluation of dist at $b_{\mathrm{L,max}}$ and $b_{\mathrm{L,min}}$ yields

$$\operatorname{dist}(b_{\mathrm{L,max}}) = b^{-}_{\mathrm{R,max}} - b^{+}_{\mathrm{R,max}} > 0\,, \tag{3.70a}$$

$$\operatorname{dist}(b_{\mathrm{L,min}}) = b^{-}_{\mathrm{R,min}} - b^{+}_{\mathrm{R,min}} < 0\,. \tag{3.70b}$$

Therefore, a value b_{L} with $b_{\mathrm{L,min}} < b_{\mathrm{L}} < b_{\mathrm{L,max}}$ and $\operatorname{dist}(b_{\mathrm{L}}) = 0$ must exists. By Remark 3.15 the corresponding value of b_{R} must lie between $b^{+}_{\mathrm{R,min}}$ and $b^{+}_{\mathrm{R,max}}$.

The existence of more intersections of $p^{\pm}$ is prevented by (3.62). ☐

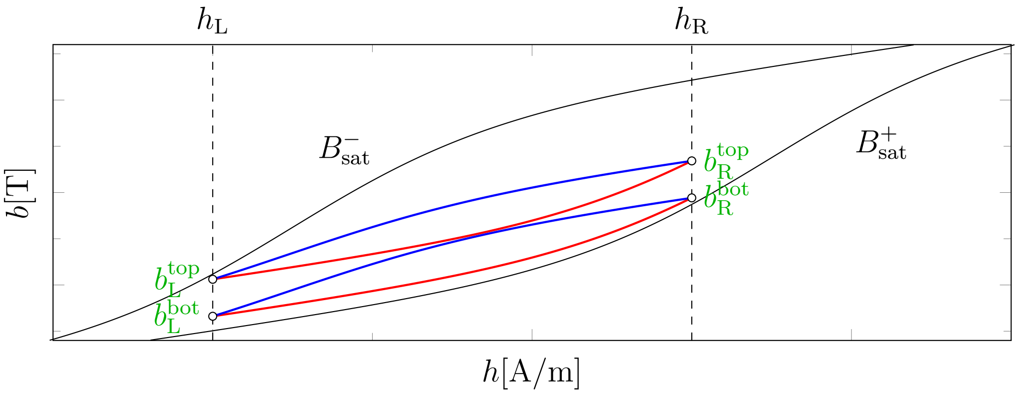

Figure 3.18.: Idea of the proof of Lemma 3.58. Paths based on μ^+_diff are shown in red and μ^-_diff in blue.

Lemma 3.58: The values b_L and b_R in Lemma 3.57 are unique.

Proof. This is proven by contradiction. Assuming there exists two stable curves for the given parameters h_L, h_R. Let the turning points be denoted as $b^\mathrm{top}_\mathrm{L}, b^\mathrm{top}_\mathrm{R}, b^\mathrm{bot}_\mathrm{L}, b^\mathrm{bot}_\mathrm{R}$ with $b^\mathrm{bot}_\mathrm{L} < b^\mathrm{top}_\mathrm{L}$ and $b^\mathrm{bot}_\mathrm{R} < b^\mathrm{top}_\mathrm{R}$ as shown in Figure 3.18. Let $p^\pm_\mathrm{top} = p^\pm_\mathrm{top}(h)$ be the paths going through $(h_\mathrm{L}, b^\mathrm{top}_\mathrm{L}) \in I$ and likewise $p^\pm_\mathrm{bot} = p^\pm_\mathrm{bot}(h)$ through $(h_\mathrm{L}, b^\mathrm{bot}_\mathrm{L}) \in I$. Each of the curves is closed, i.e.,

$$\begin{aligned}\int_{h_\mathrm{L}}^{h_\mathrm{R}} \mu^+_\mathrm{diff}(h, p^+_\mathrm{top})\,\mathrm{d}h &= \int_{h_\mathrm{L}}^{h_\mathrm{R}} \mu^-_\mathrm{diff}(h, p^-_\mathrm{top})\,\mathrm{d}h\,,\\ \int_{h_\mathrm{L}}^{h_\mathrm{R}} \mu^+_\mathrm{diff}(h, p^+_\mathrm{bot})\,\mathrm{d}h &= \int_{h_\mathrm{L}}^{h_\mathrm{R}} \mu^-_\mathrm{diff}(h, p^-_\mathrm{bot})\,\mathrm{d}h\end{aligned} \tag{3.71}$$

holds. Subtracting these two equations leads to

$$\int_{h_\mathrm{L}}^{h_\mathrm{R}} \underbrace{\mu^+_\mathrm{diff}(h, p^+_\mathrm{top}) - \mu^+_\mathrm{diff}(h, p^+_\mathrm{bot})}_{<0}\,\mathrm{d}h = \int_{h_\mathrm{L}}^{h_\mathrm{R}} \underbrace{\mu^-_\mathrm{diff}(h, p^-_\mathrm{top}) - \mu^+_\mathrm{diff}(h, p^-_\mathrm{bot})}_{>0}\,\mathrm{d}h\,. \tag{3.72}$$

Arguing that $p^\pm_\mathrm{top} > p^\pm_\mathrm{bot}$ holds by Remark 3.15 and application of the monotonicity (Lemma 3.6) in the second component of $\mu^\pm_\mathrm{diff}$ results in a contradiction. Therefore for a given set of parameters only one unique stable loop can exists. ☐

3.2.6. Convergence to Stable Loops in the Case of Non-closed Paths

Lemma 3.59: Given $h_\mathrm{L}, h_\mathrm{R} \in \mathbb{R}$ with $h_\mathrm{L} < h_\mathrm{R}$ and any b_L with $(h_\mathrm{L}, b_\mathrm{L}) \in I$. Starting with $b_\mathrm{L} = B_0$. Create a path p^+_0 w.r.t. $(h_\mathrm{L}, B_0) \in I$ and hereinafter another path p^-_0 w.r.t. $\big(h_\mathrm{R}, p^+_0(h_\mathrm{R})\big) \in I$. The following iterative scheme is applied. For $k \in \mathbb{N}$ define p^+_k w.r.t. $\big(h_\mathrm{L}, p^-_{k-1}(h_\mathrm{L})\big)$ and path p^-_k w.r.t. $\big(h_\mathrm{R}, p^+_k(h_\mathrm{R})\big)$.

The paths p_k^+ and p_{k-1}^- share the common point $\big(h_{\mathrm{L}}, p_k^+(h_{\mathrm{L}})\big) = \big(h_{\mathrm{L}}, p_{k-1}^-(h_{\mathrm{L}})\big) = (h_{\mathrm{L}}, B_k) \in I$. They form (in general) an open loop, i.e., $p_k^+(h_{\mathrm{R}}) \neq p_{k-1}^-(h_{\mathrm{R}})$. The paths p_k^+ and p_k^- converge for $k \to \infty$ to the stable loop defined in Lemmas 3.57 and 3.58.

Proof. Define $\varphi : \big[B^+_{\mathrm{sat}}(h_{\mathrm{L}}), B^-_{\mathrm{sat}}(h_{\mathrm{L}})\big] \to \big[B^+_{\mathrm{sat}}(h_{\mathrm{L}}), B^-_{\mathrm{sat}}(h_{\mathrm{L}})\big]$ with

$$\begin{aligned}\varphi(b_k) &= \underbrace{b_k + \int_{h_{\mathrm{L}}}^{h_{\mathrm{R}}} \mu^+_{\mathrm{diff}}\big(h, p_k^+(h)\big)\,\mathrm{d}h}_{=p_k^+(h_{\mathrm{R}})} + \int_{h_{\mathrm{R}}}^{h_{\mathrm{L}}} \mu^-_{\mathrm{diff}}\big(h, p_k^-(h)\big)\,\mathrm{d}h \\ &= \underbrace{p_k^+(h_{\mathrm{R}}) + \int_{h_{\mathrm{R}}}^{h_{\mathrm{L}}} \mu^-_{\mathrm{diff}}\big(h, p_k^-(h)\big)\,\mathrm{d}h}_{=p_k^-(h_{\mathrm{L}})} = p_k^-(h_{\mathrm{L}})\end{aligned} \tag{3.73}$$

with p_k^+ defined w.r.t. (h_{L}, b_k) and p^- w.r.t. $\big(h_{\mathrm{R}}, p_k^+(h_1)\big)$. This corresponds to going from h_{L} to h_{R} on path p_k^+, stopping in the turning point $\big(h_{\mathrm{R}}, p_k^+(h_{\mathrm{R}})\big)$ and going back to h_{L} via p_k^-. This is one cycle of a sweeping excitation (see Definition 3.52). So $b_k = p_k^+(h_{\mathrm{L}})$, $p_k^+(h_{\mathrm{R}}) = p_k^-(h_{\mathrm{R}})$ and $p_k^-(h_{\mathrm{L}}) = \varphi(b_k)$ applies in particular.

A stable loop exists and is unique as proven in Lemmas 3.57 and 3.58. It consist of the turning points $(h_{\mathrm{L}}, b_{\mathrm{L}}^{\mathrm{fix}})$ and $(h_{\mathrm{R}}, b_{\mathrm{R}}^{\mathrm{fix}})$ and paths p^+_{fix} and p^-_{fix}. It fulfills $b_{\mathrm{L}}^{\mathrm{fix}} = \varphi\left(b_{\mathrm{L}}^{\mathrm{fix}}\right)$ and is therefore the only fixed point of φ.

It will be proven that for any $b_k \in \big[B^+_{\mathrm{sat}}(h_{\mathrm{L}}), B^-_{\mathrm{sat}}(h_{\mathrm{L}})\big] \setminus \big\{b_{\mathrm{L}}^{\mathrm{fix}}\big\}$

$$|\varphi(b_{\mathrm{L}}^{\mathrm{fix}}) - \varphi(b_k)| = |b_{\mathrm{L}}^{\mathrm{fix}} - \varphi(b_k)| < |b_{\mathrm{L}}^{\mathrm{fix}} - b_k| \tag{3.74}$$

holds. With (3.74) it is proven, that φ is a contraction and $b_{\mathrm{L}}^{\mathrm{fix}}$ is an attractive fixed point on the whole definition domain of φ. Thus φ is unconditionally convergent with limit value $b_{\mathrm{L}}^{\mathrm{fix}}$. By construction of φ and rearranging

$$\begin{aligned}\varphi(b_{\mathrm{L}}^{\mathrm{fix}}) - \varphi(b_k) = b_{\mathrm{L}}^{\mathrm{fix}} - b_k &+ \int_{h_{\mathrm{L}}}^{h_{\mathrm{R}}} \underbrace{\mu^+_{\mathrm{diff}}\big(s, p^+_{\mathrm{fix}}(s)\big) - \mu^+_{\mathrm{diff}}\big(s, p_k^+(s)\big)}_{\substack{<0,\text{ if } b_{\mathrm{L}}^{\mathrm{fix}} > b_k \\ >0,\text{ if } b_{\mathrm{L}}^{\mathrm{fix}} < b_k}}\,\mathrm{d}s \\ &+ \int_{h_{\mathrm{R}}}^{h_{\mathrm{L}}} \underbrace{\mu^-_{\mathrm{diff}}\big(s, p^-_{\mathrm{fix}}(s)\big) - \mu^-_{\mathrm{diff}}\big(s, p_k^-(s)\big)}_{\substack{>0,\text{ if } b_{\mathrm{L}}^{\mathrm{fix}} > b_k \\ <0,\text{ if } b_{\mathrm{L}}^{\mathrm{fix}} < b_k}}\,\mathrm{d}s\end{aligned} \tag{3.75}$$

holds. Using the monotoncity of $\mu^{\pm}_{\mathrm{diff}}$ in the second component (see Lemma 3.6) and the ordering of the paths (see Remark 3.15) yield the signs of the terms. Note that integration limits are swapped for the second term. Thus, both integrals yield the same sign for the cases $b_{\mathrm{L}}^{\mathrm{fix}} \gtrless b_k$. Altogether this results in

$$\begin{aligned} 0 < \varphi(b_{\mathrm{L}}^{\mathrm{fix}}) - \varphi(b_k) = b_{\mathrm{L}}^{\mathrm{fix}} - \varphi(b_k) < b_{\mathrm{L}}^{\mathrm{fix}} - b_k &\quad, \text{ if } b_{\mathrm{L}}^{\mathrm{fix}} > b_k\,, \\ 0 > \varphi(b_{\mathrm{L}}^{\mathrm{fix}}) - \varphi(b_k) = b_{\mathrm{L}}^{\mathrm{fix}} - \varphi(b_k) > b_{\mathrm{L}}^{\mathrm{fix}} - b_k &\quad, \text{ if } b_{\mathrm{L}}^{\mathrm{fix}} < b_k\,, \end{aligned} \tag{3.76}$$

which proves (3.74). ☐

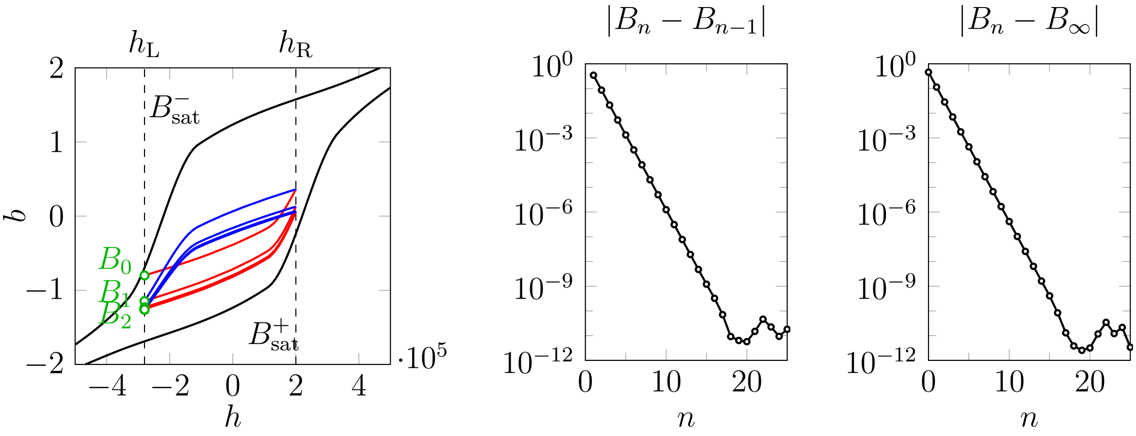

(a) bh-loops (b) Differences (c) Differences

Figure 3.19.: Numerical example of convergence for sweeping. The left turning points are denoted as B_k. The paths are solved numerically by a Runge–Kutta method (RK45, rtol=10^{-8}, atol=10^{-9}). Comparable figures can be found in [38, 39].

Remark 3.60. Lemma 3.59 proves, that sweeping (going back and forth) between h_L and h_R using Tellinen's model converges toward a unique stable loop. A numerical example is given in Figure 3.19. The model behaves predictably and well behaved. The stable state is almost reached after only a few cycles. The assumption of simple excitation may not agree for many applications. There are certainly examples of this as shown in Section 2.4. But with this it can still prove that Tellinen's model permanently tries to reach a stable state.

3.3. Solver Strategies

The goal of this section is to provide an overview of how Tellinen's model can be integrated into the benchmark problem (2.13). This is done with a numerical background. In Chapter 5 the finite difference method with an iterative solver is applied to (2.13). To realize this, the previous placeholder $h = \nu(b)$ in (2.13) has to be replaced by Tellinen's model.

This poses a few challenges. The evaluation must be done separately in each grid point. This means that the chosen approach must be reasonable in terms of computing power and memory requirements, specially because this has to be done several times per grid point and time step due to the iterative solving. It is assumed that there is no analytical solution to the ODE (3.7) of Tellinen's model.

The observation are restricted to one grid point and it is assumed that at this grid point the material is currently in state $(h_0, b_0) \in I$. The time steps of the overall simulation are chosen small enough so that the searched solution is close to the old one. This leads directly to a problem. Tellinen's model is not differentiable in exactly that state (h_0, b_0). Since it is unknown in general whether the fields increase or

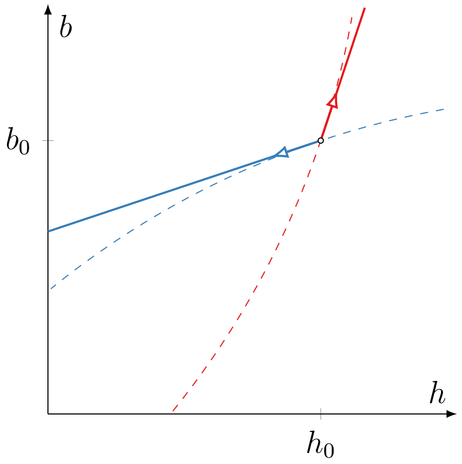

Figure 3.20.: Approach 1 based on explicit Euler. An exemplary trajectory of the paths $p^{\pm}$ are shown dashed. The section-wise linearized approximation is marked with solid lines.

decrease, this is unfortunately a fact which cannot be changed straightforward. Thus, the approach of the integration of Tellinen's model directly influences the choice of possible solution methods for the overall simulation. A detailed consideration of this follows in Chapter 5. Here, for the time being it is sufficient to present the approaches and the argumentation that there are different possibilities.

To solve the ODE (3.7), the usual numerical methods are available. Since Tellinen's model is more generally focused on fast rather than accurate representation of hysteresis, it is focused on appropriate lower order methods. Two different approaches – based on the explicit Euler method – are now presented.

It must be distinguished well between the levels discussed. When an ODE is mentioned, always the ODE (3.7) is meant, i.e., the Tellinen model. On this ODE numerical methods are applied to get a function $h = \nu(b)$, which is used in the PDE (2.13). This results in a total system, which shall be solved numerically.

3.3.1. Approach 1 – Linearizing / Explicit Euler

Let $(h_0, b_0) \in I$ be the current state. The underlying ODE (3.7) is replaced with one step of the explicit Euler method. $\mu_{\text{diff}}^{\pm}$ is evaluated at the current state, i.e., $\mu_{\text{diff}}^{\pm} = \mu_{\text{diff}}^{\pm}(h_0, b_0)$. The directional dependence is expressed by a section-wise defined function or more clearly by a min and max formulation. This results in a function $b(h)$, which calculates the corresponding b for all h.

$$\begin{aligned} b(h) = \mu(h) &= b_0 + \begin{cases} \mu_{\text{diff}}^{+} \cdot (h - h_0) & \text{if } h \geq h_0 \\ \mu_{\text{diff}}^{-} \cdot (h - h_0) & \text{if } h < h_0 \end{cases} \\ &= b_0 + \mu_{\text{diff}}^{+} \cdot \max(0, h - h_0) + \mu_{\text{diff}}^{-} \cdot \min(0, h - h_0) \end{aligned} \tag{3.77a}$$

Under the assumption that the function $b(h)$ is evaluated only close enough around (h_0, b_0), this $b(h)$ is a 1st order approximation or linearization of Tellinen's model. A visualization is given in Figure 3.20.

With $\mu_{\text{diff}}^{\pm} \geq \mu_0 > 0$ the resulting function μ is strictly monotone increasing and can be therefore be inverted.

$$\begin{aligned} h(b) = \nu(b) &= h_0 + \begin{cases} \frac{1}{\mu_{\text{diff}}^{+}}(b - b_0) & \text{if } b \geq b_0 \\ \frac{1}{\mu_{\text{diff}}^{-}}(b - b_0) & \text{if } b < b_0 \end{cases} \\ &= h_0 + \frac{1}{\mu_{\text{diff}}^{+}} \max(0, b - b_0) + \frac{1}{\mu_{\text{diff}}^{-}} \min(0, b - b_0) \end{aligned} \tag{3.77b}$$

The functions μ, ν provide a bijection between h and b. They are continuous and piece wise linear. But at h_0 or b_0 respectively, they are not differentiable.

Using this approach inside a simulation (e.g. discretization of (2.13)), it would lead to a non-linear system, because ν is non-linear. Furthermore, the system must be solved near the current state (h_0, b_0), at which ν is not differentiable. Solvers based on the derivative (like Newtons method) could be failing and showing non convergent behavior.

3.3.2. Approach 2 – Delaying Direction Information

This approach continues the first and tries to reduce the problem to a linear one. To achieve this, the information about a change of direction is delayed by one time step. The decision if $\mu_{\text{diff}} = \mu_{\text{diff}}^{+}$ or $\mu_{\text{diff}} = \mu_{\text{diff}}^{-}$ is used, is now based on what happened in the previous time step. This simplifies (3.77a) and (3.77b) to

$$\begin{aligned} b(h) = \mu(h) &= b_0 + \mu_{\text{diff}}(h - h_0)\,, \\ h(b) = \nu(b) &= h_0 + \frac{1}{\mu_{\text{diff}}}(b - b_0) \end{aligned} \tag{3.78a}$$

with

$$\mu_{\text{diff}} = \begin{cases} \mu_{\text{diff}}^{+}(h_0, b_0) & \text{, if } h\text{,}b \text{ increased last step ,} \\ \mu_{\text{diff}}^{-}(h_0, b_0) & \text{, if } h\text{,}b \text{ decreased last step .} \end{cases} \tag{3.78b}$$

If this approach is now inserted into the PDE (2.13) and rearrange, it holds

$$\sigma \frac{\partial A}{\partial t} + \frac{1}{r}\frac{\partial}{\partial r}\Big(\frac{r}{\mu_{\text{diff}}}\Big(-\frac{\partial}{\partial r}A\Big)\Big) = j + \underbrace{\frac{1}{r}\frac{\partial}{\partial r}\Big(r\Big(\frac{b_0}{\mu_{\text{diff}}} - h_0\Big)\Big)}_{j_{\text{corr}}}\,. \tag{3.79}$$

The left-hand side of (3.79) is identical to a formulation with the non-hysteresis approach $b = \mu \cdot h$. With the above mentioned approaches, it is possible to consider

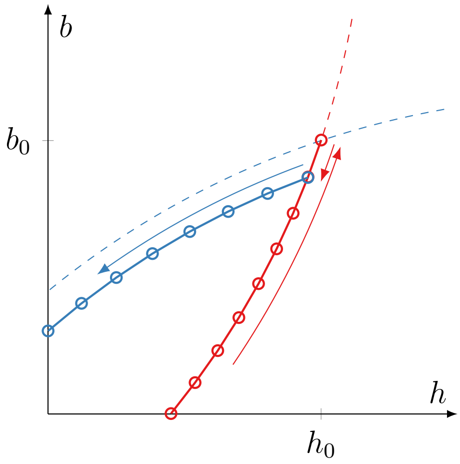

Figure 3.21.: Approach 2 based on delaying direction information. The direction of travel is counterclockwise. Instead in the actual turning point (h_0, b_0), the change from μ_{diff}^{+} (red) to μ_{diff}^{-} (blue) is delayed by one time step.

the effect of the hysteresis by an additional term, a current correction j_{corr}, on the right side of the PDE (2.13).

But there is also a disadvantage of this approach. The reversal point is not resolved precisely and the wrong value for μ_{diff} is used for one time step. See Figure 3.21 for a visualization. Depending on how large the differences between μ_{diff}^{+} and μ_{diff}^{-} are, this error is more or less significant. As mentioned in Section 2.2.2, ferromagnetic materials can have values of μ_{diff} up the range of $10^6 \cdot \mu_0$. Close to the saturation curves $B_{\text{sat}}^{\pm}$, either μ_{diff}^{+} or μ_{diff}^{-} approaches μ_0, while the other value approaches $\frac{\mathrm{d}B_{\text{sat}}^{\pm}}{\mathrm{d}h}$. This means that, especially near the boundaries $B_{\text{sat}}^{\pm}$, a difference between μ_{diff}^{+} and μ_{diff}^{-} of up to several orders of magnitude is possible. In this isolated case, any further investigations at this point are not target-oriented. Only when the benchmark problem in Chapter 5 with the concrete numerical approach, it can be investigated whether the advantages or disadvantages of the approach prevail.

3.4. Interim Conclusion & Further Remarks

Before Tellinen's model is extended in the next chapter, a brief summary of the results so far is given and outstanding issues are presented.

▶ In Section 3.1, Tellinen's model [54] is introduced and defined. The mathematical definition can be represented compactly and the ODE (3.7) is identified to be the core of the model. In parallel, an equivalent definition in (h, b_{i}) coordinates is provided. All permissible states are combined in the set I.

The model can be justified phenomenologically from the properties of ferromagnetic materials. The directional dependence of the model should be mentioned here as a particularly important property. Some notations have been introduced which will be used in the further course of the dissertation.

► One of the objectives of Section 3.2 is to verify the model for well-definedness. The investigations prove that the model results for all starting points $(h_0, b_0) \in I$ in paths that lie completely in I. It is also shown that the model can be formulated in terms of both μ and ν. Thus it is basically suitable to be integrated into the benchmark problem.

When performing the investigations, extended first order reversal curves are defined. These are providing paths p^+ and p^- for each point. With these paths it can be proven that for each sweeping excitation between the values h_L, h_R the model monotonously converges to an unique limit. Based on this statement, the model is considered to be stable.

However, during the analysis, it is noted that the resulting hysteresis loops are not necessarily simple. In principle, more than two intersection points for paths p^+ and p^- are possible. However, a global condition on $B_\mathrm{sat}^\pm$ can be derived, such that this case can no longer occur.

Not only have been shown that the model is well defined, analysis methods and approaches have been developed. These will also be applied to the extensions of the Tellinen model in the coming chapter.

► In Section 3.3, Tellinen's model is examined in terms of its integrability into the benchmark problem. It is shown that a direct integration of Tellinen's model is not reasonable in relation to the numerical background. For this purpose, the underlying ODE (3.7) of the Tellinen model is replaced by numerical approximations. These are inserted into the PDE (2.13) of the benchmark problem. Two different approaches are been discussed.

These approaches are approximating the ODE (3.7) starting from the current state (h_0, b_0) and allow the computation of the next step. In particular, the embedding of the directional dependence becomes easier with these approaches. But there are also disadvantages, especially with respect to the numerical robustness of the resulting PDE system.

However, the investigations can not be continued in isolation from the rest. This issue is addressed again in Chapter 5 and both approaches are attempted to be implemented.

4 Modifications and Extensions of Tellinen's Scalar Hysteresis Model

Tellinen's scalar hysteresis model has been introduced and analyzed in Chapter 3. This model is consistent and applicable. But it is temperature independent and so far the temperature T was assumed to be constant.

In Chapter 2, the influence of temperature was addressed briefly. Here, the material-specific Curie temperature will take an important role. Heating a ferromagnetic material to this temperature even once, completely demagnetizes it. But even before that, heat can significantly reduce the magnetization.

First, it is motivated that temperature plays an important role in applications. The current political and environmental focus on electrified vehicles is an illustrative example. An electric motor in an electrified vehicle is considered. It does not matter if it is a car, truck, train or airplane. One requirement for such vehicles is usability within a wide temperature spectrum. After all, the function must be ensured both at night in winter months and in the blazing midday sun in high summer.

But even in various situations of application, such a motor must remain within its allowed parameters. One example is the strong acceleration of a vehicle from standstill. At standstill and very slow speeds, cooling methods such as external airflow or fans driven by the motor itself may not be sufficient. However, especially with a desired strong acceleration, one wants to exert as much force as possible through the motor and one uses an accordingly high current and thus also generates corresponding losses. An even more extreme example is the blocking of an electric motor in case of overload. Depending on the design, this is comparable to an electrical short circuit and can mean the destruction of the motor with accompanying risk of fire. This is for example a reason why the stepper motor from Section 2.4 is current controlled and not voltage controlled.

For product development, but also to ensure operational safety, studies of heat generation in various application scenarios and environmental conditions are therefore necessary. For electric motors, for example, there are standards[1] that classify whether these motors are approved for continuous operation or only specific partial operation.

Now, after that it have been motivated that temperature can be significant in applications, the consequences on numerical simulations are explained. It always remains a question which effects and accuracy one wants to include in a simulation.

---

[1] international IEC 60034-1, european EN 60034-1

Using the example of temperature and losses, a brief outlook is given and then the central questions for this chapter are developed. If one allows a temperature change within the simulation, one faces a whole new set of phenomena and challenges. Materials change their density and their spatial expansion, in extreme cases even their aggregate state. Non-uniform heating causes stresses in solid materials or flows in liquid and gaseous materials. Temperature differences create a heat flow and heat exchange takes place between different materials.

Furthermore, numerical difficulties may arise if the effects act on different time scales. For example, the control of electric currents by pulse width modulation may be in the range of 10kHz, the motor rotates 50 times per second and the temperature changes rather in the range of several seconds.

These examples represent only a small sample of the consequences. One can roughly summarize that with the consideration of the temperature and losses, one ends very easily with a multi physical and multi scale simulation.

With respect to this dissertation, it is restricted to the influence of temperature on ferromagnetic materials. The central questions are:

▶ Where do losses occur, i.e., where does it get warmer?

To answer this question, a hysteresis loss model is presented that is – not exclusively but optimized – to be combined with Tellinen's model in Section 4.1. The model is based on the enclosed area of a simple closed hysteresis loop. In Section 3.2 conditions have already been worked out, such that in a stable state a suitable simple closed hysteresis loop always arises. In a second step, the loss model is extended by an approximation on nearly closed curves.

▶ How does the magnetic field react to a change of the temperature?

A proposal to answer this question is given in Section 4.2. Tellinen's original model defines an ODE that describe the change of b in relation to h. The thermal extension additionally defines another ODE to describe the change of b w.r.t. temperature T. Both ODEs are constructed similarly but still have differences. The new ODE is examined using similar approaches as in Chapter 3. It turns out that the model is mathematically well-defined and converges to a stable state for certain excitations in a well-behaved manner similar to the original Tellinen model.

4.1. Loss Model

For many of the known hysteresis models there already exist loss models (examples: [15, 23, 26]). An overview and comparison of different approaches is given in [33, 44].

In [54], Tellinen presented an approach for calculating losses. Within this approach the losses are splitted up into hysteresis and eddy-current losses. It is also possible to select excess losses or other approaches as separate sources of losses [18, 33]. In the scope of this thesis, focus lies solely on the hysteresis losses.

This section is based on [38, 39, 54]. However, a closer look at Tellinen's model is taken, especially under the aspect of integration into a simulation. Thus, a model and an algorithm will be developed, which approximates the hysteresis losses based on the enclosed area.

Motivation and Idea

A minimalistic motivation for the approach was given by Albert Einstein:

> "Energy loss during a hysteresis cycle is represented by the area enclosed by the loop. The energy is converted to heat." [4]

This idea is taken and the enclosed area is used to determine the hysteresis losses. This approach was also used by Tellinen [54]. However, several other sources [18, 21] refer to this approach.

In Section 3.2 it was already examined that Tellinen's model tends to closed or stable loops. The goal is to calculate this enclosed area without knowing a-priorily the total loop. As mentioned in Remarks 3.5 and 2.16, it should be prevented that the whole history must be stored. Instead only the current state is to be saved. The hysteresis model is applied backwards, such that the return path is predicted.

Using the SI unit system, h is in the unit of A/m and b in the unit of T. The enclosed area in the bh-plane is in the unit of $\mathrm{J/m^3}$. The specific volumetric heat capacity is material dependent and has the unit of $\mathrm{J/(K\,m^3)}$. Thus, the enclosed area can be converted directly into a temperature difference. However, it is also possible to use the enclosed area as a source term within a heat simulation.

First, the loss model is presented for the steady-state, i.e., the hysteresis loop is closed. Second, this condition is relaxed and also nearly closed curves are feasible.

Care is taken that the scope of the loss model fits to the approaches of Tellinen's model. This refers on the one hand to the mathematical complexity and computational effort at runtime. The loss model should be well understandable, easy to implement and fast to calculate. Furthermore, as few new prerequisites and input data as possible should be required. On the other hand, high accuracy or applicability on complex waveforms (compare to [33]) is not demanded. A phenomenological justification of the approach is sufficient for the purpose of this dissertation.

4.1.1. Definitions for the Steady-state Case

Basically the same basic conditions apply as described in Section 3.2. These are only briefly summarized here. A simple periodic excitation in h is assumed. There exists a unique steady-state as stated in Remark 3.60. This is defined by the turning points $(h_0, b_0), (h_1, b_1) \in I$ with $h_0 < h_1$ and paths p^+ and p^-. h is increased from

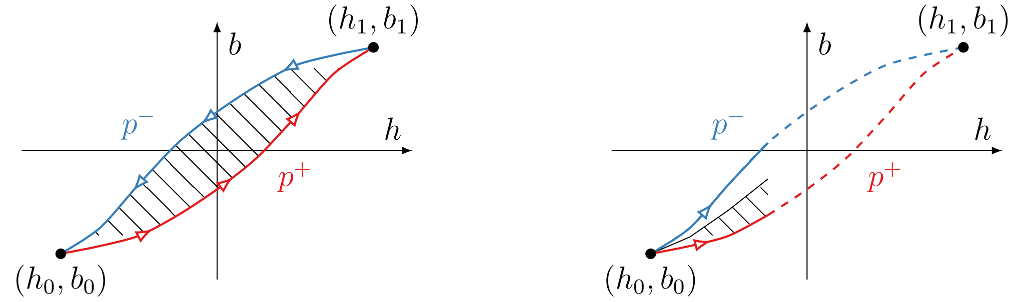

(a) A general overview of the steady-state and the defining entities.

(b) Approach for evaluating the enclosed area at intermediate steps.

Figure 4.1.: Idea of the loss model. Comparable with figures from [38, 39].

h_0 to h_1. The paths p^+ and p^- form a closed hysteresis loop with $p^+(h) \leq p^-(h)$ for all $h \in [h_0, h_1]$.

Only half a cycle is considered (h from h_0 to h_1). A graphical illustration is given in Figure 4.1(a). Without loss of generality only this case is discussed here. The situation for decreasing values of h is to deduce analogously by symmetry arguments. Whole or several cycles can then be performed one after the other and summed up.

There are no further requirements for the Tellinen model and its input parameter, i.e., this loss model fits without any restrictions.

At this point h is chosen as the independent variable and $b = b(h)$ as the dependent one. This choice will later have an influence on the selected intermediate steps. However, the overall result remains the same. An investigation follows in Section 4.1.4.

The enclosed area A can be expressed mathematically by the integral

$$A = \oint b \,\mathrm{d}h \,. \tag{4.1}$$

However, the area – not only for a complete loop, but also for any intermediate points – shall be available. The function $A^+(h)$ describes a partial area, which is created when it is started from h_0 and let the magnetic field increase to the value h. And analogously A^- for a decrease from h_1 to h. One possibility to define such $A^\pm(h)$ for $h \in [h_0, h_1]$ is

$$A^+(h) = \frac{1}{2}\int_{h_0}^{h} p^-(h) - p^+(h) \,\mathrm{d}h \geq 0 \,, \quad A^-(h) = \frac{1}{2}\int_{h_1}^{h} p^+(h) - p^-(h) \,\mathrm{d}h \geq 0 \,. \tag{4.2}$$

This allows the "so far" enclosed area to be specified proportionally to each intermediate step, as shown in Figure 4.1(b). The total area can be easily calculated by $A = A^+(h_1) + A^-(h_0) \geq 0$.

Remark 4.1. For a better understanding it should be mentioned at this point that this is especially useful later in conjunction with a heat simulation. This intermediate evaluation allows one to transfer the loss information to the heat simulation at any

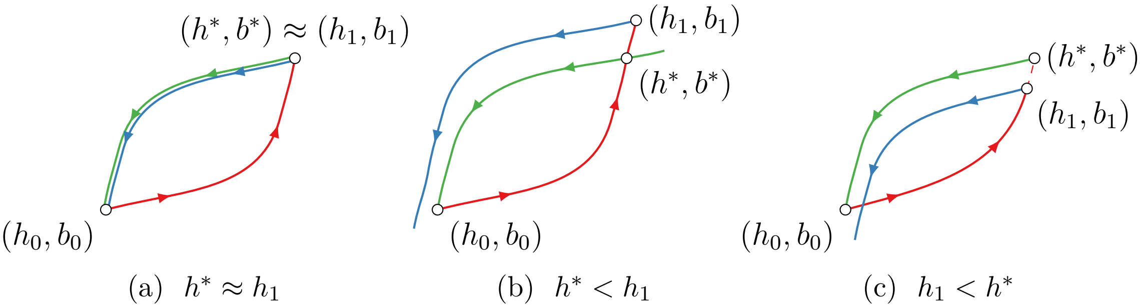

Figure 4.2.: (h_0, b_0) as starting point. (h_1, b_1) as actual turning point. (h^*, b^*) as intersection of p^+ and b_{rev}. Shown are the normal path p^+ in red, the actual return path p^- in blue and the predicted reverse path b_{rev} in green.

time. It is not necessary to pay attention, if the current state (h, b) is a turning point or if a complete loop was processed.

Remark 4.2. By construction A, A^+ and A^- are not negative. This will be a firm condition in the following. In the context of this thesis, possible negative oriented areas are not considered.

4.1.2. Extension to the Nearly Steady-State

As already examined in Section 3.2, there is a convergent behavior towards the stable state. But this means also in reverse, that there is a certain transient phase until the stable state is reached. In this section, this nearly steady-state will be analyzed. The possible errors and deviations are examined and shown. Also special features of the numerical implementation are worked out in detail.

As in the previous section, it is assumed that start is at a turning point (h_0, b_0) with a path $p^+ = p^+(h)$. Then, this path is followed to the second turning point (h_1, b_1). There the path $p^- = p^-(h)$ leads back to h_0. If there is no steady-state, then $p^-(h_0) \neq b_0$ holds.

Starting in (h_0, b_0) the predicted return path b_{rev} is calculated. The path b_{rev} is based on μ^-_{diff} w.r.t. the condition $b_{\text{rev}}(h_0) = b_0$. In steady-state as described in Section 4.1.1, b_{rev} and p^- are identical. This no longer holds in the nearly steady-state.

A visual overview is given in Figure 4.2. There are two possible situations. The predicted return path b_{rev} intersects the path p^+ before p^+ joins p^-. Or b_{rev} does not intersect with p^+ at all. In both cases, the area between p^+ and p^- is approximated by the area between p^+ and b_{rev}.

How to integrate this approach into a simulation with discretized values is described in the following Section 4.1.3. At this point, it is examined if the loss model is well-defined. Two important properties are investigated. First, how to define b_{rev} in a generally valid way. Second, under which conditions there is an enclosed, positively oriented area between p^+ and b_{rev}.

Definition of the Predicted Return Path b_{rev}

The path b_{rev} shall be based on p^- w.r.t. $(h_0, b_0) \in I$. But in contrast to p^-, $\big(h, b_{\text{rev}}(h)\big) \in I$ should hold for all h of interest. As shown in Figure 3.10, the path p^- is not completely contained in I. Remark 3.26 does not apply, because p^- is based on μ^-_{diff} and is adopted under the aspect of increasing h values. The path p^- is used in reverse. This leads to the result that there possibly exists $\hat{h} \in \mathbb{R}$, such that

$$\big(h, p^-(h)\big) \notin I \quad \text{for all } h > \hat{h} \text{ and } p^-(\hat{h}) = B^+_{\text{sat}}(\hat{h}) \tag{4.3}$$

holds. The idea for b_{rev} is now simple. It will use p^- until it leaves the valid domain I. Then b_{rev} is restricted to I. Hence the definition of $b_{\text{rev}} : \mathbb{R} \to \mathbb{R}$ is

$$b_{\text{rev}}(h) = \begin{cases} p^-(h) & \text{, if } h \leq \hat{h} \\ B^+_{\text{sat}}(h) & \text{, if } h > \hat{h} \end{cases} . \tag{4.4}$$

b_{rev} is continuous by construction and it holds $\big(h, b_{\text{rev}}(h)\big) \in I$ for all $h \in \mathbb{R}$. Thus, Tellinen's model can always be applied onto the state $\big(h, b_{\text{rev}}(h)\big)$ and b_{rev} is therefore well defined.

Restriction to Positive Oriented Areas

First of all, it is examined, when a positive oriented surface can be obtained at all. The geometrical arrangement of the paths p^+ and p^- was already analyzed in Section 3.2. As stated in Remark 3.49 there exists at most a second intersection of p^+ and p^-. Only if $(h_0, b_0) \in I^<$ applies, a positive oriented surface is obtained at all. And a second intersection of p^+ and b_{rev} at some $(h^*, b^*) \in I^>$ with $h_0 < h^*$ is guaranteed.

For $(h_0, b_0) \notin I^<$, the loss model cannot be applied. But the convergence towards the stable loop guarantees, that after a finite number of loops, the turning point (h_0, b_0) must be in $I^<$. The existence and uniqueness of the stable loop was already shown in Lemma 3.57.

Remark 4.3. It is concluded that the loss model is applicable after a transient phase. By the condition of $(h_0, b_0) \in I^<$, it can be easily checked, if the loss model can be started in (h_0, b_0).

The further consideration puts the focus on the other turning point. Let $(h^*, b^*) \in I$ denote the other intersection of p^+ and b_{rev} and let $(h_1, b_1) \in I$ the actual turning point of p^+. As shown in Figures 4.2(b) and 4.2(c), two different types of errors are possible. It can either hold $h^* < h_1$ or $h^* > h_1$.

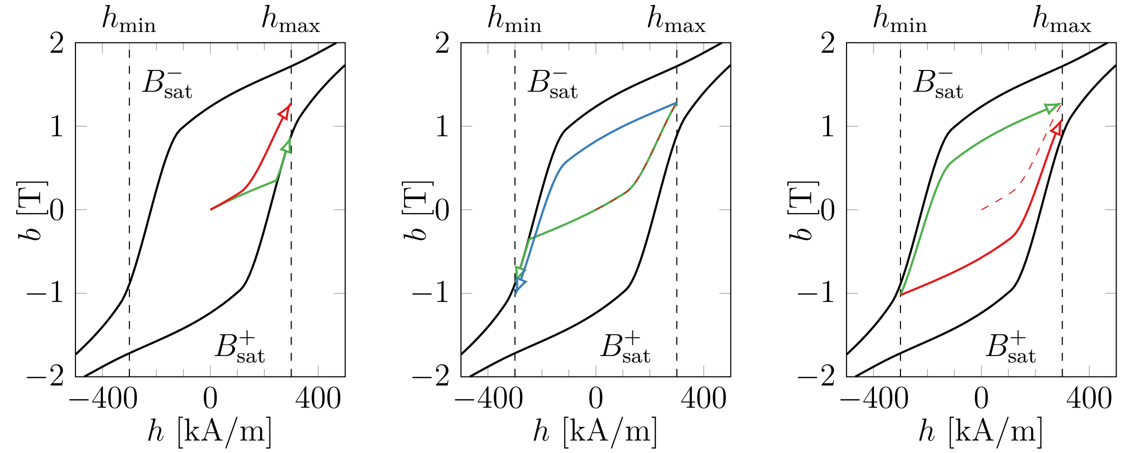

(a) First half cycle starting from $(0,0) \in I^{=}$. The loss model can not be applied, because of the geometrical order of p^{+} and b_{rev}. The path b_{rev} is restricted to I.

(b) The second half of the first cycle. The loop is clearly not closed properly, but the loss model can already be applied on most part of the intervall $[h_{\min}, h_{\max}]$.

(c) First half of the second cycle. The loop is approximately closed and the loss model can be applied on the whole interval $[h_{\min}, h_{\max}]$.

Figure 4.3.: Starting from a demagnetized state, the material is excited until $h_{\max} = 300\,\mathrm{kA/m}$, then remagnetized down to $h_{\min} = -300\,\mathrm{kA/m}$ and back to $h_{\max}$. Paths based on μ_{diff}^{+} are in red, μ_{diff}^{-} in blue and the prediction b_{rev} in green.

For the case $h^{*} < h_1$, it holds $p^{+}(h) > b_{\mathrm{rev}}(h)$ for all $h > h^{*}$, i.e., for these h values the area between p^{+} and b_{rev} is negative oriented. According to Remark 4.2, the subdomain $(h^{*}, h_1]$ is therefore excluded.

For the case $h_1 < h^{*}$ the closed area is positive oriented and the loss model can be applied without restrictions.

Summarizing the above, the conclusion of Remark 4.2 is to ignore all subdomains with $b_{\mathrm{rev}}(h) < p^{+}(h)$. The steady-state approach (4.2) can be extended to

$$A^{+}(h) = \frac{1}{2}\int_{h_0}^{h} \max\Big(0, b_{\mathrm{rev}}(h) - p^{+}(h)\Big)\,\mathrm{d}h \geq 0\,, \tag{4.5a}$$

$$A^{-}(h) = \frac{1}{2}\int_{h_1}^{h} \min\Big(0, b_{\mathrm{rev}}(h) - p^{-}(h)\Big)\,\mathrm{d}h \geq 0\,. \tag{4.5b}$$

Example

An example that shows both of the above problems, is a virgin material, i.e., $(h_0, b_0) = (0,0) \in I^{=}$. This means in particular $(h_0, b_0) \notin I^{<}$ and thus one can directly determine that the model is not yet applicable. The material is the same as in Figure 3.19.

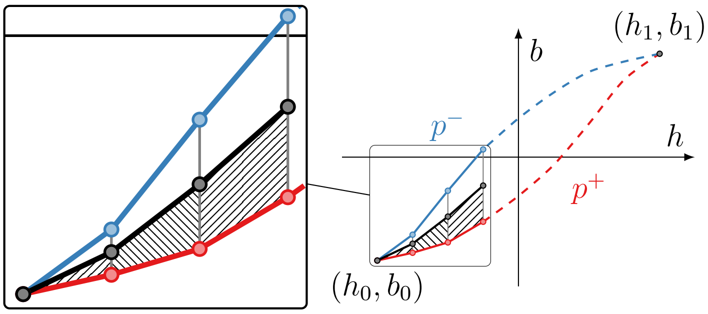

Figure 4.4.: Visualization of the loss model for the case that b is assumed as the independent variable. Comparable with figures from [38, 39].

The magnetic field strength h is increased to $h_{\max} = 300\,\mathrm{kA/m}$. The resulting paths for p^+ and b_{rev} are shown in Figure 4.3(a). The restriction of b_{rev} to I and the wrong geometrical order of p^+ and b_{rev} are clearly visible.

Next, h is decreased to $h_{\min} = -300\,\mathrm{kA/m}$. The paths p^- and b_{rev} are calculated as stated above and shown in Figure 4.3(b). The area enclosed between p^- and b_{rev} is only a very rough approximation. But the loss model can already be applied on most of the interval $[h_{\min}, h_{\max}]$.

Increasing h back to $h_{\max} = 300\,\mathrm{kA/m}$, yields already an almost satisfactory approximation of a closed loop, as shown in Figure 4.3(c). The loss model can be applied on the whole interval $[h_{\min}, h_{\max}]$.

In Figure 3.19 the convergence speed was already examined and after only a few cycles, the curves were already almost stable. The loss model is applicable after only half a cycle and after a small number of cycles it yields good approximation values.

4.1.3. Embedding Into a Simulation – a Discretized Version

Now, it is no longer regarded from a continuous observation, but from a discretized one. It is assumed that from a magnetic field simulation the states $(h^{j-1}, b^{j-1}), (h^j, b^j) \in I$ are known. These corresponds to time steps t_{j-1}, t_j accordingly. The prediction of the reverse path is introduced by the states $(h^{j-1}, b^{j-1}_{\mathrm{rev}}), (h^j, b^j_{\mathrm{rev}}) \in I$.

Now, after another step of the magnetic field simulation, a new state $(h^{j+1}, b^{j+1}) \in I$ was calculated. Firstly, the goal is to analyze the progress of the simulation to detect if there is a turning point at time t_j. This is easily checked by the condition $(h_j - h_{j-1}) \cdot (h_{j+1} - h_j) < 0$. If a turning point is detected, $b^j_{rev} = b^j$ is set. If not, nothing has to be modified.

Secondly, the new state of the reverse path $(h^{j+1}, b^{j+1}_{\mathrm{rev}})$ has to be calculated. But since the direction of change is known by h_j and h_{j+1}, it can be solved by any numerical solution methods for ODEs applied on (3.7). As a simple example the explicit Euler method can be used, i.e., as an update for b_{rev},

$$b_{\text{rev}}^{j+1} = b_{\text{rev}}^{j} + \mu_{\text{diff}}^{\pm} \cdot (h^{j+1} - h^{j}) \text{ with } \mu_{\text{diff}}^{\pm} = \begin{cases} \mu_{\text{diff}}^{+}\left(h^{j}, b_{\text{rev}}^{j}\right) & \text{, if } h^{j+1} > h^{j} \\ \mu_{\text{diff}}^{-}\left(h^{j}, b_{\text{rev}}^{j}\right) & \text{, if } h^{j+1} < h^{j} \end{cases} \tag{4.6}$$

would result.

At this point, however, one must note that it is not guaranteed that $(h^{j+1}, b_{\text{rev}}^{j+1}) \in I$ holds true. For more complex ODE solution approaches, the intermediate steps may already be outside of I. If this is the case, b_{rev}^{j+1} can be just restricted to the valid domain, by either setting $b_{\text{rev}}^{j+1} = B_{\text{sat}}^{+}(h^{j+1})$ or $b_{\text{rev}}^{j+1} = B_{\text{sat}}^{-}(h^{j+1})$, correspondingly. This ensures $(h^{j+1}, b_{\text{rev}}^{j+1}) \in I$ and has no effect on the last phase of the algorithm.

Thirdly, the newly enclosed area has to be computed. The points (h^{j}, b^{j}), (h^{j+1}, b^{j+1}), $(h^{j+1}, b_{\text{rev}}^{j+1})$ and $(h^{j}, b_{\text{rev}}^{j})$ form a trapezoid, as seen in Figure 4.4. The mathematical orientation of the area has to be taken into account. Furthermore, only positive oriented areas are of interest. This yields

$$A^{j+1} = \max\left(0, \left(h^{j+1} - h^{j}\right) \frac{(b_{\text{rev}}^{j} - b^{j}) + (b_{\text{rev}}^{j+1} - b^{j+1})}{2}\right). \tag{4.7}$$

Under the aspect of a multi rate approach – as it will be presented later in Section 5.6 – it shall be mentioned briefly that A^{j+1} is not necessarily further evaluated in this time step. But it can be easily stored by just summing up $A_{\text{sum}}^{j+1} = A_{\text{sum}}^{j} + A^{j+1}$. A_{sum} is reset to zero if an evaluation of the enclosed area was performed. Otherwise, it holds the summed area for all time step since the last evaluation.

4.1.4. Further Properties

At this point a few more properties and comparisons to Tellinen's hysteresis model shall be made.

Computational Performance and Memory Considerations

The loss model, in its discrete form in the previous section, is very modest in terms of needed memory. Only b_{rev}^{j+1} and A_{sum}^{j+1} are stored additionally. From the previous time steps only the values h^{j-1}, h^{j}, b^{j} are necessary. The loss model uses a little more memory than the pure hysteresis model. But overall, it is in the same order of magnitude for the memory usage.

In terms of computational complexity, the user has some degrees of freedom. Similar to the hysteresis model the user can choose the approach for solving the underlying ODE (3.7). It makes sense to use approximately the same complexity levels in both models.

Exchanging the Roles of h and b

Similar to Remark 3.10 the loss model allows an alternative version, if b is assumed as the independent variable and $h = h(b)$ as the dependent one.

The whole loss model could be alternatively defined w.r.t. some $h_{\mathrm{rev}} = h_{\mathrm{rev}}(b)$. The overall approach is the same, but the intermediate steps differ. The resulting trapezoids are vertical orientated, in contrast to Figure 4.4. Switching the independent variable would make the trapezoids horizontal orientated. This of course results in different values for the area at the intermediate values. The total area is calculated identically with both approaches in steady state.

Combination with Other Hysteresis Models

Basically, the loss model can be decoupled from Tellinen's model and used with other hysteresis models. Tellinen's model is just very well suited and can be easily combined together.

Also, with Tellinen's model it would be easy to use a higher quality interpolation method instead of a piece wise linear approach for b_{rev} and the resulting trapezoids. At the evaluation points $\mu^{\pm}_{\mathrm{diff}}$ provides the derivative.

If one want to combine the loss model with other hysteresis models, it must be possible to apply them backwards. It must be possible to embed the model in the magnetic field simulation and also predict the return path b_{rev}.

4.1.5. Interim Conclusion & Further Remarks

The presented loss model is based on the calculation of the enclosed area in the bh-plane. For simple closed loops the loss model describes the surface analytically correct. From a physical point of view this model is exact for simple closed loops. For this application the model offers mainly the advantage that the evaluation of the area can be done at any time and that the requirements in terms of memory and computing time are moderate.

However, a great advantage of the model is that it can already work in the nearly steady-state. The area between the actual paths p^{+} and p^{-} is approximated. In combination with the convergence property of Tellinen's model, a valid model for loss calculation is obtained after a transient phase.

The applicability for nearly steady-state will also become very important in the further course of this thesis. As already mentioned in Chapter 2 and shown later in Figure 4.5, the saturation curves $B^{\pm}_{\mathrm{sat}}$ are temperature dependent, i.e., a change in temperature disturbs the steady-state.

How exactly the model defines a materials reaction to a temperature change and how a valid state can be ensured is described in the following section.

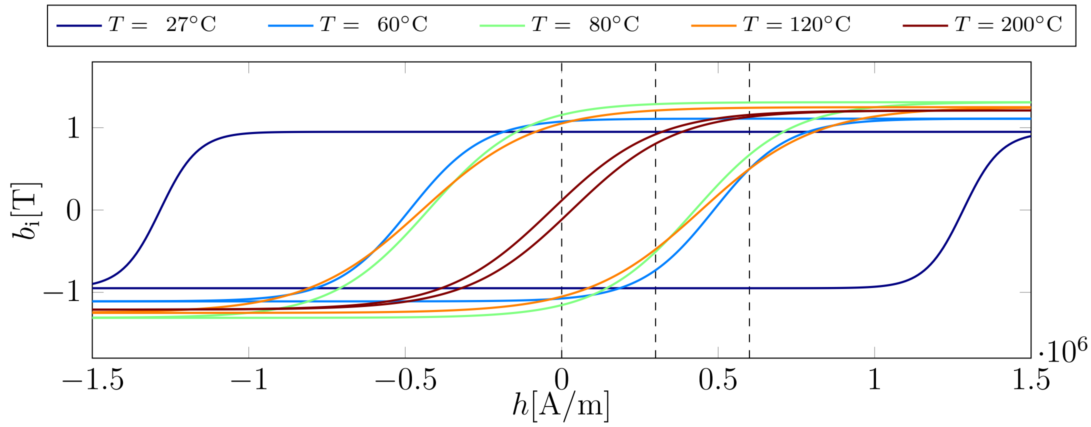

Figure 4.5.: Example material roughly based on a measurement of NdFeB [27]. Comparable figures can be found in [37, 39].

To summarize this section, the loss model in the discrete form consists of three major parts. First, an algorithm for detecting turning points and modifying b_{rev}, if necessary. Second, an approach for imitating the change in h, b and apply them onto the predicted return path b_{rev}. Third, a calculation of the enclosed area.

Thus, it is possible to specify the total power loss scaled with the volume in the unit $\mathrm{J/m^3}$. This allows further calculations and forms the basis for a simulation with a non-constant temperature.

4.2. Thermal Extension of Tellinen's Model

Parts of the following considerations have already been published by the author of this dissertation in [37, 39].

Until now, a constant temperature was assumed, so that the saturation curves $B_{\text{sat}}^{\pm}$ were independent of temperature. However, as can be seen in Figure 4.5, there may be a temperature dependence. In the example material presented, one can see clear differences between roughly room temperature 27 °C, the range 60 °C to 120 °C and 200 °C. The tendency is that with increasing temperature the saturation curves $B_{\text{sat}}^{\pm}$ become narrower and are equal in the limit to the Curie temperature.

Especially for Tellinen's model from Chapter 3, the problem arises that a previously valid state (h, b) is no longer necessarily still valid after a temperature change. So keeping the current state (h, b) constant while the temperature T changes, may lead to invalid states. The objective is therefore to define rules so that a valid state remains valid even during a change in temperature. Here, the thermal model should be understood as an extension of the original model.

To ensure that the thermal extension harmonizes as well as possible with the original model, similar approaches are used as far as possible. But as can be seen in Figure 4.6, there are differences for different h values. For example, the symmetry is broken.

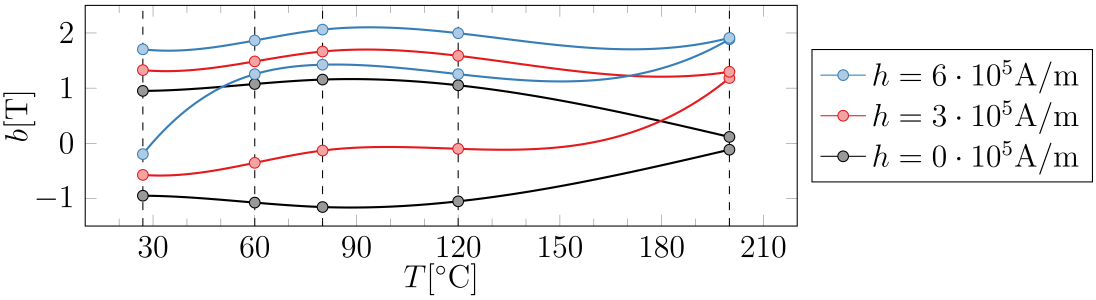

Figure 4.6.: Example curves $B^{\pm}_{\mathrm{sat}}$ for constant h and varying T based on Figure 4.5. Comparable figures can be found in [37, 39].

First, the thermal model is physically motivated in the following Section 4.2.1. The detailed mathematical definition is given in Section 4.2.2. Sections 4.2.3 and 4.2.4 contain the mathematical investigations of the thermal model similar to Section 3.2. In summary, it is discussed in Section 4.2.5 whether the model is consistent with the physical motivation.

Even if the temperature-dependent saturation curves $B^{\pm}_{\mathrm{sat}}$ are roughly based on real measured data, unfortunately dedicated measurement results – to be able to confirm the thermal model experimentally – are not available. Mathematical consideration must suffice in the scope of this work, but the model can be checked for obvious contradictions to the physics.

4.2.1. Physical Motivation

Before defining the thermal model mathematically in the following Section 4.2.2, it is motivated – similarly to Section 3.1.2 – based on the physical facts presented in Chapter 2, with which approaches and expectations the thermal model is addressed.

However, it must be briefly state up front that the thermal model will be comparable in structure to the original Tellinen model. Changes of b caused by a change of temperature T are described by a differential equation. The approach defines the values on the saturation curves $B^{\pm}_{\mathrm{sat}}$ and interpolates the intermediate values. It is distinguished whether the temperature rises ($\Delta T > 0$) or falls ($\Delta T < 0$).

Increasing Temperature The basic assumption for the model is that an increase in temperature represents an increase in energy in the system. As shown in Figure 2.6, increased energy allows the use of more favorable states w.r.t. orientation of Bloch walls and Weiß domains. This is interpreted to mean that increasing the temperature causes the White domains and Bloch walls to align much more easily. However, easier alignment of these also means less resistance to a change in the current state.

This view fits the limit of the Curie temperature T_{C}. Once this temperature is reached, the two saturation curves $B^{\pm}_{\mathrm{sat}}$ lie on top of each other. The system contains such a high amount of energy that always the most favorable states can be reached and the effect of hysteresis is nullified.

So for the case $\Delta T > 0$ it can be summarized that – motivated by physics – an increase of the willingness to change the current state can be observed and the merging of the curves $B^{\pm}_{\text{sat}}$ is an important modeling aspect.

At no time may the current working point (h, b) be outside the curves $B^{\pm}_{\text{sat}}$. It has already been proven in Section 3.2 that ODE (3.7) ensures that the valid domain I is not left. There, on the saturation curves $B^{\pm}_{\text{sat}}$, the value μ_0 is assigned one time, and the value $\frac{\mathrm{d}B^{\pm}_{\text{sat}}}{\mathrm{d}h}$ another time. No physically meaningful reason why a temperature change ΔT should favor one of the magnetic directions $\Delta h \lessgtr 0$ or rather $\Delta b \lessgtr 0$ can be stated. Thus, the influence of the upper saturation curve B^{-}_{sat} should be equal to that of the lower one B^{+}_{sat}.

The case $\Delta T > 0$ will be modeled such that the values on the saturation curves $B^{\pm}_{\text{sat}}$ are given by $\frac{\partial B^{\pm}_{\text{sat}}}{\partial T}$. If the current state w.r.t. h, b, T is maximally saturated, i.e., it lies on B^{+}_{sat} or B^{-}_{sat}, then the maximum saturation is maintained when the temperature T increases. Values between these extremes are defined by an interpolation. Graphically, this means that the model follows the measured saturation curves $B^{\pm}_{\text{sat}}$ as closely as possible.

Decreasing Temperature When the temperature T is reduced, it is again argued about the energy in the system. If the energy is decreased, the white domains and Bloch walls have less possibilities to change their orientation and position. They are more or less frozen in their current state. Using only this reasoning, one would define the approach $\frac{\partial b}{\partial T} = 0$ for $\Delta T < 0$.

However, this simple approach leads to the fact that the valid area I can be left. More precisely $B^{\pm}_{\text{sat}}$ can change so much if the temperature changes, such that a formerly valid state (h, b) is no longer valid. Therefore, the chosen approach yields that the model tries to keep b as constant as possible and that b is only changed enough such that the saturation curves $B^{\pm}_{\text{sat}}$ are respected as boundaries.

Benchmarks and Objectives The goal of the thermal extension is to define rules such that the extended model can handle changes in the saturation curves $B^{\pm}_{\text{sat}}$, regardless of the signs of $\frac{\partial B^{\pm}_{\text{sat}}}{\partial T}$. That these are taken into account as boundaries is the first benchmark. The allowed states I are extended by a temperature component and it will be proven mathematically that the model cannot leave I.

If any valid path lies on or between the curves, the limit against the Curie temperature is automatically covered. Therefore, this will not be investigated separately.

The thermal model is designed as an extension of the original model. Thus, if the curves do not change due to temperature, i.e., $\frac{\partial B^{\pm}_{\text{sat}}}{\partial T} = 0$, the original model should result. This is the second benchmark.

From a physical point of view, the process of demagnetization is important. A magnetized material should not magnetize more strongly by itself without some sort of excitation (temperature T or h field), but demagnetize if at all. The special case $h = 0$ will be examined as the third benchmark in more detail.

Unfortunately, corresponding measurements are not available, so that the thermal model cannot be verified experimentally. Nevertheless, it is checked for basic physical sense via the above benchmark problems.

Now follows first the mathematical definition of the thermal model and then the investigation. Then in Section 4.2.5, it will be discussed whether the thermal model behaves physically reasonable w.r.t. the above benchmarks.

4.2.2. Definition, Prerequisites and Input Parameters

The thermal model shall be very close to the original model. There shall be only B^{+}_{sat} as input parameters. But instead of a single curve ($\mathbb{R} \to \mathbb{R}$), it is now assumed as a surface ($\mathbb{R}^2 \to \mathbb{R}$). The previous approaches should be able to be used further on, only one new dimension, the temperature T, will be added. The partial derivative w.r.t. h shall fulfill the previous conditions for each state, i.e.,

$$\frac{\partial}{\partial h} B^{+}_{\text{sat}}(h,T) \geq \mu_0 \,, \qquad \lim_{|h| \to \infty} \frac{\partial}{\partial h} B^{+}_{\text{sat}}(h,T) = \mu_0 \,. \tag{4.8}$$

Furthermore, the vertical order between B^{+}_{sat} and B^{-}_{sat} shall be ensured. Also the limit behaviour w.r.t. h remains as before, i.e.,

$$\begin{aligned} B^{+}_{\text{sat}}(h,T) < B^{-}_{\text{sat}}(h,T) &:= -\, B^{+}_{\text{sat}}(-h,T), \\ \lim_{|h| \to \infty} \left(B^{-}_{\text{sat}}(h,T) - B^{+}_{\text{sat}}(h,T) \right) &= 0. \end{aligned} \tag{4.9}$$

The observation of the temperature is limited to an interval $[T_{\min}, T_{\max}]$. This results in the set of all valid states of

$$I_{\mathrm{T}} = \left\{ (h,b,T) \in \mathbb{R}^2 \times [T_{\min}, T_{\max}] \,\middle|\, B^{+}_{\text{sat}}(h,T) \leq b \leq B^{-}_{\text{sat}}(h,T) \right\}. \tag{4.10}$$

The relative vertical position λ within the limiting saturation surface is still needed and given by

$$\lambda = \lambda(h,b,T) = \frac{B^{-}_{\text{sat}}(h,T) - b}{B^{-}_{\text{sat}}(h,T) - B^{+}_{\text{sat}}(h,T)} \in [0,1] \,. \tag{4.11}$$

Remark 4.4. If the temperature is kept constant, the original model is obtained. The definition is taken over and only the new dimension of the temperature T is added. That means all previous properties from Chapter 3 are still valid, if you assume the temperature T to be constant and restricts the consideration to the direction h.

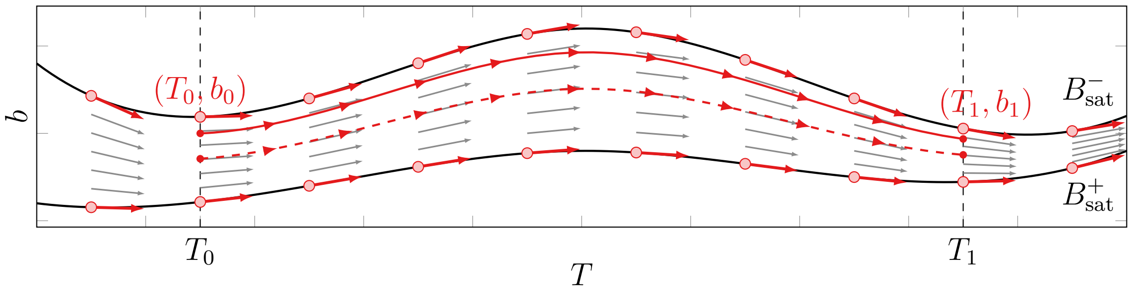

(a) Increasing temperature

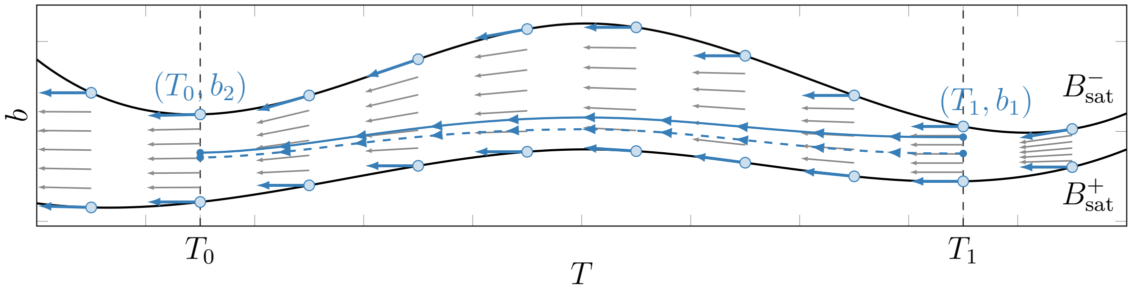

(b) Decreasing temperature

Figure 4.7.: Example for the resulting vector field of the thermal model. Note that the starting point (T_0, b_0) is not necessarily identical with the end point (T_0, b_2). Comparable figures can be found in [37, 39].

Remark 4.5. Similar approaches as in Chapter 3 are used. On the one hand, this refers to the approach how the quantities T and b are coupled. b is chosen as the dependent variable and the main part of the model consists of the partial derivative $\frac{\partial b}{\partial T}$. This is defined direction-dependent ($\Delta T > 0$ or $\Delta T < 0$) as before. On the other hand it is attempted to use similar examination methods as in Chapter 3. This should give an impression how the model reacts to temperature changes.

Definition 4.6: The core of this thermal model is the definition of the directional partial derivatives $\frac{\partial b}{\partial T}$, given by

$$\frac{\partial b}{\partial T} = \lambda \frac{\partial}{\partial T} B^+_{\mathrm{sat}}(h,T) + (1-\lambda)\frac{\partial}{\partial T} B^-_{\mathrm{sat}}(h,T) \text{ for } \Delta T > 0 \tag{4.12a}$$

and

$$\frac{\partial b}{\partial T} = \lambda \min\left(\tfrac{\partial}{\partial T} B^+_{\mathrm{sat}}(h,T), 0\right) + (1-\lambda)\max\left(\tfrac{\partial}{\partial T} B^-_{\mathrm{sat}}(h,T), 0\right) \text{ for } \Delta T < 0\,. \tag{4.12b}$$

4.2.3. Basic Properties

Like the original Tellinen model in Chapter 3, the thermal extension yields a vector field. An example is given in Figure 4.7. Also again the derivatives of the limiting saturation curves $B^{\pm}_{\mathrm{sat}}$ are significantly important for the behavior inside of I_{T}. The following considerations refer to an investigation with constant values for h.

The thermal model has no global symmetry. In Figure 4.6 the saturation curves $B_{\text{sat}}^{\pm}$ are shown for different values of h for an example material. The case of $h = 0$ yields symmetric properties and will be examined in Section 4.2.4. Furthermore it can be seen that the derivative $\frac{\partial B_{\text{sat}}^{\pm}}{\partial T}$ is generally not bounded, in contrast to $\frac{\partial B_{\text{sat}}^{\pm}}{\partial h}$.

Remark 4.7. In contrast to the saturation curves $B_{\text{sat}}^{\pm}(h)$ presented in Chapter 3, the boundaries $B_{\text{sat}}^{\pm}(h, T)|_{h=\text{const}}$ are not monotone in T, as seen in Figure 4.6.

Remark 4.8. The consideration for the temperature T is limited to an interval $[T_{\min}, T_{\max}]$ with $T_{\min} < T_{\max}$.

These altered basic assumptions – when examined $B_{\text{sat}}^{\pm}$ in the direction of T instead of h – must of course be taken into account in further investigations.

The computational effort and memory requirements are similar to the original model. The calculation of λ is equivalent and besides basic mathematical operations only evaluations of $B_{\text{sat}}^{\pm}$ at the current working point $(h_0, b_0, T_0) \in I_{\text{T}}$ are needed.

4.2.4. Definition of Paths and Convergence Behavior

In this section investigations similar to Section 3.2 shall be performed. For this purpose again paths $p^{\pm}$ are defined as solutions to initial value problems and their course is studied. Thereby the well-defined nature of the thermal model shall be shown. This means especially that $B_{\text{sat}}^{\pm}$ are respected as boundaries of I_{T}. Again, a excitation in the form of sweeping will be investigated. The existence and uniqueness of stable curves and the convergence behaviour to them will be considered.

Subdivision of the Interval $[T_{\min}, T_{\max}]$

In preparation for the mathematical investigation, (4.12b) is first examined in more detail. The definition there is as compact as possible. For a illustrative consideration an alternative formulation is useful.

Remark 4.9. Another possible formulation of (4.12b) is given by

$$\frac{\partial b}{\partial T} = \begin{cases} \lambda \dfrac{\partial}{\partial T} B_{\text{sat}}^{+} + (1-\lambda) \dfrac{\partial}{\partial T} B_{\text{sat}}^{-} & \text{if } \frac{\partial}{\partial T} B_{\text{sat}}^{+} \leq 0 \text{ and } \frac{\partial}{\partial T} B_{\text{sat}}^{-} \geq 0 \\ (1-\lambda) \dfrac{\partial}{\partial T} B_{\text{sat}}^{-} & \text{if } \frac{\partial}{\partial T} B_{\text{sat}}^{+} > 0 \text{ and } \frac{\partial}{\partial T} B_{\text{sat}}^{-} \geq 0 \\ \lambda \dfrac{\partial}{\partial T} B_{\text{sat}}^{+} & \text{if } \frac{\partial}{\partial T} B_{\text{sat}}^{+} \leq 0 \text{ and } \frac{\partial}{\partial T} B_{\text{sat}}^{-} < 0 \\ 0 & \text{if } \frac{\partial}{\partial T} B_{\text{sat}}^{+} > 0 \text{ and } \frac{\partial}{\partial T} B_{\text{sat}}^{-} < 0 \end{cases} . \tag{4.13}$$

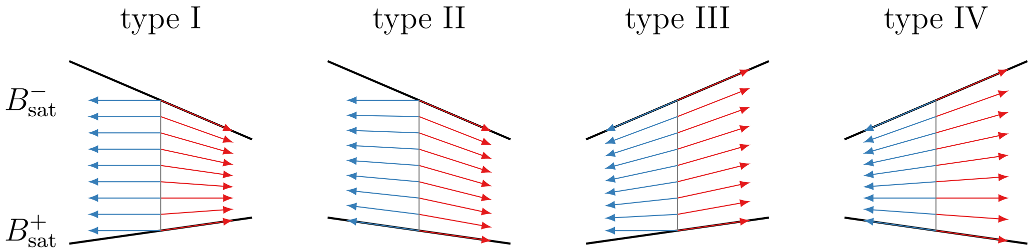

Figure 4.8.: Shown is the behavior of the thermal model for the four possible cases. Boundaries $B^\pm_{\text{sat}}$ in black. The resulting values of $\frac{\mathrm{d}}{\mathrm{d}T}p^+$ in red and $\frac{\mathrm{d}}{\mathrm{d}T}p^-$ in blue for the different types defined in Definition 4.10.

Definition 4.10: Given non-empty interval $A \subseteq [T_{\min}, T_{\max}]$. A is called of type I, II, III or IV if $\frac{\partial B^\pm_{\text{sat}}}{\partial T}$ fulfill the assigned inequalities given by (4.14) for all $T \in A$.

$$\begin{array}{cc|cc} & & \multicolumn{2}{c}{\frac{\partial}{\partial T}B^-_{\text{sat}}} \\ & & <0 & \geq 0 \\ \hline \frac{\partial}{\partial T}B^+_{\text{sat}} & >0 & \text{I} & \text{III} \\ & \leq 0 & \text{II} & \text{IV} \end{array} \tag{4.14}$$

These types cover all possible configurations and are visualized in Figure 4.8.

Now that the basic definition of the four cases has been given, it is shown that the interval $[T_{\min}, T_{\max}]$ can always be divided into corresponding sub-intervals of the four types.

Lemma 4.11: Given $h = h_0 \in \mathbb{R}$. It exists T_k $(k = 0, \ldots, n)$ with $T_{\min} = T_0 < T_1 < \ldots < T_n = T_{\max}$ such that the intervals (T_i, T_{i+1}) $(i = 0, \ldots, n-1)$ are of type I, II, III or IV.

Proof. The functions $B^\pm_{\text{sat}}(h,T)|_{h=\text{const}}$ are differentiable w.r.t. T by assumption and therefore $\frac{\partial B^\pm_{\text{sat}}(h,T)}{\partial T}|_{h=h_0}$ are continuous.

If $\frac{\partial B^+_{\text{sat}}(h,T)}{\partial T}|_{h=h_0} > 0$ holds for some $T \in (T_{\min}, T_{\max})$, this property is also true for some open interval (T^+_i, T^+_{i+1}) with $T \in (T^+_i, T^+_{i+1})$. It is assumed that the intervals (T^+_i, T^+_{i+1}) are chosen with maximal width. Then $T^+_>$ with

$$T^+_> = \left\{ T \in (T_{\min}, T_{\max}) \;\middle|\; \frac{\partial B^+_{\text{sat}}(h,T)}{\partial T}|_{h=h_0} > 0 \right\} = \bigcup_{i=0,\ldots,n_i-1} (T^+_{2i}, T^+_{2i+1}) \tag{4.15}$$

can be represented by n_i distinct open intervals with $T_{\min} \leq T^+_0 < \ldots < T^+_{2n_i-1} \leq T_{\max}$. The same holds true for

$$T^-_< = \left\{ T \in (T_{\min}, T_{\max}) \;\middle|\; \frac{\partial B^-_{\text{sat}}(h,T)}{\partial T}|_{h=h_0} < 0 \right\} = \bigcup_{j=0,\ldots,n_j-1} (T^-_{2j}, T^-_{2j+1}) \,. \tag{4.16}$$

Now combining the lists T^+_i and T^-_j, appending $T_{\min}$ and $T_{\max}$, sort the entries and remove duplicate values results in the desired list of T_k. ☐

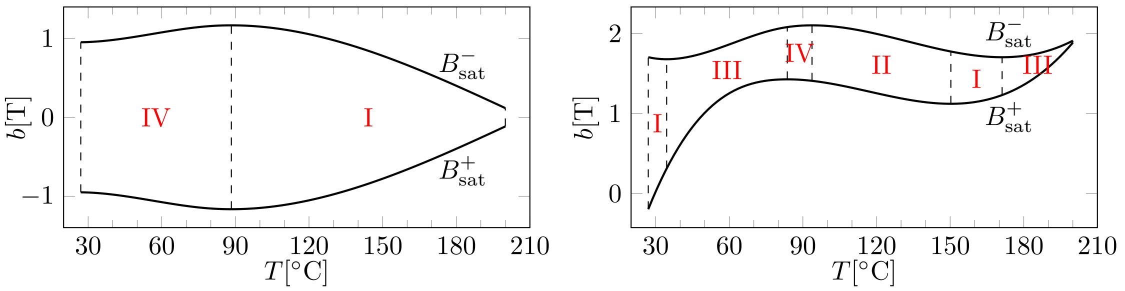

(a) $h = 0\,\mathrm{A/m}$.

(b) $h = 6 \cdot 10^5\,\mathrm{A/m}$.

Figure 4.9.: Two of the curves from Figure 4.6 are shown and marked according to their type w.r.t. Definition 4.10.

Remark 4.12. An exemplary assignment of the individual types to given curves is shown in Figure 4.9. As seen in Figure 4.9(b), all types can occur for a single set of $B^{\pm}_{\text{sat}}$.

Definition of Paths $p^{\pm}$ as Solutions of an IVP

Motivated by (4.12a), (4.12b) and Definition 3.12, now the paths $p^{\pm}$ shall be defined in the scope of a constant value of h and w.r.t. T.

Definition 4.13: Let $(h_0, b_0, T_0) \in I_T$.

$p^+ = p^+(T) : [T_{\min}, T_{\max}] \subseteq \mathbb{R} \to \mathbb{R}$ is the solution of the initial value problem

$$\begin{aligned} \frac{\mathrm{d}p^+(T)}{\mathrm{d}T} = & \overbrace{\frac{B^-_{\text{sat}}(h_0,T) - p^+(T)}{B^-_{\text{sat}}(h_0,T) - B^+_{\text{sat}}(h_0,T)}}^{=\lambda} \frac{\partial B^+_{\text{sat}}(h_0,T)}{\partial T} \\ & + \underbrace{\frac{p^+(T) - B^+_{\text{sat}}(h_0,T)}{B^-_{\text{sat}}(h_0,T) - B^+_{\text{sat}}(h_0,T)}}_{=1-\lambda} \frac{\partial B^-_{\text{sat}}(h_0,T)}{\partial T} \end{aligned} \tag{4.17}$$

with $p^+(T_0) = b_0$.

$p^- = p^-(T) : [T_{\min}, T^{\dagger}] \subseteq [T_{\min}, T_{\max}] \subseteq \mathbb{R} \to \mathbb{R}$ is the solution of the initial value problem

$$\begin{aligned} \frac{\mathrm{d}p^-(T)}{\mathrm{d}T} = & \frac{B^-_{\text{sat}}(h_0,T) - p^-(T)}{B^-_{\text{sat}}(h_0,T) - B^+_{\text{sat}}(h_0,T)} \min\left(\tfrac{\partial}{\partial T} B^+_{\text{sat}}(h_0,T), 0\right) \\ & + \frac{p^-(T) - B^+_{\text{sat}}(h_0,T)}{B^-_{\text{sat}}(h_0,T) - B^+_{\text{sat}}(h_0,T)} \max\left(\tfrac{\partial}{\partial T} B^-_{\text{sat}}(h_0,T), 0\right) \end{aligned} \tag{4.18}$$

First, it will be proven that Definition 4.13 is well defined. This concerns especially the definition domain and the check if the paths $p^{\pm}$ stay in I_{T}.

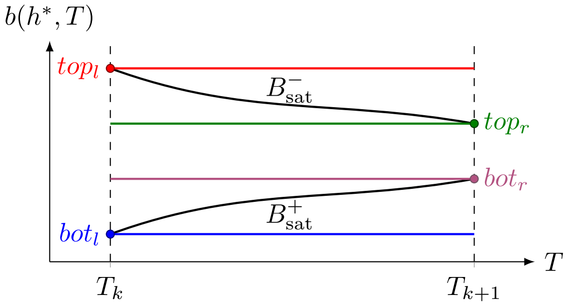

Figure 4.10.: Sketch of the notation used in the proof of Lemma 4.17. The initial values are marked with cycles. This example is of type I, so the resulting paths are all constant.

Remark 4.14. In the following, any path denoted with $p^\pm$ is defined by Definition 4.13 with respect to some $(h_0, b_0, T_0) \in I_T$.

Remark 4.15. Lemmas 4.16 and 4.17 will define and prove the domain of paths $p^\pm$ defined w.r.t. $(h_0, b_0, T_0) \in I_T$. Basic properties are also studied.

Lemma 4.16: Given $(h_0, b_0, T_0) \in I_T$ and $h = h_0$ is constant.

$p^+ = p^+(T)$ is defined on the whole interval $[T_{\min}, T_{\max}]$ and fulfills $B^+_{\text{sat}}(h_0, T) \leq p^+(T) \leq B^-_{\text{sat}}(h_0, T)$ for all $T \in [T_{\min}, T_{\max}]$. $\lambda\big(h_0, p^+(T), T\big)$ as defined in (4.11) is constant for all $T \in [T_{\min}, T_{\max}]$. p^+ is given by

$$p^+(T) = \lambda_0 B^+_{\text{sat}}(h_0, T) + (1 - \lambda_0) B^-_{\text{sat}}(h_0, T) \tag{4.19}$$

with

$$\lambda_0 = \frac{B^-_{\text{sat}}(h_0, T_0) - b_0}{B^-_{\text{sat}}(h_0, T_0) - B^+_{\text{sat}}(h_0, T_0)} \in [0, 1]\,. \tag{4.20}$$

Proof. Inserting (4.19) and its derivative

$$\frac{\mathrm{d}}{\mathrm{d}T} p^+(T) = \lambda_0 \frac{\partial}{\partial T} B^+_{\text{sat}}(h_0, T) + (1 - \lambda_0) \frac{\partial}{\partial T} B^-_{\text{sat}}(h_0, T) \tag{4.21}$$

into the IVP (4.17) results in an always true statement. The initial value is fulfilled by (4.20). The right hand side of (4.17) is Lipschitz continuous w.r.t. p^+ (it is continuously differentiable w.r.t. p^+). By the theorem of Picard-Lindelöf the solution is unique. So the unique solution is given by the explicit formulation in (4.19).

The path p^+ is a convex combination (linear combination with non-negative weights and the sum of weights is equal to one) of B^+_{sat} and B^-_{sat}. Therefore it lies between or on them. And since these function are defined on the interval $[T_{\min}, T_{\max}]$, this is also true for p^+.

Inserting (4.19) into the definition of λ in (4.11) results in $\lambda = \lambda_0$. □

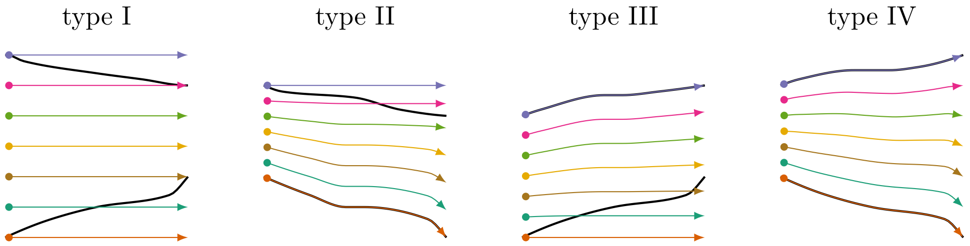

(a) Starting on the left side.

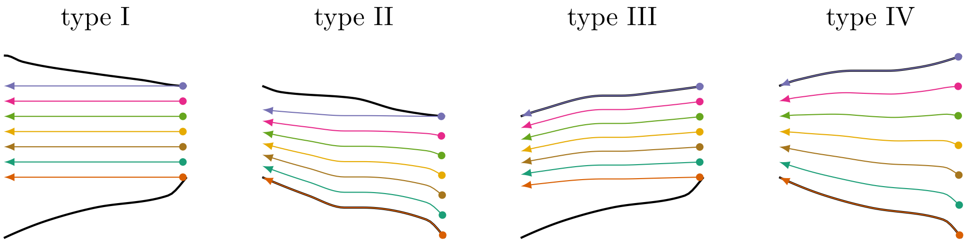

(b) Starting on the right side.

Figure 4.11.: Shown are how paths p^- can be continued on an interval $[T_k, T_{k+1}]$ of specific type. The initial values are marked with cycles. The upper rows shows initial values at $T = T_k$ and the lower row at $T = T_{k+1}$.

Lemma 4.17: Given $(h^*, b^*, T^*) \in I_T$. $h = h^*$ is constant.

$p^- = p^-(T)$ is defined on the interval $[T_{\min}, T^\dagger]$ with $T^* \le T^\dagger \le T_{\max}$ and fulfills $B^+_{\text{sat}}(h^*, T) \le p^-(T) \le B^-_{\text{sat}}(h^*, T)$ for all $T \in [T_{\min}, T^\dagger]$.

Proof. Using Lemma 4.11 to subdivide $[T_{\min}, T_{\max}]$ into intervals (T_k, T_{k+1}) with $k = 0, \ldots, n_k$, such that these intervals are of type I, II, III or IV.

W.l.o.g. assume $T^* = T_k$ for some $k \in 0, \ldots, n_k + 1$. If this is not fulfilled, add another break at T^*.

One of those intervals (T_k, T_{k+1}) is now regarded and the properties of p^- are investigated. It will be distinguished whether $T^* = T_k$ or T_{k+1} holds. In the first case, the problem is artificially extended outside of the domain I_T. Depending on b^* the resulting paths p^- may leave I_T, as shown in Figure 4.11(a). In the second case, the resulting paths p^- will stay inside of I_T for any valid b^*, as shown in Figure 4.11(b).

▶ *Idea:* If this is shown, it can be concluded that a path p^- defined w.r.t. $(h^*, b^*, T^*) \in I_T$ can be continued up to the left boundary $T_{\min}$. But going to the right, it may exit I_T at some $T^\dagger$ before it reaches $T_{\max}$. In each type, the resulting right hand side of the underlying ODE (4.18) fulfills all requirements of Lemma A.1. If suitable boundary solutions (top, bot) of the ODE are chosen, they can easily apply Lemma A.1.

▶ *Notation:* In each of the following cases an underlying ODE is defined. A sketch of the notation is given in Figure 4.10. Let top_l denote the solution of the corresponding ODE with initial value $top_l(T_k) = B^-_{\text{sat}}(h^*, T_k)$. Graphically it is the solution starting at the top left corner. In the same way an index of r refers to an initial value at

$T = T_{k+1}$, i.e., the right boundary. And if the starting value is on the lower limit B^{+}_{sat}, the solutions are called bot_l and bot_r.

▶ *type II:* The underlying ODE is given by $\frac{\mathrm{d}p^-}{\mathrm{d}T} = \lambda \frac{\partial B^{+}_{\text{sat}}}{\partial T}$, which is extended to

$$\frac{\mathrm{d}p^-}{\mathrm{d}T} = \begin{cases} \lambda \dfrac{\partial B^{+}_{\text{sat}}}{\partial T} & \text{if } B^{+}_{\text{sat}} \leq p^- \leq B^{-}_{\text{sat}} \\ 0 & \text{if } B^{-}_{\text{sat}} < p^- \end{cases} . \tag{4.22}$$

The right hand side of (4.22) is still continuous and Lipschitz-continuous in the second variable. $bot(T) = B^{+}_{\text{sat}}(h^*, T)$ is a solution of (4.22) with initial values

$$\Big(h^*, B^{+}_{\text{sat}}(h^*, T_k), T_k\Big) \text{ and } \Big(h^*, B^{+}_{\text{sat}}(h^*, T_{k+1}), T_{k+1}\Big) . \tag{4.23}$$

Let top_l denote the solution of (4.22) with initial value $top_l(T_k) = B^{-}_{\text{sat}}(h^*, T_k)$. top_l is explicitly given by the constant solution, i.e., $top_l(T) = b^*$ for all $T \in [T_k, T_{k+1}]$.

Using top_l and bot with Lemma A.1 ensures existence and uniqueness of top_r, which is a solution of (4.22) for $\Big(h^*, B^{-}_{\text{sat}}(h^*, T_{k+1}), T_{k+1}\Big)$. It holds $bot < top_r < top_l$ for all $T \in [T_k, T_{k+1}]$. It can be concluded, that for all initial values (T_k, b) with $b \in \Big[B^{+}_{\text{sat}}(h^*, T_k), top_r(T_k)\Big]$ the resulting paths p^- will stay inside on I_T for the whole domain $[T_k, T_{k+1}]$. The same is true for initial values (T_{k+1}, b) with $b \in \Big[B^{+}_{\text{sat}}(h^*, T_{k+1}), B^{-}_{\text{sat}}(h^*, T_{k+1})\Big]$.

This also means, that any initial values with (T_k, b) with $b \in \Big(top_r(T_k), B^{+}_{\text{sat}}(h^*, T_k)\Big]$ will result in paths p^- with $p^-(T_{k+1}) > B^{-}_{\text{sat}}(h^*, T_{k+1})$. These paths leave I_T and therefore cannot be continued in the next adjacent interval. The intersection of these paths and B^{-}_{sat} is at $T^{\dagger}$. All other paths will stay in I_T and can be continued.

▶ *type III:* Analogous to the case of type II. It is only necessary to interchange the consideration of the upper and lower boundaries.

▶ *type I:* This type is a combination of type I and II. Both *top* and *bot* must be separated into left and right. And the ODE must be extended above and below of I_T.

▶ *type IV:* This case is already covered by Lemma 4.16, since the underlying ODE is the same.

□

Remark 4.18. Analogous to Chapter 3 it can be stated, that every point $(h, b, T) \in I_{\mathrm{T}}$ is hit by exactly one path p^+ and one p^-. A part of the following investigations aims at making statements about further intersections of these paths. Or under which conditions they do match completely. For this purpose, the terms *stable* and *reversible* are introduced and investigated accordingly.

Remark 4.19. With Lemmas 4.16 and 4.17, one can conclude, that if the paths $p^\pm$ are applied in their intended use case ($\Delta T > 0$ or $\Delta T < 0$), the resulting composite path can not leave I_T. The boundary curves $B^\pm_{\text{sat}}$ are thus respected as such by the model and the approach is regarded as well defined.

Investigations on Reversibility of the Thermal Extension

Now that the basic definition of the paths has been completed and found to be well defined, the behavior of the model for sweeping excitations w.r.t. T will be discussed. Analogously to Chapter 3, it will be investigated under which conditions two paths $p^\pm$ form a closed curve. In the case of a sweeping excitation this corresponds to a *stable* state, i.e., in each new cycle the same paths result.

New in this section, however, is that the paths $p^\pm$ can also be identical. This means that the closed curve has no enclosed area and the forward and backward motion takes place on the same path. This is denoted as *reversible*. One focus of the investigations will be the correlation between stable and reversible. It will be shown that these properties are equivalent in some application scenarios.

The strategy can be roughly summarized as follows.

▶ First, h and T are held constant and the influence of b on the paths $p^\pm$ defined w.r.t. $(h, b, T) \in I_\text{T}$ is examined. The focus is on the derivatives $\frac{\mathrm{d}p^\pm}{\mathrm{d}T}$. This allows to gain first insights into the different behavior of the paths $p^\pm$ or, conversely, when they behave the same.

▶ Second, the definitions of stable and reversible will be introduced. From the previous investigations direct statements about the existence and uniqueness of reversible paths can be made.

▶ Then it is moved on to examinations on subintervals of only one type. There conditions, when the definitions of stable and reversible are equivalent, can be established.

▶ Afterwards, the convergence behavior for sweeping excitations is investigated and it is shown that the model always tends towards stable or reversible states.

▶ The previous investigation will be restricted to subintervals of one type. For the special case of $h = 0$ being constant, the examinations are extended to intervals of any type. It will be proven, that for $h = 0$ only the types I and IV can occur. Because of this, these types are examined in further detail. Also here a convergent behavior of the model will be found.

Remark 4.20. The following investigation has the same approach as the partition of I into $I^<$, $I^=$, $I^>$ in Section 3.2.3. The derivatives of p^+ and p^- are compared. This information will be used in many of the upcoming proofs.

Lemma 4.21: Given $T_0 \in [T_{\min}, T_{\max}]$ and $h = h_0$ constant. Let $p^{\pm}$ be paths defined w.r.t. $(h_0, b_0, T_0) \in I_T$. Depending on the signs of $\frac{\mathrm{d}}{\mathrm{d}T} B^{\pm}_{\mathrm{sat}}$ w.r.t. Definition 4.10 the following statements hold true.

i) type I

It exists $b^{\mathrm{eq}} = \frac{\frac{\partial B^-_{\mathrm{sat}}}{\partial T} B^+_{\mathrm{sat}} - \frac{\partial B^+_{\mathrm{sat}}}{\partial T} B^-_{\mathrm{sat}}}{\frac{\partial B^-_{\mathrm{sat}}}{\partial T} - \frac{\partial B^+_{\mathrm{sat}}}{\partial T}} \in \Big(B^+_{\mathrm{sat}}(h_0, T_0), B^-_{\mathrm{sat}}(h_0, T_0)\Big)$ such that

$$\frac{\mathrm{d}p^-}{\mathrm{d}T}(T_0) = 0 \begin{cases} > \frac{\mathrm{d}p^+}{\mathrm{d}T}(T_0) & \text{, if } b_0 \in \Big(b^{\mathrm{eq}}, B^-_{\mathrm{sat}}(h_0, T_0)\Big] \\ = \frac{\mathrm{d}p^+}{\mathrm{d}T}(T_0) & \text{, if } b_0 = b^{\mathrm{eq}} \\ < \frac{\mathrm{d}p^+}{\mathrm{d}T}(T_0) & \text{, if } b_0 \in \Big[B^+_{\mathrm{sat}}(h_0, T_0), b^{\mathrm{eq}}\Big) \end{cases} \tag{4.24}$$

holds.

ii) type II

$$\frac{\mathrm{d}p^-}{\mathrm{d}T}(T_0) \begin{cases} > \frac{\mathrm{d}p^+}{\mathrm{d}T}(T_0) & \text{, if } b_0 \in \Big(B^+_{\mathrm{sat}}(h_0, T_0), B^-_{\mathrm{sat}}(h_0, T_0)\Big] \\ = \frac{\mathrm{d}p^+}{\mathrm{d}T}(T_0) = \frac{\partial B^+_{\mathrm{sat}}}{\partial T}(h_0, T_0) & \text{, if } b_0 = B^+_{\mathrm{sat}}(h_0, T_0) \end{cases} \tag{4.25}$$

iii) type III

$$\frac{\mathrm{d}p^-}{\mathrm{d}T}(T_0) \begin{cases} < \frac{\mathrm{d}p^+}{\mathrm{d}T}(T_0) & \text{, if } b_0 \in \Big[B^+_{\mathrm{sat}}(h_0, T_0), B^-_{\mathrm{sat}}(h_0, T_0)\Big) \\ = \frac{\mathrm{d}p^+}{\mathrm{d}T}(T_0) = \frac{\partial B^-_{\mathrm{sat}}}{\partial T}(h_0, T_0) & \text{, if } b_0 = B^-_{\mathrm{sat}}(h_0, T_0) \end{cases} \tag{4.26}$$

iv) type IV

$$\frac{\mathrm{d}p^-}{\mathrm{d}T}(T_0) = \frac{\mathrm{d}p^+}{\mathrm{d}T}(T_0) \text{ for all } b_0 \in \Big[B^+_{\mathrm{sat}}(h_0, T_0), B^-_{\mathrm{sat}}(h_0, T_0)\Big] \tag{4.27}$$

Proof. The proof is performed separately for each type.

i) Inserting the given b^{eq} into the definition of λ in (4.11) results in

$$\lambda = \frac{\frac{\partial B^-_{\mathrm{sat}}}{\partial T}}{\frac{\partial B^-_{\mathrm{sat}}}{\partial T} - \frac{\partial B^+_{\mathrm{sat}}}{\partial T}} \text{ and } 1 - \lambda = \frac{\frac{\partial B^+_{\mathrm{sat}}}{\partial T}}{\frac{\partial B^+_{\mathrm{sat}}}{\partial T} - \frac{\partial B^-_{\mathrm{sat}}}{\partial T}} \,. \tag{4.28}$$

Inserting into

$$\frac{\mathrm{d}p^+}{\mathrm{d}T} = \lambda \underbrace{\frac{\partial B^+_{\mathrm{sat}}}{\partial T}}_{>0} + (1 - \lambda) \underbrace{\frac{\partial B^-_{\mathrm{sat}}}{\partial T}}_{<0} \tag{4.29}$$

results in $\frac{\mathrm{d}p^+}{\mathrm{d}T} = 0 = \frac{\mathrm{d}p^-}{\mathrm{d}T}$. (4.29) is strictly monotonously increasing w.r.t. λ, which itself is strictly monotonously decreasing w.r.t. b. So overall (4.29) is strictly monotonously decreasing w.r.t. b. This makes the used b^{eq} unique and proves the statement (4.24).

ii) Comparing the definitions of $p^{\pm}$ in this case yields

$$\frac{\mathrm{d}p^+}{\mathrm{d}T} = \lambda \frac{\partial B^+_{\text{sat}}}{\partial T} + \underbrace{(1-\lambda)}_{\in[0,1]} \underbrace{\frac{\partial B^-_{\text{sat}}}{\partial T}}_{<0} \begin{cases} = \quad \dfrac{\partial B^+_{\text{sat}}}{\partial T} = \dfrac{\mathrm{d}p^-}{\mathrm{d}T} & \text{if } \lambda = 1 \\ < \lambda \dfrac{\partial B^+_{\text{sat}}}{\partial T} = \dfrac{\mathrm{d}p^-}{\mathrm{d}T} & \text{else} \end{cases} . \tag{4.30}$$

The condition $\lambda = 1$ is equivalent to $b_0 = B^+_{\text{sat}}(h_0, T_0)$ and (4.25) is proven.

iii) Comparing the definitions of $p^{\pm}$ in this case yields

$$\frac{\mathrm{d}p^+}{\mathrm{d}T} = \underbrace{\lambda}_{\in[0,1]} \underbrace{\frac{\partial B^+_{\text{sat}}}{\partial T}}_{>0} + (1-\lambda) \frac{\partial B^-_{\text{sat}}}{\partial T} \begin{cases} = \quad \dfrac{\partial B^-_{\text{sat}}}{\partial T} = \dfrac{\mathrm{d}p^-}{\mathrm{d}T} & \text{if } \lambda = 0 \\ > (1-\lambda) \dfrac{\partial B^-_{\text{sat}}}{\partial T} = \dfrac{\mathrm{d}p^-}{\mathrm{d}T} & \text{else} \end{cases} . \tag{4.31}$$

The condition $\lambda = 0$ is equivalent to $b_0 = B^-_{\text{sat}}(h_0, T_0)$ and (4.26) is proven.

iv) In this case, the definition of $\frac{\mathrm{d}p^+}{\mathrm{d}T}$ and $\frac{\mathrm{d}p^-}{\mathrm{d}T}$ are identical and (4.27) is proven.

□

Remark 4.22. A conclusion of Lemma 4.21 is that a partition of I as in Section 3.2.3 cannot be done analogously. Even if there is a unique b^{eq} in the case of type I, II, III, this does not lead to a continuous function $b^{\text{eq}}(T)$. For example in case of a transition from type II to type III, b^{eq} would jump from B^+_{sat} to B^-_{sat}. In case of type IV there is no meaningful definition of b^{eq}, i.e., for the thermal model an adapted analysis approach must be pursued.

Remark 4.23. It is to investigate the behaviour of the thermal model for a sweeping excitation w.r.t. some interval $[T_0, T_1] \subseteq [T_{\min}, T_{\max}]$. For this purpose it will be first defined what is meant by stable behavior. The examinations for this are first limited to intervals with only one type.

Definition 4.24 (stable & reversible paths)**:** Given $[T_0, T_1] \subseteq [T_{\min}, T_{\max}]$ and paths $p^{\pm}$ defined w.r.t. $(h_0, b_0, T_0) \in I_T$.

$p^{\pm}$ is called *stable* on $[T_0, T_1]$, if $p^+(T_1) = p^-(T_1)$ holds and *reversible*, if $p^+(T) = p^-(T)$ for all $T \in [T_0, T_1]$.

Remark 4.25. At this point the existence and uniqueness of reversible paths $p^{\pm}$ will be proven. It will be shown, that reversible paths $p^{\pm}$ exist in intervals of type I only under certain conditions. In intervals of type II and III unique reversible paths $p^{\pm}$ exist. They lie on the saturation curves $B^{\pm}_{\text{sat}}$. In the case of type IV, one common point of p^+ and p^- is sufficient, such that the paths are identical and therefore reversible.

Lemma 4.26: Given nonempty $[T_0, T_1] \subseteq [T_{\min}, T_{\max}]$ of only one type. Let $p^{\pm} : [T_0, T_1] \to \mathbb{R}$ be defined w.r.t. $(h_0, b_0, T_0) \in I_T$.

$p^{\pm}$ are reversible if and only if one of the following conditions is true.

- The interval $[T_0, T_1]$ is of type I and $b_0 = \lambda_0 B_{\text{sat}}^{+}(h_0, T_0) + (1 - \lambda_0) B_{\text{sat}}^{-}(h_0, T_0)$ and $\frac{\partial B_{\text{sat}}^{-}}{\partial T} = \frac{-\lambda_0}{1-\lambda_0} \frac{\partial B_{\text{sat}}^{+}}{\partial T}$ for all $T \in [T_0, T_1]$ with $\lambda_0 = \left. \frac{\frac{\partial B_{\text{sat}}^{-}}{\partial T}}{\frac{\partial B_{\text{sat}}^{-}}{\partial T} - \frac{\partial B_{\text{sat}}^{+}}{\partial T}} \right|_{\substack{h=h_0 \\ T=T_0}}$ holds.
- The interval $[T_0, T_1]$ is of type II and $b_0 = B_{\text{sat}}^{+}(h_0, T_0)$ holds.
- The interval $[T_0, T_1]$ is of type III and $b_0 = B_{\text{sat}}^{-}(h_0, T_0)$ holds.
- The interval $[T_0, T_1]$ is of type IV.

Proof. $p^{+}(T) = p^{-}(T)$ for all $T \in [T_0, T_1]$ is true, if and only if $\frac{\mathrm{d}p^{+}(T)}{\mathrm{d}T} = \frac{\mathrm{d}p^{-}(T)}{\mathrm{d}T}$ for all $T \in [T_0, T_1]$ and $p^{+}(T_0) = p^{-}(T_0)$ holds. The second conditions is fulfilled by construction of $p^{\pm}$.

For type II, III and IV this is easily proven by Lemma 4.21.

For type I the value for b_0 and λ_0 are given by Lemma 4.21. It yields

$$\frac{\mathrm{d}p^{+}(T)}{\mathrm{d}T} = 0 = \lambda_0 \frac{\partial B_{\text{sat}}^{+}(T)}{\partial T} + (1 - \lambda_0) \frac{\partial B_{\text{sat}}^{-}(T)}{\partial T} = \frac{\mathrm{d}p^{-}(T)}{\mathrm{d}T} \tag{4.32}$$

for all $T \in [T_0, T_1]$ only if $\frac{\partial B_{\text{sat}}^{-}(T)}{\partial T} = \frac{-\lambda_0}{1-\lambda_0} \frac{\partial B_{\text{sat}}^{+}(T)}{\partial T}$ for all $T \in [T_0, T_1]$ is true, since λ_0 is a constant. □

Remark 4.27. The next intermediate goal is to investigate the relationship between stable and reversible curves. For this purpose the observation is limited to an interval of one type. A focus will be on the conditions under which these definitions are equivalent.

Lemma 4.28: Given nonempty $[T_0, T_1] \subseteq [T_{\min}, T_{\max}]$ of only one type. Let $p^{\pm} : [T_0, T_1] \to \mathbb{R}$ be defined w.r.t. $(h_0, b_0, T_0) \in I_T$. The following statements are true.

- For type II, III and IV, the definition of stable and reversible are equivalent.

- For type I, the paths $p^{\pm}$ are stable iff $b_0 = \lambda_0 B_{\text{sat}}^{+}(h_0, T_0) + (1 - \lambda_0) B_{\text{sat}}^{-}(h_0, T_0)$ with $\lambda_0 = \frac{B_{\text{sat}}^{-}(h_0,T_0) - B_{\text{sat}}^{-}(h_0,T_1)}{B_{\text{sat}}^{-}(h_0,T_0) - B_{\text{sat}}^{-}(h_0,T_1) + B_{\text{sat}}^{+}(h_0,T_1) - B_{\text{sat}}^{+}(h_0,T_0)} \in (0, 1)$ holds.

Proof.

- type IV: The paths $p^{\pm}$ are identical, thus in particular stable and reversible.

- type II and III: It needs to be proven, that there cannot exist stable paths $p^{\pm}$ besides the reversible ones already investigated in Lemma 4.26. These reversible paths are excluded from the current argumentation. If paths $p^{\pm}$ are stable, they fulfill

$$p^{+}(T_1) - p^{-}(T_1) = \underbrace{p^{+}(T_0) - p^{-}(T_0)}_{=b_0 - b_0 = 0} + \int_{T_0}^{T_1} \underbrace{\frac{\mathrm{d}p^{+}(\tau)}{\mathrm{d}T} - \frac{\mathrm{d}p^{-}(\tau)}{\mathrm{d}T}}_{\substack{<0 \text{ in type II} \\ >0 \text{ in type III}}} \mathrm{d}\tau = 0\,. \tag{4.33}$$

But – under these assumptions – the equation (4.33) is not valid as the integrand is strictly positive or negative, as proven in Lemma 4.21. So stable but not reversible paths $p^{\pm}$ cannot exists for intervals of type type II or III.

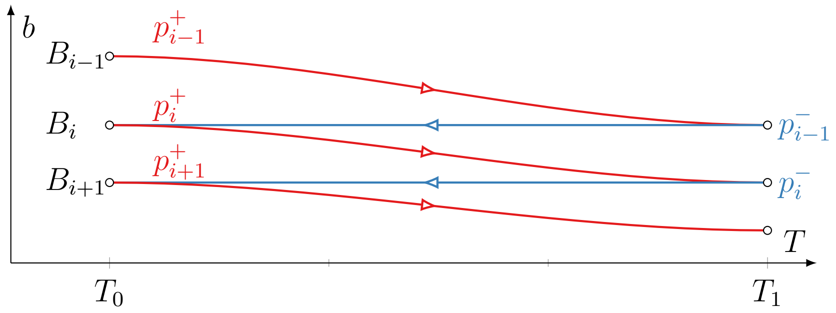

Figure 4.12.: Overview of the notation and sketch of Lemma 4.31.

► type I: In this case the path p^- is constant. So the condition to show is reduced to $p^+(T_0) = p^+(T_1)$. By definition of p^+ this results in

$$\lambda B^+_{\text{sat}}(h_0, T_0) + (1-\lambda)B^-_{\text{sat}}(h_0, T_0) = \lambda B^+_{\text{sat}}(h_0, T_1) + (1-\lambda)B^-_{\text{sat}}(h_0, T_1)\,. \tag{4.34}$$

As proven in Lemma 4.16, the λ on both sides of (4.34) is identical. Solving this for λ results in

$$\lambda = \frac{\overbrace{B^-_{\text{sat}}(h_0, T_0) - B^-_{\text{sat}}(h_0, T_1)}^{>0}}{\underbrace{B^-_{\text{sat}}(h_0, T_0) - B^-_{\text{sat}}(h_0, T_1)}_{>0} + \underbrace{B^+_{\text{sat}}(h_0, T_1) - B^+_{\text{sat}}(h_0, T_0)}_{>0}} \in (0,1)\,. \tag{4.35}$$

With $B^-_{\text{sat}}(h_0, T_0) > B^-_{\text{sat}}(h_0, T_1)$ and $B^+_{\text{sat}}(h_0, T_0) < B^+_{\text{sat}}(h_0, T_1)$, $\lambda \in (0,1)$ is shown.

□

Remark 4.29. In this subsection it has been shown that for all types only one unique set of stable paths $p^\pm$ exists. Stable and reversible paths are identical for intervals of type II, III and IV. For type I, conditions were formulated under which reversible paths can occur.

Convergence to Stable Curves

Remark 4.30. After the existence and uniqueness of stable paths has been shown, in this subsection the convergence towards stable paths will be investigated. Similar approaches as in Section 3.2.6 are chosen. The used excitation is analog to Definition 3.52. The chosen h is arbitrary but constant. The temperature is sweeped in a interval $[T_0, T_1] \subseteq [T_{\min}, T_{\max}]$.

Lemma 4.31: Given $[T_0, T_1] \subseteq [T_{\min}, T_{\max}]$ of only one type and $(h_0, b_0, T_0) \in I_T$. Let p^+_0 be defined w.r.t. (h_0, b_0, T_0) and p^-_0 w.r.t. $\left(h_0, p^+_0(T_1), T_1\right)$. For any $i \in \mathbb{N}$, let p^+_i be defined w.r.t. $\left(h_0, p^-_{i-1}(T_0), T_0\right)$ and p^-_i w.r.t. $\left(h_0, p^+_i(T_1), T_1\right)$. The sequence $B_i = p^+_i(T_0) = p^-_{i-1}(T_0)$ converges for $i \to \infty$ to $B_\infty \in \left[B^-_{\text{sat}}(h_0, T_0), B^+_{\text{sat}}(h_0, T_0)\right]$. An overview of the notation is given in Figure 4.12.

Proof.

▶ type IV:
In this case the paths $p_i^{\pm}$ are reversible and therefore all $p_i^{\pm}$ are identical.

▶ type III:
Using (4.31), it can be concluded that $B_i < B_{i+1} < B_{\text{sat}}^{-}(h_0, T_0)$ holds for all $i \in \mathbb{N}_0$, if $B_0 < B_{\text{sat}}^{-}(h_0, T_0)$. If $B_0 = B_{\text{sat}}^{-}(h_0, T_0)$, then $B_i = B_{\text{sat}}^{-}(h_0, T_0)$ for all $I \in \mathbb{N}_0$. So the sequence $(B_i)_{i \in \mathbb{N}_0}$ is strictly monotone increasing inside of I_T and bounded from top. So it must be convergent and B_∞ is given by $B_{\text{sat}}^{-}(h_0, T_0)$.

▶ type II:
Analog to case III. The sequence is strictly monotone decreasing inside of I_{T} and B_∞ is given by $B_{\text{sat}}^{+}(h_0, T_0)$.

▶ type I:
Define $\varphi : \left[B_{\text{sat}}^{-}(h_0, T_0), B_{\text{sat}}^{+}(h_0, T_0)\right] \to \left[B_{\text{sat}}^{-}(h_0, T_0), B_{\text{sat}}^{+}(h_0, T_0)\right]$ with

$$\begin{aligned}\varphi(b) = \;& \underbrace{\frac{B_{\text{sat}}^{-}(h_0, T_0) - b}{B_{\text{sat}}^{-}(h_0, T_0) - B_{\text{sat}}^{+}(h_0, T_0)}}_{=\lambda_0} B_{\text{sat}}^{+}(h_0, T_1) \\ &+ \underbrace{\frac{b - B_{\text{sat}}^{+}(h_0, T_0)}{B_{\text{sat}}^{-}(h_0, T_0) - B_{\text{sat}}^{+}(h_0, T_0)}}_{=1-\lambda_0} B_{\text{sat}}^{-}(h_0, T_1)\,.\end{aligned} \tag{4.36}$$

▷ Claim: It holds $B_{i+1} = \varphi(B_i)$ for all $i \in \mathbb{N}_0$.
The path p_i^{+} is defined w.r.t. $(h_0, B_i, T_0) \in I_T$. As proven in Lemma 4.16 the path p_i^{+} has an explicit formulation given by (4.19) and (4.20). Comparing to (4.36), one concludes that $\varphi(B_i) = p_i^{+}(T_1)$ holds. For this type, the paths p_i^{-} are constant and are given by $p_i^{-}(T) = p_i^{+}(T_1)$ for all $T \in [T_0, T_1]$. Overall, $p_i^{-}(T_0) = B_{i+1}$ is given by $\varphi(B_i)$.

▷ Claim: φ is a contraction with Lipschitz constant $k = \frac{B_{\text{sat}}^{-}(T_1) - B_{\text{sat}}^{+}(T_1)}{B_{\text{sat}}^{-}(T_0) - B_{\text{sat}}^{+}(T_0)} \in (0, 1)$.
Let $b_1, b_2 \in \left[B_{\text{sat}}^{-}(h_0, T_0), B_{\text{sat}}^{+}(h_0, T_0)\right]$. Using (4.36), it yields

$$|\varphi(b_1) - \varphi(b_2)| = \underbrace{\frac{B_{\text{sat}}^{-}(h_0, T_1) - B_{\text{sat}}^{+}(h_0, T_1)}{B_{\text{sat}}^{-}(h_0, T_0) - B_{\text{sat}}^{+}(h_0, T_0)}}_{=k \in (0,1)} |b_1 - b_2|\,. \tag{4.37}$$

For this type of interval, it holds $B_{\text{sat}}^{+}(h_0, T_0) < B_{\text{sat}}^{+}(h_0, T_1)$ and $B_{\text{sat}}^{-}(h_0, T_0) > B_{\text{sat}}^{-}(h_0, T_1)$. Thus in particular $B_{\text{sat}}^{-}(h_0, T_1) - B_{\text{sat}}^{+}(h_0, T_1) < B_{\text{sat}}^{-}(h_0, T_0) - B_{\text{sat}}^{+}(h_0, T_0)$ holds. And with the global condition $B_{\text{sat}}^{-}(h_0, T) > B_{\text{sat}}^{+}(h_0, T)$, it follows $k \in (0, 1)$.

All prerequisites of the Banach fixed-point theorem are met, so convergence and a unique fix point are guaranteed. The resulting stable paths are given in Lemma 4.28.

□

Remark 4.32. Lemma 4.31 proves that, limited to an interval of one type, the thermal model shows convergent behavior for a sweeping excitation. For type I the set of stable paths lies inside of I_{T}. In type II it is the lower boundary B^{+}_{sat} and it is strictly monotonically approaching this limit. In type III the model tends strictly monotonically upwards to its limit B^{+}_{sat}. And for type IV all paths are reversible. This gives a rough impression of the model's behavior.

Analysis of the Special Case $h = 0$

In this section the special case $h = 0$ is examined. This means that there are no external excitations like currents.

Before proceeding to the detailed investigations, the expectations for the model are first explained and the procedure is roughly outlined.

Physical motivation: Without excitation ($h = 0$) it is expect that the magnetic flux density b at temperature T_0 is not increased, if the material is heated up to T_1 and cooled down again to T_0. As motivated in Sections 2.2 and 4.2.1 an increase of the temperature increases the total energy in the system. The movement of Bloch walls are made easier by an increased temperature. In the limit, if the temperature reaches the Curie temperature, the hysteresis, i.e., ferromagnetic properties of the material are nullified. This is why one of the benchmarks for the thermal model is that the material is demagnetized, when it is strongly heated. It is argued that the Bloch walls have to overcome a potential maximum to actual achieve a smaller energy level. In the model two different behavior can be seen.

▶ One is that the magnetic flux density b is not permanently altered, if the temperature is increased and decreased back to starting temperature. This is identified with the case, if the Bloch walls do not gain enough energy to actually overcome the potential maximum. As the temperature decreases they get back to their starting position. This behavior is reversible.

▶ The other behavior is observed, if the added energy actually made Bloch walls move. These are now permanently in a more favorable state w.r.t. energy. This result in a lower amplitude of b.

Sketch of the approach: The following examinations are structured as follows.

▶ First, it will be proven that only type I and IV can occur for $h = 0$.

▶ Second, the relative vertical position, i.e., λ, along paths $p^{\pm}$ in intervals of either type I or type IV is examined.

▶ Third, an interval of mixed type is investigated. It will be proven that a sweeping excitation w.r.t. temperature T converges to the solution $b = 0$.

► Forth, it will be discussed what consequences the results so far have. It is checked whether this fits the physical motivation.

Lemma 4.33: For $h = 0$ only types I and IV can occur.

Proof. For $h = 0$ with (4.9), it yields

$$B^{+}_{\mathrm{sat}}(0,T) = -B^{-}_{\mathrm{sat}}(0,T) \text{ and } \frac{\partial}{\partial T} B^{+}_{\mathrm{sat}}(0,T) = -\frac{\partial}{\partial T} B^{-}_{\mathrm{sat}}(0,T)\,. \tag{4.38}$$

Thus by Definition 4.10, types II and III are not possible. □

Remark 4.34. Since according to Lemma 4.33 only types I and IV can occur, the following consideration is limited to those. First, an investigation is performed under the condition that the considered interval is of one type and $h = 0$. There, the focus is on the investigation of how λ, as defined in (4.11), changes along paths $p^{\pm}$. Second, an interval with arbitrary division of type I and IV will be examined. It will be proven that there can only be one set of stable paths $p^{\pm}$ and that these are given by $p^{\pm} = 0$. Finally, it can be shown that the thermal model for $h = 0$ and sweeping excitations w.r.t. T converges towards the solution $b = p^{\pm} = 0$.

Lemma 4.35: Consider nonempty interval $[T_{\mathrm{L}}, T_{\mathrm{R}}] \subseteq [T_{\min}, T_{\max}]$ of type IV. Use $\lambda(h, b, T)$ as given in (4.11).

► For any path p^{+} defined w.r.t. $(0, b_{\mathrm{l}}, T_{\mathrm{L}}) \in I_{\mathrm{T}}$, the function

$$\lambda^{+}(T) = \lambda\Big(0, p^{+}(T), T\Big) = \lambda(0, b_{\mathrm{l}}, T_{\mathrm{L}}) \tag{4.39}$$

is constant for $T \in [T_{\mathrm{L}}, T_{\mathrm{R}}]$.
► For any path p^{-} defined w.r.t. $(0, b_{\mathrm{r}}, T_{\mathrm{R}}) \in I_{\mathrm{T}}$, the function

$$\lambda^{-}(T) = \lambda\Big(0, p^{-}(T), T\Big) = \lambda(0, b_{\mathrm{r}}, T_{\mathrm{R}}) \tag{4.40}$$

is constant for $T \in [T_{\mathrm{L}}, T_{\mathrm{R}}]$.

Proof. The path p^{+} is defined w.r.t. the left boundary $(0, b_{\mathrm{l}}, T_{\mathrm{L}})$ and with Lemma 4.16 it is defined on the whole interval $[T_{\mathrm{L}}, T_{\mathrm{R}}]$. The same is true for p^{-} defined w.r.t. the right boundary $(0, b_{\mathrm{r}}, T_{\mathrm{R}})$. Hence both paths are well defined on $[T_{\mathrm{L}}, T_{\mathrm{R}}]$.

The first statement for p^{+} was already proven in Lemma 4.16. For intervals of type IV the underlying ODE of the paths $p^{\pm}$ are equal, thus, the same proof yields the second statement. □

Lemma 4.36: Consider interval $(T_{\mathrm{L}}, T_{\mathrm{R}}) \subseteq [T_{\min}, T_{\max}]$ of type I. Use λ as given in (4.11).

- ▶ For any path p^+ defined w.r.t. $(0, b_\mathrm{l}, T_\mathrm{L}) \in I_\mathrm{T}$, the function

$$\lambda^+(T) = \lambda\Big(0, p^+(T), T\Big) = \lambda(0, b_\mathrm{l}, T_\mathrm{L}) \tag{4.41}$$

is constant for $T \in [T_\mathrm{min}, T_\mathrm{min}]$.

- ▶ Let path p^- defined w.r.t. $(0, b_\mathrm{r}, T_\mathrm{R}) \in I_\mathrm{T}$ and define function $\lambda^-(T) = \lambda\Big(0, p^-(T), T\Big)$.
  - ▷ If $\lambda^-(T_\mathrm{R}) \in \Big[0, \frac{1}{2}\Big)$ holds, λ^- is strictly monotonously decreasing on the interval $[T_\mathrm{L}, T_\mathrm{R}]$ and $\lambda^-(T) \in \Big[0, \frac{1}{2}\Big)$ holds for all $T \in [T_\mathrm{L}, T_\mathrm{R}]$.
  - ▷ If $\lambda^-(T_\mathrm{R}) \in \Big(\frac{1}{2}, 1\Big]$ holds, λ^- is strictly monotonously increasing on the interval $[T_\mathrm{L}, T_\mathrm{R}]$ and $\lambda^-(T) \in \Big(\frac{1}{2}, 1\Big]$ holds for all $T \in [T_\mathrm{L}, T_\mathrm{R}]$.
  - ▷ If $\lambda^-(T_\mathrm{R}) = \frac{1}{2}$ holds, λ^- is constant on the interval $[T_\mathrm{L}, T_\mathrm{R}]$.

Proof. The path p^+ is defined w.r.t. the left boundary $(0, b_\mathrm{l}, T_\mathrm{L})$ and with Lemma 4.16 it is defined on the whole interval $[T_\mathrm{L}, T_\mathrm{R}]$. The same is true for p^- defined w.r.t. the right boundary $(0, b_\mathrm{r}, T_\mathrm{R})$. Hence both paths are well defined on $[T_\mathrm{L}, T_\mathrm{R}]$.

The first statement for p^+ was already proven in Lemma 4.16.

The second statement is proven by examination of the derivative of λ^-. By using the definition of λ in (4.11), it yields

$$\lambda^-(T) = \lambda\Big(0, p^-(T), T\Big) = \frac{B^-_\mathrm{sat}(0,T) - p^-(T)}{B^-_\mathrm{sat}(0,T) - B^+_\mathrm{sat}(0,T)}\,. \tag{4.42}$$

For the sake of short notation, $B^\pm_\mathrm{sat} = B^\pm_\mathrm{sat}(0,T)$, $\partial B^\pm_\mathrm{sat} = \frac{\partial B^-_\mathrm{sat}(0,T)}{\partial T}$, $p^- = p^-(T)$ and $\mathrm{d}p^- = \frac{\mathrm{d}p^-(T)}{\mathrm{d}T}$ are used as abbreviations.

In the case of type I, $\mathrm{d}p^- = 0$ and $\partial B^-_\mathrm{sat} < 0$ applies. The condition $h = 0$ yields $B^-_\mathrm{sat} = -B^+_\mathrm{sat}$ and $\partial B^-_\mathrm{sat} = -\partial B^+_\mathrm{sat}$. Now, calculating the derivative of λ^- and using these properties result in

$$\begin{aligned}
\frac{\mathrm{d}\lambda^-(T)}{\mathrm{d}T} &= \frac{\Big(\partial B^-_\mathrm{sat} - \overbrace{\mathrm{d}p^-}^{=0}\Big)\overbrace{\Big(B^-_\mathrm{sat} - B^+_\mathrm{sat}\Big)}^{=2B^-_\mathrm{sat}} - \Big(B^-_\mathrm{sat} - p^-\Big)\overbrace{\Big(\partial B^-_\mathrm{sat} - \partial B^+_\mathrm{sat}\Big)}^{=2\partial B^-_\mathrm{sat}}}{\underbrace{\Big(B^-_\mathrm{sat} - B^+_\mathrm{sat}\Big)^2}_{=4{B^-_\mathrm{sat}}^2}} \\
&= p^- \frac{\overbrace{\partial B^-_\mathrm{sat}}^{<0}}{\underbrace{2\,{B^-_\mathrm{sat}}^2}_{>0}} \begin{cases} < 0 & \text{if } p^- > 0 \\ = 0 & \text{if } p^- = 0 \\ > 0 & \text{if } p^- < 0 \end{cases}.
\end{aligned} \tag{4.43}$$

In the special case of $h = 0$, it can be explicitly associated the sign of p^- with values of λ^-, i.e.,

$$p^- > 0 \Leftrightarrow \lambda^- \in \left[0, \frac{1}{2}\right), \quad p^- = 0 \Leftrightarrow \lambda^- = \frac{1}{2}, \quad p^- < 0 \Leftrightarrow \lambda^- \in \left(\frac{1}{2}, 1\right]. \tag{4.44}$$

Since $p^- = 0$ is a valid solution, no other path can cross it. Therefore, if $p^- > 0$ holds for one specific $T \in [T_\mathrm{L}, T_\mathrm{R}]$, it is automatically true on the whole interval. Analogous statements follow for $p^- =$ and $p^- < 0$. In conclusion, the statements of the lemma are proven. $\square$

Remark 4.37. Lemmas 4.35 and 4.36 are proving that the relative position λ^+ of any path p^+ stays constant. For a path p^-, λ^- is constant, if the interval is of type IV. But for type I it is not constant. The path p^- represent the way back, i.e., it is followed backwards. In this perspective, the path p^- strives towards $b = 0$ respectively $\lambda = \frac{1}{2}$.

Lemma 4.38: Let $h = 0$. Considered is the interval $[T_\mathrm{L}, T_\mathrm{R}] \subseteq [T_\mathrm{min}, T_\mathrm{max}]$ with $T_\mathrm{L} < T_\mathrm{R}$.

All sets of stable paths $p^\pm$ are reversible. A set of stable paths is given by $p^\pm = 0$. If interval $[T_\mathrm{L}, T_\mathrm{R}]$ is not solely of type IV, this is the only set of stable paths.

Proof. This proof is divided into three parts.

- First, it is assumed that interval $[T_\mathrm{L}, T_\mathrm{R}]$ is solely of type IV.
- Second, if it is solely of type I.
- Third, if it is mixed of types I and IV.

As proven in Lemma 4.33, these are the only cases that can occur.

Let paths $p^\pm$ be defined w.r.t. $(0, b_\mathrm{L}, T_\mathrm{L}) \in I_T$ and defined on the whole interval $[T_\mathrm{L}, T_\mathrm{R}]$.

1) If $[T_\mathrm{L}, T_\mathrm{R}]$ is solely of type IV, this was already proven in Lemma 4.28. In this case is was already shown that stable and reversible are equivalent. And choosing $b_0 = 0$ yields the solution $p^\pm = 0$.

2) For only type I it was already proven in Lemma 4.28, that only one unique set of stable paths exists. It will be proven, that this stable paths fulfills the conditions in Lemma 4.26 and therefore is reversible.

Inserting (4.38) into (4.35) results in $\lambda = 0.5$. Then, all conditions in Lemma 4.26 are true, if $\lambda = 0.5$ and (4.38) holds. The resulting paths are $p^\pm = 0$.

3) Now, assume $[T_\mathrm{L}, T_\mathrm{R}]$ is not of one type only. Using 1) and 2), it can be concluded that the paths $p^\pm = 0$ are also stable and reversible for this case. This case is represented by a constant $\lambda = 0.5$. It will be shown that any other set of paths can not be stable.

Due to symmetry, w.l.o.g. only paths $p^\pm > 0$, i.e., $\lambda \in [0, 0.5)$, are investigated. Let paths $p^\pm$ be defined w.r.t. $(0, b_\mathrm{L}, T_\mathrm{L}) \in I_T$ and $b_\mathrm{L} > 0$ be stable. It will be proven by contradiction, that these do not exists.

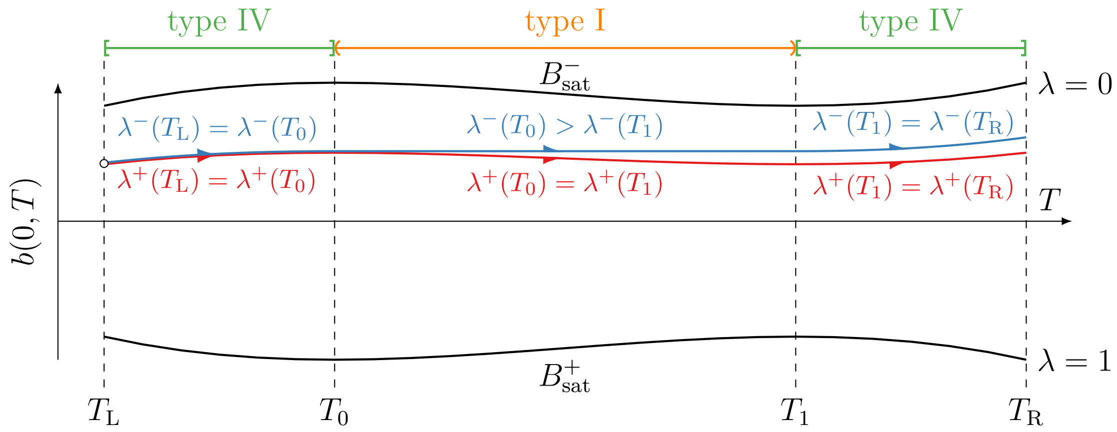

Figure 4.13.: Example of the progression of $\lambda^\pm$ for $h = 0$. The interval (T_0, T_1) is of type I and the rest of type IV. $\lambda^\pm$ diverge in (T_0, T_1) and are constant elsewhere.

Define $\lambda^\pm : [T_\mathrm{L}, T_\mathrm{R}] \to [0,1]$ with $\lambda^\pm(T) = \frac{B^-_\mathrm{sat}(0,T) - p^\pm(T)}{B^-_\mathrm{sat}(0,T) - B^+_\mathrm{sat}(0,T)}$. Paths $p^\pm$ being stable is equivalent to

$$\lambda^+(T_\mathrm{L}) = \lambda^-(T_\mathrm{L}) \text{ and } \lambda^+(T_\mathrm{R}) = \lambda^-(T_\mathrm{R})\,. \tag{4.45}$$

The former is true, by using the same $(0, b_1, T_\mathrm{L}) \in I_T$ as initial value for both paths.

The following procedure is illustrated in Figure 4.13. The interval $[T_\mathrm{L}, T_\mathrm{R}]$ can be partitioned into smaller subintervals with each being of one type only. With Lemmas 4.35 and 4.36 the behavior of $\lambda^\pm$ in each of these subintervals has been proven. The values of $\lambda^\pm$ is examined by successively running through these subintervals.

Regardless, whether the subinterval is of type I or IV, λ^+ is constant. Thus, it holds $\lambda^+(T) = \lambda^+(T_\mathrm{L})$ for all $T \in [T_\mathrm{L}, T_\mathrm{R}]$. This implies that (4.45) can reformulated to the condition $\lambda^-(T_\mathrm{L}) = \lambda^-(T_\mathrm{R})$. This statement will now be contradicted.

Per assumption, interval $[T_\mathrm{L}, T_\mathrm{R}]$ is not of one type only. So it must exists a $T^* \in [T_\mathrm{L}, T_\mathrm{R}]$ of type I. Since the functions $B^\pm_\mathrm{sat}$ are continuously differentiable and type I is defined with strict inequalities w.r.t. $\frac{\partial B^\pm_\mathrm{sat}}{\partial T}$, there exists an open interval $(T_0, T_1) \subset [T_\mathrm{L}, T_\mathrm{R}]$ of type I. According to Lemma 4.36, $\lambda^-(T_0) > \lambda^-(T_1)$ holds.

The exact division into type I and IV of $[T_\mathrm{L}, T_0]$ is not known. Even though, Lemmas 4.35 and 4.36 can be used to get the inequalities $\lambda^-(T_\mathrm{L}) \geq \lambda^-(T_0)$ and $\lambda^-(T_1) \geq \lambda^-(T_\mathrm{R})$.

If the above inequalities are combined, the result is

$$\underbrace{\lambda^-(T_\mathrm{L}) \geq \rlap{$\overbrace{}^{\text{type I only}}$}\lambda^-(T_0)}_{\text{mixed types}} > \underbrace{\lambda^-(T_1) \geq \lambda^-(T_\mathrm{R})}_{\text{mixed types}}\,. \tag{4.46}$$

This contradicts (4.45) and so no set of stable paths besides $p^\pm = 0$ can exist.

□

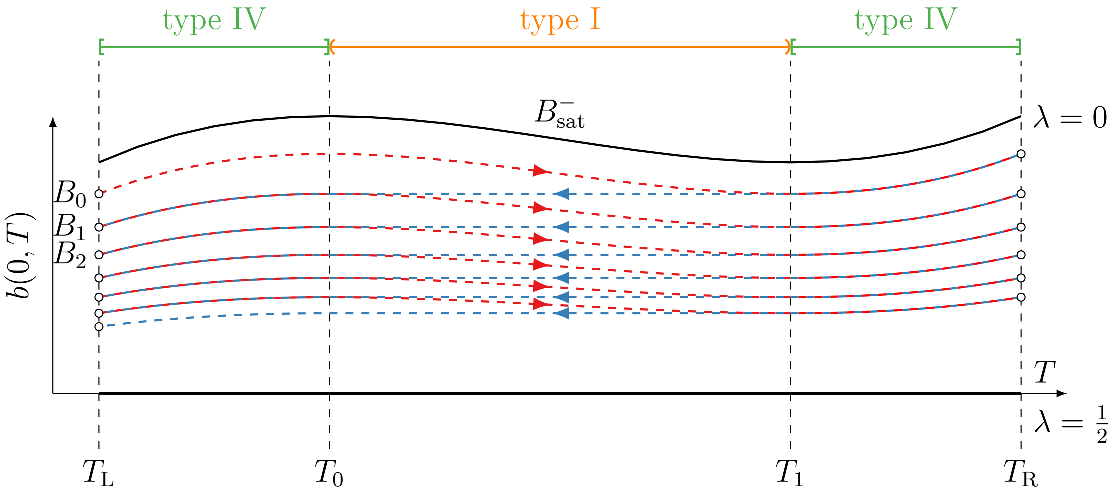

Figure 4.14.: Sketch of the convergence of paths p_i^+ (red) and p_i^- (blue) for $h = 0$. The interval (T_0, T_1) is of type I and the rest of type IV.

Remark 4.39. To conclude this subsection, the convergence properties of a sweeping excitation is proven. Holding the temperature T constant and sweeping in h was already examined in Section 3.2 by Lemma 3.59 and fig. 3.19. Next, $h = 0$ is fixed and T will be sweeping. It will be shown that the thermal extension of the model, behaves very similar to the original model. An example is given in Figure 4.14.

Lemma 4.40: Let $h = 0$. Given nonempty $[T_{\text{L}}, T_{\text{R}}] \subseteq [T_{\min}, T_{\max}]$ and $(0, B_0, T_{\text{L}}) \in I_T$. Define path p_0^- w.r.t. $(0, b_0, T_{\text{L}})$, i.e., it holds $p_0^-(T_{\text{L}}) = B_0$.

For any $k \in \mathbb{N}$, let p_k^+ be defined w.r.t. $\left(0, p_{k-1}^-(T_{\text{L}}), T_{\text{L}}\right)$ and p_k^- w.r.t. $\left(0, p_k^+(T_{\text{R}}), T_{\text{R}}\right)$. The sequence $B_k = p_k^+(T_{\text{L}}) = p_{k-1}^-(T_{\text{L}})$ is convergent with

$$\lim_{k\to\infty} B_k = B_\infty \in \left[B^+_{\text{sat}}(0, T_{\text{L}}), B^-_{\text{sat}}(0, T_{\text{L}})\right]. \tag{4.47}$$

If interval $[T_{\text{L}}, T_{\text{R}}]$ is not solely of type IV, then $B_\infty = 0$ holds.

Proof. If $[T_{\text{L}}, T_{\text{R}}]$ is of type IV only, paths p_k^+ and p_k^- are reversible and thus $B_k = B_0$ for all $k \in \mathbb{N}$ holds.

Now, it is assumed that interval $[T_{\text{L}}, T_{\text{R}}]$ is not solely of type IV. In Lemma 4.38 it was already proven, that $B_0 = 0$ would also result in reversible paths and thus $B_k = B_0$ for all $k \in \mathbb{N}$ holds in this case. So it remains to show that convergence occurs for start values $B_0 \neq 0$. W.l.o.g. it is assumed $B_0 > 0$ using symmetry arguments.

▶ First, it will be proven that the sequence B_k is strictly monotonically decreasing for all $B_0 > 0$. The reasoning is very similar to the proof of Lemma 4.38. Given any $B_k \in \left(0, B^-_{\text{sat}}(0, T_{\text{L}})\right]$. As specified, path p_k^+ is defined w.r.t. $(0, B_k, T_{\text{L}})$ and p_k^- is defined w.r.t. $\left(0, p_k^+(T_{\text{R}}), T_{\text{R}}\right)$. By this definition it holds $p_k^+(T_{\text{R}}) = p_k^-(T_{\text{R}})$. Define $\lambda_k^\pm : [T_{\text{L}}, T_{\text{R}}] \to [0, 1]$ with $\lambda_k^\pm(T) = \frac{B^-_{\text{sat}}(0,T) - p_k^\pm(T)}{B^-_{\text{sat}}(0,T) - B^+_{\text{sat}}(0,T)}$.

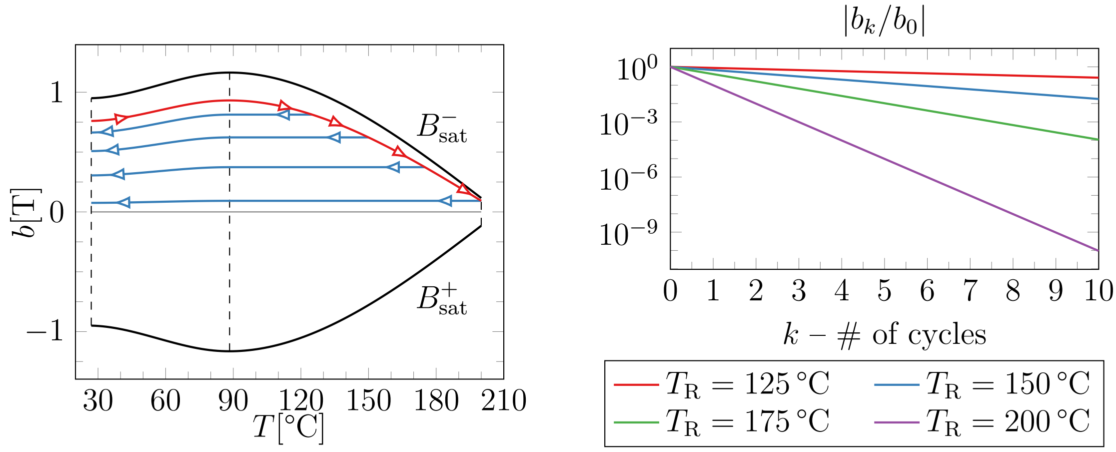

(a) Shown is the first cycle of heating (red) and cooling (blue) for different values of T_R. Note that heating up to $T_\mathrm{R} = 200\,°\mathrm{C}$ significantly reduces the magnetization.

(b) Shown is $|b_k/b_0|$. b_k represent the magnetization at $T = T_\mathrm{L} = 27\,°\mathrm{C}$ after k cycles of heating and cooling.

Figure 4.15.: Shown are results for a sweeping excitation w.r.t. $T \in [T_\mathrm{L}, T_\mathrm{R}]$ for different values of T_R.

Using already proven statements in the proof of Lemma 4.38, it can be concluded that λ_k^+ is constant and λ_k^- is strictly monotonically decreasing. Thus it yields

$$\underbrace{\lambda_k^+(T_\mathrm{L}) = \rlap{$\overbrace{\phantom{\lambda_k^+(T_\mathrm{R}) = \lambda_k^-(T_\mathrm{R})}}^{p_k^+(T_\mathrm{R})=p_k^-(T_\mathrm{R})}$}\lambda_k^+(T_\mathrm{R})}_{\lambda_k^+\ \text{constant}} = \underbrace{\lambda_k^-(T_\mathrm{R}) < \lambda_k^-(T_\mathrm{L})}_{\lambda_k^-\ \text{decreasing}}. \tag{4.48}$$

So finally

$$B_k = \underbrace{p_k^+(T_\mathrm{L}) > p_k^-(T_\mathrm{L})}_{\lambda_k^+(T_\mathrm{L})<\lambda_k^-(T_\mathrm{L})} = B_{k+1} \tag{4.49}$$

applies.

▶ Second, it will be shown that $B_{k+1} > 0$ holds. This results in convergence. The above defined paths $p_k^\pm$ can not cross the paths $p^\pm = 0$. And since they are defined w.r.t. some $B_k > 0$, they are strictly positive on their whole definition domain. Therefore $B_{k+1} > 0$ holds.

□

Application example: aging of permanent magnets

To summarize the behavior of the thermal model, a concrete example is used. For this purpose, different initial situations are used and simulated a sweeping excitation w.r.t. T and constant $h = 0$. As material the one already presented in Figures 4.5, 4.6 and 4.9(a) is used and it is shown again in Figure 4.15(a). This material is hard ferromagnetic, i.e., among other applications suitable as a permanent magnet.

At this point it is emphasized again that only a mathematical analysis of the thermal model is possible here. Unfortunately, there are no measured values available to check the model against. Even though the model may not correspond to real measured data, the comparison of the two approaches from the original and the thermal model is interesting from a mathematical perspective.

The benchmark will initiate the material in the state $(h, b, T) = (0, b_0, 27) \in I_{\mathrm{T}}$ and then in a sweeping fashion increase the temperature to $T_{\mathrm{R}} \in (27, 200]$ and decreasing is back to $T_{\mathrm{L}} = 27\,°\mathrm{C}$. The values b_k with $k \in \mathbb{N}_0$ denotes the magnetic flux density at temperature T_{L} after k cycles of excitation. This corresponds to the approach taken in Lemmas 4.31 and 4.40. Now, the results for different combinations of b_0 and T_{R} will be shown.

1) For $b_0 = 0$, Lemma 4.38 proves that $b_k = 0$ for all $k \in \mathbb{N}_0$ holds, regardless of the choice of T_{R}. A demagnetized material does not gain any magnetization by changing the temperature. This corresponds to the physical expectations.

2) $b_0 = 0.8 \cdot B^{-}_{\mathrm{sat}}(0, 27)$ is chosen. The material is therefore magnetized by 80 % of its maximum value. Now depending on the choice of T_{R} a different behavior occurs. As seen in Figure 4.15(a), at the temperature of $\approx 88\,°\mathrm{C}$ the boundary curves $B^{\pm}_{\mathrm{sat}}$ are changing signs in their derivative. By Definition 4.10 the interval $[27, 88]$ is of type IV and the interval $(88, 200]$ of type I.

In this benchmark $T_{\mathrm{R}} \in (27, 88]$ is chosen. Because the resulting interval $[T_{\mathrm{L}}, T_{\mathrm{R}}]$ is of type IV, the paths p^{+} and p^{-} are reversible, as proven in Lemma 4.26. By Lemma 4.35 the relative vertical position λ is constant. Thus the thermal model is holding the relative magnetization constant, i.e., $b(0, T) = 0.8 \cdot B^{-}_{\mathrm{sat}}(0, T)$ for all $T \in [T_{\mathrm{L}}, T_{\mathrm{R}}]$. This means that heating the material up to a temperature of $88\,°\mathrm{C}$ does not reduce its (relative) magnetization and $b_k = b_0$ for all $k \in \mathbb{N}$ holds.

3) Choosing the same b_0 as in 2), but $T_{\mathrm{R}} \in (88, 200]$. The interval $[T_{\mathrm{L}}, T_{\mathrm{R}}]$ is now of mixed type. By Lemma 4.40 the sequence b_k is convergent with $\lim_{k\to\infty} b_k = 0$. It holds $|b_{k+1}| < |b_k|$ for all $k \in \mathbb{N}_0$. So each cycle of heating and cooling reduces the magnetization of the material, if the temperature exceed $88\,°\mathrm{C}$. The rate of reduction depends on T_{R}. For values $T_{\mathrm{R}} \in \{125\,°\mathrm{C}, 150\,°\mathrm{C}, 175\,°\mathrm{C}, 200\,°\mathrm{C}\}$, the results are shown in Figure 4.15(b). A decrease in the form of $|b_{k+1}| = \alpha |b_k|$ with $\alpha \in (0, 1)$ is recognizable and the α is depending on the choice of T_{R}. For the example shown in Figure 4.15(b), the resulting values of α are presented in Table 4.1.

Table 4.1.: A decrease of the magnetization in the form $|b_{k+1}| = \alpha |b_k|$ can be observed. For different value of T_{R} the resulting α are listed. α is rounded to three decimals.

T_{R} [°C]	125	150	175	200
α	0.873	0.668	0.401	0.099

If the temperature is approaching the Curie temperature, the boundaries $B_{\text{sat}}^{\pm}$ are getting narrower. The Curie temperature is the smallest temperature such that $B_{\text{sat}}^{+} = B_{\text{sat}}^{-}$ holds. This contradicts the definition of the thermal model, in particular (4.9). Nevertheless, it can be concluded that the thermal model successfully reproduce the behavior for heating up almost to the Curie temperature. The magnetization is almost completely lost, if the saturation curves $B_{\text{sat}}^{\pm}$ are almost the same, see Figure 4.15(b) and table 4.1 for an example.

Remark 4.41. In Lemma 4.40 it was proven that $|b_{k+1}| < |b_k|$ holds. The numerical example has shown a loss of magnetization in the form of $|b_{k+1}| = \alpha|b_k|$ with $\alpha \in (0, 1)$. In the next step the decrease pattern is examined more closely. The goal is to derive the factor α only from the saturation curves $B_{\text{sat}}^{\pm}$, i.e., without the actual calculation of any paths p^+ and p^-.

Analysis of the special case $h = 0$ – Part 2

As motivated in Remark 4.41, it will be proven that a sweeping excitation w.r.t. $T \in [T_{\text{L}}, T_{\text{R}}]$ and $h = 0$ results in a sequence $(b_k)_{k\in\mathbb{N}_0}$ with $b_{k+1} = \alpha b_k$ with $\alpha \in (0, 1)$, if the interval $[T_{\text{L}}, T_{\text{R}}]$ is not solely of type IV. The following arguments are structured as follows.

▶ A $\hat{\lambda}$ is defined as an alternative to λ. $\hat{\lambda}$ describes the relative vertical position between the boundary curves $B_{\text{sat}}^{\pm}$. Only the range is adjusted from $\lambda \in [0, 1]$ to $\hat{\lambda} \in [-1, 1]$ and the orientation is reversed. Thus one can transfer previous statements about λ simply to $\hat{\lambda}$. The big advantage of $\hat{\lambda}$ over λ is, however, that one can make very simple statements in the case $h = 0$.

▶ This will exploited directly in the investigation of an interval of solely one type.

▶ Finally, a corresponding α can be explicitly specified for an interval that is not exclusively type IV.

Definition 4.42: Based on λ from (4.11), $\hat{\lambda} : I_{\text{T}} \to [-1, 1]$ is defined with

$$\hat{\lambda}(h, b, T) = -2\lambda(h, b, T) + 1\,. \tag{4.50}$$

For the special case of $h = 0$, (4.50) is equivalent to

$$\hat{\lambda}(0, b, T) = \frac{b}{B_{\text{sat}}^{-}(0, T)} \in [-1, 1]\,. \tag{4.51}$$

Remark 4.43. $\hat{\lambda}$ is actually just another way to describe the relative position of a point $(h, b, T) \in I_{\text{T}}$ between the boundaries $B_{\text{sat}}^{\pm}$. A sketch is given in Figure 4.16.

Remark 4.44. Since $\hat{\lambda}$ can be derived linearly from λ, the previous statements can be transferred with only minimal changes. In particular, if λ is constant along a path p, this is also true for $\hat{\lambda}$.

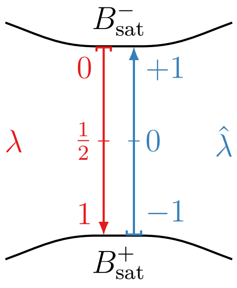

Figure 4.16.: A sketch of the relation of λ and $\hat{\lambda}$.

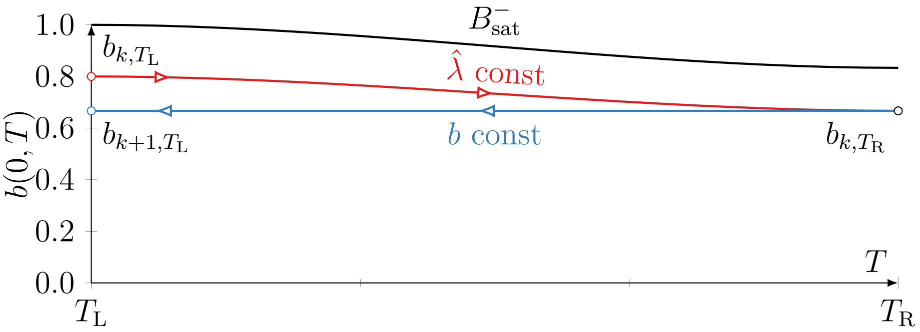

Figure 4.17.: A sketch of the proof of Lemma 4.45. The path p^+ is shown in red and p^- in blue.

Lemma 4.45: Let $[T_{\mathrm{L}}, T_{\mathrm{R}}] \subseteq [T_{\mathrm{min}}, T_{\mathrm{max}}]$ with $T_{\mathrm{L}} < T_{\mathrm{R}}$ and $(T_{\mathrm{L}}, T_{\mathrm{R}})$ of type I. Hold $h = 0$ constant. Starting in $(0, b_0, T_{\mathrm{L}}) \in I_{\mathrm{T}}$ and sweeping w.r.t. $T \in [T_{\mathrm{L}}, T_{\mathrm{R}}]$ results in the sequence $(b_k)_{k\in\mathbb{N}_0}$ with b_k denoting the magnetic flux density b at temperature T_{L} after k cycles of heating and cooling. It holds $b_{k+1} = \alpha b_k$ for all $k \in \mathbb{N}_0$ with $\alpha = \frac{B^-_{\mathrm{sat}}(0,T_{\mathrm{R}})}{B^-_{\mathrm{sat}}(0,T_{\mathrm{L}})} \in (0, 1)$.

Proof. A sketch of the proof and the notation used is given in Figure 4.17.

First, a more precise notation is introduced. Let denote b_k as $b_{k,T_{\mathrm{L}}}$ to emphasize the evaluation at temperature T_{L}. Sweeping w.r.t. $T \in [T_{\mathrm{L}}, T_{\mathrm{R}}]$ results in two processes: Initially the increase of the temperature from T_{L} to T_{R} and then the decrease back to T_{L}.

For any $k \in \mathbb{N}_0$, the starting point is given by $(h, b, T) = (0, b_k, T_{\mathrm{L}}) \in I_{\mathrm{T}}$ and let p^+ be defined w.r.t. this point. Along path p^+, λ is constant as proven in Lemma 4.36. It also follows directly that $\hat{\lambda}$ is also constant along p^+. Let $b_{k,T_{\mathrm{R}}} = p^+(T_{\mathrm{R}})$. Define p^- w.r.t. $(0, b_{k,T_{\mathrm{R}}}, T_{\mathrm{R}})$. Path p^- is constant on the interval $[T_{\mathrm{L}}, T_{\mathrm{R}}]$ by Definition 4.6. The overall result is thus:

$$\begin{aligned} \hat{\lambda}(T_{\mathrm{L}}) = \hat{\lambda}(T_{\mathrm{R}}) \quad &\Leftrightarrow \quad \frac{b_{k,T_{\mathrm{L}}}}{B^-_{\mathrm{sat}}(0,T_{\mathrm{L}})} = \frac{b_{k,T_{\mathrm{R}}}}{B^-_{\mathrm{sat}}(0,T_{\mathrm{R}})} \\ &\Leftrightarrow \quad \frac{B^-_{\mathrm{sat}}(0,T_{\mathrm{R}})}{B^-_{\mathrm{sat}}(0,T_{\mathrm{L}})} b_{k,T_{\mathrm{L}}} = b_{k,T_{\mathrm{R}}} = b_{k+1,T_{\mathrm{L}}} \,. \end{aligned} \tag{4.52}$$

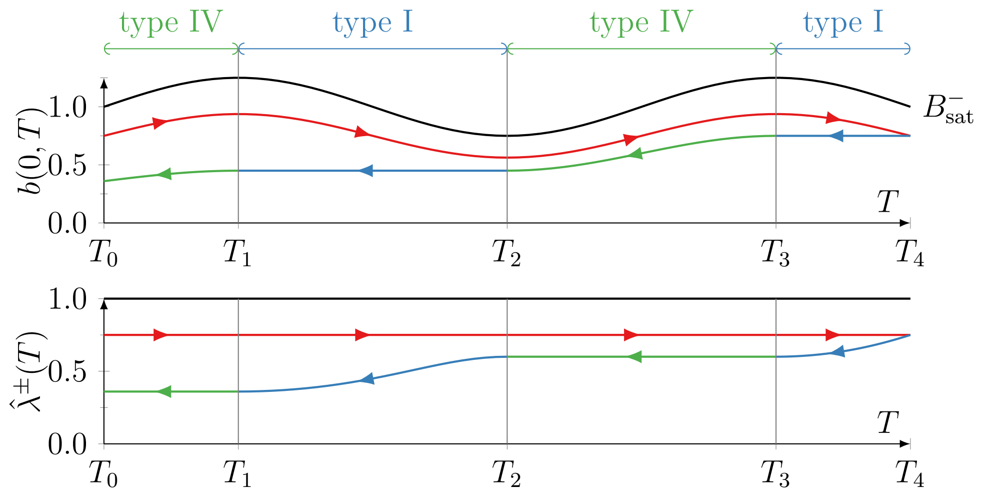

Figure 4.18.: A sketch of the proof of Lemma 4.47. Values based on path p^+ are shown in red and p^- in blue and green.

Because interval $[T_\mathrm{L}, T_\mathrm{R}]$ is of type I, B_{sat}^{-} is strictly monotonously decreasing and thus $B_{\mathrm{sat}}^{-}(0, T_\mathrm{L}) > B_{\mathrm{sat}}^{-}(0, T_\mathrm{R})$ holds. With $h = 0$, B_{sat}^{-} is positive, i.e., $B_{\mathrm{sat}}^{-} > 0$. This leads to the statements $\alpha = \frac{B_{\mathrm{sat}}^{-}(0,T_\mathrm{R})}{B_{\mathrm{sat}}^{-}(0,T_\mathrm{L})} \in (0, 1)$ and $b_{k+1} = \alpha \cdot b_k$. ☐

Remark 4.46. Lemma 4.45 is now to be extended for intervals of arbitrary mixed type.

Lemma 4.47: Let $[T_\mathrm{L}, T_\mathrm{R}] \subseteq [T_{\min}, T_{\max}]$ with $T_\mathrm{L} < T_\mathrm{R}$. Hold $h = 0$ constant.

Let $T_\mathrm{L} = T_0 < \ldots < T_n = T_\mathrm{R}$ be a subdivision of $[T_\mathrm{L}, T_\mathrm{R}]$ such that for all $j \in \{0, \ldots, n-1\}$ the interval (T_j, T_{j+1}) is of one type only.

Starting in $(0, b_0, T_\mathrm{L}) \in I_\mathrm{T}$ and sweeping w.r.t. $T \in [T_\mathrm{L}, T_\mathrm{R}]$ results in the sequence $(b_k)_{k \in \mathbb{N}_0}$ with b_k denoting the magnetic flux density b at temperature T_L after k cycles of heating and cooling. It holds

$$b_{k+1} = \alpha \cdot b_k \text{ for all } k \in \mathbb{N}_0 \text{ with } \alpha = \prod_{\substack{j \in \{0,\ldots,n-1\} \\ (T_j, T_{j+1}) \text{ type I}}} \frac{B_{\mathrm{sat}}^{-}(0, T_{j+1})}{B_{\mathrm{sat}}^{-}(0, T_j)} \in (0, 1]\,. \tag{4.53}$$

Proof. The approach is strongly based on the proof of Lemma 4.45. A sketch of the proof is given in Figure 4.18 and an overview of the used statements is presented in Table 4.2.

Let $(h, b, T) = (0, b_k, T_\mathrm{L}) \in I_\mathrm{T}$ be given. Define path p^+ w.r.t. $(0, b_k, T_\mathrm{L})$ and path p^- w.r.t. $(0, p^+(T_\mathrm{R}), T_\mathrm{R})$. These paths represent the forward and backward paths through the entire interval $[T_\mathrm{L}, T_\mathrm{R}]$. It applies $b_k = p^+(T_\mathrm{L})$ and $b_{k+1} = p^-(T_\mathrm{L})$. Let $\hat{\lambda}^{\pm}(T)$ denote $\hat{\lambda}$ along the paths $p^{\pm}$, i.e., $\hat{\lambda}^{\pm}(T) = \hat{\lambda}(0, p^{\pm}(T), T)$.

The interval $[T_\mathrm{L}, T_\mathrm{R}]$ is subdivided into (T_j, T_{j+1}) for $j \in \{0, \ldots, n-1\}$ like described in Lemma 4.47. Existence of such a partition was proven in Lemma 4.11. Now,

Table 4.2.: Summary of the behavior of paths $p^{\pm}$ and $\hat{\lambda}$ for $h = 0$ on an interval (T_j, T_{j+1}) of one type only.

type of (T_j, T_{j+1})	I	IV
$p^+(T)$	$p^+(T_j) = \frac{B^-_{\text{sat}}(0,T_j)}{B^-_{\text{sat}}(0,T_{j+1})} p^+(T_{j+1})$	$p^+(T_j) = \frac{B^-_{\text{sat}}(0,T_j)}{B^-_{\text{sat}}(0,T_{j+1})} p^+(T_{j+1})$
$\hat{\lambda}^+(T)$	$\hat{\lambda}^+(T_j) = \hat{\lambda}^+(T_{j+1})$	$\hat{\lambda}^+(T_j) = \hat{\lambda}^+(T_{j+1})$
$p^-(T)$	$p^-(T_j) = p^-(T_{j+1})$	$p^-(T_j) = \frac{B^-_{\text{sat}}(0,T_j)}{B^-_{\text{sat}}(0,T_{j+1})} p^-(T_{j+1})$
$\hat{\lambda}^-(T)$	$\hat{\lambda}^-(T_j) = \frac{B^-_{\text{sat}}(0,T_{j+1})}{B^-_{\text{sat}}(0,T_j)} \hat{\lambda}^-(T_{j+1})$	$\hat{\lambda}^-(T_j) = \hat{\lambda}^-(T_{j+1})$

it is iterated through the individual intervals (T_j, T_{j+1}) using the statements from Table 4.2.

Starting at $T = T_\text{L} = T_0$ on path p^+, $\hat{\lambda}^+$ is constant on the interval $[T_0, T_1]$ regardless whether it is type I or IV. The same is true on any interval $[T_j, T_{j+1}]$. If this is repeated until $T_n = T_\text{R}$ is reached,

$$\hat{\lambda}^+(T_\text{L}) = \hat{\lambda}^+(T_\text{R}) \tag{4.54}$$

is obtained.

Now, the intervals $[T_j, T_{j+1}]$ are going through backwards. If the interval is of type I, it holds

$$\hat{\lambda}^-(T_j) = \underbrace{\frac{B^-_{\text{sat}}(0, T_{j+1})}{B^-_{\text{sat}}(0, T_j)}}_{=\alpha_j \in (0,1)} \hat{\lambda}^-(T_{j+1}) \,. \tag{4.55}$$

For type I it holds $0 < B^-_{\text{sat}}(0, T_{j+1}) < B^-_{\text{sat}}(0, T_j)$.

If the interval $[T_j, T_{j+1}]$ is of type IV, it holds

$$\hat{\lambda}^-(T_j) = \hat{\lambda}^-(T_{j+1}) \,. \tag{4.56}$$

So in this case $\alpha_j = 1$ is defined.

Concatenating all the intervals $[T_j, T_{j+1}]$ yields

$$\hat{\lambda}^-(T_\text{L}) = \underbrace{\left(\prod_{j \in \{0,\ldots,n-1\}} \alpha_j \right)}_{=\alpha} \hat{\lambda}^-(T_\text{R}) = \alpha \hat{\lambda}^+(T_\text{L}) \,. \tag{4.57}$$

An alternative formulation of α is given by

$$\alpha = \prod_{\substack{j \in \{0,\ldots,n-1\} \\ (T_j, T_{j+1}) \text{ type I}}} \underbrace{\frac{B^-_{\text{sat}}(0, T_{j+1})}{B^-_{\text{sat}}(0, T_j)}}_{\in (0,1)} \in (0, 1] \,. \tag{4.58}$$

If there is no interval (T_j, T_{j+1}) of type I, α is equal to one. If now the explicit definitions of $\hat{\lambda}^+$ and $\hat{\lambda}^-$ is used, it yields

$$\hat{\lambda}^+(T_\mathrm{L}) = \frac{p^+(T_\mathrm{L})}{B^-_\mathrm{sat}(0, T_\mathrm{L})} = \frac{b_k}{B^-_\mathrm{sat}(0, T_\mathrm{L})}\,, \quad \hat{\lambda}^-(T_\mathrm{L}) = \frac{p^-(T_\mathrm{L})}{B^-_\mathrm{sat}(0, T_\mathrm{L})} = \frac{b_{k+1}}{B^-_\mathrm{sat}(0, T_\mathrm{L})}\,. \tag{4.59}$$

Combining (4.57) and (4.59) gives

$$b_{k+1} = \alpha \cdot b_k \tag{4.60}$$

with α defined in (4.58). ☐

4.2.5. Interim Conclusion & Further Remarks

At this point the thermal model is evaluated. In doing so, mathematical aspects are addressed and the model is evaluated against the physical background.

▶ From a mathematical point of view, the model is very satisfactory because of the following points.

▷ The thermal model is mathematically well-defined. For all valid states I_T it is defined and it was proven that analytical solutions cannot leave this domain. It is important to note that this is only true if the model is applied in the correct direction (paths p^+ if $\Delta T > 0$ and p^- if $\Delta T < 0$).

For analysis purposes, the model is deliberately applied backwards (paths p^+ if $\Delta T < 0$ and p^- if $\Delta T > 0$) and partially continued it outside of I_T. In pure application, however, this is not relevant.

▷ The approaches used are very similar to the original model. By making slight adjustments, these can be applied to the thermal problem. From a mathematical point of view, it is interesting to see how these changes affect the behavior of the solutions (paths $p^\pm$). More different versions could be created, studied and applied to other problems.

▷ The result is a model that defines different behaviors for the four directions $\Delta h \gtrless 0$, $\Delta T \gtrless 0$. The thermal model is designed as an extension of the original one. If the temperature is assumed to be constant, the original model results again.

▷ Using sweeping excitation to interact with the model, it was demonstrated that convergent behavior is exhibited for h and T (with $h = 0$) directions. In general, the model proves to be well-behaved and stable.

▶ From a physical point of view, the model was evaluated in such a way that it roughly represents the physical conditions and benchmarks presented in Section 4.2.1. But there are also aspects that would require further investigation and possible adjustments. In the context of the dissertation it was concentrated on the mathematical aspects and these inconsistencies are accepted. Nevertheless, the analysis allows the reader a critical look at the model. Finally, a few aspects shall be listed.

$\triangleright$ The model shown remains purely academic and it cannot be validated by means of experimental measurements. However, it was possible to mathematically investigate and evaluate the model to the extent that possibilities of a measurement arises. Criteria has been developed by which it can be identified when reversible and non-reversible behavior appears. For the special case of $h = 0$ and a sweeping excitation, the modeled demagnetization can be quantified.

$\triangleright$ The natural limit of the Curie temperature T_{C} is covered by the model. Mathematically, the model is defined up to but exclusive to this temperature. If the Curie temperature is reached, B_{sat}^{+} and B_{sat}^{-} are identical and the model is no longer applicable. For all lower temperatures, however, the model is applicable and analytical solutions take into account increasingly narrower $B_{\mathrm{sat}}^{\pm}$. From a numerical point of view, there could be problems if $B_{\mathrm{sat}}^{\pm}$ are very close to each other. But this is already true for the original model.

From a physical point of view, the thermal model reproduces the transition suitably. If $B_{\mathrm{sat}}^{\pm}$ are identical, the relation

$$b = f(h, T) \tag{4.61}$$

with a suitable function f can be applied. If a limit analysis $T \to T_{\mathrm{C}}$ is performed whereby $B_{\mathrm{sat}}^{\pm}$ converge to each other, the difference between the directional derivatives $\frac{\partial b}{\partial T}$ for $\Delta T \gtrless 0$ converges to zero.

But if there is no difference whether $\Delta T < 0$ or $\Delta T > 0$ is considered, then

$$\frac{\partial b}{\partial T} = \frac{\partial f}{\partial T} \tag{4.62}$$

is a reasonable modeling approach. Thus, the thermal model reverts to a normal definition based on a function f as shown in (4.61) in the limit $T \to T_{\mathrm{C}}$.

$\triangleright$ In the physical motivation it was mentioned that magnetic fields do not amplify without excitation. Yet it is observed – although $h = 0$ holds – that the modeled b field can increase in the absolute sense, if the temperature T is increased (type I). The model take the assumption into account in a very special way and the b field does not grow in the relative sense. It was proven that λ does not change in this case. In the relative reference to the maximum possible magnetization ($B_{\mathrm{sat}}^{\pm}$), b does not increase.

How exactly real materials behave in this situation could and would have to be investigated by experimental measurements and compared with the model. At this point, it remains open whether the model depicts this correctly.

$\triangleright$ If there is no excitation, i.e., $h = 0$, and the temperature reaches approximately the Curie temperature, a permanent magnet permanently loses part of its magnetization. This is reflected in the model as far as it goes. It was proven, that sweeping w.r.t. temperature with intervals of type IV converges to the solution $b = 0$.

So a one-time sweep cycle maps this. However, the model reduces the magnetization by a percentage value in each cycle. This behavior may be in conflict with the given physical motivation. The basic motivation is based on energy levels and the alignment of the Bloch walls and Weiß domain that can be achieved with them.

If the temperature is sweeped between T_0 and T_1, the same maximal energy level is always reached at T_1. According to the model, each cycle would change the orientation toward one that is more favorable in terms of energy, resulting in a smaller b field. No motivation – why in each new cycle an even more optimized orientation can be found – could be stated. Since the maximum achievable energy, determined by T_1, does not change, it can be argued that the most optimal orientation must already be reached after the first cycle.

The basic behavior of the model with w.r.t. $h = 0$ and changing the temperature is considered to be suitable. But the fact that the weakening of the magnetization shows up in each cycle of a sweeping excitation needs further investigation, which is unfortunately not in the scope of this thesis.

5 Simulation of a Benchmark Problem with the Finite Difference Method

In order to discuss the feasibility and aspects of the used implementation, a benchmark problem consisting of two coupled simulations will be presented in this section. A schematic overview of the structure of the benchmark problem is given in Figure 5.1. This illustration already somewhat foreshadows the sections to come.

The first simulation is a magnetic field simulation. This simulation will use Tellinen's model from Section 3.1 for the integration of the hysteresis effect. At this point the embedding of the model into the spatial simulation is of special interest. Secondly, a heat simulation describes the diffusion process of the temperature T. The loss model from Section 4.1 is applied. Analyzing the results of the magnetic simulation, it integrates the magnetic hysteresis losses as source terms into the heat simulation. The thermal extension of Tellinen's model from Section 4.2 takes into account the resulting temperature changes and ensures that a valid state is permanently guaranteed for Tellinen's model. The result is a coupled simulation covering the effects of hysteresis, hysteresis losses and temperature diffusion.

For both simulations the respective fundamental equation is a parabolic partial differential equation. The numerical approach in both cases is the method of finite differences.

First the general benchmark problem is presented. Then the underlying grids are defined as a preparation for the individual simulations. Next, all necessary steps and equations for the magnetic field and heat simulations are presented. Other aspects of the coupling of the simulations are also discussed. Finally, numerical results are presented and discussed.

5.1. Overview of the Benchmark Problem

The benchmark problem basically consists of an infinite long copper conductor encased in an iron cover, as shown in Figure 5.2. The materials copper and iron are representative for materials without hysteresis and ferromagnetic with hysteresis, respectively. The materials are numbered with I and II. Overall, the focus will be put on an academic example. However, the chosen parameters are based as good as possible on physically meaningful and real measurements.

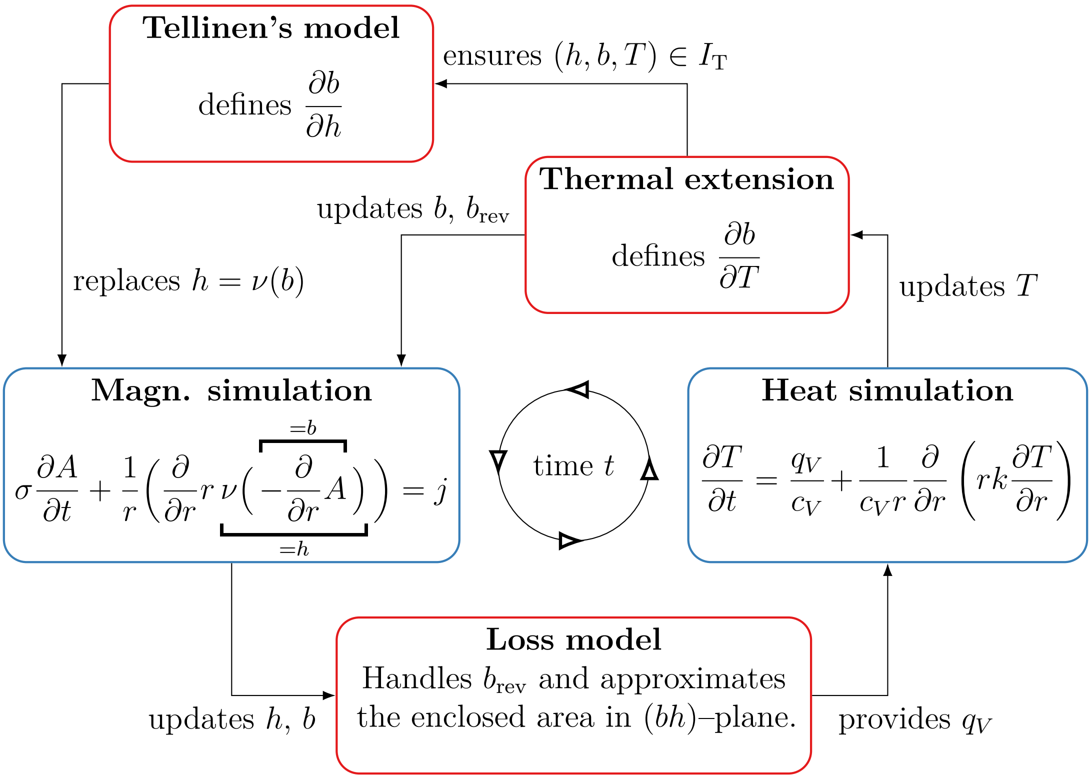

Figure 5.1.: Schematic structure of the benchmark problem.

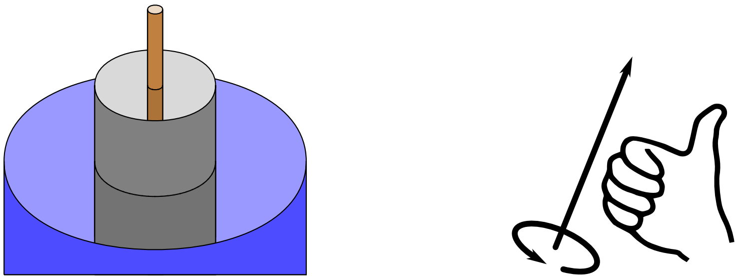

Figure 5.2.: Left: Visual overview of the benchmark problem. The copper conductor is shown in brown, the iron sheath in gray and the surrounding air in blue. Right: The expected shape of the magnetic fields based on the right hand rule. [3]

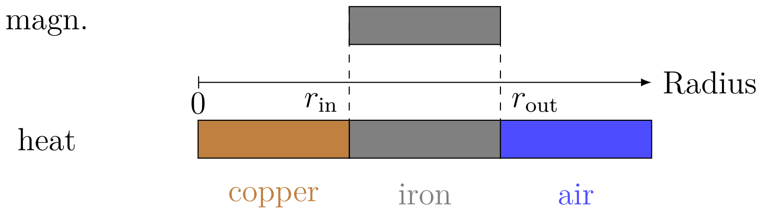

Figure 5.3.: Overview of the mathematical domains of the benchmark problem. Note that the magnetic simulation is only applied on the interval $[r_{\text{in}}, r_{\text{out}}]$. The heat simulation covers the complete domain $[0, r_{\text{out}}]$.

The benchmark problem will be described in cylindrical coordinates (r, φ, z). Along the z-axis all parameters and variables are assumed to be constant. The current density j is restricted to the z-axis, i.e., $\vec{j} = \begin{pmatrix} 0 & 0 & j_z \end{pmatrix}^\top$. Using the right-hand rule determines that the fields $\vec{B}$ and $\vec{H}$ have no z component. Furthermore the benchmark problem is assumed to be axis-symmetric w.r.t. the z-axis. This assumption additionally eliminates the radial component of the fields. Overall, the fields exhibit only an angular part, i.e., $\vec{B} = \begin{pmatrix} 0 & b & 0 \end{pmatrix}^\top$ and $\vec{H} = \begin{pmatrix} 0 & h & 0 \end{pmatrix}^\top$. The corresponding vector potential results in $\vec{A} = \begin{pmatrix} 0 & 0 & A_z \end{pmatrix}^\top$. Hence by the symmetry w.r.t. the z-axis and the being constant along z, these variables and parameters are only dependent on the radius r and time t. This allows to reduce the problem to scalar quantities. For the application of Tellinen's model this is an important prerequisite. Also the heat equation can be reduced to a one dimensional problem. Details are shown in the corresponding sections.

The interval $[0, r_{\text{out}}]$ is the complete computational domain. The magnetic simulation is restricted to the domain of iron at $[r_{\text{in}}, r_{\text{out}}]$ with $0 < r_{\text{in}} < r_{\text{out}}$. Copper is allocated at $[0, r_{\text{in}}]$. The heat simulation is carried out on the whole domain, but has to take into account the material transition at $r = r_{\text{in}}$. An overview of the setting is given in Figure 5.3.

5.2. Discretization Grids: Definition and Alignment

In this section, the grids used are defined first. A more detailed motivation and justification for the grids follow later in the corresponding sections. A visual illustration of the grid alignment is shown in Figure 5.4.

For both – thermal and magnetic – simulations, an offset grid is used in addition to the standard grid. The respective variables and parameters are each assigned to one of the grids. The magnetic offset grid is aligned with the standard thermal grid to ensure that both simulations are as perfectly matched as possible. Thus, all temperature-dependent parameters of the magnetic simulation and the loss model are superimposed with the temperature from the thermal simulation. This means that no further steps (such as interpolation) need to be performed to couple these two systems.

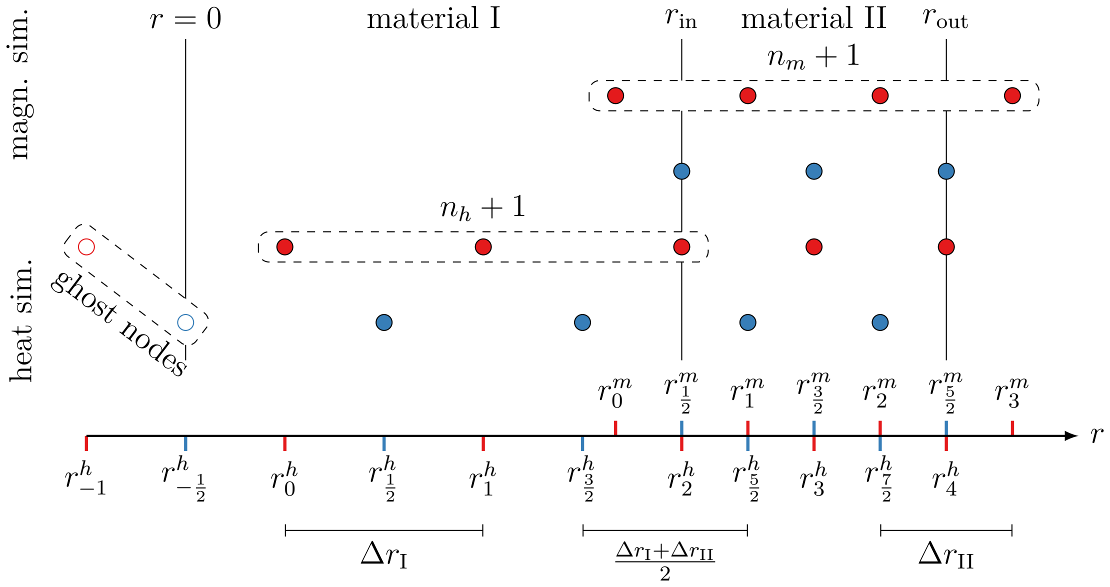

Figure 5.4.: Visualization of the grid alignment. The standard grid is shown in red, the offset grid in blue and ghost nodes marked explicitly. This example is based on $n_h = 2$ and $n_m = 3$.

The magnetic simulation is only defined on the domain $[r_{\text{in}}, r_{\text{out}}]$ while the thermal one is defined on $[0, r_{\text{out}}]$. The thermal simulation needs special grid point placements at the origin $r = 0$ and at the material interface $r = r_{\text{in}}$. To easily match these conditions, two radial grid sizes Δr_{I} and Δr_{II} are introduced. Unfortunately, this makes the material interface a bit more difficult because in addition to the non-constant parameters, different grid sizes also occur. In terms of time, both simulations are based on the same equidistant grid $t_j = j \cdot \Delta t$.

Let $n_m + 1$ be the number of standard grid points of the magnetic simulation and let n_h be the number of additional grid points of the thermal simulation on the domain $(0, r_{\text{in}})$. The standard grid of the thermal simulation has $n_m + n_h$ grid points. This results in the step sizes

$$\Delta r_{\text{I}} = \frac{r_{\text{in}}}{n_h + \frac{1}{2}}\,, \qquad \Delta r_{\text{II}} = \frac{r_{\text{out}} - r_{\text{in}}}{n_m - 1}\,. \tag{5.1}$$

Let the magnetic grid be defined by:

$$\text{standard} \qquad r_i^m = r_{\text{in}} + \left(i - \frac{1}{2}\right)\Delta r_{\text{II}} \qquad \text{for } i \in \{0, \dots, n_m\} \tag{5.2a}$$

$$\text{offset} \qquad r_{i+\frac{1}{2}}^m = r_{\text{in}} + i\Delta r_{\text{II}} \qquad \text{for } i \in \{0, \dots, n_m - 1\} \tag{5.2b}$$

And the thermal grid by:

$$\text{standard} \qquad r_i^h = \begin{cases} \left(i + \frac{1}{2}\right)\Delta r_{\text{I}} & \text{for } i \in \{0, \dots, n_h - 1\} \\ r_{\text{in}} + (i - n_h)\Delta r_{\text{II}} & \text{for } i \in \{n_h, \dots, n_m + n_h - 1\} \end{cases} \tag{5.3a}$$

$$\text{offset} \quad r_{i+\frac{1}{2}}^h = \begin{cases} (i + 1)\,\Delta r_{\text{I}} & \text{for } i \in \{0, \dots, n_h - 1\} \\ r_{\text{in}} + (i + \frac{1}{2} - n_h)\Delta r_{\text{II}} & \text{for } i \in \{n_h, \dots, n_m + n_h - 2\} \end{cases} \tag{5.3b}$$

Remark 5.1. The standard and the offset grid of the magnetic simulation are equidistant with step size Δr_{II}. The thermal standard grid only has the grid sizes Δr_{I} and Δr_{II}. But the thermal offset grid has an irregular grid size of $\frac{\Delta r_{\mathrm{I}}+\Delta r_{\mathrm{II}}}{2}$ between $r^h_{n_h-\frac{1}{2}}$ and $r^h_{n_h+\frac{1}{2}}$. Furthermore, $r^h_{n_h}$ is generally not centered between $r^h_{n_h-\frac{1}{2}}$ and $r^h_{n_h+\frac{1}{2}}$.

By construction all grid points r^h_i and $r^h_{i+\frac{1}{2}}$ are positive. The ghost nodes r^h_{-1} and $r^h_{-\frac{1}{2}}$ are considered separately in Section 5.4.3. To ensure that $r^m_0 > 0$ holds, the condition

$$n_m > 1 + \frac{1}{2}\frac{r_{\mathrm{out}} - r_{\mathrm{in}}}{r_{\mathrm{in}}} \tag{5.4}$$

must be fulfilled.

Remark 5.2. For ease of notation, a subscript of i will always denote the spatial index and a superscript of j the time index, e.g. $b^j_i \approx b(r = r_i, t = t_j)$.

In the following section the magnetic simulation and in the next but one section the thermal simulation will be investigated in detail. The motivation and reasons for the special choice of the grids are also discussed.

5.3. Magnetic Field Simulation

The magnetic field simulation is based on the Curl-Curl Equation in cylindrical coordinates (2.13) with corresponding boundary conditions. The used grid r^m with grid size $\Delta r = \Delta r_{\mathrm{II}}$ is already defined in the previous Section 5.2.

The unknowns A_i and σ are assigned to the standard grid r^m_i. σ is assumed to be constant with $\sigma \in \mathbb{R}^+_0$. The quantities h and b on the other hand are placed on the offset grid $r^m_{i+\frac{1}{2}}$. An overview is given in Figure 5.5. At this point the function ν remains undefined. Approaches how to replace ν have already been presented in Section 3.3.

The following applies by the method of finite difference with implicit backward difference in time:

$$b^{j+1}_{i+\frac{1}{2}} = \frac{A^{j+1}_i - A^{j+1}_{i+1}}{\Delta r} \quad \text{for } i \in \{0, \ldots, n_m - 1\}, \tag{5.5a}$$

$$h^{j+1}_{i+\frac{1}{2}} = \nu^{j+1}_{i+\frac{1}{2}}\left(b^{j+1}_{i+\frac{1}{2}}\right) \quad \text{for } i \in \{0, \ldots, n_m - 1\}, \tag{5.5b}$$

$$\sigma\frac{A^{j+1}_i - A^j_i}{\Delta t} + \frac{1}{r_i}\left(\frac{r_{i+\frac{1}{2}}h^{j+1}_{i+\frac{1}{2}} - r_{i-\frac{1}{2}}h^{j+1}_{i-\frac{1}{2}}}{\Delta r}\right) = 0 \quad \text{for } i \in \{1, \ldots, n_m - 1\}. \tag{5.5c}$$

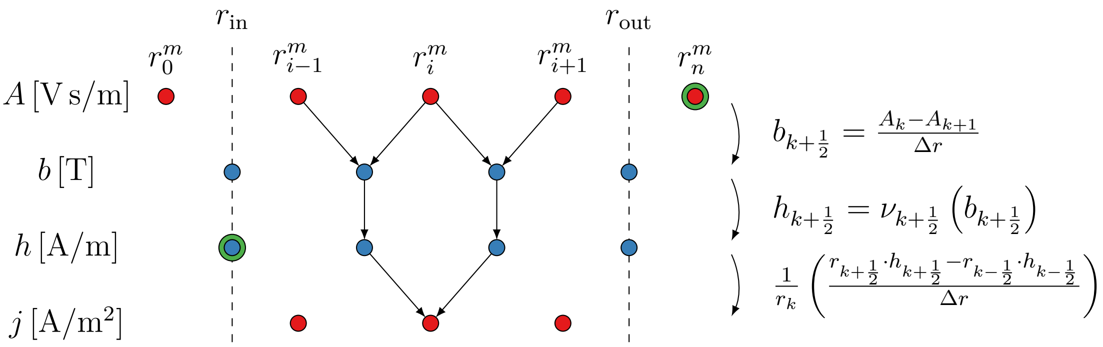

Figure 5.5.: Visualization of the grid used in the magnetic field simulation. The primary grid is shown in red, the offset grid in blue and boundary conditions marked in green. In addition, the associated quantities and equations are assigned to the grids.

The resulting system is "tridiagonal", i.e., solving (5.5) for i is only based on the unknowns A_{i-1}, A_i, A_{i+1}. However, whether the resulting system is linear or non-linear depends on the choice of ν.

In order for this to result in a well defined system, appropriate boundary conditions need to be worked out. This is done in the following Section 5.3.1. But also there ν is not determined in more detail and at first, it is still regarded as an unknown function. To investigate this issue in more detail, different approaches from Section 3.3 for ν are considered afterwards in Sections 5.3.2 and 5.3.3. Unfortunately, it will turn out that not all approaches are successful.

5.3.1. Reducing the Computational Domain via Boundary Conditions

As foreshadowed in Section 5.2, the magnetic field simulation shall not be performed on the entire definition domain. Instead, the simulation is restricted in the spatial sense to the interval $[r_{\text{in}}, r_{\text{out}}]$, i.e., to the iron only. The embedding in the overall simulation is done by suitable boundary conditions, which are derived in this section.

The specially constructed benchmark has already been transformed into cylindrical coordinates and reduced to scalar quantities in Section 2.1.5. This resulted in the partial differential equation (2.13), which is now extended by boundary conditions.

For this kind of problem at least one of the boundary conditions must be of Dirichlet type to ensure a unique solution. The inner boundary at $r = r_{\text{in}}$ will take into account the applied current in the copper domain. Therefore, the outer boundary condition at $r = r_{\text{out}}$ is set as a homogeneous Dirichlet condition, i.e., $A\Big|_{r=r_{\text{out}}} = 0$.

At first, a simplified example to illustrate the assumptions and relationships is discussed. Then this insight is applied to the benchmark problem.

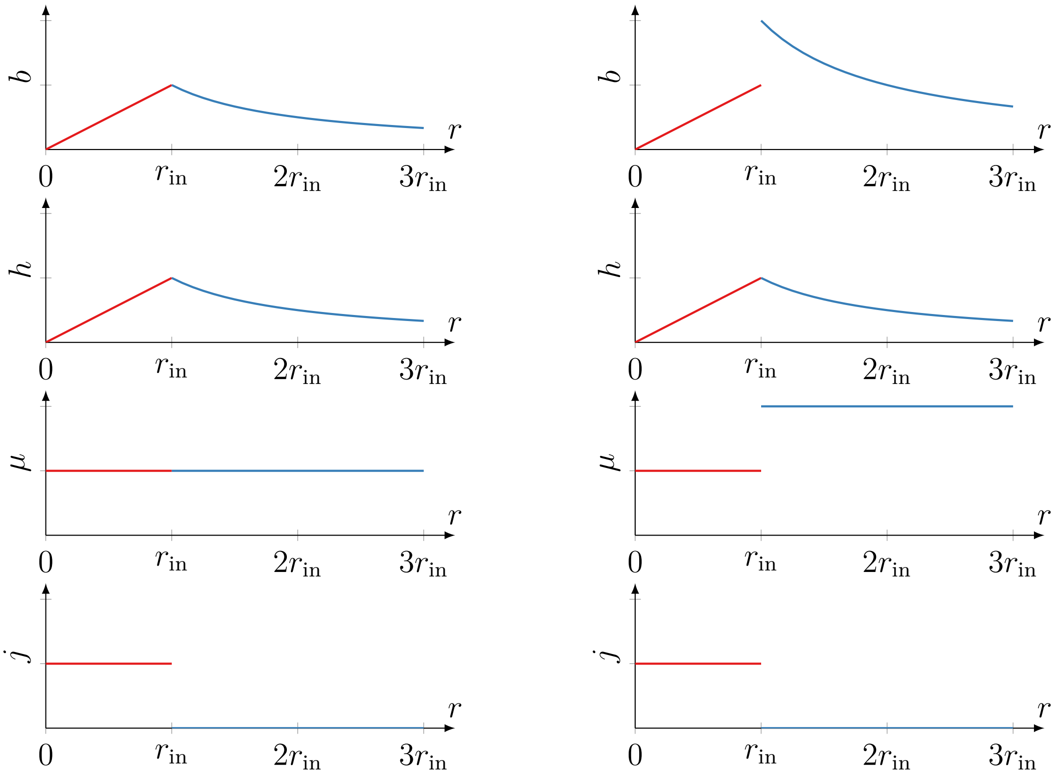

(a) μ constant (b) μ piece wise constant

Figure 5.6.: Tangential components of the magnetic fields at a material interface.

One of the popular examples from the introductory literature for electromagnetism is the magnetic field of a current-carrying conductor. This corresponds approximately to the benchmark problem, if the iron sheath is omitted. The same derivation is used for the cylindrical coordinates and reduction to scalar quantities as before. The relation $b = \mu \cdot h$ is assumed with μ as constant at first and second as piece wise constant.

This segment works towards two different statements. First, which field results from the current-carrying conductor and second, which conditions must apply at a material transition.

For a simplified case, the solution of the magnetic field of a current-carrying conductor is known analytically. In this simplified case, a static consideration is assumed, i.e., $\frac{\partial A}{\partial t} = 0$. This can be alternatively simulated by using $\sigma = 0$. Furthermore, a uniform distribution of the current is assumed and the current is restricted it to the area of the copper, i.e., to $[0, r_{\text{in}})$. Assuming $\mu = \mu_0$ over the whole domain, an applied current I (not current density j) creates the fields

$$b_{\text{tang}}(r) = \begin{cases} \dfrac{\mu_0 I}{2\pi r_{\text{in}}^2} r & \text{, if } r < r_{\text{in}} \\ \dfrac{\mu_0 I}{2\pi} \dfrac{1}{r} & \text{, if } r \geq r_{\text{in}} \end{cases}, \qquad h_{\text{tang}}(r) = \begin{cases} \dfrac{I}{2\pi r_{\text{in}}^2} r & \text{, if } r < r_{\text{in}} \\ \dfrac{I}{2\pi} \dfrac{1}{r} & \text{, if } r \geq r_{\text{in}} \end{cases} \tag{5.6}$$

with b_{tang}, h_{tang} being the tangential components and the other components are zero. This example is visualized in Figure 5.6(a).

Now, a material transition is added. For this introductory example, μ is defined as

$$\mu = \mu(r) = \begin{cases} \mu_0 & \text{, if } r < r_{\text{in}} \\ 2\mu_0 & \text{, if } r \geq r_{\text{in}} \end{cases} . \tag{5.7}$$

In general, the fields $\vec{H}$, $\vec{B}$ at a material transition behave differently. More precisely, the tangential and normal components are subject to different calculations. Even if in the example only tangential transitions are needed, both are briefly explained based on [134, 137].

At a material transition the *normal* component of the $\vec{B}$ field is continuous. Conversely, if the μ values of the materials differ, this means that the normal component of the $\vec{H}$ field is not continuous.

The consideration of the *tangential* component takes into account surface currents along the interface. Assuming these surface currents to be zero, the tangential component of the $\vec{H}$ field is continuous and the tangential component of the $\vec{B}$ field is not.

The assumption of the surface currents to be zero is valid, because the current is assumed to be equally distributed in the conductor. No current singularity at the interface occurs. As stated in [134], this applies to almost all applications.

Figure 5.6 compares the differences and similarities between the constant μ example and the piece wise constant μ one. From these relations, suitable boundary condition for the benchmark problem can be derived.

The tangential component of the $\vec{H}$ field is continuous as stated above and is represented by h within the benchmark problem. Within the copper domain it assumed that $b = \mu \cdot h$ with constant μ holds and therefore the introductory examples can be used as reference and calculate h at the boundary $r = r_{\text{in}}$ via (5.6). Depending on whether the current I in the SI unit of A or the current density j in A/m^2 is selected as the the specified value at time t, the result is denoted by h_{ref} and given by

$$h(r,t)|_{r=r_{\text{in}}} = \frac{I(t)}{2\pi r_{\text{in}}} = \frac{r_{\text{in}} j(t)}{2} = h_{\text{ref}}(t) \, . \tag{5.8}$$

This gives the boundary value problem that is to solve numerically:

$$\sigma \frac{\partial A}{\partial t} + \frac{1}{r} \frac{\partial}{\partial r} \Big(r \nu \big(- \frac{\partial}{\partial r} A \big) \Big) = 0 \tag{5.9a}$$

with the boundary conditions

$$\nu \big(- \frac{\partial}{\partial r} A \big) \Big|_{r=r_{\text{in}}} = h_{\text{ref}}(t) \, , \qquad\qquad A \Big|_{r=r_{\text{out}}} = 0 \tag{5.9b}$$

with constant $\sigma \in \mathbb{R}_0^+$, functions ν and h_{ref} on the interval $r \in [r_{\text{in}}, r_{\text{out}}]$.

Remark 5.3. The function ν remains unspecified for the last time. Various approaches were already derived from Tellinen's model in Section 3.3. In the following Sections 5.3.2 and 5.3.3, these approaches are combined with the benchmark problem and their numerical solvability is investigated.

For general context and to evaluate the used approaches, it shall be briefly drawn attention to the effects of the conditions at a material transition. In Section 2.2.2 it has already mentioned that ferromagnetic materials differ from non-ferromagnetic ones – among other things – in an amplification of the magnetic field by several orders of magnitude. This is now specified in more detail and considered separately to tangential and normal components. Due to these differences it can be emphasized here once again how important the course of the fields is for a correct calculation.

Unfortunately, restrictions can be derived for the approaches from these circumstances. Based on the above conditions, a refraction law can be derived similar to the refraction of light. This is shown in more detail in [137], for example.

If the μ values differ by several orders of magnitude, this means that the field lines move out of the ferromagnetic material almost normal to the interface. An example calculation in [137] shows for example with μ_r values of 10^3 and 1, that with an angle of 85° inside the ferromagnetic material nevertheless only an angle on the outside of 0.6° arises.

Remark 5.4. In the scope of this dissertation, this means two things.

▶ On the one hand, a steady transition of the fields cannot be observed at a material transition in general. On the material interface, the fields reorient themselves abruptly and a clear reference direction is needed for the used approach of reducing the multidimensional fields to scalar quantities. This can lead to problems.

▶ On the other hand, the benchmark problem is constructed to have only tangential components. With this background, it can only be emphasized again that this is an academic benchmark problem. Already small normal components inside the ferromagnetic material can dominantly influence the behavior outside the material. For piece wise constant μ and the relation $b = \mu \cdot h$ a corresponding refraction law can be found in literature. But an investigation including hysteresis and in particular Tellinen's model exceeds the scope of this dissertation. The specially constructed benchmark problem is found to be sufficient and only tangential transitions are used. This again shows the complexity of including hysteresis in a simulation.

5.3.2. Replacing ν and Solving the System – Unsuccessful Approaches

Now, the previously unknown function ν is to be replaced by a suitable approach based on Tellinen's hysteresis model. It is investigated how the resulting system can be solved numerically.

Not only the working approach shall be presented to the reader, but also failed ones. This is to illustrate the influence of the choice of modeling ν on the overall simulation. Numerical but also modeling aspects will be addressed.

A Simple Approach

At first the approach (3.78) is analyzed. In short, this approach is characterized by the core idea that the decision whether to use μ_{diff}^{+} or μ_{diff}^{-} follows from the previous time step. Thus this decision lags behind one time step. As an advantage, the ν simplifies to a polynomial of first order, if $\mu_{\text{diff}}^{\pm}$ is evaluated at the current and known state. This comes with the tradeoff that the reversal points within the hysteresis loop are no longer resolved cleanly, as discussed in Section 3.3.2.

With $\alpha_i = \frac{r_{i-\frac{1}{2}}}{r_i}$, $\beta_i = \frac{r_{i+\frac{1}{2}}}{r_i}$ and $\gamma = \frac{\Delta t}{\Delta r^2}$ the system (5.5) can be represented by the linear system

$$\begin{aligned}
&\begin{pmatrix} -\frac{\alpha_i \gamma}{\mu_{i-\frac{1}{2}}} \\ \sigma + \gamma \left(\frac{\alpha_i}{\mu_{i-\frac{1}{2}}} + \frac{\beta_i}{\mu_{i+\frac{1}{2}}} \right) \\ -\frac{\beta_i \gamma}{\mu_{i+\frac{1}{2}}} \end{pmatrix}^{\top} \begin{pmatrix} A_{i-1}^{j+1} \\ A_i^{j+1} \\ A_{i+1}^{j+1} \end{pmatrix} = \\
&\qquad \sigma A_i^j + \gamma \left(\alpha_i \left(h_{i-\frac{1}{2}}^j - \frac{b_{i-\frac{1}{2}}^j}{\mu_{i-\frac{1}{2}}} \right) + \beta_i \left(\frac{b_{i+\frac{1}{2}}^j}{\mu_{i+\frac{1}{2}}} - h_{i+\frac{1}{2}}^j \right) \right) . \qquad (5.10\text{a})
\end{aligned}$$

The boundary conditions are given by

$$A_0^{j+1} - A_1^{j+1} = \Delta r \mu_{\frac{1}{2}} \left(h_{\text{ref}}(t_j) - h_{\frac{1}{2}}^j \right) , \qquad A_{n_m}^{j+1} = 0 \, . \qquad (5.10\text{b})$$

The resulting system (5.10) is weak diagonally dominant ensuring analytical solvability and efficient numerically solvers. For a single time step, this approach is very promising. But in the benchmark problem, problems arise when several time steps are performed in succession. As already predicted in Figure 3.21, a certain amount of imprecision is expected at turning points of the hysteresis loops.

Unfortunately, this phenomenon seems to worsen dramatically in the spatial simulation in the benchmark problem. Instead of calculating only one time step with the wrong $\mu_{\text{diff}}^{\pm}$ value, the simulation oscillates over a larger time range between μ_{diff}^{+} and μ_{diff}^{-} after a turning point was passed. The new values for h^{j+1} and b^{j+1} are iteratively dependent on h^j and b^j. There are no meaningful values resulting from the long lasting wrong choice of $\mu_{\text{diff}}^{\pm}$.

The reasons for this undesireable behavior are not suspected in the numerical solution of the system (5.10), because it can be solved with sufficient accuracy. The problems are justified by the simplified modeling of the detection of the reversal points. The effect is stronger the larger the difference of μ_{diff}^{+} and μ_{diff}^{-} and the time step size Δt is. The first aspect is given by the material and thus not a direct choice of the user. The second aspect is up to the user to decide, but even a small chosen Δt has not been a guarantee that it worked out.

Because it is planned to simulate a longer overall period – such that effects of the slower changing temperature can be identified – Δt shall not be chosen too small due to increasing computational time. However, tests with very small Δt have not been successful either. The very simple detection of the direction by directly comparing b^{j+1} with b^{j} is prone to noise when the values are very close to each other. So if the values do not differ sufficiently – which can happen with a small Δt – there are problems as well.

At this point, a small aspect should be mentioned, that will be taken up later in the discussion of the numerical results. Provided that $\sigma > 0$ holds, there is a limited propagation speed of the magnetic fields. This means that depending on the radius the respective turning points in the hysteresis loop are reached at different times and destabilizes the system additionally.

Overall, a configuration of parameters – that allowed to solve (5.10) securely without significant oscillation at the turning points – is not found.

A More Complex Approach

To improve this situation, the more complex approach (3.77b) from Section 3.3.1 is investigated next. If the time delayed decision – whether to use μ_{diff}^{+} or μ_{diff}^{-} – does not work, this decision is shifted back to the current time step and incorporated into the approach for ν. This results in a piecewise linear function ν that looks like a V as shown in Figure 3.20, which is continuous but not differentiable at the current values.

Inserting (3.77b) into (5.5) and using the boundary conditions (5.10b) results in a non-linear system of equations. This system is continuous but not differentiable, since the functions $\nu_{i+\frac{1}{2}}$ are not differentiable. Via construction the searched new solution A^{j+1} is unfortunately also nearby the current working point, for which the $\nu_{i+\frac{1}{2}}$ are not differentiable.

A typical approach to solve systems coming from finite differences is for example the Newton Rhapson method. This approach was tested, but difficulties with convergence arose. The single points of non-differentiability of $\nu_{i+\frac{1}{2}}$ therefore are disturbing the system so much that a reliable solution process is not possible with this kind of solver strategies. If one uses this special approach how the ν can be replaced by Tellinen's model, one can no longer use solver methods based on the derivative. Thus only derivative-free solvers for non-linear systems can be used with this approach. The better and more up-to-date representation of the turning points is traded for a numerically more difficult system to solve. In general, suitable solvers exist [12], but significantly increased complexity and computational costs are expected.

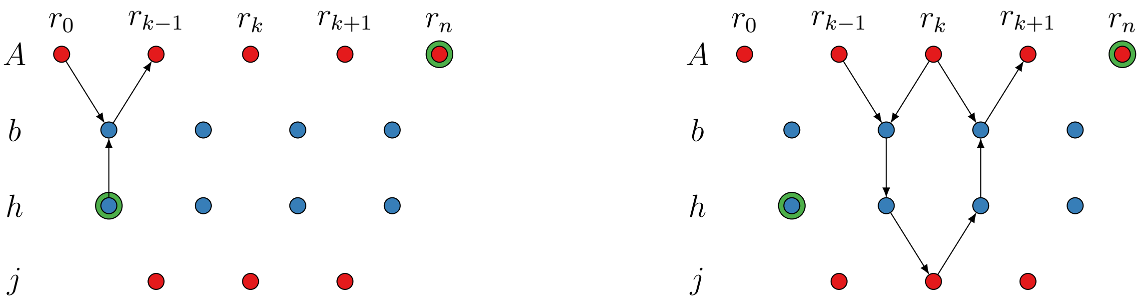

Figure 5.7.: Idea of the solution approach. Notice the direction of flow represented by the arrows.

However, the special properties of the benchmark problem are to be used and the above system shall be reduced complexity wise from a non-linear system to a non-linear scalar problem. Derivative-free methods for solving scalar non-linear problems are much more common. Such a reduction is presented in the next section.

5.3.3. Replacing ν and Solving the System – Successful Approach

As before, (3.77a) and (3.77b) are used to model the link between the fields b and h. But instead of a system of non-linear equations as in the previous Section 5.3.2, this approach aims at a single non-linear equation.

Let the last time step be t^j and assume all variables are known for this time step. The variable are to be calculated for the new time t^{j+1}. The current values of $\mu^{\pm}_{i+\frac{1}{2}} = \mu^{\pm}_{\mathrm{diff}}\left(h^j_{i+\frac{1}{2}}, b^j_{i+\frac{1}{2}}\right)$ are calculated.

The boundary condition $\nu\Big(-\frac{\partial}{\partial r}A\Big)\Big|_{r=r_{\mathrm{in}}} = h_{\mathrm{ref}}(t)$ can be solved for A^{j+1}_1 and results in

$$A^{j+1}_1 = A^{j+1}_0 - \Delta r\left(b^j_{\frac{1}{2}} + \begin{cases}\mu^+_{\frac{1}{2}}\max\left(0, h_{\mathrm{ref}}(t^{j+1}) - h^j_{\frac{1}{2}}\right)\\ \mu^-_{\frac{1}{2}}\min\left(0, h_{\mathrm{ref}}(t^{j+1}) - h^j_{\frac{1}{2}}\right)\end{cases}\right). \tag{5.11}$$

Now, the value of A^{j+1}_{i+1} is determined iteratively from the known values A^{j+1}_i and A^{j+1}_{i-1}. A visual overview is given in Figure 5.7. At first $h^{j+1}_{i-\frac{1}{2}}$ is calculated by

$$h^{j+1}_{i-\frac{1}{2}} = h^j_{i-\frac{1}{2}} + \begin{cases}\dfrac{1}{\mu^+_{i-\frac{1}{2}}}\max\left(0, \dfrac{A^{j+1}_{i-1} - A^{j+1}_i}{\Delta r} - b^j_{i-\frac{1}{2}}\right)\\ \dfrac{1}{\mu^-_{i-\frac{1}{2}}}\min\left(0, \dfrac{A^{j+1}_{i-1} - A^{j+1}_i}{\Delta r} - b^j_{i-\frac{1}{2}}\right)\end{cases}. \tag{5.12}$$

Equation (5.5) can be solved for $h^{j+1}_{i+\frac{1}{2}}$ by

$$h^{j+1}_{i+\frac{1}{2}} = \frac{r_{i-\frac{1}{2}}}{r_{i+\frac{1}{2}}} h^{j+1}_{i-\frac{1}{2}} - \sigma \frac{r_i}{r_{i+\frac{1}{2}}} \frac{\Delta r}{\Delta t} \left(A^{j+1}_i - A^j_i \right) . \tag{5.13}$$

Analog to (5.11) A^{j+1}_{k+1} can be calculated by

$$A^{j+1}_{i+1} = A^{j+1}_i - \Delta r \left(b^j_{i+\frac{1}{2}} + \begin{cases} \mu^+_{i+\frac{1}{2}} \max\left(0, h^{j+1}_{i+\frac{1}{2}} - h^j_{i+\frac{1}{2}}\right) \\ \mu^-_{i+\frac{1}{2}} \min\left(0, h^{j+1}_{i+\frac{1}{2}} - h^j_{i+\frac{1}{2}}\right) \end{cases} \right) . \tag{5.14}$$

If this procedure is continued iteratively, the value for A^{j+1}_n can be calculated. This calculation can be aggregated to a well defined function f with $f\left(A^{j+1}_0\right) = A^{j+1}_n$.

Remark 5.5. Within this approach both fields and conversion directions – $b = \mu(h)$ and $h = \nu(b)$ – are needed. Hence more complex modelations for ν may not be valid for this approach because $\mu = \nu^{-1}$ is not well defined or easily computable.

With (3.77a) and (3.77b) as the chosen method to embed Tellinen's model, the resulting function f is continuous but not differentiable.

The remaining boundary condition from (5.9b) is satisfied by $f(A_0) \overset{!}{=} 0$. Thus overall, the root of a continuous function f is being looked for. For the numerical determination of roots, derivative-free methods like bisection or other bracketing methods [159–164] are valid. The start interval can be searched in a small neighborhood around A^j_0.

Lemma 5.6: The above defined function f is strictly monotone increasing, has a definition domain and range of $\mathbb{R}$ and thus has a unique solution to $f(A_0) = 0$.

Proof. All values for the time step t^j are considered already calculated and those at time step t^{j+1} as unknown. It will be proven that for all $\check{A}^{j+1}_0$ and $\hat{A}^{j+1}_0$ with $\check{A}^{j+1}_0 < \hat{A}^{j+1}_0$ the estimate $f\left(\check{A}^{j+1}_0\right) < f\left(\hat{A}^{j+1}_0\right)$ holds. The function f is defined iteratively over all grid points, so the intermediate points $\check{A}^{j+1}_i$ and $\hat{A}^{j+1}_i$ for $i = 0, \ldots, n$ are obtained. The approach is to show that

$$\hat{A}^{j+1}_i = \check{A}^{j+1}_i + \epsilon_i \tag{5.15a}$$

for all $i \in \{0, \ldots, n\}$ and

$$0 < \epsilon_0 = \epsilon_1 < \epsilon_2 < \ldots < \epsilon_n \tag{5.15b}$$

holds using induction.

▶ Initial case: $i \in \{0,1,2\}$
By assumption $\check{A}_0^{j+1} < \hat{A}_0^{j+1}$ a $\epsilon_0 \in \mathbb{R}^{>0}$ exists, such that

$$\hat{A}_0^{j+1} = \check{A}_0^{j+1} + \epsilon_0 \tag{5.16a}$$

holds. Inserting this into (5.11) yields

$$\hat{A}_1^{j+1} = \check{A}_1^{j+1} + \epsilon_1 \text{ with } \epsilon_0 = \epsilon_1 \tag{5.16b}$$

because all other variables are constant. Equations (5.16a) and (5.16b) imply

$$\check{A}_0^{j+1} - \check{A}_1^{j+1} = \hat{A}_0^{j+1} - \hat{A}_1^{j+1} \tag{5.16c}$$

and using (5.12) with $i = 1$ results in

$$\check{h}_{\frac{1}{2}}^{j+1} = \hat{h}_{\frac{1}{2}}^{j+1} \,. \tag{5.16d}$$

Starting with the definition of $\hat{h}_{\frac{3}{2}}^{j+1}$ in (5.13) with $i = 1$ and using (5.16b) and (5.16d) provides

$$\check{h}_{\frac{3}{2}}^{j+1} > \hat{h}_{\frac{3}{2}}^{j+1} \,. \tag{5.16e}$$

The implementation of ν is strictly monotone increasing and thus (5.14) in combination with (5.16b) and (5.16e) gives

$$\hat{A}_2^{j+1} > \check{A}_2^{j+1} + \epsilon_1 \,. \tag{5.16f}$$

So there is a $\epsilon_2 > \epsilon_1$ such that

$$\hat{A}_2^{j+1} = \check{A}_2^{j+1} + \epsilon_2 \tag{5.16g}$$

holds.

▶ Induction step: $i-1, i \to i+1$ with $i \geq 2$
It is presumed

$$\hat{A}_{i-1}^{j+1} = \check{A}_{i-1}^{j+1} + \epsilon_{i-1} \,, \qquad \hat{A}_i^{j+1} = \check{A}_i^{j+1} + \epsilon_i \tag{5.17a}$$

with $\epsilon_{i-1} < \epsilon_i$ and want to show that a ϵ_{i+1} with $\epsilon_i < \epsilon_{i+1}$ and

$$\hat{A}_{i+1}^{j+1} = \check{A}_{i+1}^{j+1} + \epsilon_{i+1} \tag{5.17b}$$

exists. First, (5.17a) is used to obtain the estimate

$$\hat{A}_{i-1}^{j+1} - \hat{A}_i^{j+1} < \check{A}_{i-1}^{j+1} - \check{A}_i^{j+1} \tag{5.17c}$$

and combining with (5.12) yields

$$\hat{h}_{i-\frac{1}{2}}^{j+1} < \check{h}_{i-\frac{1}{2}}^{j+1} \,. \tag{5.17d}$$

The rest follows very similar to the initial case. By utilization of (5.13)

$$\hat{h}^{j+1}_{i+\frac{1}{2}} < \check{h}^{j+1}_{i+\frac{1}{2}} \tag{5.17e}$$

is obtained and finally by (5.14)

$$\hat{A}^{j+1}_{i+1} > \check{A}^{j+1}_{i+1} + \epsilon_i \,. \tag{5.17f}$$

It follows that an ϵ_{i+1} exists with all the required properties.

► Is was shown that for all $\hat{A}^{j+1}_0 = \check{A}^{j+1}_0 + \epsilon_0$ the relation $\hat{A}^{j+1}_n = \check{A}^{j+1}_n + \epsilon_n$ with $0 < \epsilon_0 < \epsilon_n$ follows. The n-th entry is equal to the function evaluation of f at A^{j+1}_0 , strict monotonicity was thus shown.

► None of the computational steps has produced any constraints on the argument of f, which is why the domain of f is whole $\mathbb{R}$.

► In addition, it was shown that for all $\epsilon > 0$ and A^{j+1}_0, it holds

$$\epsilon = A^{j+1}_0 + \epsilon - A^{j+1}_0 < f\left(A^{j+1}_0 + \epsilon\right) - f\left(A^{j+1}_0\right) \,. \tag{5.18}$$

So for any two values $\check{A}^{j+1}_0, \hat{A}^{j+1}_0 \in \mathbb{R}$ with $\check{A}^{j+1}_0 < \hat{A}^{j+1}_0$ or respectively $\hat{A}^{j+1}_0 = \check{A}^{j+1}_0 + \epsilon$ for some $\epsilon > 0$, the secant slope is

$$\frac{f\left(\hat{A}^{j+1}_0\right) - f\left(\check{A}^{j+1}_0\right)}{\hat{A}^{j+1}_0 - \check{A}^{j+1}_0} = \frac{f\left(\check{A}^{j+1}_0 + \epsilon\right) - f\left(\check{A}^{j+1}_0\right)}{\epsilon} > 1 \,. \tag{5.19}$$

Using the information that

- ▷ f is continuous,
- ▷ f has a domain of $\mathbb{R}$,
- ▷ f is strictly monotonously increasing on the whole $\mathbb{R}$,
- ▷ the secant slope is bounded from below by 1,

it can be concluded that the range of f must not be bounded and thus is the whole $\mathbb{R}$.

► A scalar function that has a domain and range of $\mathbb{R}$, is continuous and strictly monotonously is invertible for any argument and thus the problem $f(A_0) = 0$ is well defined in the sense that a solution A_0 exists and is unique.

□

5.3.4. Interim Conclusion

Tellinen's hysteresis model allows different approaches to replace ν in the Curl-Curl Equation, which are having a strong influences on the properties of the resulting system. Three different approaches are presented and the resulting system are examined in terms of numerical solvability.

In general, it can be stated that Tellinen's model is docile, if examined isolated, but the integration into a spatially resolved simulation poses a challenge. Two aspects can be isolated, that are relevant. Tellinen's model is direction dependent and the direction is not known in advance. These aspect can be mitigated through certain compromises. Nevertheless, there are difficulties to achieve a working simulation for two of the three approaches. Only if the solving strategy is adapted very closely to the benchmark problem, a numerically stable solvable problem is achieved, which at the same time meets the physical expectations.

In the benchmark problem, the system of equations is reduced to a scalar equivalent and more standard derivative-free methods are applied. But there are numerical methods for solving non-linear systems, where the system does not have to be differentiable [12].

The limitation in the choice of algorithms is certainly a disadvantage, but since there are suitable approaches, this is not a critical aspect. This problem is not exclusive to Tellinen's model, but applies generally to the effect of hysteresis, which is directional in essence and thus, not differentiable.

In turn, however, it is possible to show that Tellinen's model can be applied flexibly, allowing a certain degree of adaption to user needs.

5.4. Thermal Simulation

A standard example of parabolic PDE is the heat or diffusion equation

$$\frac{\partial T}{\partial t} = \frac{\partial^2 T}{\partial x^2}\,. \tag{5.20}$$

There is extensive basic literature on this problem, which deals with the mathematical [101–103] aspects, but also with the physical [99] ones. An important aspect of this thesis is the balance between mathematical simplifications and physical modeling. The above approach (5.20) is not sufficient to model a material transition within the simulation area. The steps required to physically model and mathematically solve the benchmark problem are described.

The basic structure of the subsequent sections is as follows. First, a general form of the heat diffusion equation is presented. Nevertheless, the chosen formulation has some prerequisites. These are presented second.

Then the general approach using finite differences is presented. For discretizing the heat equation the general θ-scheme [100, 101, 144] will be used. The advantage is that by varying θ one can choose between the approaches of forward ($\theta = 0$) and backward ($\theta = 1$) difference and the Crank-Nicolson [142] method ($\theta = 0.5$). A discussion of advantages and disadvantages of the methods with respect to the benchmark problem follows in Section 5.4.7.

Table 5.1.: An overview of the variables of the heat equation (5.21) and (5.22) and their physical units and descriptions.

Variable	Unit	Description
T	K or °C	temperature
r	m	radius
k	$\mathrm{W/(m\,K)}$	thermal conductivity
q_V	$\mathrm{W/m^3 = J/(s\,m^3)}$	generated energy per second and unit volume
ρ	$\mathrm{kg/m^3}$	density
c_ρ	$\mathrm{J/(kg\,K)}$	specific heat capacity
c_V	$\mathrm{J/(m^3\,K)}$	volumetric heat capacity

After that, special parts of the simulation domain are investigated. For parts with constant parameter the general approach is simplified. Furthermore the radii of $r = 0$ and $r = r_{\text{out}}$ are examined more closely under the aspect of boundary conditions and $r = r_{\text{in}}$ is analyzed separately with the material interface between copper and iron.

5.4.1. Heat/Diffusion Equation

A more general formulation of the heat equation is given by

$$\frac{\partial}{\partial x}\left(k\frac{\partial T}{\partial x}\right) + q_V = \underbrace{\rho c_\rho}_{c_V} \frac{\partial T}{\partial t}\,. \tag{5.21}$$

An overview of the involved variables and parameters is given in Table 5.1. For ease of notation $c_V = \rho c_\rho$ is used.

The general structure, geometric design and symmetry of the benchmark problem reduces the dimension to one. As before the coordinate transformation from cartesian (5.21) to cylindrical (5.22) coordinates results in additional occurrence of r and $\frac{1}{r}$ terms.

$$\frac{1}{r}\frac{\partial}{\partial r}\left(rk\frac{\partial T}{\partial r}\right) + q_V = c_V\frac{\partial T}{\partial t} \tag{5.22}$$

With minor changes, similar assumptions as in [104] are made. Since the benchmark problem consists of two different materials, the parameters $c_V = c_V(r)$ and $k = k(r)$ must be modeled as dependent from the radius. To be more precise the parameters are assumed to be piece wise constant. Furthermore, it is assumed that the parameters are independent of time and temperature. In the general case the parameter $k = k(r)$ must be inside of the derivative and can not easily be extracted from it.

An ideal heat coupling between the materials is presumed. A closer look at the material interface follows in Section 5.4.4. In addition, heat transport by convection is neglected.

In this section it is assumed that $q_{V,i}^{j+1}$ is already known from the magnetic field simulation and the evaluation of the loss model. This will be discussed in Section 5.5.

The variables and parameters T, q_V, c_V are allocated on the standard grid and k on the offset grid. The radius r occurs on both grids. The numbering of the grids was already introduced in Section 5.2. The number of unknowns in the standard grid is given by $n + 1 = n_h + n_m$.

At this point the general case is discussed first. More detailed investigations for the critical points ($r = 0$ and material interface at $r = r_{\text{in}}$) will follow in the next sections.

Rearranging (5.22) yields

$$\frac{\partial T}{\partial t} = \frac{q_V}{c_V} + \frac{1}{c_V r}\frac{\partial}{\partial r}\left(rk\frac{\partial T}{\partial r}\right) . \tag{5.23}$$

For the spatial discretization central differences and the offset grid are used (as before for the magnetic simulation in Section 5.3). The time discretization is using the θ-scheme. To show the different numbering of the radii, a superscript of h is used here to clarify that it is the heat numbering. This results in

$$\begin{aligned}\frac{T_i^{j+1} - T_i^j}{\Delta t} = {} & \frac{\theta q_{V,i}^{j+1} + (1-\theta) q_{V,i}^j}{c_{V,i}} \\ & + \theta \left[\frac{1}{c_{V,i} r_i^h} \frac{r_{i+\frac{1}{2}}^h k_{i+\frac{1}{2}} \frac{T_{i+1}^{j+1} - T_i^{j+1}}{r_{i+1}^h - r_i^h} - r_{i-\frac{1}{2}}^h k_{i-\frac{1}{2}} \frac{T_i^{j+1} - T_{i-1}^{j+1}}{r_i^h - r_{i-1}^h}}{r_{i+\frac{1}{2}}^h - r_{i-\frac{1}{2}}^h} \right] \\ & + (1-\theta) \left[\frac{1}{c_{V,i} r_i^h} \frac{r_{i+\frac{1}{2}}^h k_{i+\frac{1}{2}} \frac{T_{i+1}^{j} - T_i^{j}}{r_{i+1}^h - r_i^h} - r_{i-\frac{1}{2}}^h k_{i-\frac{1}{2}} \frac{T_i^{j} - T_{i-1}^{j}}{r_i^h - r_{i-1}^h}}{r_{i+\frac{1}{2}}^h - r_{i-\frac{1}{2}}^h} \right] \end{aligned} \tag{5.24}$$

Using

$$\begin{aligned} \alpha_i &= \frac{r_{i-\frac{1}{2}}^h}{r_i^h} \frac{k_{i-\frac{1}{2}}}{\left(r_i^h - r_{i-1}^h\right)} \gamma_i , & \beta_i &= \frac{r_{i+\frac{1}{2}}^h}{r_i^h} \frac{k_{i+\frac{1}{2}}}{\left(r_{i+1}^h - r_i^h\right)} \gamma_i , \\ \gamma_i &= \frac{\Delta t}{c_{V,i}\left(r_{i+\frac{1}{2}}^h - r_{i-\frac{1}{2}}^h\right)} , & \delta_i &= \frac{\theta q_{V,i}^{j+1} + (1-\theta) q_{V,i}^j}{c_{V,i}} \end{aligned} \tag{5.25a}$$

the system (5.24) can be displayed with $i = 1, \ldots, n-1$ as

$$\begin{pmatrix} -\theta\alpha_i \\ 1 + \theta(\alpha_i + \beta_i) \\ -\theta\beta_i \end{pmatrix}^{\top} \cdot \begin{pmatrix} T_{i-1}^{j+1} \\ T_i^{j+1} \\ T_{i+1}^{j+1} \end{pmatrix} = \delta_i + \begin{pmatrix} (1-\theta)\alpha_i \\ 1 - (1-\theta)(\alpha_i + \beta_i) \\ (1-\theta)\beta_i \end{pmatrix}^{\top} \cdot \begin{pmatrix} T_{i-1}^{j} \\ T_i^{j} \\ T_{i+1}^{j} \end{pmatrix} . \tag{5.25b}$$

This system yields only $n-1$ equation for $n+1$ unknowns. The missing two equations are derived in the following sections by considering the boundary conditions at $r = 0$ and $r = r_{\text{out}}$.

5.4.2. Finite Differences with Piece-wise Constant Material Parameters and Piece-wise Equidistant Grid

The benchmark problem consists of two domains $[0, r_{\text{in}})$ and $(r_{\text{in}}, r_{\text{out}}]$. They will be labeled with an index of I or II accordingly. Within each the material parameters k, c_v are constant and the grid is equidistant. As defined in Section 5.2 the material interface is at $r = r_{\text{in}} = r^h_{n_h}$. An analysis of the material interface at $r = r_{\text{in}}$ is given in Section 5.4.4.

So at this point the index ranges of $i \in \{1, \dots, n_h - 1\}$ and $i \in \{n_h + 1, \dots, n - 1\}$ are of interest. Within these ranges the grid is equidistant, such that

$$r^h_i - r^h_{i-1} = r^h_{i+1} - r^h_i = r^h_{i+\frac{1}{2}} - r^h_{i-\frac{1}{2}} = \begin{cases} \Delta r_{\text{I}} & \text{for } i \in \{1, \dots, n_h - 1\} \\ \Delta r_{\text{II}} & \text{for } i \in \{n_h + 1, \dots, n - 1\} \end{cases} \tag{5.26}$$

holds. And with marking the values of c_V and k accordingly, it yields

$$c_{V,i} = \begin{cases} c_{V,\text{I}} & \text{for } i \in \{0, \dots, n_h - 1\} \\ c_{V,\text{II}} & \text{for } i \in \{n_h + 1, \dots, n\} \end{cases}, \tag{5.27a}$$

$$k_{i\pm\frac{1}{2}} = \begin{cases} k_{\text{I}} & \text{for } i \in \{1, \dots, n_h - 1\} \\ k_{\text{II}} & \text{for } i \in \{n_h + 1, \dots, n - 1\} \end{cases}. \tag{5.27b}$$

5.4.3. Finite Differences in Cylindrical Coordinates at $r = 0$

To deal with the singularity around $r = 0$ – introduced by the cylindrical coordinate transformation – at least two common approaches are available by literature. One possible approach for constant parameter k is based on applying the chain rule on the spatial derivative.

$$\frac{k}{r}\frac{\partial}{\partial r}\left(r\frac{\partial T}{\partial r}\right) = k\frac{\partial^2 T}{\partial r^2} + \frac{k}{r}\frac{\partial T}{\partial r}. \tag{5.28}$$

Next apply L'Hospital's rule on the second part.

$$\lim_{r\to 0}\frac{k}{r}\frac{\partial T}{\partial r} = k\frac{\partial^2 T}{\partial r^2} \tag{5.29}$$

The heat equation is represented by the modified terms for $r = 0$ and can be solved with the usual approaches of finite differences. Details about this approach can be found in literature, for example [101].

For this thesis an approach based on a special placed grid and ghost nodes is used [105]. The grid introduced in Section 5.2 already satisfies the requirements. It is constructed in such way, that $r^h_0 = \frac{1}{2}\Delta r_{\text{I}}$ and $r^h_{\frac{1}{2}} = \Delta r_{\text{I}}$ holds. If the numbering is artificially extended to the ghost nodes r^h_{-1} and $r^h_{-\frac{1}{2}}$, it would result in $r^h_{-\frac{1}{2}} = 0$ and due to symmetry in $r^h_{-1} = r^h_0$. A visual overview is given in Figure 5.8. With these

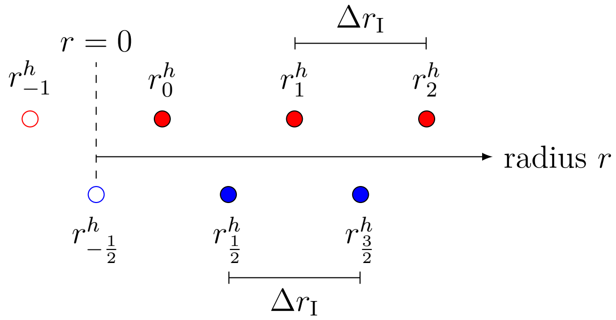

Figure 5.8.: Grid of the heat simulation around $r=0$. The standard grid is shown in red and the offset grid in blue. Additionally the ghost nodes r_{-1}^h and $r_{-\frac{1}{2}}^h$ are marked.

ghost nodes the same approach as for inner grid points (5.24) can be used. For the sake of uniform notation and clarity, the same format as (5.25a) and (5.25b) is used. This results in

$$\begin{pmatrix} 1+\theta(\alpha_0+\beta_0) \\ -\theta\beta_0 \end{pmatrix}^\top \cdot \begin{pmatrix} T_0^{j+1} \\ T_1^{j+1} \end{pmatrix} = \delta_0 + \begin{pmatrix} 1-(1-\theta)(\alpha_0+\beta_0) \\ (1-\theta)\beta_0 \end{pmatrix}^\top \cdot \begin{pmatrix} T_0^{j} \\ T_1^{j} \end{pmatrix} . \tag{5.30a}$$

δ_i from (5.25a) can be naturally extend to include $i=0$ and the other parameters for $i=0$ are given by

$$\alpha_0 = 0\,, \qquad \beta_0 = \frac{r_{\frac{1}{2}}^h}{r_0^h} \cdot \frac{k_{\frac{1}{2}}}{\Delta r_\mathrm{I}^h}\gamma_0\,, \qquad \gamma_0 = \frac{\Delta t}{c_{V,\mathrm{I}} \cdot \Delta r_\mathrm{I}^h} . \tag{5.30b}$$

5.4.4. Finite Differences at Material Interface at $r = r_\mathrm{in}$ with Different Grid Sizes

At the material interface of ideal coupled materials the temperature and heat flux are continuous [104]. So for any fixed time t it holds

$$T_\mathrm{I}(t,r)\Big|_{r=r_\mathrm{in}} = T_\mathrm{II}(t,r)\Big|_{r=r_\mathrm{in}}\,, \qquad k_\mathrm{I}\frac{\partial T_\mathrm{I}(t,r)}{\partial r}\Big|_{r=r_\mathrm{in}} = k_\mathrm{II}\frac{\partial T_\mathrm{II}(t,r)}{\partial r}\Big|_{r=r_\mathrm{in}} . \tag{5.31}$$

The material interface is at $r = r_\mathrm{in} = r_{n_h}^h$, so $i = n_h$ is considered. As stated in Remark 5.1 the standard grid changes the grid size without an intermediate step. The offset grid, on the other hand, has an averaged step at the transition. An overview is given in Figure 5.9. In specific terms the step sizes result in

$$r_{n_h} - r_{n_h-1} = \Delta r_\mathrm{I}\,, \quad r_{n_h+\frac{1}{2}} - r_{n_h-\frac{1}{2}} = \frac{\Delta r_\mathrm{I} + \Delta r_\mathrm{II}}{2}\,, \quad r_{n_h+1} - r_{n_h} = \Delta r_\mathrm{II} . \tag{5.32}$$

The grid sizes and k can therefore be assigned precisely in each case. The parameter c_V does not. It is located on the standard grid and therefore cannot be clearly assigned to material I or II at the transition. A weighted average, i.e.,

$$c_{V,n_h} = \frac{\Delta r_\mathrm{I} \cdot c_{V,\mathrm{I}} + \Delta r_\mathrm{II} \cdot c_{V,\mathrm{II}}}{\Delta r_\mathrm{I} + \Delta r_\mathrm{II}}\,, \tag{5.33}$$

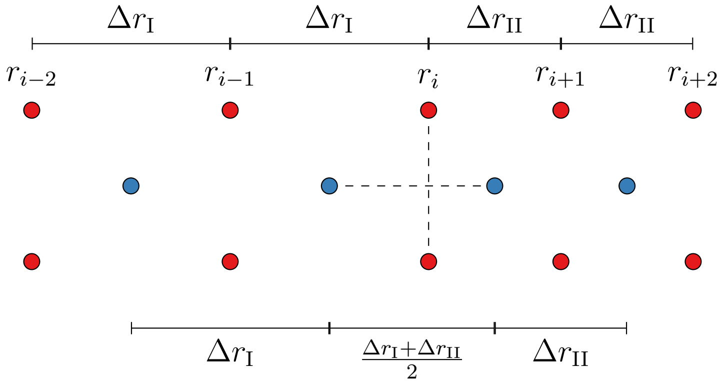

Figure 5.9.: Overview of the grid sizes at the material interface at $r_i = r_{\mathrm{in}}$. The standard grid is shown in red and the offset grid in blue.

is used [98]. This gives the parameters

$$\begin{aligned} \alpha_{n_h} &= \frac{r^h_{n_h-\frac{1}{2}}}{r^h_{n_h}} \frac{k_{\mathrm{I}}}{\Delta r_{\mathrm{I}}} \gamma_{n_h}\,, & \beta_{n_h} &= \frac{r^h_{n_h+\frac{1}{2}}}{r^h_{n_h}} \frac{k_{\mathrm{II}}}{\Delta r_{\mathrm{II}}} \gamma_{n_h}\,, \\ \gamma_{n_h} &= \frac{\Delta t}{\frac{\Delta r_{\mathrm{I}} \cdot c_{V,\mathrm{I}} + \Delta r_{\mathrm{II}} \cdot c_{V,\mathrm{II}}}{\Delta r_{\mathrm{I}}+\Delta r_{\mathrm{II}}} \cdot \frac{\Delta r_{\mathrm{I}}+\Delta r_{\mathrm{II}}}{2}}\,, & \delta_{n_h} &= \frac{\theta q^{j+1}_{V,n_h} + (1-\theta) q^j_{V,n_h}}{\frac{\Delta r_{\mathrm{I}} \cdot c_{V,\mathrm{I}} + \Delta r_{\mathrm{II}} \cdot c_{V,\mathrm{II}}}{\Delta r_{\mathrm{I}}+\Delta r_{\mathrm{II}}}}\,. \end{aligned} \tag{5.34}$$

5.4.5. Boundary Condition at $r = r_{\mathrm{out}}$

At $r = r_{\mathrm{out}}$ a boundary condition is needed. Typically, three different types of boundary conditions are discussed in the literature [99, 101, 103]. Dirichlet boundary conditions apply to the solution itself, while Neumann conditions apply to the derivative of the solution. Robin boundary conditions combines the two approaches in a weighted combination.

In the context of this thesis Dirichlet boundary conditions are used, i.e.,

$$T(t, r = r_{\mathrm{out}}) = 27\,^\circ\mathrm{C} \text{ for all } t \in [0, t_{\max}]\,. \tag{5.35}$$

The outside of the iron sheath is cooled by the air, which is assumed to be of constant temperature. As a condition a perfect material interface is assumed. Therefore a constant surface temperature at $r = r_{\mathrm{out}}$ is considered.

Embedded in the former notation and with $n = n_h + n_m - 1$, this results in

$$\begin{pmatrix} -\theta\alpha_n \\ 1+\theta(\alpha_n+\beta_n) \end{pmatrix}^{\top} \cdot \begin{pmatrix} T^{j+1}_{n-1} \\ T^{j+1}_{n} \end{pmatrix} = \delta_n + \begin{pmatrix} (1-\theta)\alpha_n \\ 1-(1-\theta)(\alpha_n+\beta_n) \end{pmatrix}^{\top} \cdot \begin{pmatrix} T^{j}_{n-1} \\ T^{j}_{n} \end{pmatrix} \tag{5.36a}$$

with

$$\alpha_n = \beta_n = \gamma_n = \delta_n = 0\,. \tag{5.36b}$$

Because (5.36a) reduces to $T^{j+1}_n = T^j_n$, the starting temperature T^0_n defines the surface temperature for all time steps.

5.4.6. Overview of the Resulting System of Equations

Now, when the previous sections are combined, the following definitions of the parameters result from (5.25a), (5.30b), (5.34) and (5.36b).

$$\alpha_i = \begin{cases} 0 & \text{for } i = 0 \\ \frac{r^h_{i-\frac{1}{2}}}{r^h_i} \frac{k_{\mathrm{I}}}{\Delta r_{\mathrm{I}}} \gamma_i & \text{for } i \in \{1, \dots, n_h\} \\ \frac{r^h_{i-\frac{1}{2}}}{r^h_i} \frac{k_{\mathrm{II}}}{\Delta r_{\mathrm{II}}} \gamma_i & \text{for } i \in \{n_h + 1, \dots, n-1\} \\ 0 & \text{for } i = n \end{cases} \tag{5.37a}$$

$$\beta_i = \begin{cases} \frac{r^h_{i+\frac{1}{2}}}{r^h_i} \frac{k_{\mathrm{I}}}{\Delta r_{\mathrm{I}}} \gamma_i & \text{for } i \in \{0, \dots, n_h - 1\} \\ \frac{r^h_{i+\frac{1}{2}}}{r^h_i} \frac{k_{\mathrm{II}}}{\Delta r_{\mathrm{II}}} \gamma_i & \text{for } i \in \{n_h, \dots, n-1\} \\ 0 & \text{for } i = n \end{cases} \tag{5.37b}$$

$$\gamma_i = \begin{cases} \frac{\Delta t}{c_{V,\mathrm{I}} \Delta r_{\mathrm{I}}} & \text{for } i \in \{0, \dots, n_h - 1\} \\ \frac{\Delta t}{\frac{\Delta r_{\mathrm{I}} \cdot c_{V,\mathrm{I}} + \Delta r_{\mathrm{II}} \cdot c_{V,\mathrm{II}}}{\Delta r_{\mathrm{I}} + \Delta r_{\mathrm{II}}} \cdot \frac{\Delta r_{\mathrm{I}} + \Delta r_{\mathrm{II}}}{2}} & \text{for } i = n_h \\ \frac{\Delta t}{c_{V,\mathrm{II}} \Delta r_{\mathrm{II}}} & \text{for } i \in \{n_h + 1, \dots, n-1\} \\ 0 & \text{for } i = n \end{cases} \tag{5.37c}$$

$$\delta_i = \begin{cases} \frac{\theta q^{j+1}_{V,i} + (1-\theta) q^j_{V,i}}{c_{V,\mathrm{I}}} & \text{for } i \in \{0, \dots, n_h - 1\} \\ \frac{\theta q^{j+1}_{V,n_h} + (1-\theta) q^j_{V,n_h}}{\frac{\Delta r_{\mathrm{I}} \cdot c_{V,\mathrm{I}} + \Delta r_{\mathrm{II}} \cdot c_{V,\mathrm{II}}}{\Delta r_{\mathrm{I}} + \Delta r_{\mathrm{II}}}} & \text{for } i = n_h \\ \frac{\theta q^{j+1}_{V,i} + (1-\theta) q^j_{V,i}}{c_{V,\mathrm{II}}} & \text{for } i \in \{n_h + 1, \dots, n-1\} \\ 0 & \text{for } i = n \end{cases} \tag{5.37d}$$

For ease of notation matrix A is defined by

$$A = \begin{pmatrix} \alpha_0 + \beta_0 & -\beta_0 & & & \\ -\alpha_1 & \alpha_1 + \beta_1 & -\beta_1 & & \\ & \ddots & \ddots & \ddots & \\ & & -\alpha_{n-1} & \alpha_{n-1} + \beta_{n-1} & -\beta_{n-1} \\ & & & -\alpha_n & \alpha_n + \beta_n \end{pmatrix} \in \mathbb{R}^{(n+1)\times(n+1)} . \tag{5.38}$$

The equations (5.25b), (5.30a) and (5.36a) can be combined into the linear system of equations

$$\Big(\mathbb{1} + \theta A\Big) \vec{T}^{j+1} = \vec{\delta} + \Big(\mathbb{1} - (1-\theta) A\Big) \vec{T}^j . \tag{5.39}$$

Here $\mathbb{1}$ describes the unit matrix and $\vec{T}^{j+1}$, $\vec{T}^j$, $\vec{\delta} \in \mathbb{R}^{n+1}$ the vectors for index $i = 0, \dots, n$.

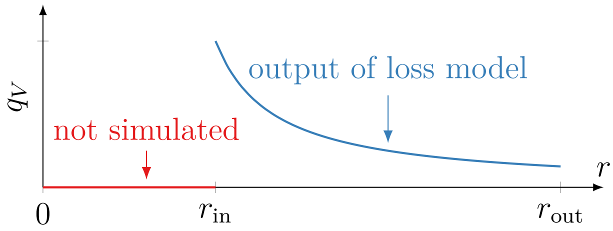

Figure 5.10.: Expected results for q_v for fixed t. Of special importance is the discontinuous jump at $r = r_{\text{in}}$.

Remark 5.7. The matrix $(\mathbb{1} + \theta A)$ is tridiagonal and strictly diagonal dominant. From this it follows directly that the matrix $(\mathbb{1} + \theta A)$ is invertible and the system of equations (5.39) has a unique solution.

5.4.7. Further Remarks

The previous sections allow the application of different numerical methods by choosing $\theta \in [0, 1]$ accordingly. The choice of $\theta = 0.5$ is of special interest because the resulting Crank-Nicolson method [142] is of second order in time and is unconditionally stable [141, 143, 144]. Other θ values result in only first order w.r.t. time.

But the Crank-Nicolson method ($\theta = 0.5$) shows an oscillating and overshooting behavior, if the problem has non-continuous properties [141, 143, 144]. Although the start temperature is chosen as constant, i.e., $T(t = 0, r) = 27$ for all $r \in [0, r_{\text{out}}]$, the resulting benchmark problem has a discontinuous jump in q_V. Only hysteresis losses of the iron are considered. And these losses are mainly dependent on the magnitude change of the field. With the expected radial decline of the magnetic fields, the largest values for q_V are expected at r_{in}. But since the copper is modeled without hysteresis losses, it holds $q_V(t, r) = 0$ for all $t \in [0, t_{\max}], r \in [0, r_{\text{in}})$. Figure 5.10 shows the expected curve for q_V at a fixed time t. This is later confirmed by the simulation and discussed in Section 5.6.

Although there are more advanced methods and approaches to reduce oscillation (e.g. [141, 143, 144]), all further simulations of this thesis are performed with $\theta = 1$. This result in the backwards difference scheme for the time derivative. This approach is also unconditionally stable and has no tendency to the above mentioned oscillations [143, 144]. But is only of first order in time.

The choice of $\theta = 0$ is not of interest for this benchmark problem. It would yield the oscillation as a negative characteristic and is additionally only conditionally stable [103]. In some cases this explicit approach has advantages w.r.t. computational costs. But for the benchmark the resulting system of equation for implicit approaches is tridiagonal and diagonal dominant. For this kind of problem algorithms with $\mathcal{O}(n)$ and advanced solvers exists (e.g. [154–158]). So the explicit approach has no advantages and is therefore not pursued further.

5.5. Co-Simulation and Multirate

In this section the interaction of the individual components is to be regarded. These components are

- the original Tellinen scalar hysteresis model (Chapter 3),
- the thermal extension to it (Section 4.2),
- the loss model (Section 4.1),
- the magnetic field simulation (Section 5.3),
- the heat simulation (Section 5.4).

Up to now, each of these components have been analyzed individually. In many places, comments have already been made on how to put these components together and where the connecting links are. Now it will be shown how the overall simulation is designed. The overall result is a coupled simulation, which includes both the magnetic field and the thermal aspects as shown in Figure 5.1.

There are two major simulation approaches – based on corresponding PDE's – describing once the magnetic and once the thermal properties. There are some common variables such as the temperature T, such that a simultaneous solving is not trivially possible. The two simulations are performed separately, i.e., decoupled as much as possible. The models play the role of links between these two simulations. This presents a few important issues that are discuss below.

- In what order are the individual steps performed?
- Which variables are changed in each step and which remain constant?
- How is it ensured that the respective model's definition domains are respected?

It is initially assumed that the magnetic field simulation operates on a faster time scale than the heat simulation. This will be investigated in the second half of this section under the aspect of multirate approaches. This assumption is also confirmed and discussed by numerical results in Section 5.6. So in the consideration it is not only a thematic decoupling, but also one regarding the time scales involved.

As a starting point for a new time step the magnetic simulation is chosen, so it is a fastest-first approach. This means that the magnetic field simulation is carried out first, while assuming the temperature to be constant. Information that influences the temperature is picked up by the loss model and stored temporarily for later processing.

Second, the results of the magnetic field simulation are coupled into the heat simulation, which is then solved. Third, the thermal result are fed back onto the magnetic domain. Applying the thermal extension of Tellinen's model ensure a valid state after these steps. So, the used approach does not solve both simulations simultaneously but one after the other. It is therefore a co-simulation. How exactly the simulations and models are coupled and which data is exchanged is described next.

▶ Tellinen's model ⇀ magnetic simulation
How Tellinen's model can be integrated into the magnetic field simulation and what effects this has, has already been discussed in Section 5.3. The ν is replaced by a suitable approach and the approaches to solve the magnetic simulation are chosen accordingly. For the reduced and adjusted benchmark problem, appropriate procedures were already presented. However, it must be ensured that all states are valid, i.e., $(h, b, T) \in I_{\mathrm{T}}$ for all spatial coordinates and at all time steps.

▶ magnetic simulation
Withing this step the temperature T is assumed to be constant and so are $B_{\mathrm{sat}}^{\pm}$ w.r.t. T. Thus, the original Tellinen model can be applied. For the discrete time step increment from t^j to t^{j+1}, the magnetic simulation is solved as described in Section 5.3. From the freshly calculated A_k^{j+1} the values of $h_{k+\frac{1}{2}}^{j+1}$ and $b_{k+\frac{1}{2}}^{j+1}$ are derived.

▶ magnetic simulation ⇀ loss model
After the time step update, the variables $h_{k+\frac{1}{2}}^{j}$, $h_{k+\frac{1}{2}}^{j+1}$, $b_{k+\frac{1}{2}}^{j}$ and $b_{k+\frac{1}{2}}^{j+1}$ are available.

▶ loss model
With these updated values of h and b, a new step for b_{rev} can be calculated as defined in Section 4.1. A new trapeziod can be calculated and its enclosed area is added to the corresponding summed up area, now denoted by q_V (individually for each spatial coordinate). At this point, the option arises to make another time step in the magnetic simulation or to switch over to the thermal simulation.

▶ loss model ⇀ heat simulation
The summed up enclosed areas of the trapezoids are integrated into the heat simulation as source terms q_V. After they have been used in the heat simulation, these are reset to zero. Only after at least one step in the magnetic simulation has been performed, there are hysteresis losses again.

▶ heat simulation
Within the heat simulation the magnetic variables are assumed to be constant. The heat simulation is solved as described in Section 5.4. This is done by standard procedures and is only somewhat complicated by the material transition. New values T_k^{j+1} are obtained. Depending on whether the magnetic simulation was performed only once or several times, a different Δt for the heat simulation than in the magnetic one may result.

▶ heat simulation ⇀ thermal extension
The new T_k^{j+1} and old T_k^{j} values are available.

▶ thermal extension
The temperature T_k^{j+1} is analyzed at each spatial coordinate and the values of $b_{k+\frac{1}{2}}^{j+1}$ and $b_{\mathrm{rev},k+\frac{1}{2}}^{j+1}$ are adjusted as defined in Section 4.2.

▶ thermal extension ⇀ magnetic simulation
The current states $\left(h_{k+\frac{1}{2}}^{j+1}, b_{k+\frac{1}{2}}^{j+1}, T_{k+\frac{1}{2}}^{j+1}\right) \in I_{\mathrm{T}}$ and $\left(h_{k+\frac{1}{2}}^{j+1}, b_{\mathrm{rev},k+\frac{1}{2}}^{j+1}, T_{k+\frac{1}{2}}^{j+1}\right) \in I_{\mathrm{T}}$ are ensured to be valid.

This closes the circle of one time step and this procedure can now be applied iteratively, as previously shown in Figure 5.1.

The procedure described above allows to use one of the simplest multi rate procedures and that is that the fast part is executed several times compared to the slow part. Due to its structure, the loss model can cache the summed up enclosed area and then be integrated into the heat simulation as needed. Thus, both simulations can be performed asynchronously from each other. Of course, it is up to the user to decide whether such an approximation is sufficient and what calculation time is acceptable.

In the presented benchmark problem, no multi scale option is used. In each run, both the magnetic and heat simulation is performed. There are two main reasons for this.

First, that in the context of this thesis the used computational resources are only secondary. The focus is on the modeling of the physical features and the embedding of these in a multiphysics simulation. The used approaches still have a lot of potential to improve the numerical speed. This remains open for further research. The short insight and the evaluation that the models basically offer possibilities is sufficient at this point.

Second,it is investigated and demonstrated in the benchmark that the effects are indeed on different time scales. For this purpose numerical investigations follow in the next Section 5.6.

Further literature on Co-Simulation and multirate is given by [145–149, 152, 153] for example.

5.6. Numerical Results

In this section, numerical results are presented. With these it is tried to validate the model and prove its technical feasibility. Based on the observations, positive but also restricting features are pointed out. In addition, contradictions to the physical principles are looked for.

This section is designed as follows.

► First, the parameters of the simulation are discussed. Unless otherwise stated, all results in this section are based on these parameters. An opinion is given which parameters are close to real material properties and which are more academic.

► Second, results of numerical simulation are presented. The reader is given an overview of how the models perform. In doing so, examples are provided that demonstrate that the model works as theoretically studied. But also new aspects will be taken up, which have arisen during the numerical implementation. In this way the reader is enabled to form an informed opinion about the approaches and models.

Table 5.2.: Parameters of the benchmark problem

Description	Value
numerical method for calculation of b_{rev}	RK3
spatial base unit	meter
r_{in}	$0.05\,\mathrm{m} = 5\,\mathrm{cm}$
r_{out}	$0.15\,\mathrm{m} = 15\,\mathrm{cm}$
n_m	60
n_h	20
Δr_{I}	$\approx 0.2439\,\mathrm{cm}$
Δr_{II}	$\approx 0.1695\,\mathrm{cm}$
time base unit	second
t_0	$0\,\mathrm{s}$
t_{max}	$480\,\mathrm{s} = 8\,\mathrm{min}$
Δt	$\frac{1}{50 \cdot 256}\mathrm{s} = 78.125\,\mathrm{\mu s}$
magnetic parameters	
σ	$10\,1/(\mathrm{kW\,m})$
$h_{\mathrm{ref}}(t)$	$60\,\mathrm{kA/m} \cdot \sin(50\,\mathrm{Hz} \cdot 2\pi \cdot t)$
thermal parameters	
k_{I}	$385\,\mathrm{W/(m\,K)}$
k_{II}	$79.5\,\mathrm{W/(m\,K)}$
$c_{V,\mathrm{I}}$	$3.450\,\mathrm{MJ/(m^3\,K)}$
$c_{V,\mathrm{II}}$	$3.537\,\mathrm{MJ/(m^3\,K)}$

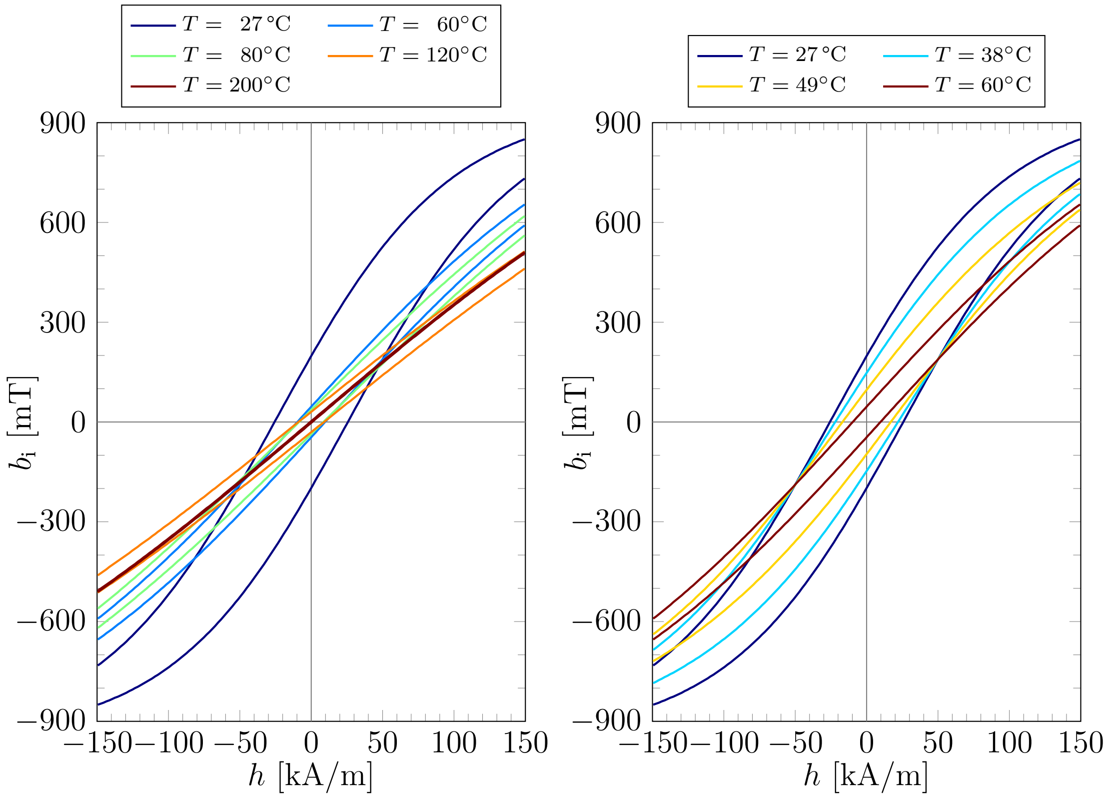

(a) measured/constructed curves (b) interpolated curves for $T \in [27, 60]$.

Figure 5.11.: $(b_\mathrm{i}h)$–curves of the benchmark material at different temperatures T.

5.6.1. Parameters

It is tried to choose the parameters realistically, but in some aspects no real values are available and in other places certain effects are to be shown. Therefore the parameters are to be understood as academic examples. As a result, there is no specific application for which the parameters could be optimized for. The parameters are chosen such that as many effects as possible are strongly pronounced and can be discussed.

An overview of the parameters is listed in Table 5.2. This includes the typical values for spatial and temporal resolution and defining details of the benchmark problem. The thermal properties can also be briefly described using the constants c_V and k for the two different materials. The magnetic properties can not be summarized so easily and therefore a description of the magnetic material used follows next section.

Magnetic Material Parameters

The material used has a significant influence on the simulation and one material has already been presented in Figure 4.5. However, this material belongs to the hard ferromagnetic materials and is therefore not a useful material in combination with the benchmark problem. The application problem is more suitable for softer

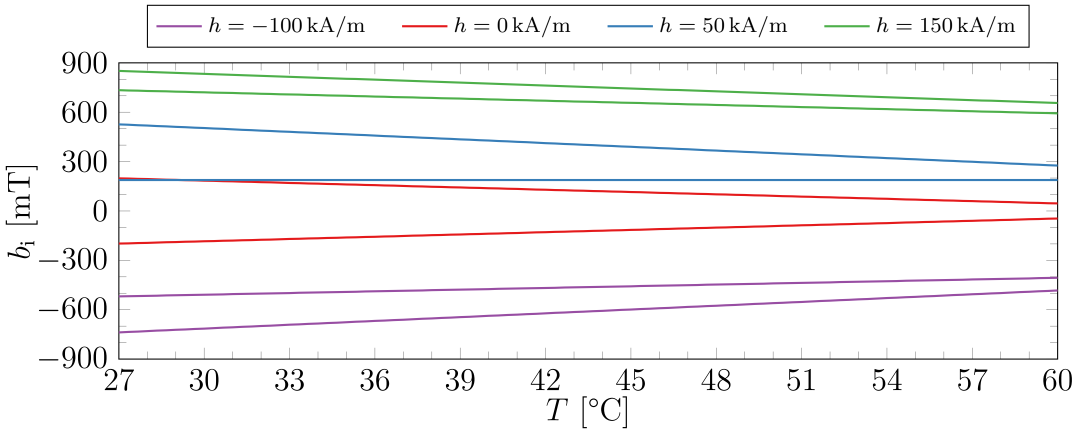

Figure 5.12.: $(b_\mathrm{i}T)$–curves of the benchmark material at different values of h.

ferromagnetic materials. The material at hand is adapted by reducing H_c by a factor of 50. This has made the material curves narrower by this factor. The resulting material is shown in Figures 5.11 and 5.12.

In the benchmark problem a maximum temperature of about 50 °C is reached and 27 °C is set as the initial and ambient temperature. Measurements (academic/constructed) of the saturation curves $B^{\pm}_\mathrm{sat}$ are available for temperatures 27 °C and 60 °C. Linear interpolation is used to obtain the saturation curves $B^{\pm}_\mathrm{sat}$ for all $T \in [27, 60]$, i.e.,

$$B^{\pm}_\mathrm{sat}(h,T) = \frac{60-T}{33} B^{\pm,27\,°\mathrm{C}}_\mathrm{sat}(h) + \frac{T-27}{33} B^{\pm,60\,°\mathrm{C}}_\mathrm{sat}(h)\,. \tag{5.40}$$

The saturation curves $B^{\pm,27\,°\mathrm{C}}_\mathrm{sat}$, $B^{\pm,60\,°\mathrm{C}}_\mathrm{sat}$ fulfill all the required properties of the original Tellinen model and thus (5.40) fulfills all the conditions of the thermal extension. This results in the intermediate values as presented in Figure 5.11(b).

Reasons for the Choice of Parameters

The combination of the amplitude of the excitation h_ref and the width of the saturation curves $B^{\pm}_\mathrm{sat}$ is chosen to almost reach saturation in the simulation. This allows to investigate some effects most efficient.

If the saturation curves $B^{\pm}_\mathrm{sat}$ would be narrower and/or the excitation h_ref higher, the solutions would be almost exclusively the saturation curves $B^{\pm}_\mathrm{sat}$ themselves. This would maximize the enclosed area in the loss calculation, but it would be hard studying the curves in the interior.

On the other hand, if the excitation h_ref is too small and/or the saturation curves $B^{\pm}_\mathrm{sat}$ are very wide, there would hardly be any difference between μ^{+}_diff and μ^{-}_diff. The enclosed area would be very small and barely a temperature change would result. The forward and backward paths of Tellinen's model would be nearly identical and difficult to see.

The parameters k and c_V are roughly based on the values of copper and iron. The exact values of the material parameters vary somewhat depending on the literature, see [99, 132, 11] for example. The value of σ is intentionally chosen much smaller than the value of iron. It is just integrated to prove that the simulation works with a $\sigma > 0$. But a σ in the order of iron would make the discussion of the results much more complex, because the effects overlap with those of the hysteresis. Comments on that will follow.

The chosen parameters are a compromise and purely academic in nature, but thereby show all the effects. The paths coming from of Tellinen's model shall be visually far enough apart, such that a typical hysteresis loop results. The areas enclosed in each case should be large enough so that there is a noticeable increase in temperature T and thus change in $B^{\pm}_{\text{sat}}$. At the same time, however, the main activity should take place inside the curves $B^{\pm}_{\text{sat}}$.

5.6.2. Results

Now, the numerical results are processed and discussed. If not stated otherwise, all of the following result are based on the parameters presented in the previous Section 5.6.1. Results of different chapters of this thesis will be presented and discussed. A list with rough information, motivations and questions follows.

▶ magnetic simulation
The magnetic simulation as in Section 5.3 in combination with Tellinen's model from Chapter 3 is of special importance for this dissertation. The previous investigations on the hysteresis model have so far been isolated and the question remains how the model behaves in a spatially resolved simulation. That there can be numerical problems, depending on how exactly the model is integrated, has already been mentioned. It will be shown that the chosen approaches work in the sense that the hysteresis model behaves the same as when considered in isolation. Critical aspects are for example if the $B^{\pm}_{\text{sat}}$ boundaries are kept and if the turning points in the hysteresis loops are recognized cleanly, i.e., if the change between μ^{+}_{diff} and μ^{-}_{diff} works. The magnetic behavior is checked physical reasonableness, this concerns especially the starting phase ($t \approx 0$) and the steady state ($t \gg 0$). The influence of the parameter σ is briefly discussed.

▶ heat simulation
The results of the heat simulation introduced in Section 5.4 are checked for reasonableness and fulfillment of the requirements. Aspects are for example the boundary conditions, the material transition at r_{in} and the transition to a steady state. The heat flux is calculated from the temperature distribution and checked to see if it is continuous.

▶ loss model
In the theoretical consideration in Section 4.1 some properties were attributed to the loss model which will now be verified numerically. First, the starting phase is examined. How fast does the model take hold and provide an approximation of the

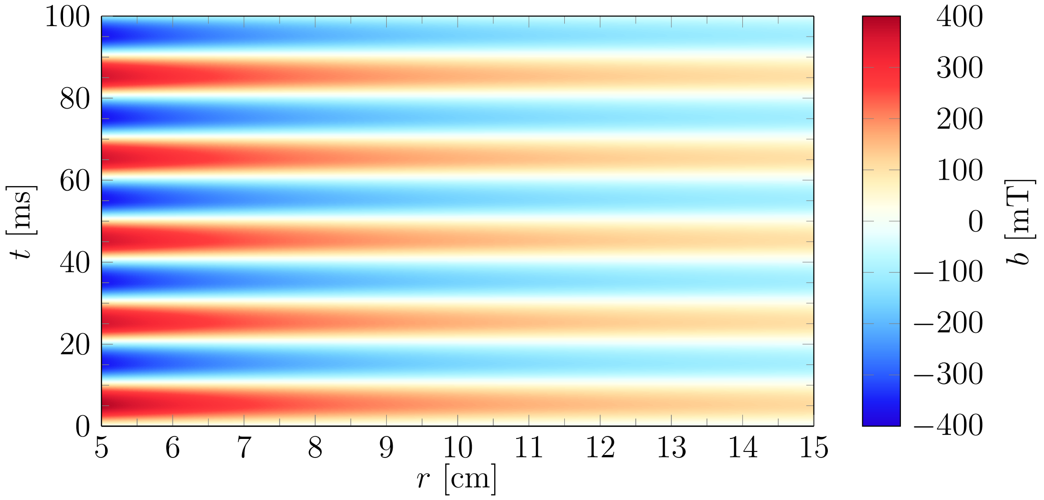

Figure 5.13.: Results of b for the first 100 ms of the simulation.

return path by b_{rev}? Second, the saturation phase is analyzed. How closely do the actual return path and its prediction b_{rev} match?

▶ involved time scales
The magnetic and thermal effects are expected to act on different time scales, as described earlier in Section 5.5. This expectation is checked and the effects are compared with each other. For this purpose, among other things, an analysis in the frequency spectrum – by means of Fourier transformation – is performed.

Magnetic Simulation and Tellinen's Model

In this paragraph, the numerical results concerning the magnetic simulation from Section 5.3 and Tellinen's model Chapter 3 are presented. Using these data, it is checked whether the simulation produces physically meaningful values and if Tellinen's model still works in conjunction with this spatially resolved simulation.

First, a rough overview is given. The Figure 5.13 shows the first 100 ms of the b field. The 50 Hz excitation, i.e., period of 20 ms, can be clearly seen and also the drop with increasing radius. In this overview, it looks very regular and already very periodic. So the magnetic simulation seems to reach a steady state quickly.

For the radii 6 cm and 14 cm a more detailed illustration can be found in Figure 5.14. Since the h field is predefined by the boundary condition at a radius of 5 cm, the evaluation is deliberately chosen not to be at this boundary.

If the two radii are compared, roughly the same pattern results. The b field is slightly lagging behind the h field. While the maxima and minima are synchronous in time, the zero crossings are not.

This corresponds to the expectations. Tellinen's model couples the direction of change of h and b directly, such that there can be no deviation there. However, one can see in the extrema that the h field behaves nicely smooth (matching the sine of

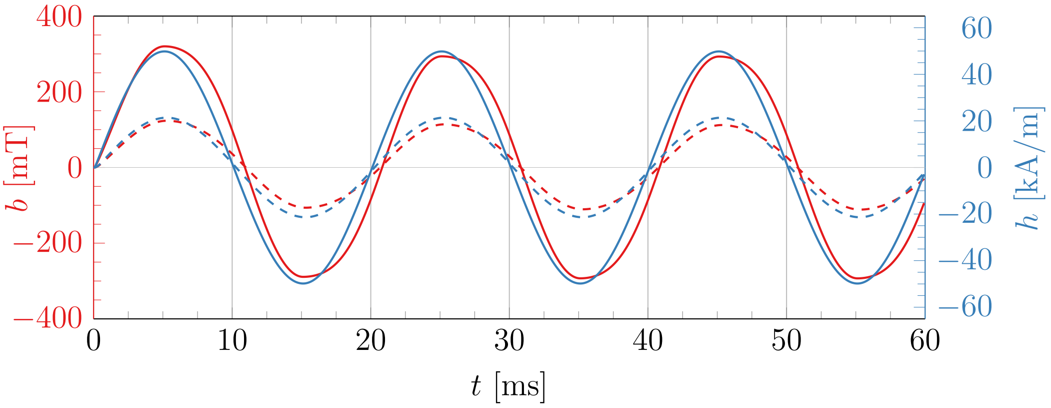

Figure 5.14.: Values of h and b for the first 60 ms of the simulation at radius $r = 6\,\text{cm}$ (solid) and $r = 14\,\text{cm}$ (dashed).

the excitation), but the b field contains a bend. There, such a change of direction happened and it was switched from μ^+_{diff} to μ^-_{diff} or vice versa. What kind of hysteresis loop results from this, will be examined in a moment.

Furthermore, it can be seen in Figure 5.14 that a steady state is indeed established very quickly. As early as the second cycle, there is actually no longer any visible difference between the cycles. Another small detail can be seen in this figure. If the curves of the different radii are compared, a small phase shift can be identified, which can be seen particularly well between the zero crossings.

This is caused by the parameter σ, which is the electrical conductivity and affects the temporal component of the underlying PDE. An increase in the value causes this phase offset to increase. This allows a quick intermediate check with the physical background of a perfect conductor. Such a perfect conductor is defined by its non-existing resistance R or its infinitely large σ. This has the consequence that in a perfect conductor the magnetic field can not change, the time lag is so to speak infinitely large.

The simulation including Tellinen's model thus shows this desired behavior to some extent. However, a small σ is chosen deliberately, such that this effect is not too strong. The focus lies on Tellinen's model and another significant effects with a time delay are undesired. Otherwise, it would not be distinguishable which effect are responsible for these superimposed lags. It is good that it can be shown that the approaches also work with a $\sigma > 0$ and that the physical trend is correctly reproduced. But in the further course, the influence of σ is regarded as small and therefore neglected.

Instead, it is investigated whether the implementation results in a reasonable hysteresis loop. For this sake, the first 60 ms of the h and b values from Figure 5.14 at a radius of 6 cm are taken and displayed in bh coordinates, resulting in Figure 5.15. The general course looks good and as expected. The curves approaches the boundaries $B^{\pm}_{\text{sat}}$, but do not reach them, as desired. The first cycle is clearly different from the other two because this one starts at point $(0, 0)$. But the other two are visually very

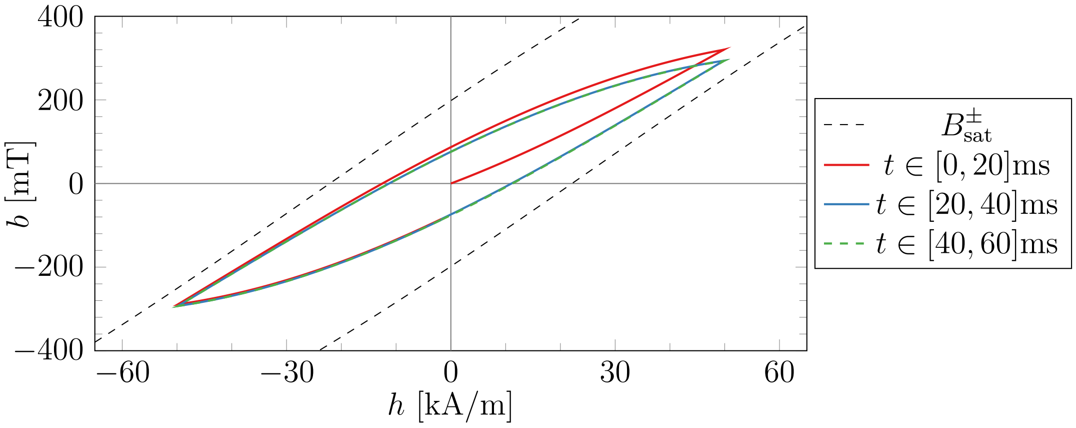

(a) Overview.

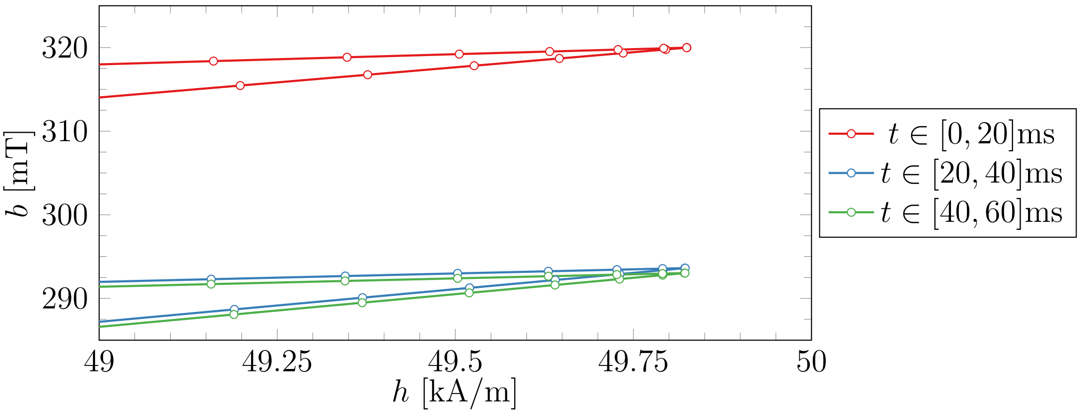

(b) Zoom on turning points. Marked are the actual calculation points.

Figure 5.15.: Hysteresis loop for the first 60 ms of the simulation at radius $r = 6\,\text{cm}$.

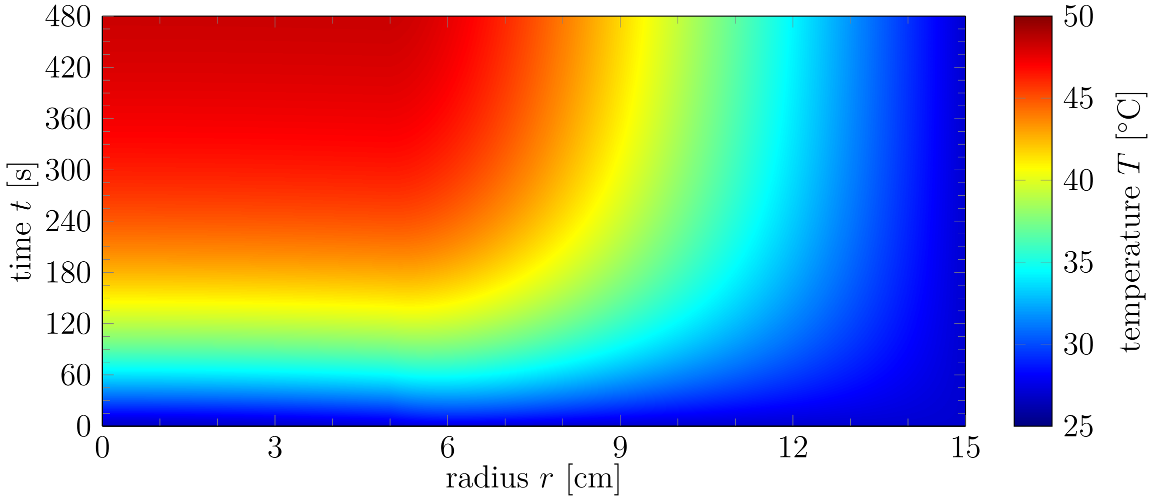

(a) overview

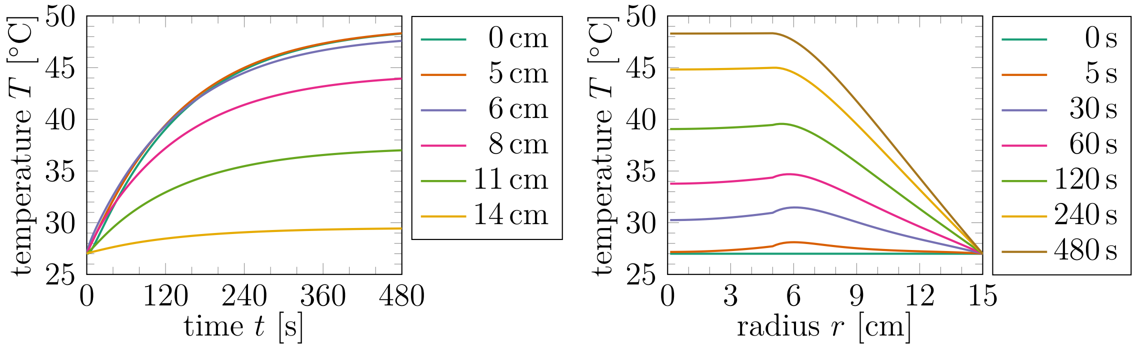

(b) constant radius r

(c) constant time t

Figure 5.16.: Result of the benchmark problem: temperature T.

similar. Here, it can be clearly seen that the steady state is already established after actually one cycle.

In Figure 5.15(b), it is shown that the chosen approaches correctly resolve the hysteresis loop turning points. The actual calculation points result in a sharp tip at the turning point and also the change between μ^{+}_{diff} and μ^{-}_{diff} works without delay. The fact – that these critical aspects are presented correctly – proves that the chosen approaches are successful. Tellinen's model is successfully integrated into the Curl-Curl Equation, such that the characteristic properties of the model are also evident in the spatially resolved simulation.

Heat Simulation

This paragraph focuses on the numerical results of the thermal simulation, in particular on the rough time scale. Further investigations on the finer time scale will follow in the section on the involved time scales. The overview of the temperature is given in Figure 5.16 and so far complies with the expectations. Individual aspects will now be discussed in more detail.

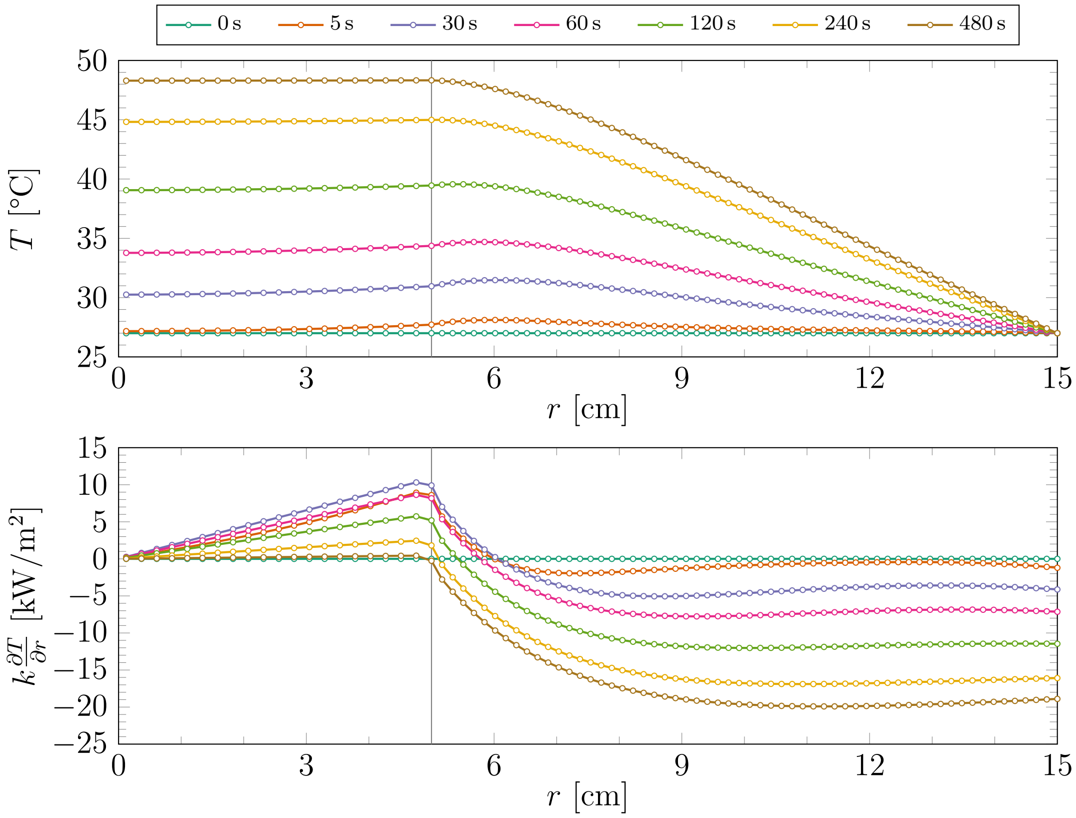

Figure 5.17.: Result of the benchmark problem: temperature T and heat flux $k\frac{\partial T}{\partial r}$.

The temperature rises most rapidly at a radius of slightly less than 6 cm. Two effects overlap here. On the one hand, the magnetic fields are strongest at a radius of 5 cm and thus generate the greatest power loss there. For radii larger than 5 cm this drops slowly. On the other hand, for a radius of less than 5 cm, no losses have been simulated, such that the heat can diffuse there easily.

The Figure 5.16(c) show that the generated heat at a radius around 5 cm to 6 cm diffuses towards the center of the simulation ($r = 0$ cm). The boundary condition there is fulfilled with a slope of zero. In the same way, the boundary condition at the outer edge ($r = 15$ cm) of the simulation is kept correctly fixed at a temperature of 27 °C.

Between these limits, continuous but not differentiable values for the temperature T are obtained. This is in line with expectations and physical requirements. It is required that $k\frac{\partial T}{\partial r}$ is continuous, which is fulfilled according to Figure 5.17.

The ending in the temporal sense of the simulation is also found to be satisfactory. For the radii below 5 cm, the temperature is constant and outside there is a drop towards the outer edge. Since the magnetic fields are in stable state, the loss model also gives consistent thermal excitations and the thermal simulation also transitions to a stable state. The maximal temperature reached is about 48 °C and is securely in the defined temperature range of the material used, which is 27 °C to 60 °C.

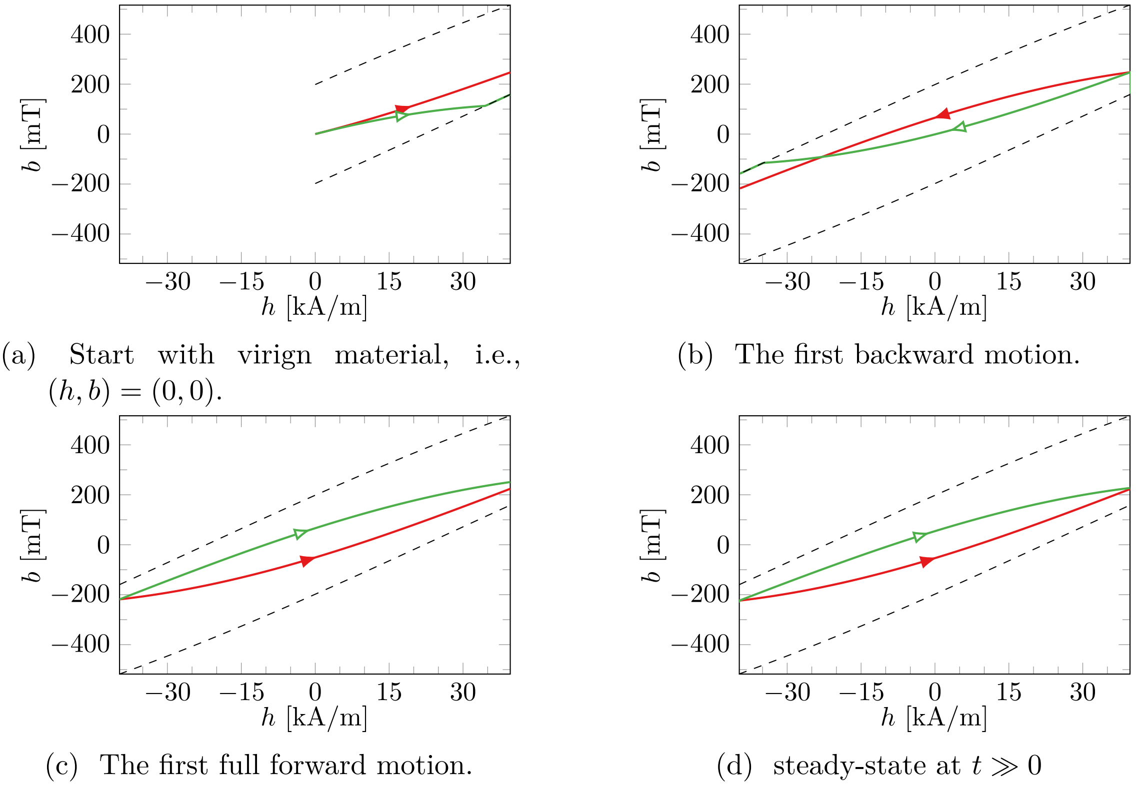

(a) Start with virign material, i.e., $(h, b) = (0, 0)$.

(b) The first backward motion.

(c) The first full forward motion.

(d) steady-state at $t \gg 0$

Figure 5.18.: For a fixed radius $r = 7.5\,\mathrm{cm}$ the benchmark results of b (red) and b_{rev} (green) are shown. The saturation curves $B^{\pm}_{\mathrm{sat}}$ are marked with dashed lines. The subplots are showing different time intervals. Figures 5.18(a) to 5.18(c) are directly consecutive and form the starting phase. For comparison, Figure 5.18(d) shows the curves at the end of the simulation.

In summary, no problems with the heat simulation are detected and the prerequisites are rated as fulfilled.

Loss Model – Starting Phase

The basis of the loss model is the prediction of the return path b_{rev}. In Figure 5.18 the path of b and b_{rev} at different times are shown. The simulation is started with an unmagnetized material, i.e., at $t = 0$ it holds $(h, b) = (0, 0) \in I$. The excitation is sinusoidal.

In the first quarter of a cycle of the sinus, the value of h increases until the first turning point. In Figure 5.18(a) it can be seen that the loss model can not yet be applied, in the sense that it outputs an energy of zero. While h is increasing the path of b lies above of b_{rev}. This means the enclosed area is negative orientated and therefore ignored.

In the next phase h is decreased until the second turning point is reached, as shown in Figure 5.18(b). The loss model begins to take effect. The approximation of

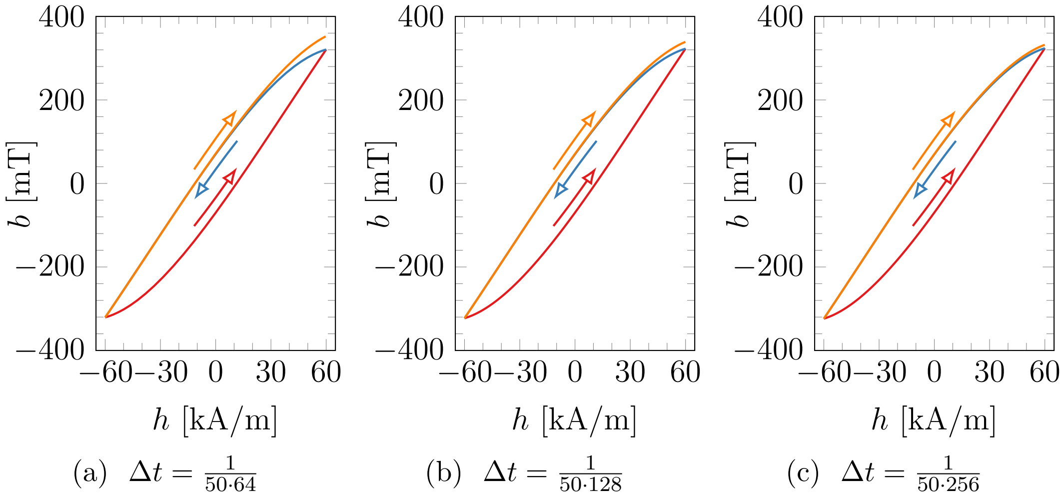

(a) $\Delta t = \frac{1}{50 \cdot 64}$ (b) $\Delta t = \frac{1}{50 \cdot 128}$ (c) $\Delta t = \frac{1}{50 \cdot 256}$

Figure 5.19.: Analysis of the influence of the time step size on the loss model. The simulation is run several times and only Δt was changed. The excitation is a 50 Hz sine wave and the evaluation is done at a radius of 5 cm. The red and blue paths are the actual forward and backward paths in steady state ($t \gg 0$, last cycle of the simulation) and the orange path is the predicted path b_{rev}.

the enclosed area is not yet good, but already a rough approximation. As seen in Figures 5.18(a) and 5.18(b) the restriction of b_{rev} to I is simple and effective.

The next plot Figure 5.18(c) shows the next phase. h is again increased. The loss model is already in nearly steady-state. The loop formed by b and b_{rev} is almost closed. After only one cycle of the sinusoidal excitation, the approximation of the enclosed loop is already quite good. The difference to the steady-state is small, as compared in Figures 5.18(c) and 5.18(d).

One aspect, which cannot be read from the result in Figure 5.18, is the change in temperature T. If the temperature T changes sufficiently during one cycle, it is quite possible that no closed curves result, i.e., b_{rev} and the actual return path differ significantly. An examination of the various time scales involved is coming up. However, it should be noted in advance that the temperature changes sufficiently slowly that this effect can be neglected.

In Sections 3.2 and 4.1.2 the convergence of Tellinen's hysteresis model and the loss model was already discussed. The numerical benchmark problem now supports the assumption, that the convergent behavior remains even after an embedding in an overall simulation. Already a few cycles are sufficient to get into nearly steady-state.

Loss Model – Influence of Time Step Size in Steady State

This investigation takes place in steady state, i.e., the simulation has already run through very many cycles of the periodic excitation and $t \gg 0$ holds. In this state, the temperature T is considered constant. The excitation is of sweeping type, such the situation is the same as in Section 4.1 in which the loss model without temperature dependence was presented. Ideally, the predicted return path b_{rev} should match the actual return path. However, as can be seen in Figure 5.19, this is not the case and there are deviations.

Figure 5.19 shows the last cycle of the simulation. Starting from the turning point at the bottom left, the simulation calculates the course in the (bh)–plane along the red path. At the same time, the return path b_{rev} is predicted using the loss model and is shown in orange. For comparison, the actual return path is drawn in blue. The red and the blue path thus result in exactly one cycle of the hysteresis loop and for a simple notation these are denoted with p^{+} and p^{-}.

The simulation is performed with 64, 128 and 256 intermediate time steps for each cycle. The temporal resolution has a direct impact on the simulation and the loss model seems to be particularly affected. This will now be investigated.

For the coarsest resolution, the largest deviation results, in the sense that the enclosed area is estimated to be too large. With finer resolution the approximation b_{rev} becomes better. This results in different temperatures T. In concrete terms, the values are 49.91 °C, 48.86 °C and 48.33 °C. As a result, the hysteresis loops $(p^{+} + p^{-})$ are slightly different in the three simulations.

The investigation does not focus on the exact numerical values of the deviation and also in general it is well known that an increased resolution provides an improved approximation when solving differential equations numerically.

Instead, it is focused on the fact that the magnetic field computation of the paths $p^{\pm}$ is based on an adjusted explicit Euler and thus is only of order one. The prediction of the return path b_{rev} in the benchmark is performed by using a third order Runge Kutta method. Despite the worse order, a closed hysteresis loop results for the normal paths $p^{\pm}$, while that is not the case for b_{rev}. This is attributed to the properties of the original Tellinen model and will now be discussed.

The big difference between $p^{\pm}$ and b_{rev} is that Tellinen's model is applied backwards, so to speak, with the roles of μ^{+}_{diff} and μ^{-}_{diff} reversed.

For the paths $p^{\pm}$, it was found in Chapter 3 that they behave in a well-behaved manner. This includes convergent behavior. By implication, this means that b_{rev} tends to behave divergently in the sense that it is error amplifying. While $p^{\pm}$ converge to the stable state, so it is an attractor for them, the stable state is a repeller for b_{rev}. Deviations from the stable state are thus amplified.

This means that the backward application of Tellinen's model turns out to be numerically much more difficult. For b_{rev} to approximate the path p^{-} sufficiently well, the numerical methods for computing b_{rev} must be of higher order than the ones for $p^{\pm}$. Although it is not preferred for computational time technical reasons, using implicit methods to compute b_{rev} can be useful here.

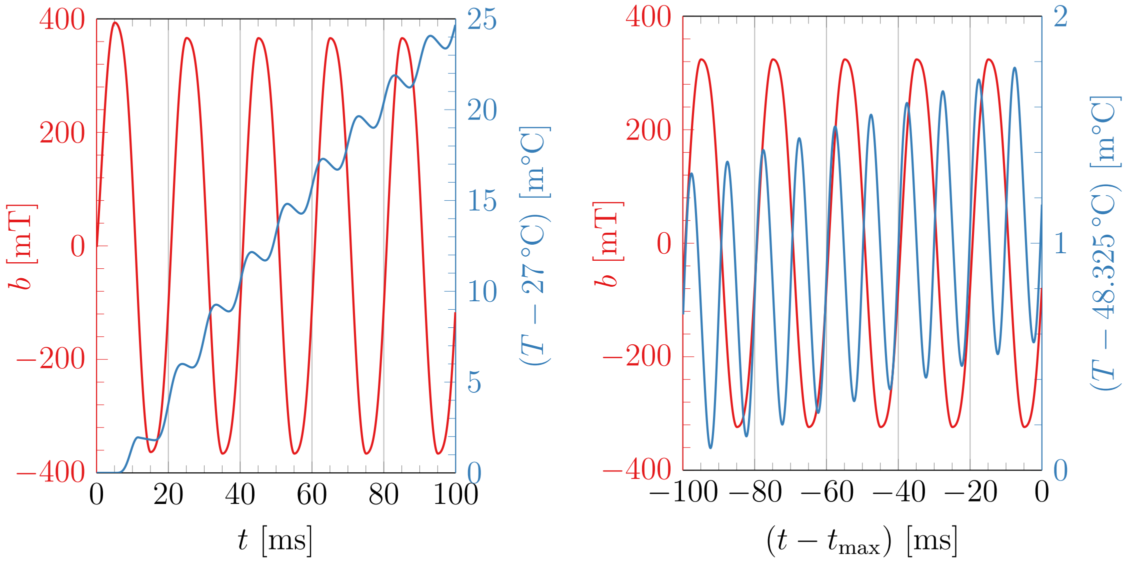

(a) first 100 ms

(b) last 100 ms

Figure 5.20.: Magnetic flux density b and temperature T for the first and last 100 ms of the simulation at a fixed radius of 5 cm.

Unfortunately, these properties of the loss model make it an important aspect in determining the required temporal resolution. The loss model requires finer temporal resolution than the original Tellinen model. This can be partly counteracted by using higher order and implicit methods for the calculation of b_{rev}. Unfortunately, this results in higher computational effort.

This problem could also be reduced by a more intelligent or dynamic use of the loss model. In this section, the steady state, i.e., p^+ and p^- already form a closed curve, is considered. In this case, the loss model offers no advantages but only the above disadvantages. The enclosed area could be determined by $p^\pm$. One possibility would be to use the loss model only if the paths $p^\pm$ are not yet closed. As soon as the stable state is almost reached, the loss model is switched off and the method of the area calculation is changed.

Comparison of the Time Scales

To provide further justification why such a multiphysics simulation is numerically demanding, the involved time scales are presented. No approaches from the field of numerical multi scale methods are applied within the simulation and thus the temperature is resolved as finely in time as the magnetic fields. The time scales of the magnetic fields h, b and the temperature T shall now be compared. An overview of these quantities has already been given in Figures 5.14 and 5.16.

The Figure 5.20 shows the first and last 100 ms of the simulation for the quantities b and T at a radius of 5 cm. This radius was chosen because the strongest magnetic fields occur there and therefore also rather high temperature changes.

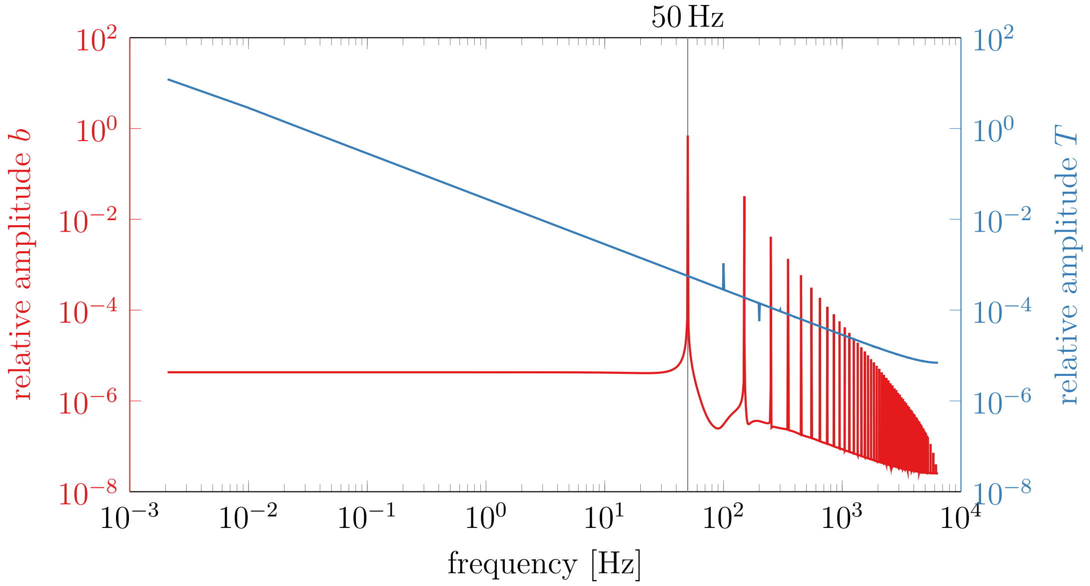

Figure 5.21.: Results of the discrete Fast Fourier Transformation (FFT) for b and T.

As expected, the magnetic field is dominated by the 50 Hz excitation (period of 20 ms). The temperature T seems to be influenced by two different effects.

On the one hand, there is always a short-term increase in temperature, synchronous with the timing when b changes rapidly. At this time the state (h, b) is at the widest point of the hysteresis loop and the loss model calculates the largest partial areas. This happens on the forward and backward direction of the hysteresis loop, resulting in a doubled frequency of 100 Hz. So this fits the expectations.

On the other hand, a short-term drop of the temperature T is seen in the areas where the state (h, b) is near to the reversal points within the hysteresis loop. There, the loss model provides only small subareas and accordingly only a small increase of the temperature T. In this case, the temperature T is diffused spatially and the boundary conditions result in an overall tendency to cool to room temperature of 27 °C. So also here the simulation shows a suitable behavior to the expectations.

Both effects together do not exactly cancel each other out in the simulation. The result is a slight slow increase of the temperature T. This effect is stronger at the start of the simulation and decreases towards the end. If the simulation is continued in time, an equilibrium and a steady state is expected.

In order to analyze if the optical detected frequencies are correct and to check if there are other frequencies of importance, a discrete Fast Fourier Transformation[1] (FFT) with normalization is performed on the simulation results for b and T.

The results of the FFT are shown in Figure 5.21. The flux density b clearly shows the dominant frequency of 50 Hz. In addition, there are further harmonics of odd order. The temperature T is mainly characterized by frequencies < 1 Hz. There is also a small peak at 100 Hz and an even smaller resonance at 200 Hz.

---

[1] https://docs.scipy.org/doc/scipy/reference/tutorial/fft.html

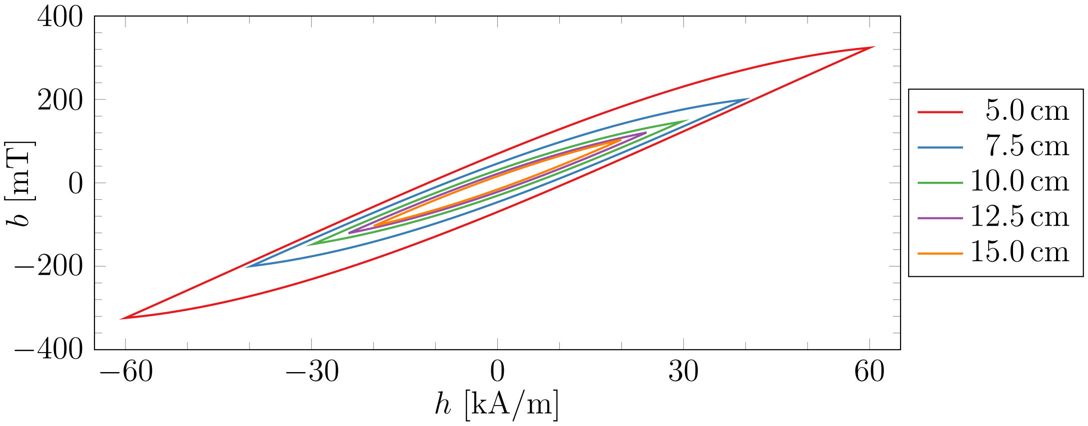

Figure 5.22.: Last hysteresis loop at different radii.

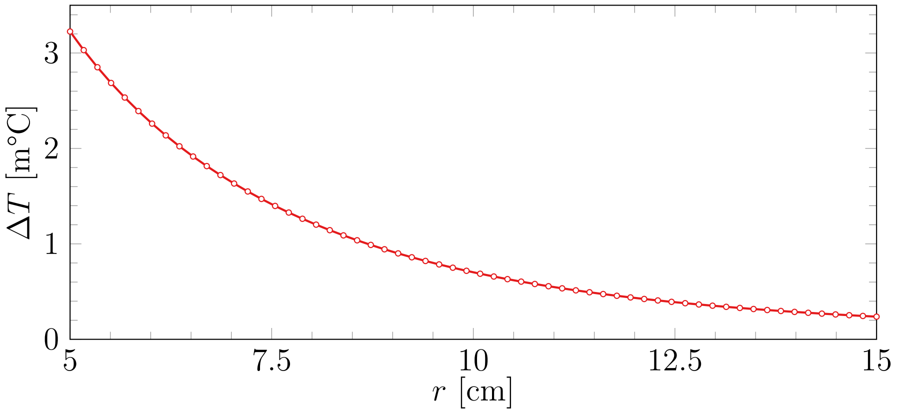

Figure 5.23.: Theoretically temperature change ΔT by hysteresis losses for the last cycle of the hysteresis loop.

All occurring frequencies can be explained by the conditions of the simulation and the models. No unexpected frequencies are recognized and thus, these simulation results are considered to be in agreement with the expectations and models. By using the FFT method, the difference in the time scales of b and T is clearly seen.

Now, the influence of a single pass of the hysteresis loop is investigated. The time domain is set to the last cycle in the simulation. Depending on the radius different hysteresis loop occur, as shown in Figure 5.22. To determine the influence of a single cycle, the enclosed area is calculated, the material constant c_V is considered and the temperature difference ΔT is obtained. Results are shown in Figure 5.23. Without scaling the values with c_V this corresponds to the source term q_V and are consistent with the expectation in Figure 5.10.

For radius $r = 5\,\text{cm}$, a value of roughly $\Delta T \approx 3\,\text{m°C}$ is obtained. With this number and a period of 20 ms, a rise of 1 °C would need more than 6 s. But as one can see in Figure 5.20, only a fraction of this is achieved as an actual increase. Thus, it remains that the temperature T and the magnetic field b differ by several orders of magnitude with respect to the time scale.

At this point another time scale is motivated, that of the current j. By clever and simplified assumptions, the current j is built into the simulation via appropriate boundary conditions. If one would like to extend the simulation by a more complex consideration of the current j, a further time scale in the range of kHz appears very easily. An application could be a noisy current signal or that the current is controlled by a pulse width modulation (PWM). An example: depending on the motor type, a measurement of the current motor position and a coupled electronically regulated control of the involved currents is necessary for varying the speed of the motor. Such a simulation must cover time scales in the range of mHz to kHz. So even though in the benchmark simulation the multi scale capability of the loss model was not exploited, it is a clear positive feature.

6 Conclusions and Outlook

In general, the goal of this thesis is achieved. A multiphysics simulation is implemented, which includes both the thermal and magnetic aspects including hysteresis. The results are mostly in line with the presented physically motivated expectations. It must be acknowledged that the numerical methods are strongly tailored to the benchmark problem and can not be unmodified applied to general problems.

The investigations reveal detailed reasons and in many places the problem is not the specifically chosen hysteresis model, but the general phenomenon of dependence on direction of magnetic hysteresis. Not only working but also non-functioning approaches are presented and their influence on the other aspects is shown.

It must be admitted that the used approaches are not the most complex and that if the individual components are considered in isolation, higher quality approaches are possible. The complexity in the scope of this dissertation results from the fact that the main focus is not the isolated consideration, but the simultaneous integration of the components into a multiphysics simulation. It is illustrated in Figure 5.1, how the individual components interact with each other.

Through the self-performed implementation, it is proven that the collected approaches can indeed be combined into a multiphysics simulation. All the necessary steps to perform such a simulation are listed. Problems and approaches to solutions from different areas are addressed. The thought process starting with the isolated modeling of a phenomenon, the investigation of which behavior is expected from the physical contexts, the development of suitable analysis methods and finally the holistic implementation in a complex simulation environment is portrayed. Methods from different areas of applied and pure mathematics as well as fundamental knowledge of physics are utilized and combined.

Each of the individual components models a physical aspect. A partially simplified representation of the physical principles at the beginning of this dissertation allows the models to be checked for reasonableness. No gross violations are found and good agreement between expectation and analysis is shown in many areas. For further research there is the possibility to elaborate the physical phenomena more profoundly and evaluate the presented models in more detail.

Suitable investigation methods are developed for analyses and evaluations. The used approaches prove to be suitable and flexible enough to be applied – not only to the original Tellinen's model – but also to the derived extensions. These approaches may also prove useful for other models based on directional differential equations and interpolation between two boundaries.

In summary, it is proven that the models have docile properties. The stability and convergence of the models in particular are of significant importance. The models are well-defined and analytical solutions stay within the definition domain. They can be applied without restriction and strive towards a stable solution. These studies go beyond those already published and cover a significant part of the field of application. Nevertheless, there are still opportunities to intensify the investigations.

The claim of the original Tellinen model to be a simple, easy to understand and fast hysteresis model is confirmed and also the extensions preserve this claim. Thus, in the context of this dissertation, it is perfectly fine to have more complex hysteresis models that have a different focus.

While there are several comparisons between hysteresis models, these mainly focus on the isolated view. Demonstrations of how to embed these models into a spatially and temporally resolved simulations are much rarer. One of these gaps is filled by this dissertation.

One way to improve the original Tellinen model can be achieved in conjunction with the first order reversal curves. Tellinen's model is based on interpolation between boundary curves and does not include measured information in the interior. The measured inner curves can be integrated into the interpolation, resulting in a stepwise interpolation. A measurement of such inner curves is interesting under different view points. If the investigated material indeed behaves very linearly – as in the interpolation of the original model – this is a confirmation that this material is well approximated. If the result is that the material does not behave linearly, a justification is found, why there are differences between a theoretical simulation and real experiment. After different materials are examined this way, perhaps patterns can be identified as to which types of materials are particularly well or poorly modeled by Tellinen's model.

One point, that is only briefly addressed in this dissertation, is the processing of measured data points so that the interpolated data is a valid input for Tellinen's model. It is assured that appropriate mathematical methods exist, but not that they are optimized for this use case. One-dimensional monotonicity-preserving interpolation has already been extensively researched. This can easily be adapted for the needs of the original model. The two-dimensional input data in the extended model, requires analogous properties in one dimension, which is more complex to achieve. Also, the research and extensions of the original model have produced an increased requirement for smoothness of the input data. A further discussion and analysis, which methods are particularly suitable or can be adapted and optimized, is still pending.

Part I.

Appendix

A Theoretical Background: Ordinary Differential Equations

In the context of this dissertation, solutions of ordinary differential equations (ODEs) are considered at various points. The core definition (3.7) of the Tellinen's hysteresis model is particularly noteworthy. But also in the further analysis, ODEs with adapted right-hand sides are frequently used in Chapters 3 and 4.

Initial value problems in the form

$$\begin{aligned} y' &= f(t, y) \\ y(t_0) &= y_0 \end{aligned} \tag{A.1}$$

with $y : \mathbb{R} \to \mathbb{R}$ are considered. Since in the course of this thesis many different right hand sides f are considered, an analysis approach adapted particularly to these f is presented here. The focus is on the definition range of the solution y. As simple criteria as possible are detailed, so that the solution y exists on an interval $[t_{\min}, t_{\max}]$ with $t_{\min} \leq t_0 \leq t_{\max}$. Often the goal is to show that y is defined on the whole domain of the real numbers $\mathbb{R}$.

At this point, the focus will be on argumentation by using commonly known propositions and lemmas from literature such as [92, 93, 95, 97].

The basis for the Picard-Lindelöf theorem is the Lipschitz continuity w.r.t. the second argument of f. For any (x, y) and (x, z) of interest and arbitrary norm $\|\cdot\|$, a constant $L > 0$ exists, such that

$$\|f(x, y) - f(x, z)\| \leq L \cdot \|y - z\| \tag{A.2}$$

holds. The exact numerical value of L is not of interest. As a sufficient condition for the existence of such L, boundedness of the partial derivative $\frac{\partial f}{\partial y}$ is used. In the considered f this is an easy property to check.

The theorem of Picard-Lindelöf ensures existence and uniqueness of the solution y of (A.1) for any suitable initial value (t_0, y_0) on a domain $[t_0 - \epsilon, t_0 + \epsilon]$ with $\epsilon > 0$. Thus solutions $y_0(t)$ and $y_1(t)$, respectively defined to initial values (t_0, y_0) and (t_0, y_1) with $y_0 \neq y_1$, are without common points.

Global variants of Picard Lindelöf's theorem extend the domain of definition to an interval (α, β) with $t_0 \in (\alpha, \beta)$. Here $\alpha = -\infty$ and $\beta = \infty$ are feasible. In the later case, the definition range is already maximal.

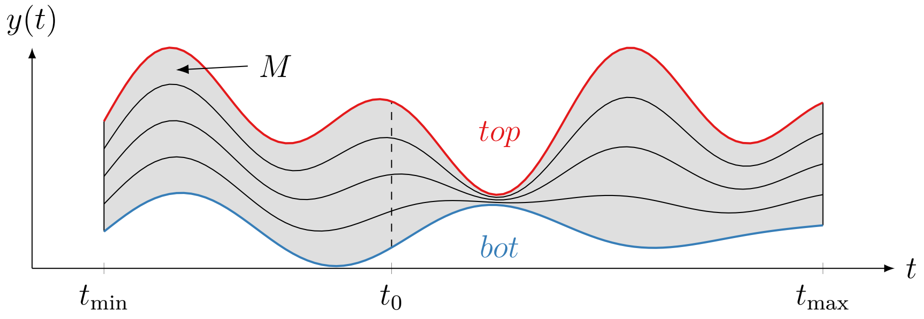

Figure A.1.: Illustration of Lemma A.1. Shown is the set M, the boundaries *top* (red), *bot* (blue) and some solutions in between (black).

What is interesting now is the case of $\beta < \infty$. The case $-\infty < \alpha$ follows analogously and is not explained explicitly. If $\beta < \infty$ holds, it means that the solution y is unbounded at β, i.e., it yields

$$\lim_{t \to \beta^-} |y(t)| = \infty\,. \tag{A.3}$$

Simple criteria for the f are introduced such that the case (A.3) cannot occur on an interval $[t_{\min}, t_{\max}]$. If there exist a $\beta < \infty$, $t_{\max} < \beta$ would have to hold. The argument also works for $t_{\max} \to \infty$, such that the entire range $\mathbb{R}$ is also covered.

Lemma A.1: Given a non-empty $T = [t_{\min}, t_{\max}]$ and differentiable functions $\mathit{top}, \mathit{bot} : T \to \mathbb{R}$ with $\mathit{top}(t) > \mathit{bot}(t)$ for all $t \in T$. Let

$$M = \Big\{(t, y) \in T \times \mathbb{R} \mid \mathit{bot}(t) \leq y \leq \mathit{top}(t)\Big\}\,. \tag{A.4}$$

Given continuous function $f : M \subset \mathbb{R} \times \mathbb{R} \to \mathbb{R}$ being globally Lipschitz-continuous w.r.t. the second variable. Let *top* and *bot* be solutions of the initial value problem

$$y' = f(t, y) \tag{A.5}$$

with $\big(t_0, \mathit{top}(t_0)\big), \big(t_0, \mathit{bot}(t_0)\big) \in M$ as initial values.

Then any solution $y : \mathbb{R} \to \mathbb{R}$ of (A.5) with $y(t_0) = y_0$ and $(t_0, y_0) \in M$ is defined on the domain T and fulfills $\mathit{bot}(t) \leq y(t) \leq \mathit{top}(t)$ for all $t \in T$. This statement is also valid for $T = \mathbb{R}$.

Proof. An overview of the involved quantities is given in Figure A.1. Based on the global version of the Picard Lindelhöf's theroem a maximal interval (α, β) exists, within all solutions y are well defined and unique. If $(\alpha, \beta) = \mathbb{R}$ holds, all properties follow directly from the existence and uniqueness of the solutions. For the case $(\alpha, \beta) \neq \mathbb{R}$, it will be proven by contradiction that $[t_{\min}, t_{\max}] \subset (\alpha, \beta)$ holds.

Assuming that either $\beta \leq t_{\max}$ or $t_{\min} \leq \alpha$ holds, a contradiction for the former case is shown. The later case follows analogously.

β is assumed to be maximal, such that β can not be chosen greater because the solution y is unbounded, i.e., (A.3) holds. But it exists solutions *top*, *bot* that are defined on the closed interval $[t_{\min}, t_{\max}]$, which implies that they are bounded. *top* and *bot* are the most upper and lower boundary of M. An unbounded solution y must therefore cross the bounded boundaries *top* or *bot*. This is a contradiction to the uniqueness of solutions. Hence it is concluded that $t_{\max} < \beta$ must apply.

In summary, either $(\alpha, \beta) = \mathbb{R}$ is valid or at least $[t_{\min}, t_{\max}] \subset (\alpha, \beta)$. On the interval $[t_{\min}, t_{\max}]$ all solutions are well-defined and unique. $\square$

Remark A.2. Thus, in order to apply Lemma A.1, it is sufficient to check the partial derivative $\frac{\partial f}{\partial y}$ for boundedness for a given inital value problem (A.1) and to specify upper and lower bounds *top*, *bot*.

Bibliography

[1] B. Balasubramanian et al. "Synergistic computational and experimental discovery of novel magnetic materials". In: *Molecular Systems Design & Engineering* 5.6 (2020), pp. 1098–1117. DOI: `10.1039/d0me00050g`.

[2] BIPM. *Le système international d'unités / the international system of units ('the SI brochure')*. Ninth. Bureau international des poids et mesures, 2019. ISBN: 978-92-822-2272-0. URL: `http://www.bipm.org/en/si/si_brochure/`.

[3] W. Commons. *File:Right-hand grip rule.svg — Wikimedia Commons, the free media repository.* [Online; accessed 11-March-2021]. 2020. URL: `https://commons.wikimedia.org/w/index.php?title=File:Right-hand_grip_rule.svg&oldid=501577878`.

[4] A. Einstein and A. Beck. *The collected papers of Albert Einstein: the swiss years : writings, 1909-1911.* The Collected Papers of Albert Einstein [English Translation]. Princenton University Press, 1993. ISBN: 9780691102504.

[5] Gorchy. *NdFeB-domains.* Wikimedia Commons. License: `https://commons.wikimedia.org/wiki/Commons:GNU_Free_Documentation_License,_version_1.2`, Last accessed: 27.01.2021. 2005. URL: `https://en.wikipedia.org/wiki/File:NdFeB-Domains.jpg`.

[6] D. R. Lide, ed. *CRC handbook of chemistry and physics, internet version 2005.* CRC Press, 2005. URL: `http://www.hbcpnetbase.com`.

[7] H. P. Myers. *Introductory solid state physics.* CRC press, 1997.

[8] C. R. Nave. *Hyperphysics.* Retrieved february 1, 2021. URL: `http://hyperphysics.phy-astr.gsu.edu/hphys.html`.

[9] M. Sakurai et al. "Discovering rare-earth-free magnetic materials through the development of a database". In: *Physical Review Materials* 4.11 (Nov. 2020), p. 114408. DOI: `10.1103/physrevmaterials.4.114408`.

[10] D. D. Stancil. "Magnetic susceptibilities". In: *Theory of Magnetostatic Waves.* Springer New York, 1993, pp. 20–59. DOI: `10.1007/978-1-4613-9338-2_2`.

[11] P. Tipler. *Physics for scientists and engineers.* New York: Freeman, W.H., 2004. ISBN: 0716743892.

[12] S. Wörz and H. Bernhardt. "A global convergent derivative-free method for solving a system of non-linear equations". In: *Numerical Algorithms* 76.1 (Dec. 2016), pp. 109–124. DOI: `10.1007/s11075-016-0246-0`.

[13] S. Zurek. *Database of magnetic properties.* Online. Last accessed: 15.03.2022. URL: `https://e-magnetica.pl/`.

Hysteresis & Ferromagnetism

[14] A. Aharoni. *An introduction to the theory of ferromagnetism.* Nov. 2000. ISBN: 978-0198508090.

[15] A. P. S. Baghel and S. V. Kulkarni. "Dynamic loss inclusion in the Jiles-Atherton (JA) hysteresis model using the original JA approach and the field separation approach". In: *Magnetics, IEEE Transactions on* 50 (Feb. 2014), pp. 369–372. DOI: `10.1109/TMAG.2013.2284381`.

[16] A. Bergqvist, D. Lin, and P. Zhou. "Temperature-dependent vector hysteresis model for permanent magnets". In: *IEEE Transactions on Magnetics* 50.2 (Feb. 2014), pp. 345–348. ISSN: 1941-0069. DOI: `10.1109/TMAG.2013.2282822`.

[17] A. Bergqvist. "Magnetic vector hysteresis model with dry friction-like pinning". In: *Physica B: Condensed Matter* 233.4 (June 1997), pp. 342–347. DOI: `10.1016/s0921-4526(97)00319-0`.

[18] G. Bertotti. "General properties of power losses in soft ferromagnetic materials". In: *IEEE Transactions on Magnetics* 24.1 (Jan. 1988), pp. 621–630. ISSN: 1941-0069. DOI: `10.1109/20.43994`.

[19] E. Cardelli, E. Della Torre, and E. Pinzaglia. "Using the reduced Preisach vector model to predict the cut angle influence in Si-Fe steels". In: *IEEE Transactions on Magnetics* 41.5 (2005), pp. 1560–1563. DOI: `10.1109/TMAG.2005.845051`.

[20] E. Cardelli. "Chapter 4 - advances in magnetic hysteresis modeling". In: ed. by K. Buschow. Vol. 24. Handbook of Magnetic Materials. Elsevier, 2015, pp. 323–409. DOI: `10.1016/bs.hmm.2015.10.002`.

[21] S. Chikazumi. *Physics of ferromagnetism.* International Series of Monographs on Physics. OUP Oxford, 2009. ISBN: 9780191569852.

[22] M. Dosaev et al. "Hysteresis effect in operation of small wind power generators". In: *2010 Asia-Pacific Power and Energy Engineering Conference.* 2010, pp. 1–4. DOI: `10.1109/APPEEC.2010.5449013`.

[23] L. R. Dupré, R. Van Keer, and J. A. A. Melkebeek. "An iron loss model for electrical machines using the Preisach theory". In: *IEEE Transactions on Magnetics* 33.5 (Sept. 1997), pp. 4158–4160. ISSN: 1941-0069. DOI: `10.1109/20.619695`.

[24] L. Dupré and J. Melkebeek. "Electromagnetic hysteresis modeling: From material science to finite element analysis of devices". In: (Jan. 2003).

[25] Ferroxcube. *Soft ferrites and accessories – data handbook.* Online. Accessed 03.03.2020. 2013. URL: `https://www.ferroxcube.com/en-global/download/download/11`.

[26] G. Friedman and I. D. Mayergoyz. "Hysteretic energy losses in media described by vector Preisach model". In: *IEEE Transactions on Magnetics* 34.4 (July 1998), pp. 1270–1272. ISSN: 1941-0069. DOI: `10.1109/20.706518`.

[27] M. Ghezelbash et al. “Temperature dependence of magnetic hysteresis loop of NdFeB with uniaxial anisotropy by LIBS technique”. In: *Journal of Superconductivity and Novel Magnetism* 30.7 (July 2017), pp. 1893–1898. ISSN: 1557-1947. DOI: `10.1007/s10948-017-3984-x`.

[28] A. P. Guimarães. *Principles of nanomagnetism*. Springer Berlin Heidelberg, 2009. DOI: `10.1007/978-3-642-01482-6`.

[29] V. Hassani, T. Tjahjowidodo, and T. N. Do. “A survey on hysteresis modeling, identification and control”. In: *Mechanical Systems and Signal Processing* 49 (Dec. 2014). DOI: `10.1016/j.ymssp.2014.04.012`.

[30] H. Hauser et al. “Effect of structural changes on hysteresis properties of steel”. In: *Journal of Magnetism and Magnetic Materials* 320.20 (2008). Proceedings of the 18th International Symposium on Soft Magnetic Materials, e983–e987. ISSN: 0304-8853. DOI: `10.1016/j.jmmm.2008.04.101`.

[31] D. C. Jiles. “A self consistent generalized model for the calculation of minor loop excursions in the theory of hysteresis”. In: *1992 IEEE International Magnetics Conference (INTERMAG)*. 1992, pp. 207–207. DOI: `10.1109/INTMAG.1992.696390`.

[32] S. Kobayashi et al. “Effects of cold rolling on magnetic minor hysteresis loops of duplex stainless steels”. In: *Philosophical Magazine* 97.6 (2017), pp. 419–430. DOI: `10.1080/14786435.2016.1263401`.

[33] A. Krings and J. Soulard. “Overview and comparison of iron loss models for electrical machines”. In: *Journal of Electrical Engineering* 10.3 (2010). Updated and revised version of conference paper from the 5th International Conference and Exhibition on Ecological Vehicles and Renewable Energies (EVER 10), Monte-Carlo, MONACO, MAR 25-28, 2010QC 20120120, pp. 162–169.

[34] B. Krüger. “Current-driven magnetization dynamics: analytical modeling and numerical simulation”. PhD thesis. Universität Hamburg, 2011.

[35] M. Kuepferling et al. “Magnetic hysteresis in plastically deformed low-carbon steel laminations”. In: *Journal of Magnetism and Magnetic Materials - J MAGN MAGN MATER* 316 (Sept. 2007). DOI: `10.1016/j.jmmm.2007.03.120`.

[36] J. Kühn. “Tellinen’s hysteresis model in the magnetic field computation with uncertainties”. MA thesis. Bergische Universität Wuppertal, 2016.

[37] J. Kühn, A. Bartel, and P. Putek. “A thermal extension of Tellinen’s scalar hysteresis model”. In: *Scientific Computing in Electrical Engineering*. Ed. by G. Nicosia and V. Romano. Cham: Springer International Publishing, 2020, pp. 55–63. ISBN: 978-3-030-44101-2.

[38] J. Kühn, A. Bartel, and P. Putek. “A hysteresis loss model for Tellinen’s scalar hysteresis model”. In: *Scientific Computing in Electrical Engineering*. Ed. by M. van Beurden, N. Budko, and W. Schilders. Cham: Springer International Publishing, 2021, pp. 241–250. ISBN: 978-3-030-84238-3.

[39] J. Kühn, A. Bartel, and P. Putek. “A thermal extension and loss model for Tellinen’s hysteresis model”. In: *COMPEL - the international journal for computation and mathematics in electrical and electronic engineering* 40.2 (Jan. 2021), pp. 126–141. DOI: `10.1108/compel-07-2019-0306`.

[40] J. Macki, P. Nistri, and P. Zecca. “Mathematical models for hysteresis”. In: *SIAM Review* 35 (Mar. 1993), pp. 94–123. DOI: `10.1137/1035005`.

[41] T. Matsuo. “Rotational saturation properties of isotropic vector hysteresis models using vectorized stop and play hysterons”. In: *IEEE Transactions on Magnetics* 44.11 (Nov. 2008), pp. 3185–3188. DOI: `10.1109/tmag.2008.2001656`.

[42] I. D. Mayergoyz. *Mathematical models of hysteresis*. Springer, 1991. ISBN: 978-1-4612-7767-5. DOI: `10.1007/978-1-4612-3028-1`.

[43] P. Melo and R. E. Araújo. “An overview on Preisach and Jiles-Atherton hysteresis models for soft magnetic materials”. In: *Technological Innovation for Smart Systems*. Ed. by L. M. Camarinha-Matos, M. Parreira-Rocha, and J. Ramezani. Cham: Springer International Publishing, 2017, pp. 398–405. ISBN: 978-3-319-56077-9. DOI: `10.1007/978-3-319-56077-9_39`.

[44] M. Ployard et al. “Comparison of iron loss models under synchronous generator waveforms”. In: *2018 XIII International Conference on Electrical Machines (ICEM)*. 2018, pp. 1123–1129. DOI: `10.1109/ICELMACH.2018.8506863`.

[45] F. Preisach. “Über die magnetische Nachwirkung”. In: *Zeitschrift für Physik* 94.5-6 (May 1935), pp. 277–302. DOI: `10.1007/bf01349418`.

[46] L. Prigozhin et al. “On the energy-based variational model for vector magnetic hysteresis”. In: *IEEE Transactions on Magnetics* 52.12 (Dec. 2016), pp. 1–11. ISSN: 0018-9464. DOI: `10.1109/TMAG.2016.2599143`.

[47] A. Raghunathan et al. “Theoretical model of temperature dependence of hysteresis based on mean field theory”. In: *IEEE Transactions on Magnetics* 46.6 (June 2010), pp. 1507–1510. ISSN: 0018-9464. DOI: `10.1109/TMAG.2010.2045351`.

[48] D. Ribbenfjard and G. Engdahl. “Modeling of dynamic hysteresis with Bergqvist’s lag model”. In: *IEEE Transactions on Magnetics* 42.10 (2006), pp. 3135–3137. DOI: `10.1109/TMAG.2006.880138`.

[49] M. J. Sablik and D. C. Jiles. “Modeling the effects of torsional stress on hysteretic magnetization”. In: *IEEE Transactions on Magnetics* 35.1 (1999), pp. 498–504. DOI: `10.1109/20.737472`.

[50] S. Steentjes et al. “Iron-loss and magnetic hysteresis under arbitrary waveforms in NO electrical steel: a comparative study of hysteresis models”. In: *IEEE Transactions on Industrial Electronics* 64.3 (Mar. 2017), pp. 2511–2521. ISSN: 0278-0046. DOI: `10.1109/TIE.2016.2570200`.

[51] J. Stoker and W. T. Nisbet. “Hysteresis effects in non-reciprocal and rotary field ferrite phase shifters”. In: *IEE Colloquium on Ferrite Materials, Devices and Applications*. 1989, pp. 8/1–8/7.

[52] H. W. F. Sung and C. Rudowicz. “A closer look at the hysteresis loop for ferromagnets - a survey of misconceptions and misinterpretations in textbooks”. In: (Oct. 30, 2002).

[53] S. Takahashi et al. “Analysis of minor hysteresis loops of cold rolled low carbon steel”. In: *IEEE Transactions on Magnetics* 42.11 (2006), pp. 3782–3784. DOI: `10.1109/TMAG.2006.879147`.

[54] J. Tellinen. “A simple scalar model for magnetic hysteresis”. In: *IEEE Transactions on Magnetics* 34.4 (July 1998), pp. 2200–2206. ISSN: 0018-9464. DOI: `10.1109/20.703856`.

[55] H. L. Toms, R. G. Colclaser, and M. P. Krefta. “Two-dimensional finite element magnetic modeling for scalar hysteresis effects”. In: *IEEE Transactions on Magnetics* 37.2 (Mar. 2001), pp. 982–988. ISSN: 1941-0069. DOI: `10.1109/20.917181`.

[56] A. Visintin. “Mathematical models of hysteresis”. In: ed. by I. M. G. Bertotti. Vol. 1. The Science of Hysteresis. Elsevier, 2006. Chap. 1, pp. 1–123. ISBN: 0-123-69431-0.

[57] S. E. Zirka et al. “Inverse hysteresis models for transient simulation”. In: *IEEE Transactions on Power Delivery* 29.2 (Apr. 2014), pp. 552–559. ISSN: 0885-8977. DOI: `10.1109/TPWRD.2013.2274530`.

Barkhausen effect

[58] G. Bertotti. “Dynamics of magnetic domain walls and Barkhausen noise in metallic ferromagnetic systems”. In: *Springer Proceedings in Physics*. Springer Berlin Heidelberg, 1987, pp. 135–139. DOI: `10.1007/978-3-642-73107-5_27`.

[59] C. Casavola, C. Pappalettere, and F. Tursi. “Calibration of Barkhausen noise for residual stress measurement”. In: *Conference Proceedings of the Society for Experimental Mechanics Series*. Springer New York, Sept. 2012, pp. 255–266. DOI: `10.1007/978-1-4614-4226-4_30`.

[60] L. Ceniga and F. Kováč. “Influence of annealing process on magnetic properties and Barkhausen noise of the Fe-W-B amorphous alloy”. In: *Czechoslovak Journal of Physics* 52.S1 (Jan. 2002), A73–A76. DOI: `10.1007/s10582-002-0016-1`.

[61] M. Ishihara, T. Sakamoto, and H. Minami. “Grain size measurement using Barkhausen noise method”. In: *Nondestructive Characterization of Materials IV*. Springer US, 1991, pp. 277–282. DOI: `10.1007/978-1-4899-0670-0_33`.

[62] D. C. Jiles. “Dynamics of domain magnetization and the Barkhausen effect”. In: *Czechoslovak Journal of Physics* 50.8 (2000), pp. 893–924. DOI: `10.1023/a:1022846128461`.

[63] Y. N. Kharitonov and V. M. Rudyak. “Demonstration of the Barkhausen effect in ferroelectrics and in ferromagnetics”. In: *Soviet Physics Journal* 18.12 (Dec. 1975), pp. 1766–1767. DOI: `10.1007/bf00892811`.

[64] M. Neslušan et al. “Nondestructive monitoring of rail surface damage via Barkhausen noise technique”. In: *Proceedings of the 17th International Conference on New Trends in Fatigue and Fracture*. Springer International Publishing, Nov. 2017, pp. 287–297. DOI: `10.1007/978-3-319-70365-7_34`.

[65] N. I. Noskova et al. “Structure and Barkhausen effect parameters of amorphous alloys after various heat treatments”. In: *Russian Journal of Nondestructive Testing* 40.9 (Sept. 2004), pp. 620–624. DOI: `10.1007/s11181-004-0008-2`.

[66] Z. Qu et al. “Nondestructive detection and analysis of skidding damage for bearing steel 100cr6 using improved magnetic Barkhausen noise technique”. In: *Journal of Nondestructive Evaluation* 38.4 (Sept. 2019). DOI: `10.1007/s10921-019-0634-1`.

[67] V. M. Rudyak and V. B. Khazankin. “Relation between the Barkhausen effect and the remanent magnetization of ferromagnets”. In: *Soviet Physics Journal* 12.5 (May 1969), pp. 632–634. DOI: `10.1007/bf00814854`.

[68] A. A. Samimi et al. “Correlation between AC core loss and surface magnetic Barkhausen noise in electric motor steel”. In: *Journal of Nondestructive Evaluation* 33.4 (Sept. 2014), pp. 663–669. DOI: `10.1007/s10921-014-0260-x`.

[69] J. C. Sánchez, M. F. de Campos, and L. R. Padovese. “Comparison between different experimental set-ups for measuring the magnetic Barkhausen noise in a deformed 1050 steel”. In: *Journal of Nondestructive Evaluation* 36.4 (Sept. 2017). DOI: `10.1007/s10921-017-0445-1`.

[70] J. P. Sethna, O. Perkovic, and K. A. Dahmen. “Hysteresis, avalanches, and Barkhausen noise”. In: *Scale Invariance and Beyond*. Springer Berlin Heidelberg, 1997, pp. 87–97. DOI: `10.1007/978-3-662-09799-1_6`.

[71] J. C. Slonczewski. “Theory of Bloch-line and Bloch-wall motion”. In: *Journal of Applied Physics* 45.6 (1974), pp. 2705–2715. DOI: `10.1063/1.1663654`.

[72] K. Šterbaková, A. Zentková, and A. Zentko. “The Barkhausen effect and the anomalous magnetization losses in metallic ferromagnets”. In: *Czechoslovak Journal of Physics* 54.S4 (2004), pp. 55–58. DOI: `10.1007/s10582-004-0030-6`.

[73] K. Stierstadt. “Über den Barkhausen-Effekt”. In: *Die Naturwissenschaften* 54.21 (1967), pp. 553–558. DOI: `10.1007/bf00602325`.

[74] K. Stierstadt and H. J. Geile. “Die Temperaturabhängigkeit des magnetischen Barkhausen-Effekts. II”. In: *Zeitschrift für Physik* 180.1 (Feb. 1964), pp. 66–79. DOI: `10.1007/bf01380642`.

[75] K. Stierstadt. “Der magnetische Barkhausen-Effekt”. In: *Springer Tracts in Modern Physics*. Springer Berlin Heidelberg, 1966, pp. 2–106. DOI: `10.1007/bfb0045894`.

[76] K. Tiitto. "Use of Barkhausen noise in fatigue". In: *Review of Progress in Quantitative Nondestructive Evaluation.* Springer US, 1990, pp. 1845–1853. DOI: `10.1007/978-1-4684-5772-8_237`.

Maxwell's equation

[77] M. Chaichian et al. "The electromagnetic field". In: *Electrodynamics: An Intensive Course.* Berlin, Heidelberg: Springer Berlin Heidelberg, 2016, pp. 115–168. ISBN: 978-3-642-17381-3. DOI: `10.1007/978-3-642-17381-3_3`.

[78] J. Donnevert. *Maxwell's equations.* Springer Vieweg, 2020. ISBN: 978-3-658-29375-8. DOI: `10.1007/978-3-658-29376-5`.

[79] É. Gourgoulhon. "Maxwell equations". In: *Special Relativity in General Frames: From Particles to Astrophysics.* Berlin, Heidelberg: Springer Berlin Heidelberg, 2013, pp. 585–627. ISBN: 978-3-642-37276-6. DOI: `10.1007/978-3-642-37276-6_18`.

[80] H. A. Haus et al. *Res.6-001 electromagnetic fields and energy.* License: Creative Commons BY-NC-SA. Massachusetts Institute of Technology: MIT OpenCourseWare, 2008. URL: `https://ocw.mit.edu/resources/res-6-001-electromagnetic-fields-and-energy-spring-2008`.

[81] B. P. Kosyakov. "Solutions to maxwell's equations". In: *Introduction to the Classical Theory of Particles and Fields.* Berlin, Heidelberg: Springer Berlin Heidelberg, 2007, pp. 141–193. ISBN: 978-3-540-40934-2. DOI: `10.1007/978-3-540-40934-2_4`.

[82] S. E. Kruger. "The three quasistatic limits of the Maxwell equations". In: ().

[83] J. Larsson. "Electromagnetics from a quasistatic perspective". In: *American Journal of Physics* 75.3 (2007), pp. 230–239. DOI: `10.1119/1.2397095`.

[84] U. Römer. "Numerical approximation of the magnetoquasistatic model with uncertainties and its application to magnet design". PhD thesis. Technische Universität Darmstadt, 2015.

[85] G. Rousseaux. "Forty years of galilean electromagnetism (1973-2013)". In: *Eur. Phys. J. Plus* 128.8 (2013), p. 81. DOI: `10.1140/epjp/i2013-13081-5`.

Monotonocity Preserving Interpolation

[86] S. Fredenhagen, H. J. Oberle, and G. Opfer. "On the construction of optimal monotone cubic spline interpolations". In: *Journal of Approximation Theory* 96.2 (1999), pp. 182–201. ISSN: 0021-9045. DOI: `10.1006/jath.1998.3247`.

[87] F. N. Fritsch and R. E. Carlson. "Monotone piecewise cubic interpolation". In: *SIAM Journal on Numerical Analysis* 17.2 (1980), pp. 238–246. ISSN: 00361429. URL: `https://www.jstor.org/stable/2156610`.

[88] J. Kühn. “Analyse der Erzeugung von monotonen Materialkurven mit Ausgleichssplines”. BA thesis. Bergische Universität Wuppertal, 2012.

[89] C. Manni. “Monotone interpolation of order 3 by C2 cubic splines”. In: *IMA Journal of Numerical Analysis* 17.2 (Apr. 1997), pp. 305–320. DOI: `10.1093/imanum/17.2.305`.

[90] C. Pechstein and B. Jüttler. “Monotonicity-preserving interproximation of B–H-curves”. In: *Journal of Computational and Applied Mathematics* 196.1 (Nov. 2006), pp. 45–57. ISSN: 0377-0427. DOI: `10.1016/j.cam.2005.08.021`.

[91] S. Reitzinger, B. Kaltenbacher, and M. Kaltenbacher. *A note on the approximation of B-H curves for nonlinear magnetic field computations*. SFB013 “Numerical and Symbolic Scientific Computing”. Jan. 2003. URL: `http://www.sfb013.uni-linz.ac.at/reports/2002/pdf-files/sfb02-30.pdf`.

Ordinary and partial differential equations

[92] K. Atkinson, W. Han, and D. Stewart. *Numerical solution of ordinary differential equations*. Jan. 2009. ISBN: 9780470042946. DOI: `10.1002/9781118164495`.

[93] D. F. Griffiths and D. J. Higham. *Numerical methods for ordinary differential equations: initial value problems*. Springer Undergraduate Mathematics Series. Springer London, 2010. ISBN: 9780857291486.

[94] C. Grossmann, H.-G. Roos, and M. Stynes. *Numerical treatment of partial differential equations*. Springer Berlin Heidelberg, 2007. DOI: `10.1007/978-3-540-71584-9`.

[95] P. F. Hsieh and Y. Sibuya. *Basic theory of ordinary differential equations*. Universitext (1979). Springer New York, 1999. ISBN: 9780387986999.

[96] P. Knabner and L. Angermann. *Numerical methods for elliptic and parabolic partial differential equations*. 1st ed. Vol. 44. Texts in Applied Mathematics. New York: Springer, 2003. ISBN: 978-0-387-95449-3. DOI: `10.1007/b97419`.

[97] R. Thompson and W. Walter. *Ordinary differential equations*. Graduate Texts in Mathematics. Springer New York, 2013. ISBN: 9781461206019.

Heat/Diffusion Equation and Finite Differences

[98] M. Ascher. “Explicit solutions of the one-dimensional heat equation for a composite wall”. In: *Mathematics of Computation* 14 (1960), pp. 346–353.

[99] T. L. Bergman et al. *Fundamentals of heat and mass transfer*. 8th ed. Wiley, 2017. ISBN: 978-1-119-32042-5.

[100] H. P. Langtangen. *Finite difference computing with exponential decay models*. 1st ed. Switzerland: SpringerOpen, 2016. ISBN: 978-3-319-29439-1. DOI: `10.1007/978-3-319-29439-1`.

[101] H. P. Langtangen and S. Linge. *Finite difference computing with PDEs: a modern software approach.* 1st ed. SpringerOpen, 2017. ISBN: 978-3-319-55456-3. DOI: `10.1007/978-3-319-55456-3`.

[102] P. M. Lascaux. “Lectures on numerical methods for time dependent equations : applications to fluid flow problems”. In: 1976.

[103] R. LeVeque. *Finite difference methods for ordinary and partial differential equations: steady-state and time-dependent problems (classics in applied mathematics classics in applied mathemat).* Society for Industrial and Applied Mathematics, 2007. ISBN: 978-0-89871-629-0. DOI: `10.1137/1.9780898717839`.

[104] E. Schachinger and B. Schnizer. “General solution of the two-dimensional heat equation for two concentric domains of different material”. In: *Wärme - und Stoffübertragung* 14 (1980), pp. 7–13. DOI: `10.1007/BF01613619`.

[105] R. Schneider. *Explicit and implicit finite-difference methods for the diffusion equation in two dimensions.* Tech. rep. Forschungszentrum Karlsruhe GmbH Technik und Umwelt (Germany). Inst. fuer Hochleistungsimpuls- und Mikrowellentechnik; Forschungszentrum Karlsruhe GmbH Technik und Umwelt (Germany). Programm Kernfusion ; 2003. URL: `http://hdl.handle.net/10068/185052`.

First Order Reversal Curves

[106] I. Bodale, L. Stoleriu, and A. Stancu. “Reversible and irreversible components evaluation in hysteretic processes using first and second-order magnetization curves”. In: *Magnetics, IEEE Transactions on* 47 (Feb. 2011), pp. 192–197. DOI: `10.1109/TMAG.2010.2083679`.

[107] J. Davies et al. “Magnetization reversal and nanoscopic magnetic-phase separation in La1-x Srx CoO3”. In: *Physical Review B - PHYS REV B* 72 (Oct. 2005). DOI: `10.1103/PhysRevB.72.134419`.

[108] M. Gutowski. “Better FORC diagrams”. In: *Conference: 10th International Symposium on Hysteresis Modeling and Micromagnetics, HMM 2015.* May 2015.

[109] C. R. Pike. “First-order reversal-curve diagrams and reversible magnetization”. In: *Phys. Rev. B* 68 (10 Sept. 2003), p. 104424. DOI: `10.1103/PhysRevB.68.104424`.

[110] C. R. Pike, A. P. Roberts, and K. L. Verosub. “Characterizing interactions in fine magnetic particle systems using first order reversal curves”. In: *Journal of Applied Physics* 85.9 (1999), pp. 6660–6667. DOI: `10.1063/1.370176`.

[111] C. R. Pike et al. “An investigation of multi-domain hysteresis mechanisms using FORC diagrams”. In: *Physics of the Earth and Planetary Interiors* 126.1 (2001). Rock Magnetism Enters the New Millenium. A Celebration of Fifty Years of Neel’s Theories, pp. 11–25. ISSN: 0031-9201. DOI: `10.1016/S0031-9201(01)00241-2`.

[112] A. P. Roberts, C. R. Pike, and K. L. Verosub. “First-order reversal curve diagrams: A new tool for characterizing the magnetic properties of natural samples”. In: *Journal of Geophysical Research: Solid Earth* 105.B12 (2000), pp. 28461–28475. DOI: `10.1029/2000jb900326`.

Demagnetization

[113] T. M. Baynes, G. J. Russell, and A. Bailey. “Comparison of stepwise demagnetization techniques”. In: *IEEE Transactions on Magnetics* 38.4 (July 2002), pp. 1753–1758. ISSN: 1941-0069. DOI: `10.1109/TMAG.2002.1017767`.

[114] K. Berger et al. “Magnetization and demagnetization studies of an HTS bulk in an iron core”. In: *IEEE Transactions on Applied Superconductivity* 26.4 (June 2016), pp. 1–7. ISSN: 1558-2515. DOI: `10.1109/TASC.2016.2517628`.

[115] R. R. Doell and A. Cox. “Analysis of alternating field demagnetization equipment”. In: *Methods in Palaeomagnetism*. Ed. by D. W. Collinson, K. M. Creer, and S. K. Runcorn. Vol. 3. Developments in Solid Earth Geophysics. Elsevier, 2013, pp. 241–253. DOI: `https://doi.org/10.1016/B978-1-4832-2894-5.50048-3`.

[116] V. Panchanathan. *Demagnetization of iron-neodymium-boron type permanent magnets without loss of coercivity.* Patent Number: 4.900.374. Feb. 1990.

Shape optimization of electric motors

[117] L.-Y. Hsu and M.-C. Tsai. “Tooth shape optimization of brushless permanent magnet motors for reducing torque ripples”. In: *Journal of Magnetism and Magnetic Materials* 282 (2004). International Symposium on Advanced Magnetic Technologies, pp. 193–197. ISSN: 0304-8853. DOI: `https://doi.org/10.1016/j.jmmm.2004.04.044`.

[118] A. Jabbari, M. Shakeri, and A. Nabavi. “Shape optimization of permanent magnet motors using the reduced basis technique”. In: *International Journal of Mechanical and Mechatronics Engineering* 3.1 (2009), pp. 61–66. ISSN: eISSN: 1307-6892.

[119] K. I. Laskaris and A. G. Kladas. “Permanent-magnet shape optimization effects on synchronous motor performance”. In: *IEEE Transactions on Industrial Electronics* 58.9 (Sept. 2011), pp. 3776–3783. ISSN: 1557-9948. DOI: `10.1109/TIE.2010.2093481`.

[120] P. Putek et al. “Shape and topology optimization of a permanent-magnet machine under uncertainties”. In: *Journal of Mathematics in Industry* 6.1 (Nov. 2016), p. 11. ISSN: 2190-5983. DOI: `10.1186/s13362-016-0032-6`.

[121] M. Seo et al. “Loss reduction optimization for heat capacity improvement in interior permanent magnet synchronous machine”. In: *IEEE Transactions on Magnetics* 54.11 (Nov. 2018), pp. 1–5. ISSN: 1941-0069. DOI: `10.1109/TMAG.2018.2843176`.

Stepper motors

[122] B. Aranjo, P. K. Soori, and P. Talukder. “Stepper motor drives for robotic applications”. In: *2012 IEEE International Power Engineering and Optimization Conference Melaka, Malaysia.* June 2012, pp. 361–366. DOI: `10.1109/PEOCO.2012.6230890`.

[123] D. Baker. “2 phase hybrid stepping motors”. In: *IEE Colloquium on Stepper Motors and Their Control.* 1994, pp. 2/1–2/3.

[124] R. Innes. “Industrial applications of stepper control systems”. In: *IEE Colloquium on Stepper Motors and Their Control.* Jan. 1994, pp. 5/1–5/3.

[125] I. Ionică et al. “Numerical analysis of a hybrid stepper motor for the electromagnetic torque calculation”. In: *2019 11th International Symposium on Advanced Topics in Electrical Engineering (ATEE).* Mar. 2019, pp. 1–6. DOI: `10.1109/ATEE.2019.8724921`.

[126] J. Kołota and S. Stępień. “Analysis of 3D model of reluctance stepper motor with a novel construction”. In: *2017 22nd International Conference on Methods and Models in Automation and Robotics (MMAR).* 2017, pp. 955–958. DOI: `10.1109/MMAR.2017.8046958`.

[127] B. Liu et al. “Compensation of load-dependent position error for a hybrid stepper motor”. In: *2017 IEEE International Conference on Mechatronics and Automation (ICMA).* Aug. 2017, pp. 846–851. DOI: `10.1109/ICMA.2017.8015926`.

[128] H. L. Oo et al. “Modelling and control of an open-loop stepper motor in Matlab/Simulink”. In: *2017 IEEE Conference of Russian Young Researchers in Electrical and Electronic Engineering (EIConRus).* 2017, pp. 869–872. DOI: `10.1109/EIConRus.2017.7910693`.

[129] R. P. Praveen et al. “Design and finite element analysis of hybrid stepper motor for spacecraft applications”. In: *2009 IEEE International Electric Machines and Drives Conference.* 2009, pp. 1051–1057. DOI: `10.1109/IEMDC.2009.5075334`.

[130] M. Y. Tarnini. “Fast and cheap stepper motor drive”. In: *2015 International Conference on Renewable Energy Research and Applications (ICRERA).* Nov. 2015, pp. 689–693. DOI: `10.1109/ICRERA.2015.7418499`.

[131] W. Yang and X. Sun. “Magnetic field finite element analysis and thrust characteristics calculation of a linear and rotary stepper motor”. In: *2011 International Conference on Electrical and Control Engineering.* Sept. 2011, pp. 2311–2314. DOI: `10.1109/ICECENG.2011.6057429`.

Electronics

[132] S. Ellingson. *Electromagnetics.* VT Publishing, Aug. 2018. DOI: `10.21061/electromagnetics-vol-1`.

[133] T. Harriehausen and D. Schwarzenau. *Moeller Grundlagen der Elektrotechnik.* Springer Fachmedien Wiesbaden, 2020. DOI: `10.1007/978-3-658-27840-3`.

[134] J. Heintze. *Lehrbuch zur Experimentalphysik Band 3: Elektrizität und Magnetismus.* Ed. by P. Bock. Springer Berlin Heidelberg, 2016. DOI: `10.1007/978-3-662-48451-7`.

[135] K. Küpfmüller, W. Mathis, and A. Reibiger. *Theoretische Elektrotechnik.* Springer Berlin Heidelberg, 2013. DOI: `10.1007/978-3-642-37940-6`.

[136] B. Morgenstern. *Elektronik.* Vieweg+Teubner Verlag, 1997. DOI: `10.1007/978-3-322-85053-9`.

[137] S. Paul and R. Paul. *Grundlagen der Elektrotechnik und Elektronik 2.* Springer Berlin Heidelberg, 2019. DOI: `10.1007/978-3-662-58221-3`.

[138] L. Warnes. *Electronic and electrical engineering.* Macmillan Education UK, 2003. DOI: `10.1007/978-0-230-21633-4`.

[139] C. Weddigen and W. Jüngst. *Elektronik.* Springer Berlin Heidelberg, 1986. DOI: `10.1007/978-3-662-06985-1`.

[140] D. Zastrow. *Elektronik.* Vieweg+Teubner Verlag, 2002. DOI: `10.1007/978-3-663-01107-1`.

Crank-Nicolson Oscillations

[141] D. Britz, O. Østerby, and J. Strutwolf. “Damping of Crank-Nicolson error oscillations”. In: *Computational biology and chemistry* 27 (Aug. 2003), pp. 253–63. DOI: `10.1016/S0097-8485(02)00075-X`.

[142] J. Crank and P. Nicolson. “A practical method for numerical evaluation of solutions of partial differential equations of the heat-conduction type”. In: *Mathematical Proceedings of the Cambridge Philosophical Society* 43.1 (1947), pp. 50–67. DOI: `10.1017/S0305004100023197`.

[143] R. C. Harwood, L. Zhang, and V. S. Manoranjan. “Oscillation-free method for semilinear diffusion equations under noisy initial conditions”. In: (2016).

[144] O. Østerby. “Five ways of reducing the Crank-Nicolson oscillations”. In: *BIT Numerical Mathematics* 43 (Jan. 2003), pp. 811–822. DOI: `10.1023/B:BITN.0000009942.00540.94`.

Co-Simulation and Multirate

[145] A. Bartel and M. Günther. *Inter/extrapolation-based multirate schemes – a dynamic-iteration perspective.* 2020.

[146] A. Bartel et al. "Dynamic iteration for coupled problems of electric circuits and distributed devices". In: *SIAM Journal on Scientific Computing* 35.2 (Jan. 2013), B315–B335. DOI: `10.1137/120867111`.

[147] M. Günther, ed. *Coupled multiscale simulation and optimization in nanoelectronics.* Springer Berlin Heidelberg, 2015. DOI: `10.1007/978-3-662-46672-8`.

[148] G. Jovanovic-Dolecek. *Advances in multirate systems.* Sept. 2017, pp. 1–221. DOI: `10.1007/978-3-319-59274-9`.

[149] P. Novák et al. "Engineering of coupled simulation models for mechatronic systems". In: *Service Orientation in Holonic and Multi-agent Manufacturing.* Ed. by T. Borangiu, A. Thomas, and D. Trentesaux. Cham: Springer International Publishing, 2015, pp. 3–11. ISBN: 978-3-319-15159-5. DOI: `10.1007/978-3-319-15159-5_1`.

[150] S. Schöps. "Coupling and simulation of lumped electric circuits refined by 3-d magnetoquasistatic conductor models using mna and fit". MA thesis. Bergische Universität Wuppertal, 2008.

[151] S. Schöps. "Multiscale modeling and multirate time-integration of field/circuit coupled problems". PhD thesis. Bergische Universität Wuppertal, 2011.

[152] B. Schweizer, ed. *IUTAM symposium on solver-coupling and co-simulation.* Springer International Publishing, 2019. DOI: `10.1007/978-3-030-14883-6`.

[153] M. Verhoef et al. "Case studies in co-modelling and co-simulation". In: *Collaborative Design for Embedded Systems: Co-modelling and Co-simulation.* Ed. by J. Fitzgerald, P. G. Larsen, and M. Verhoef. Berlin, Heidelberg: Springer Berlin Heidelberg, 2014, pp. 141–152. ISBN: 978-3-642-54118-6. DOI: `10.1007/978-3-642-54118-6_7`.

Solving linear tridiagonal systems

[154] J. Abderramán Marrero and V. Tomeo. "A fast and reliable numerical solver for general bordered -tridiagonal matrix linear equations". In: *Journal of Computational and Applied Mathematics* 318 (Aug. 2016). DOI: `10.1016/j.cam.2016.10.004`.

[155] M. Elmikkawy and F. Atlan. "Algorithms for solving linear systems of equations of tridiagonal type via transformations". In: *Applied Mathematics* 05 (Jan. 2014), pp. 413–422. DOI: `10.4236/am.2014.53042`.

[156] W. Ford. "Chapter 9 - algorithms". In: *Numerical Linear Algebra with Applications.* Ed. by W. Ford. Boston: Academic Press, 2015, pp. 163–179. ISBN: 978-0-12-394435-1. DOI: `10.1016/B978-0-12-394435-1.00009-0`.

[157] H. Macintosh et al. “Implementation of parallel tridiagonal solvers for a heterogeneous computing environment”. In: *ANZIAM Journal* 56 (Feb. 2016), p. 446. DOI: `10.21914/anziamj.v56i0.9371`.

[158] P. Valero-Lara et al. “A fast solver for large tridiagonal systems on multi-core processors (Lass library)”. In: *IEEE Access* 7 (2019), pp. 23365–23378. DOI: `10.1109/access.2019.2900122`.

Bracketing methods for solving scalar root problems

[159] A. Asghar. “Comparative study of existing bracketing methods with modified bracketing algorithm for solving nonlinear equations in single variable”. In: (Apr. 2016).

[160] M. Dowell and P. Jarratt. “A modified regula falsi method for computing the root of an equation”. In: *BIT Numerical Mathematics* 11.2 (June 1971), pp. 168–174. ISSN: 1572-9125. DOI: `10.1007/BF01934364`.

[161] S. Intep. “A review of bracketing methods for finding zeros of nonlinear functions”. In: *Applied Mathematical Sciences* 12.3 (2018), pp. 137–146. DOI: `10.12988/ams.2018.811`.

[162] D. E. Muller. “A method for solving algebraic equations using an automatic computer”. In: *Mathematical Tables and Other Aids to Computation* 10.56 (1956), pp. 208–215. ISSN: 08916837. DOI: `10.2307/2001916`. URL: `http://www.jstor.org/stable/2001916`.

[163] C. Ridders. “A new algorithm for computing a single root of a real continuous function”. In: *IEEE Transactions on Circuits and Systems* 26.11 (Nov. 1979), pp. 979–980. ISSN: 1558-1276. DOI: `10.1109/TCS.1979.1084580`.

[164] A. Suhadolnik. “Combined bracketing methods for solving nonlinear equations”. In: *Applied Mathematics Letters* 25.11 (2012), pp. 1755–1760. ISSN: 0893-9659. DOI: `10.1016/j.aml.2012.02.006`.